

Plasma spray deposition on surfaces with curvature

Ba, Te

2011

Ba, T. (2011). Plasma spray deposition on surfaces with curvature. Doctoral thesis, Nanyang Technological University, Singapore.

<https://hdl.handle.net/10356/48646>

<https://doi.org/10.32657/10356/48646>

Plasma Spray Deposition on Surfaces with Curvature



by

Ba Te

A thesis submitted to the
Nanyang Technological University
in partial fulfillment of the requirements for the degree of
Doctor of Philosophy

School of Mechanical and Aerospace Engineering
Nanyang Technological University

2011

Abstract

Plasma spraying has been widely used to apply coatings on complex engineering components due to its high deposition rate and wide choice of materials. However, the complexity of the components shape leads to the deficiency of the plasma spraying process. In addition, the coating profile continues to change, which will affect the subsequent spraying. Hitherto, the desired coating profiles need to be optimized, mostly by costly and extensive trial and error tests done by highly-trained manpower. A deposition model thus is desirable to predict the continuously changing profiles on complex surfaces. By this means, the cost and effort of the spraying test will be reduced significantly.

Curved surface or even more complex component surface can be considered to comprise of multiple flat surfaces. A semi-empirical methodology to predict the deposit formation on curved substrates has been developed in this thesis. The methodology is developed by three vital steps:

- Computational fluid dynamics (CFD) analysis to obtain the spatial distribution of particles and their corresponding in-flight parameters.
- Droplet splatting behavior analysis to establish correlations for spread factor, aspect ratio and elongation factor with respect to the impact velocity and impact angle.
- Modeling of deposit growth with time, with the data acquired in the particles parameters simulation and the correlations for splat morphologies.

In the CFD analysis using FLUENT V6.03©, the spraying process is modeled as a three-dimensional steady state plasma plume by the volumetric heating of the arc gas in the torch. Solutions of the plasma flow velocity and temperature fields are firstly obtained. Particles are introduced into and interact with the plasma flow by a one-way coupling method. The heat and momentum equations are solved

to obtain the spatial distributions of the particles and their corresponding in-flight parameters, including velocity, temperature, size and mass flow rate. SprayWatch® on-line diagnostics system is used to measure the particles velocity and flight angle for the freestream case (with no substrate inclusion). The simulated results captured by a plane at the distance 80 mm agree well with the SprayWatch® measurements. The particle parameters from simulation are used in the deposition code, while the SprayWatch® measurements are used for selection of droplet parameters in the simulation of droplet splatting behavior. The effect of substrate inclusion and shape on the particle in-flight behavior is also investigated. It is found that the substrate inclusion and shape (concave or convex) significantly influence the plasma flow fields in the vicinity of the substrate. The particles parameters remain relatively unaffected if their size is larger than a threshold value ($10\text{ }\mu\text{m}$).

The analysis of droplet splatting behavior is divided into two aspects:

- A droplet impacts onto the flat substrate under normal impact.
- A droplet impacts onto the curved substrate at different impact angles.

Individual splats are captured by the substrates with the help of a shutter system to avoid excessive particles impacting onto the substrate. The substrate is thin stainless steel sheets with a mean arithmetic surface roughness R_a of $0.2\text{ }\mu\text{m}$. The curved substrate is formed by wrapping the substrate sheet around a cylindrical surface. Before spraying, the substrate sheets are preheated at 873 K in order to capture relatively regular splats. After spraying, the curved substrate is flattened for characterization. The splats are characterized by scanning electronic microscopy (SEM) for flat substrate and optical microscope for curved substrate. The splat 3D profiles are measured by using the confocal imaging profiler.

Simulations are also carried out by Flow-3D®, a Volume of Fluid (VOF) featured CFD package to complement the experimental work. Spread factor and aspect ratio of the simulation results fall in the range of their experimental counterparts, which validate the numerical models. Formulae of spread factor, aspect ratio and elongation factors are derived to simplify the splat geometries, with respect to the impact

velocity and impact angle. Combining the simulation and experiments, droplet splatting behavior such as fringe elevation, jetting and fingering are analyzed. Jetting is found to occur at the early stage of the impacting, while fingers occurs after the droplet flattening ceases.

Having obtained the correlations of splat shapes with the impact velocity and impact angles, together with the particle parameters from the FLUENT© simulation, the deposition code is implemented to predict the deposit growth procedure. The deposit profile is updated at preset time steps, which makes the simulation more realistic, since the deposit profile affects the impact angle of individual particles. The impact angle is determined by the profile surface normal at the impact point. The prediction reasonably mimic the deposit growth with time. Good agreement of the peak deposit thickness is found between the simulation and SprayWatch© images.

Acknowledgments

Almost four years have passed, during which I devote myself to the research work in the Nanyang Technological University. There are many people whom I would like to thank from the bottom of my heart.

First and foremost, I would like to offer my sincere thanks to my supervisor Associate Professor Ng Heong Wah, for his immeasurable support during my study. His intuitive insight into a wide range of disciplines as well as his enthusiasm for the problems inspire me through the work. He always provides me English language guidance and writing skills advice.

I want to express my deepest gratitude to my senior student, Dr. Kang Changwei, who has lead me into the world of computational fluid dynamics and tutored me the operation of some of the facilities.

I would like to acknowledge all of the technicians in the CAE Lab 1, the Metrology Laboratory and the Materials Laboratory, whose computing and handling lab equipment expertise has aided me tremendously in the work.

Many thanks go to Mr. Sa'don Ahmed in the Innovation@MAE lab, my friends Ms. Zhang Ying in the School of Mechanical and Aerospace Engineering, Dr. Jiang Hui and Ms. Yuan Quan in the School of Materials Science and Engineering, who always try to find and fabricate materials for me and provide me measurement equipment.

Last but not least, my thanks go to my beloved parents who lives in the small and beautiful countryside of China. They are always understanding and supportive and never fail to pour me with unconditional love and care.

Table of Contents

Abstract	I
Acknowledgments	IV
List of Nomenclatures	IX
List of Figures	XIII
List of Tables	XXII
Chapter 1 Introduction	1
1.1 Background	1
1.2 Motivation of the Work	3
1.3 Objectives and Organization of the Thesis	5
Chapter 2 Literature Review	8
2.1 Introduction	8
2.2 Facilities and Powder	9
2.2.1 Facilities of the plasma spraying system	9
2.2.1.1 Spray torch	9
2.2.1.2 Powder feeder	10
2.2.1.3 Control console and cooling system	12
2.2.2 Powder	12
2.3 Investigations on Plasma Flow Field and In-flight Particle Behavior	15
2.3.1 Numerical investigations	15
2.3.1.1 Plasma flow Field	15
2.3.1.2 Particle behavior	19
2.3.2 Experimental Observations	24
2.3.2.1 Plasma field observation	24
2.3.2.2 Particle behavior observation	24
2.4 Investigations on Droplet Impacting Behavior	29
2.4.1 Parameters affecting droplet impact outcome	29
2.4.1.1 Properties of the impacted surface	30
2.4.1.2 Properties of the droplet	31
2.4.2 Experimental investigations	32
2.4.3 Theoretical and numerical methods for droplet impacting	35
2.4.3.1 The Madejski model	36
2.4.3.2 Heat transfer and solidification	39
2.4.3.3 Effects of viscosity, surface tension and wettability	42
2.4.3.4 Effect of oblique impact	44
2.5 Deposit Formation	48
2.5.1 Simulation work on Deposit Formation	48
2.5.2 Particle Rebound and Deposition Efficiency	53
Chapter 3 Experiments on the Plasma Spray Process	56

Table of Contents

3.1	Introduction	56
3.2	Spray facilities and parameters	58
3.3	In-flight particle behavior diagnostics by SprayWatch©	60
3.3.1	Measurement Volume and Focus Distance	60
3.3.2	Particle Velocity Measurement	62
3.3.3	Particle Temperature measurement	62
3.3.4	Observation by SprayWatch©	63
3.4	Single splat capture experiments	65
3.4.1	The substrate preparation	65
3.4.2	Experimental setup	67
3.4.3	Substrate temperature evolution evaluation	68
3.4.4	Experimental image analysis	72
3.4.4.1	Types of splats on the flat substrate.	72
3.4.4.2	Splat shape on the curved substrate	74
3.5	Experiments on Deposit Formation	79
3.5.1	Experimental setup	79
3.5.2	Deposition Efficiency	81
3.5.3	Calibration of the dimensions of images from SprayWatch©	81
3.5.4	3D profile measurement of sprayed deposit	82
Chapter 4	Simulation Methodologies	85
4.1	Introduction	85
4.2	Modeling and Simulation Methodology on Plasma Field and In-flight Particles	86
4.2.1	Geometry Design	86
4.2.2	Computing Strategy for Plasma Field	88
4.2.3	Plasma Flow Modeling	89
4.2.3.1	Governing equations	89
4.2.3.2	Plasma heat generation	90
4.2.3.3	Wall functions	90
4.2.4	Operating Parameters and Boundary Conditions	92
4.2.5	Particle dynamics and heat transfer modeling	93
4.3	Modeling and Simulation Methodology on Droplet Impact Behavior	96
4.3.1	Computing Strategy	96
4.3.1.1	Volume of Fluid (VOF) and Fractional and Volume Obstacle Representation (FAVOR™) method	96
4.3.1.2	The transport equations	97
4.3.2	Model Setup	99
4.3.2.1	Normal impact	99
4.3.2.2	Droplet impact on curved surfaces	103
4.3.3	Slices and lines for splat geometry evaluation	105
4.4	Numerical Methodology of Deposition Formation	107
4.4.1	Review on the geometrical relations	107

Table of Contents

4.4.2	Modeling assumptions	108
4.4.3	Data acquisition and manipulation	109
4.4.4	Time segmentation and deposit update	110
4.4.5	Determination of computational domain and gridding considerations	112
4.4.6	Modeling of single splat geometry on the deposit profile	113
4.4.7	Modeling of multiple overlapping splats	119
4.4.8	Overall model procedure and case implementation	121
Chapter 5	Results and Discussion	126
5.1	Introduction	126
5.2	Plasma Field Generation and In-flight Particle Behavior	127
5.2.1	Data acquisition lines and surfaces	127
5.2.2	Grid independence tests and verification of simulation model	130
5.2.3	Temperature and velocity distributions along axial centerline	131
5.2.4	Plasma plume thermal field	134
5.2.5	Plasma velocity field	136
5.2.6	Particles in-flight temperature, velocity and trajectory	141
5.2.7	Comparison between SprayWatch© diagnostics and the simulation	151
5.3	Droplet Impact Behavior and Splat Morphologies	153
5.3.1	Geometric quantities definition	153
5.3.2	Effect of impact parameters on the droplet impact behavior	156
5.3.2.1	Characterization of individual splats from confocal profiles on flat substrates.	156
5.3.2.2	Evolution of droplet morphology during impact	157
5.3.2.3	Effects of thermal parameters on splatting behavior	161
5.3.2.4	Effect of droplet velocity	167
5.3.2.5	Measurement of splat parameters	171
5.3.2.6	Summary on droplet splatting behavior	172
5.3.3	Splat morphology on the curved substrates	175
5.3.3.1	Splats characterization and analysis	176
5.3.3.2	Effects of surface curvature on the splat shape	180
5.3.3.3	Effect of impact angle on droplet flattening behavior on curved substrate	183
5.4	Deposit Formation	189
5.4.1	Experimental observations and analysis	189
5.4.2	Comparison between simulation results and experimental results of deposits	196
Chapter 6	Conclusions and Future Work	202
6.1	Conclusions	202
6.1.1	Introduction	202

Table of Contents

6.1.2	Plasma plume and in-flight particle behavior	203
6.1.3	Droplet splatting behavior on flat and curved substrate	204
6.1.3.1	Droplet splatting behavior on flat substrate	204
6.1.3.2	Droplet splatting behavior on curved substrate ..	205
6.1.4	Simulation and Experiment on Deposit Formation	205
6.1.5	Contributions	206
6.2	Suggested Future Work	208
Appendix A	List of Publications	209
Appendix B	Governing Differential Equation for Plasma Flow	210
Appendix C	Thermodynamic and Transport Properties of Gases	212
C.1	Argon Gas	212
C.2	Air	213
C.3	Mixture of Gases	214
Appendix D	Input Data Calculation for FLUENT© Simulation	215
Appendix E	Liquidus and Solidus Temperature of YSZ	217
Appendix F	The Ellipse Circumference Approximation	218
Appendix G	2D Cartesian Coordinates Transformation	220
Appendix H	The Deposition Code	222
References	228

List of Nomenclatures

a^*	Empirical constant (= 9.81)
a	Major radius of an ellipse (m)
a'	Projected major radius of an elliptical splat (m)
A_s	Splat area (m ²)
A_p	Surface area of the particle (m ²)
A_w	Interface area within the cell (m ²)
A_x	Area open to the flow in the x direction
A_y	Area open to the flow in the y direction
A_z	Area open to the flow in the z direction
b	Minor radius of an elliptical splat (m)
b'	Projected minor radius of an elliptical splat (m)
c	Focus distance of an elliptical splat (m)
C	Specific heat capacity (J/kgK)
C_μ	Empirical constant (= 0.09)
$C_{1\varepsilon}$	Empirical constant (= 1.44)
$C_{2\varepsilon}$	Empirical constant (= 1.92)
C_∞	Specific heat capacity of the plasma (J/kgK)
C_D	Drag coefficient
d	Splat diameter (m)
D	Particle (droplet) diameter (m)
DoF	Depth of the measurement volume of SprayWatch© (mm)
E	Arc voltage (V)
F	The VOF function value
F_D	Viscous drag force of the particle (N)
f_x	Viscous acceleration in the x -direction (m/s ²)
f_y	Viscous acceleration in the y -direction (m/s ²)
f_z	Viscous acceleration in the z -direction (m/s ²)
$FOVX$	Width of the measurement volume of SprayWatch© (mm)
$FOVY$	Height of the measurement volume of SprayWatch© (mm)
G_k	Product of the eddy viscosity and viscous dissipation terms
H	Enthalpy (J/kg)
h	Heat transfer coefficient (W/mK)
H_v	Latent heat of vaporization (J/kg)

List of Nomenclatures

H_f	Latent heat of fusion (J/kg)
I_A	Arc current (A)
I	Macroscopic mixture internal energy (J/kg)
I_t	Turbulent intensity (%)
k	Thermal conductivity (J/gK)
K	von Kármán constant (= 0.42)
l	Splat elongation distance under an oblique impact (m)
l'	Projected splat elongation distance under an oblique impact (m)
L	Length of the curved substrate (mm)
mfr	Mass flow rate of the particles from FLUENT® simulation
m_p	Mass of particle (kg)
p	Pressure (Pa)
P'''_{in}	Constant heat source (W/m ³)
q	Heat transfer rate through a specific surface in a cell (W)
Q_c	Convective heat transfer (J)
$R1$	Inner radius of the curved substrate (mm)
$R2$	Outer radius of the curved substrate (mm)
Re_d	Reynolds number based on the particle diameter (m/s)
S_Φ	Source term
S_e	Splat circumference (m)
t	Splat thickness (m)
t'	Deposit growth distance (m)
t_p	Deposit peak thickness (m)
t_{pm}	Deposit maximum peak thickness (m)
T_b	Boiling point of yttria stabilized zirconia (K)
T_l	Liquidus temperature of yttria stabilized zirconia (K)
T_m	Melting point of yttria stabilized zirconia (K)
T_s	Solidus temperature of yttria stabilized zirconia (K)
T_E	Plasma temperature at an element point adjacent to the wall (K)
T_i	Initial particle temperature (K)
T	Particle temperature (K)
T_W	Plasma temperature on the substrate wall (K)
T_∞	Local temperature of the plasma (K)
T_{dif}	Heat conduction diffusion term (W/m ³)
T_{sor}	Liquid-substrate heat transfer (W/m ³)
u, v, w	Velocity components in x , y and z directions (m/s)
U	Velocity magnitude (m/s)
U_E	Plasma velocity at an element point adjacent to the wall (m/s)

List of Nomenclatures

V	Droplet velocity (m/s)
\vec{V}	Velocity vector (m/s)
V'	Velocity vector fluctuation (m/s)
V_a	Plasma torch anode volume (m ³)
V_F	Volume open to the flow
V_n	Volume fraction for species n
V_p	Particle velocity vector (m/s)
V_s	Splat Volume (m ³)
W	Width of the curved substrate (mm)
wsx	Shear stress in the x -direction (N/m)
wsy	Shear stress in the y -direction (N/m)
wsz	Shear stress in the z -direction (N/m)
W_p	Energy increase of the particle (J)
X_p	Position of the particle motion (m)
y	Distance from element to the wall (m)
Y_n	Mass fraction for species n
y_E	Distance from adjacent element point to the wall (m)
Subscript	
∞	Far field region
l	Liquidus state
p	Particle
s	Solidus state
t	Turbulent state
w	Property of the wall
mix	Mixture properties
Greek symbols	
α	Elongation angle (rad)
ε	Turbulent kinetic energy dissipation rate (m ² /s ²)
ζ	Aspect ratio of an elliptical splat
η	Torch efficiency (%)
Γ_Φ	Diffusion coefficient
κ	Turbulent kinetic energy (m ² /s ²)
μ	Dynamic viscosity (kg/ms)
ν	Kinematic viscosity (kg/ms)
θ	Droplet impact angle (degree)
ξ	Spread factor of the splat
χ	Elongation factor of the splat
Φ	Process variable

List of Nomenclatures

ρ	Density (kg/ms)
τ_w	Wall shear stress (Pa)
Dimensionless numbers	
Pr	Prandtl number
Re	Reynolds number
U^*	Dimensionless mean velocity
y^*	Dimensionless distance from element to the wall
y_T^*	Dimensionless thermal sublayer thickness

List of Figures

Fig. 1.1	Schematic illustration of plasma spraying process with three regimes.	2
Fig. 1.2	(a) The world's largest gas turbine blades in Irsching power station in Bavaria (Reference Number: PN200909-06, Siemens photo newsletter) and (b) the plasma spraying process to apply coatings on the blade (Reference Number: PN200807-01, Siemens photo newsletter). .	3
Fig. 1.3	Thesis organization chart, showing relationships between chapters.	6
Fig. 2.1	A typical configuration of the plasma spraying system.	9
Fig. 2.2	Illustration of a DC plasma torch design, taking SG-100 as an example (Praxair Surface Technologies Inc., 1998).	10
Fig. 2.3	Design of a common volumetric feeder (reproduced after [9]). .	11
Fig. 2.4	Relation between the powder feed rate and the wheel spinning speed for different types of materials [10].	11
Fig. 2.5	Equilibrium zirconia-yttria phase diagram[15].	13
Fig. 2.6	Effect of electromagnetic force on the radial (a) plasma temperature and (b) velocity at the torch exit. Current $I = 750$ A; Ar (0.59 scmh)[34].	17
Fig. 2.7	Influence of different $k - \epsilon$ turbulence models on the computed flow (a) temperatures and (b) velocities in the axial torch axis. 17.7 KW, 85 l/min Ar-H ₂ [40].	19
Fig. 2.8	Schematic of the particle geometry and heating model[57].	22
Fig. 2.9	Particle surface temperature and melting state for different sizes of ZrO ₂ particles, comparing with experimental data[59].	23
Fig. 2.10	The influence of (a) arc current and (b) gas flow rate on an argon plasma jet ($I = 200$ A)[60].	24
Fig. 2.11	Particle trajectories and number flux distributions. Alumina powder diameter $= 18.0 \pm 3 \mu\text{m}$; carrier gas flow rate 5.5 l/min[61].	25
Fig. 2.12	Particle trajectories with water-cooled powder injection probe at jet fringe[61].	25
Fig. 2.13	Particle number flux, velocity, and surface temperature profiles at $Z = 75$ mm. Alumina powder diameter $= 18.0 \pm 3 \mu\text{m}$; carrier gas flow rate 5.5 l/min; Ar-H ₂ 90 l/min; 29.2 kW[61].	26
Fig. 2.14	YSZ particle temperature and velocity at the spray distance of 130 mm[6].	27
Fig. 2.15	The optical layout of PDA system[62].	27

List of Figures

Fig. 2.16	SEM of typical morphologies of sprayed alumina in (a) cross -section view and (b) a top view[65], showing the accumulated layer structure of the coating.	29
Fig. 2.17	Illustration of parameters affecting droplet impact phenomena.	30
Fig. 2.18	Diagram of the apparatus designed by Worthington to view droplet impact behavior[76].	32
Fig. 2.19	Engravings of instantaneous photographs of the splash of a milk droplet falling 20 cm on to smoked glass by Worthington[76].	33
Fig. 2.20	Experimental apparatus used to capture droplet impact behavior[77].	34
Fig. 2.21	Schematic of radiation images capturing system for plasma spray particles designed by McDonald et al.[84]	35
Fig. 2.22	Coordinate system definition (reproduced after Madejski). (a) $t' = 0$, (b) $t' > 0$ (reproduced after Madejski[90]).	36
Fig. 2.23	Perfect formation of disk-shaped splat from a spherical molten droplet.	37
Fig. 2.24	Dependence of fraction of disk splat and coating adhesion strength on substrate temperature[103].	40
Fig. 2.25	Relationship between thermal conductivity of substrate and transition temperature[102].	40
Fig. 2.26	Comparison between experimental observations and simulation results for the spreading and simultaneous solidification of a tin droplet on an alumina substrate[98].	41
Fig. 2.27	Interface velocity as a function of the interface location from the contact surface for a 1 μm thick pure zirconia splat quenched on a zirconia substrate: effect of the thermal contact[64].	42
Fig. 2.28	Viscous dissipation dominating region was above the lines representing the criteria for different materials. The shadowed area represented the typical conditions in plasma spraying[107].	43
Fig. 2.29	Experimental set-up to perform the tests by Montavon et al., showing spray angle definition[108].	45
Fig. 2.30	Water droplet impact onto a stainless steel (a) inclined surface (b) edge with right angle surfaces[77].	45
Fig. 2.31	Profile of side view of a 2 mm diameter water droplet at 1 m/s onto (a) a 45° stainless steel inclined surface and (b) 1 mm high stainless steel edge. Photographs at left, simulation results at right[77].	46
Fig. 2.32	Infrared image of the HVOF thermal spray impinging on a flat plate[111].	47
Fig. 2.33	Build up of two splats: (a) and (b) two distinct splats, (c) build up of these two splats[112].	48
Fig. 2.34	Actual and simulated cross sections of porous APS and HPPS coatings[112].	49
Fig. 2.35	Schematic diagram of a thermal spray process[114].	50

List of Figures

Fig. 2.36	Schematic diagram of the impact splat shapes when overlapping with the other splats[115].	51
Fig. 2.37	In situ observation of deposit formation by Shinoda et al. (a) 12s, (b) 43s, (c) 64s after powder injection. (d) after deposition.	53
Fig. 2.38	Images of particles (a) impacting on the perpendicular substrate, (b) deflected by the substrate in an inclination angle 60°.	54
Fig. 3.1	Schematic illustration of the workflow of the experiments. The shaded square area represents the measurement area of the SprayWatch®.	57
Fig. 3.2	Schematic illustration of the SG-100 torch gun.	58
Fig. 3.3	SEM photograph of yttria partially stabilized (8wt%) zirconia (YSZ) powder showing near-perfect spherical particles.	59
Fig. 3.4	SprayWatch setting for particle in-flight parameters diagnostics and definition of some measurement terms.	61
Fig. 3.5	Side view of the measurement volume in the plasma spray plume.	62
Fig. 3.6	Example of the captured image of plasma spray process by SprayWatch®.	63
Fig. 3.7	Particle (a) velocity magnitude and (b) flight angle distribution histogram and probability plot from SprayWatch® diagnostics.	64
Fig. 3.8	Particle temperature measured by SprayWatch®. Median values, upper boundary and lower boundary values are shown respectively with the time frame.	64
Fig. 3.9	EDS analysis spectrum of the substrate surface.	66
Fig. 3.10	Quarz tube heater used for substrate sheets preheating.	66
Fig. 3.11	The fixing of substrate sheet around the cylindrical holder	67
Fig. 3.12	Plasma spray system setting for the single splat capturing, showing the “shutter system”.	68
Fig. 3.13	Substrate sheet surface temperature measurement system.	69
Fig. 3.14	The thermocouple attachment under the substrate sheet.	69
Fig. 3.15	Data logger used to record the temperature data from the thermocouples.	69
Fig. 3.16	The three phases during splat capture experiment	70
Fig. 3.17	Substrate sheet surface temperature development behavior during and after spraying without a shutter blockage.	71
Fig. 3.18	Substrate sheet surface temperature development behavior with 4 s preheat phase.	71
Fig. 3.19	Substrate sheet surface temperature evolution behavior with 2 s preheat phase.	72
Fig. 3.20	A broad view of the substrate with many splats on it.	73
Fig. 3.21	Typical splats found on the flat substrate.	73
Fig. 3.22	The conversion between splat location on curved substrate sheet and the flatten sheet.	74
Fig. 3.23	The locating of the splat under microscope.	75

List of Figures

Fig. 3.24	Optical micrographs of splats produced at different impact angles.	77
Fig. 3.25	Example of snapshots of splats at different impact angles under confocal imaging profiler.	78
Fig. 3.26	Curved specimen used in the deposit formation experiment. ..	79
Fig. 3.27	Illustration of three experimental cases being carried out. The deposit resides on (a) case 1, the upper part of the substrate surface; (b) case 2, the middle part of the substrate surface; (c) case 3, the lower part of the substrate surface.	80
Fig. 3.28	An example of image at the focus distance 215 mm by SprayWatch© for dimensions calibration. A metal ruler is included for reference purpose.	82
Fig. 3.29	The measurement volume length and height correlate with the focus distance.	83
Fig. 3.30	TalyScan 150 3D scanning system.	83
Fig. 3.31	Deposit profiles from TalyScan measurements.	84
Fig. 4.1	Model of computational domain of plasma spray.	86
Fig. 4.2	3D view of computational domain of plasma spray.	87
Fig. 4.3	Schematic illustration of substrate shape.	87
Fig. 4.4	Schematic Illustrations of substrate orientation: (a) concave case (b) convex case.	88
Fig. 4.5	Illustration of computational domain and mesh setup for droplet impacting perpendicularly on the substrate. The computational domain includes a quarter of the droplet and part of the substrate beneath it.	99
Fig. 4.6	Illustration of velocity selection based on the particle velocity distribution from SprayWatch© diagnostics.	102
Fig. 4.7	Illustration of splat thickness evaluation on a curve surface. ..	104
Fig. 4.8	Illustration of computational domain and meshing in the cylindrical coordinate (conformed to the substrate).	104
Fig. 4.9	Lines and sections definition to extract simulation variables and splat morphology dimensions.	105
Fig. 4.10	Center surface of the computational domain, showing the bottom surface (side view) conformed to the curved shape of the substrate.	106
Fig. 4.11	Illustration of simplified splat morphology under normal impact and oblique impact.	108
Fig. 4.12	Illustration of acquisition of particles in-flight parameters used for deposit simulation at the virtual plane.	109
Fig. 4.13	Illustration of time segmentation of author's code for deposit simulation.	111
Fig. 4.14	Illustration of the coordinate system in the author's code and the alignment of the substrate.	112

List of Figures

Fig. 4.15	Out-of-plane view of the deposit (a) without annotation (b) with annotation, showing the halo phenomena. The deposit is taken from case 2, the one formed in the middle part of the substrate.	113
Fig. 4.16	The two-dimensional computational domain for deposit profile and its gridding.	113
Fig. 4.17	Determination of (a) the impact surface facet vertex and (b) the computation of the surface normal at the impact point.	114
Fig. 4.18	Projection of a single elliptical splat on the deposit surface onto the $x - y$ two-dimensional plane and the transformation between the global coordinate system and the splat coordinate system.	115
Fig. 4.19	Determination of nodes for an individual splat thickness calculation.	118
Fig. 4.20	Node advancement along z axis caused by single splat depositing.	120
Fig. 4.21	Schematic illustration of the deposition model depicting the thickness build-up of two overlapping splats.	120
Fig. 4.22	Flowchart of the the deposit model implementation procedure.	122
Fig. 4.23	Determination of the deposit position and apex height for case 1.	125
Fig. 4.24	Determination of the deposit position and apex height for case 2.	125
Fig. 4.25	Determination of the deposit position and apex height for case 3.	125
Fig. 5.1	Schematic Illustration of centerline and YZ- and XZ-plane slices.	127
Fig. 5.2	Schematic illustration of side view of parallel data acquisition surface.	128
Fig. 5.3	Schematic illustration of inner region and outer region of the parallel data acquisition surface.	129
Fig. 5.4	Schematic Illustration of flattening parallel curved surface into developed surface: (a) original surface; (b) developed surface.	129
Fig. 5.5	Grid independence tests for Freestream by comparison of contours of (a) temperature and (b) velocity in XZ plane. ..	130
Fig. 5.6	Verification of simulation model by comparison with experimental data from McKelliget et al.[129] in (a) temperature and (b) axial velocity along centerline.	131
Fig. 5.7	Prediction of axial centerline distribution of (a) plasma temperature, (b) plasma velocity. Fr stands for freestream case, S1 and S2 represent the two substrates, C and V represent concave and convex orientations respectively.	133
Fig. 5.8	Comparison of plasma temperature contours in XZ- and YZ-planes for the substrate S1 in the concave (C) and convex (V) orientations.	134

List of Figures

Fig. 5.9	Comparison of plasma temperature contours in XZ- and YZ-planes for the substrate S2 in the concave (C) and convex (V) orientations.	135
Fig. 5.10	Temperature contours in near and far surfaces for four different cases with substrates. S1 and S2 represent the two substrates, C and V represent concave and convex orientations respectively.	136
Fig. 5.11	Comparison of plasma velocity contours in XZ- and YZ-planes for S1-C case. C represents concave orientation. ...	137
Fig. 5.12	Velocity contours in near and far surfaces for four different cases with substrates. S1 and S2 represent the two substrates, C and V represent concave and convex orientations respectively.	138
Fig. 5.13	Plasma velocity vectors in XZ- and YZ-planes of four cases with substrates. S1 and S2 represent the two substrates, C and V represent concave and convex orientations respectively.	139
Fig. 5.14	Plasma velocity vectors in near surface of four cases with substrates. S1 and S2 represent the two substrates, C and V represent concave and convex orientations respectively. ...	140
Fig. 5.15	Injection types: (a) point Injection; (b) surface Injection.	141
Fig. 5.16	Trajectories of particles injected from injection port center: #1, 2.20 μm ; #2, 4.78 μm ; #3, 7.35 μm ; #4, 9.95 μm ; #5, 12.5 μm	142
Fig. 5.17	Particles temperature profile along their trajectories. #1, 2.20 μm ; #2, 4.78 μm ; #3, 7.35 μm ; #4, 9.95 μm ; #5, 12.5 μm . ..	143
Fig. 5.18	Particles velocity profile along their trajectories. #1, 2.20 μm ; #2, 4.78 μm ; #3, 7.35 μm ; #4, 9.95 μm ; #5, 12.5 μm . ..	144
Fig. 5.19	Particle distribution comparison between freestream and S2-C with 3 μm uniform particles injection. Y' scale is larger than the X axis for a better illustration.	145
Fig. 5.20	Particle distribution comparison between freestream and S2-C with 5 μm uniform particles injection. Y' scale is larger than the X axis for a better illustration.	146
Fig. 5.21	Particle distribution comparison between freestream and S2-C with 10 μm uniform particles injection. Y' scale is larger than the X axis for a better illustration.	146
Fig. 5.22	Comparison of contours of particle in-flight parameters; results from the S2-C case is illustrated in the left column, while the corresponding freestream case in the right column. .	147
Fig. 5.23	Particle temperature distribution histogram (lower figure) and probability plot (upper figure) in S2-C case.	149
Fig. 5.24	Particle temperature and mean temperature distribution versus diameter.	150
Fig. 5.25	Particle velocity magnitude distribution histogram and probability plot from (a) SprayWatch© diagnostics and (b) simulation.	151

List of Figures

Fig. 5.26	Particle velocity magnitude distribution histogram and probability plot from (a) SprayWatch© diagnostics and (b) simulation.	152
Fig. 5.27	Illustration of a molten droplet impacting on the substrate to form a disk-shape splat.	153
Fig. 5.28	Perfect formation of (a) a circular splat from normal impact and (b) an elliptical splat from oblique impact.	155
Fig. 5.29	Idealized illustration of the aerial view of the splat for the case of normal impact and oblique impact.	156
Fig. 5.30	(a) Image maps and (b) 3D shaded rendering images constructed from the profile data acquired by confocal imaging profiler.	157
Fig. 5.31	Evolution of droplet morphology during its impact perpendicularly onto the substrate. The contour is based on the value of Volume of Fluid.	158
Fig. 5.32	Evolution of droplet morphology at the center surface during its impact perpendicularly onto the substrate. The contour is based on the value of Volume of Fluid.	160
Fig. 5.33	Cross section view of a splat at the center surface, showing different extents of fringe elevation under different droplet temperature. The contour is based on the value of Volume of Fluid.	163
Fig. 5.34	Cross section view of a splat at the center surface, showing different extents of fringe elevation under different heat transfer coefficient. The contour is based on the value of Volume of Fluid.	164
Fig. 5.35	Cross section view of a splat at the center surface at different time frame, under a low heat transfer coefficient $2 \times 10^5 \text{ W/m}^2\text{K}$. The contour is based on the value of Volume of Fluid.	165
Fig. 5.36	Cross section view of a splat at the center surface, showing different extents of fringe elevation for different substrate surface temperature. The contour is based on the value of Volume of Fluid.	166
Fig. 5.37	Cross section of a splat at the bottom surface, showing different spread degree for different velocity. The contour is based on the value of Volume of Fluid.	169
Fig. 5.38	Cross section of a splat at the bottom surface, showing different jetting behavior at different combinations of substrate temperature, droplet temperature and interface heat transfer coefficient. The contour is based on the value of Volume of Fluid.	170
Fig. 5.39	Relationship of splat spread factor and the droplet velocities derived from the simulation.	172
Fig. 5.40	Illustration of the formation of short and long fingers.	173

List of Figures

Fig. 5.41	Droplet morphology evolution during impact in the case of high velocity (400 m/s) and high temperature (3800 K). Legend displays 0 values for all contour range due to fully liquidus state at these time frames in the simulation.	175
Fig. 5.42	SEM photo of the splat, showing two-layer characteristic, short and longer fingers.	176
Fig. 5.43	An illustration of an ellipse, which is a simplified splat shape, used to represent a splat shape at oblique impact. (a) Example splat at the impact angle 46° , (b) Simplified elliptical shape.	177
Fig. 5.44	Aspect ratio calculated from the splats with respect to the impact angle.	178
Fig. 5.45	Spread factors of splats at different impact angles of the substrate.	178
Fig. 5.46	Image and 3D surface contours of some of the splats at different impact angles, which are reconstructed from confocal data. The unit along all the three axes are μm , the curved surface radius is 13.8 mm.	179
Fig. 5.47	Bottom surfaces of splats on curved surface at the impact angle of 0° (a-c) and under normal impact on flat surface (d-f). The radius of the curved surface is 13.5 mm, the curvature direction is along the x axis. The contour is based on the value of Volume of Fluid.	181
Fig. 5.48	Bottom surfaces of splats on curved substrate with diameter (a) 1mm and (b) 2mm.	182
Fig. 5.49	Illustration of extraction of the elliptical distance c and elongation distance l , showing the case at impact angle $\theta = 40^\circ$ under velocity 200 m/s.	183
Fig. 5.50	“Bottom surfaces” of splats on curved surface (radius 13.8 mm) at different impact angles, impact velocity of 120 m/s.	184
Fig. 5.51	“Bottom surface” of splats on curved surface (radius 13.8 mm) at different impact angles, impact velocity of 200 m/s.	185
Fig. 5.52	“Bottom surface” of splats on curved surface (radius 13.8 mm) at different impact angles, impact velocity of 300 m/s.	185
Fig. 5.53	Relationship of aspect ratio (ζ) and the impact angle θ derived from the simulation.	186
Fig. 5.54	Relationship of the elongation factor χ with respect to the impact angle under different velocities.	188
Fig. 5.55	Side view of deposit growing for case 1 by SprayWatch® diagnostics.	190
Fig. 5.56	Maximum curvature evaluation of the deposit at the last time frame for case 1.	191
Fig. 5.57	Rebound phenomenon occurs during the depositing.	192
Fig. 5.58	Out-of-plane view of the as-sprayed substrates.	194
Fig. 5.59	Contours of (a) number of particles (b) mass flow rate in the virtual plane from simulation results for the freestream case.	195

List of Figures

Fig. 5.60	Simulated deposit growth on the flat surface.	196
Fig. 5.61	Side view of experimentally obtained deposit on the flat substrate[113].	197
Fig. 5.62	Deposit profile growth for case 1 from (a-c) SprayWatch© diagnostics and (d-f) simulation . Time frame 1: 4s, time frame 2: 6s, time frame 3: 9s.	198
Fig. 5.63	Deposit profile growth for case 2 from SprayWatch© diagnostics (a-c) and simulation (d-f). Time frame 1: 2s, time frame 2: 3s, time frame 3: 5s.	199
Fig. 5.64	Deposit profile growing for case 3 from SprayWatch© diagnostics (a-c) and simulation (d-f). Time frame 1: 5s, time frame 2: 6s, time frame 3: 8s.	200
Fig. 5.65	3D profiles of deposit on case 1, 2 and 3 from TalyScan (a-c) and simulation (d-f).	201
Fig. C.1	Variation of argon gas (a)density (b) specific heat (c) thermal conductivity and (d) viscosity with respect to temperature.	212
Fig. C.2	Variation of air gas (a)density (b) specific heat (c) thermal conductivity and (d) viscosity with respect to temperature. ...	213
Fig. E.1	Equilibrium phase diagram of Yttria-Zirconia system	217
Fig. G.1	Illustration of 2D Cartesian coordinate transformation.	220

List of Tables

Table 2.1	Collection of zirconia properties from the literature.	14
Table 2.2	A collection of spread factor ξ related constants a and b obtained from the literature.	38
Table 2.3	A collection of spread factor ξ obtained by plasma-sprayed zirconia on various substrates. Surface roughness is denoted by Ra, substrate temperature T_s . The spread factor ξ is average value, while the range is in the braces.	38
Table 2.4	The maximal residual errors resulting from different cell sizes. .	50
Table 2.5	Equations to describe splat shapes in the Ghafouri-Azar[114] and Xue[115] model.	52
Table 2.6	Collection of deposition efficiencies from the literature.	55
Table 3.1	Experimental spray parameters.	58
Table 4.1	Dimensional specifications and orientation of substrates in five model cases.	88
Table 4.2	The process variables, diffusion coefficients and source terms for Equation 4.1.	90
Table 4.3	Operating parameters for plasma simulation	92
Table 4.4	Thermophysical properties of YSZ, stainless steel substrate and interface parameters between droplet and substrate.	100
Table 4.5	Initial conditions for numerical simulation.	101
Table 4.6	Simulation cases implemented for the normal impact.	103
Table 4.7	Image dimension calibration for cases 1 to 3 and the final maximal deposit projected thickness t_{pm}	124
Table 5.1	Simulation cases implemented for the normal impact with fixed velocity 200 m/s.	161
Table 5.2	Simulation cases implemented for the normal impact with fixed interface heat transfer coefficient 10^6 W/m ² K, droplet temperature 3500 K, substrate temperature 823 K. . . .	167
Table 5.3	The impact parameters setting for the simulations on droplet jetting behavior.	170
Table 5.4	Calculated splat area, volume, diameter and the corresponding spread factor.	171
Table 5.5	Spread factor of splats when droplets impact at the impact angle of 0° on curved substrate surface and on flat surface under normal impact.	180
Table 5.6	Spread factor of splats when droplets impact at impact angle 0° with surface curvatures in the simulation.	182

List of Tables

Table 5.7	Major radius a , minor radius b , spread factor ξ and aspect ratio ζ of splats when droplets impact at different impact angles with different impact velocities.	184
Table 5.8	Elliptical splat focus distance c and elongation distance l at different impact angles under different impact velocities derived from the simulation.	187
Table 5.9	Comparison of maximum peak deposit thickness t_{pm} (mm) for three cases.	197

Chapter 1

Introduction

1.1 Background

Plasma spraying is a technique by which finely-divided metallic or non-metallic (typically ceramic) materials are deposited in a molten or semi-molten state on a prepared substrate. The application of this process, is to impart desired properties to the industrial components and parts working under severe conditions. Conventionally, it is used to produce coatings easily and flexibly with excellent wear- and corrosion-[1 and 2], thermal-[3] or fracture-[4] resistance. Apart from the fundamental specification of increasing the life-cycle (i.e. ensuring minimal rates of change in both shape and constitution) of material surface, there is also a list of additional requirements - economic considerations and environmental compatibility - that have to be taken into account when designing an industrial surface-coating process.

The extensive applications of plasma spray coating is attributable to various advantages:

- It is a rapid and instantaneous fabrication process, i.e., the coatings are formed within minutes.
- High deposition rates.
- Versatility of the feedstock materials: metal or non-metal such as ceramic and hydroxyapatite(HA); pure material or mixture (functionally graded materials).
- Vacuum environment can be employed to avoid the oxidation of metallic feedstock.

Based on the underlying physical and chemical events occurring during the entire process, plasma spray system can be considered to be comprised of three regimes, as shown in **Fig. 1.1**.

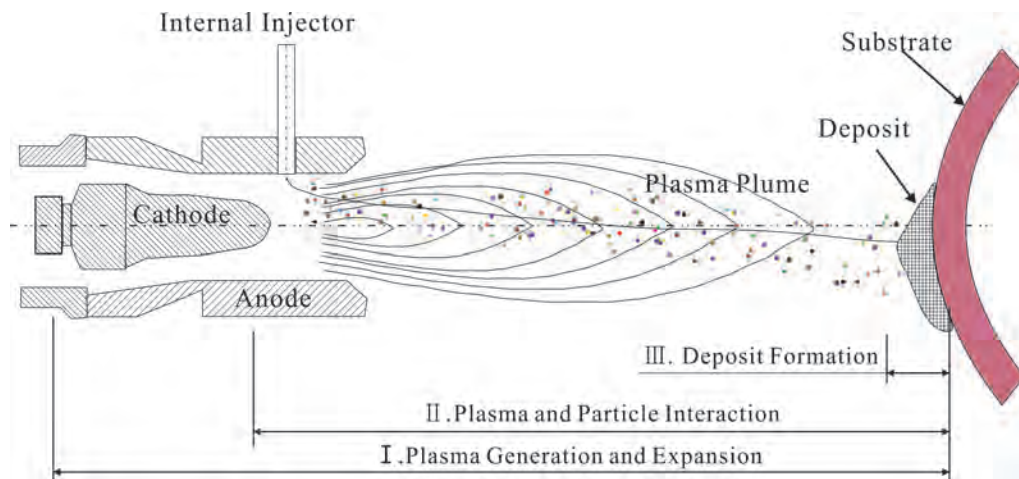


Fig. 1.1 Schematic illustration of plasma spraying process with three regimes.

These three regimes are interrelated. However, they can be separated for investigation convenience, together with the process parameters. In regime I (plasma generation and expansion), a high intensity electric arc is struck between the cathode and anode to ionize the plasma forming gases to generate a heat source capable of melting any particulate materials. The plasma gas expands from the torch into the atmosphere environment or a vacuum chamber. In regime II (plasma and particle interaction), the feedstock powders are fed into the plasma gas to be heated, melted and accelerated through heat and momentum transfer. The powder particles (molten or semi-molten) eventually impact on the substrate. In regime III (droplet splatting and deposit formation), with high velocity. Every single particle, usually considered as a droplet in analytical and numerical investigations, experiences deforming, spreading, solidifying and some other physical or chemical transition, to form a splat (lamella). The deposit is built from the accumulation of millions or even more of such lamellas.

1.2 Motivation of the Work

In the industry, such as aerospace and motor industry, a considerable number of mechanical parts are not of a simple flat shape, for example, the gas turbine blade. **Fig. 1.2** shows the record-breaking turbine blades used in Irsching power station in Bavaria (January 2008) and the plasma spraying process to apply coatings on the blade. Moreover, the requirements for coating on specimen may be different for various applications. For example, there is a special requirement for the coating thickness on the turbine blade, i.e., thicker at the leading edge, and reducing towards the trailing edge. In the deposition procedure, the coating morphology changes continuously with the spraying, which could be considered as varying surface for the subsequent particles. All these highlight the necessity of investigation on spraying complex surfaces.

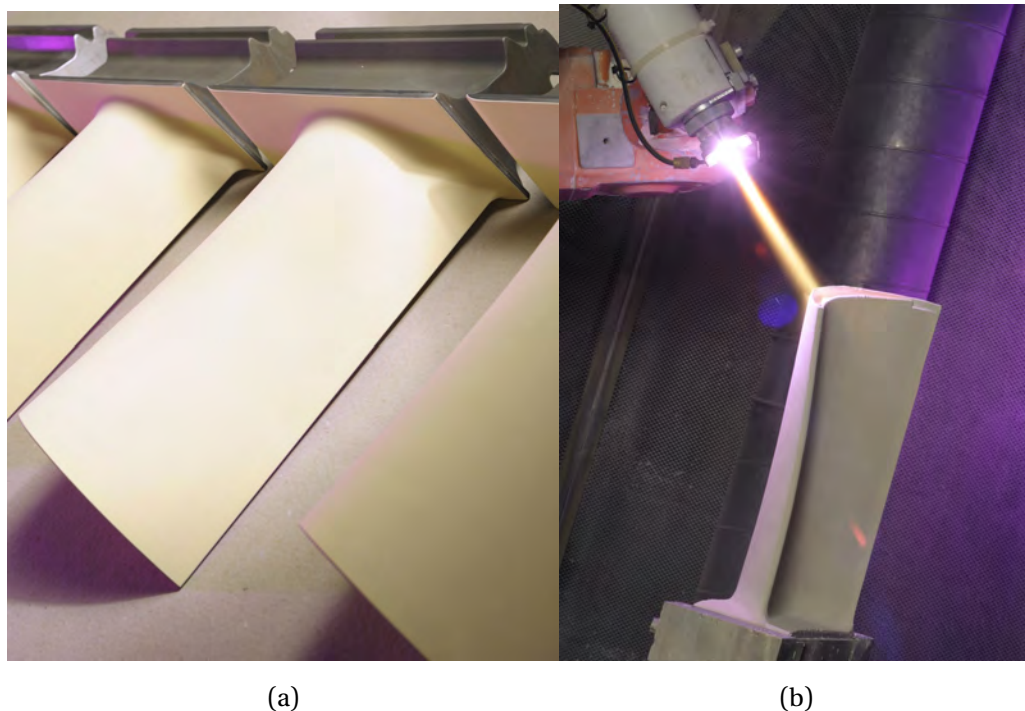


Fig. 1.2 (a) The world's largest gas turbine blades in Irsching power station in Bavaria (Reference Number: PN200909-06, Siemens photo newsletter) and (b) the plasma spraying process to apply coatings on the blade (Reference Number: PN200807-01, Siemens photo newsletter).

Most of the complex industrial components can be considered as a curved shape, or composed of some simple shapes including curved surface. Therefore it is very important to investigate the plasma spray parameters with inclusion of curved

substrates and the resultant coating qualities. The purpose of the work in this thesis is a systematic investigation on the yttria-stabilized zirconia coating growth on curved substrates by plasma spray process.

In addition, plasma spraying is a very complicated system including various process parameters, such as power source, nozzle parameter, feeding stock selection, injection methods and substrate conditions, etc. These parameters contribute synergically to the final coating quality, which makes the optimization of the plasma spray difficult in experiments and industry[5 and 6]. Therefore, numerical modeling becomes a powerful and effective auxiliary tool to improve plasma spray processes. The work in this thesis focuses on two different but complementary aspects of this process – experiments and simulations – to reasonably predict the deposition formation.

1.3 Objectives and Organization of the Thesis

One of the major objectives is to develop a simulation model for the deposit build-up on the curved surfaces. The idea originates from the observation from SprayWatch® that the particles impact on the continuously varying deposit profile. Therefore, the model is expected to mimic this procedure recorded by SprayWatch®. Besides, the model adopts data and correlations from the in-flight particles behavior and splat formation investigations. Both of these two investigations involve simulations and experiments, which should be comparable with each other. Last but not least, the investigations on the particle behavior and the splat formation, although pertinent to the deposit formation, are standalone subtopic that will yield findings of value to their individual scenarios. Detailed description of organization of the thesis is provided in the following paragraphs.

As shown in the flow chart in **Fig. 1.3**, the thesis is composed of six chapters, including **Chapter 1: “Introduction”** and **Chapter 6: “Conclusions and Future Work”**. The main body of the thesis is divided into four chapters – **Chapter 2: “Literature Review”**, **Chapter 3: “Experiments on the Plasma Spray Process”**, **Chapter 4: “Simulation Methodologies”** and **Chapter 5: “Results and Discussion”**. These chapters are in the same organization based on the three sub-topics: “plasma field and in-flight particle behavior”, “droplet impact behavior” and “deposit formation”.

The three sub-topics basically is the spray process flow, which is also the work flow of the research work. Due to the close interconnection between regime I and II, investigations on the plasma field and in-flight particles behavior are one subtopic of the thesis. One of the prerequisites of the deposit formation is the droplet impacting parameters, including particles distribution in space, mass flow rate, velocity, temperature and size. An in-depth investigation is done on the droplet splatting behavior on the substrate, which is the elementary procedure for deposit formation. The droplet splatting behavior on the flat substrate in the case of normal impact is one constituent of the second sub-topic. The purpose is to correlate the impacting parameters with different droplet splatting phenomena and splat shapes. The third

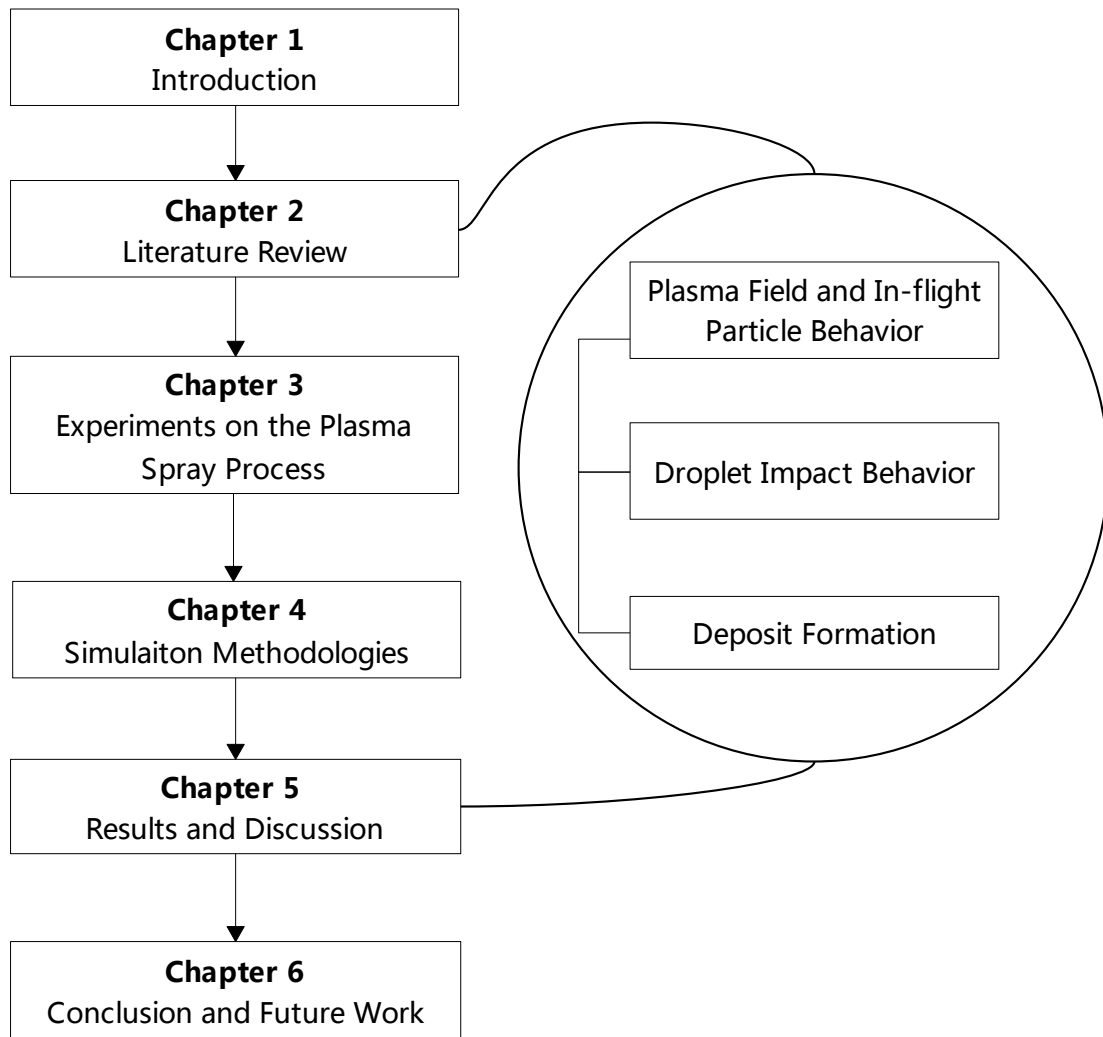


Fig. 1.3 Thesis organization chart, showing relationships between chapters.

sub-topic is the deposit formation. Based on the investigation of the previous two sub-topics, a deposit growth model is developed to simulate the plasma spray deposition by stationary torch in the real world.

Chapter 2 reviews the related knowledge and researches. For a better understanding of the thermal spray, the first section of this chapter reviews the plasma facilities and consumables, followed by the reviews on the three sub-topics. In each subtopic, simulation and experimental work are included.

Chapter 3 describes the methods and procedures to carry out the plasma spray experiments. The experiments are not merely for phenomena observation, but provide input data for simulation and validate the simulation results. The observations are presented to give intuitive pictures:

- Experimental diagnostics have been applied by using SprayWatch© to inspect the in-flight particle parameters in the freestream.
- Single splats of different shapes on the flat substrate are captured by flat substrates and curved substrates.
- Deposits are obtained by spraying YSZ particles onto different positions of a curved substrate. SparyWatch© is employed to capture the spraying procedure.

Chapter 4 expatiates the modeling methodologies to develop the simulations on the three sub-topics.

- A computational fluid model is developed by using FLUENT© to simulate a plasma field. One-way coupling scheme is used to calculate the particle dispersion in the plasma field. The heat transfer physics is included to predict the particle temperature.
- Computational fluid dynamics (CFD) model is developed by using Flow-3D® to investigate the splatting phenomena which is difficult to observe in the experiments. The model is also modified to simulate the droplet splatting behavior on curved substrate. The final splat shape is correlated to the droplet impact parameters, which is the basis for the deposit growth modeling.
- Based on the splat geometrical parameters obtained from the droplet impact investigation, a code is written in C++ programming language to simulate the deposit growth procedure.

Chapter 5 presents the results of the experiments and simulations in **Chapter 3** and **Chapter 4** respectively. Detailed discussion is employed to reveal control parameters or mechanisms of the phenomena which occur in the three sub-topics. Analysis of results from experiments and simulations works as the complementary method to each other.

Chapter 2

Literature Review

2.1 Introduction

Plasma spraying is a complicated process involving numerous parameters. As mentioned in **Chapter 1**, three different but interrelated regimes are governed by interdependent parameters. These parameters can be optimized to produce higher level of performance. A literature review is carried out to understand the three regimes: plasma generation, plasma-particle interaction and coating formation, which depict a detailed picture of the plasma spray process.

The literature review is divided into four topics. In the first topic, the atmospheric plasma spray (APS) system is described including the facilities and powder. Collections of the thermo-physical properties of the yttria-partially-stabilized zirconia (YSZ) are summarized in this part. It works as references of the zirconia properties to be used in the simulation work. In the second topic, modeling approaches on plasma plume generation and particle in-flight behaviors are reviewed. Meanwhile, some diagnostic methods used to monitor the plasma spray process are reviewed, which may provide some hints for the experiment in the author's work. In the third topic, droplet impact behavior on solid surface, including experiment and simulation is briefly reviewed. State-of-the-art researches provide references for the droplet impact simulation in the work. The last topic, discusses the deposition formation simulation work done by some researchers, essentially will provide some insight into the deposition formation mechanisms.

2.2 Facilities and Powder

A typical configuration of the plasma spraying system is delineated in **Fig. 1.1**. This section describes the design and functions of the core components, and the usage of the consumables.

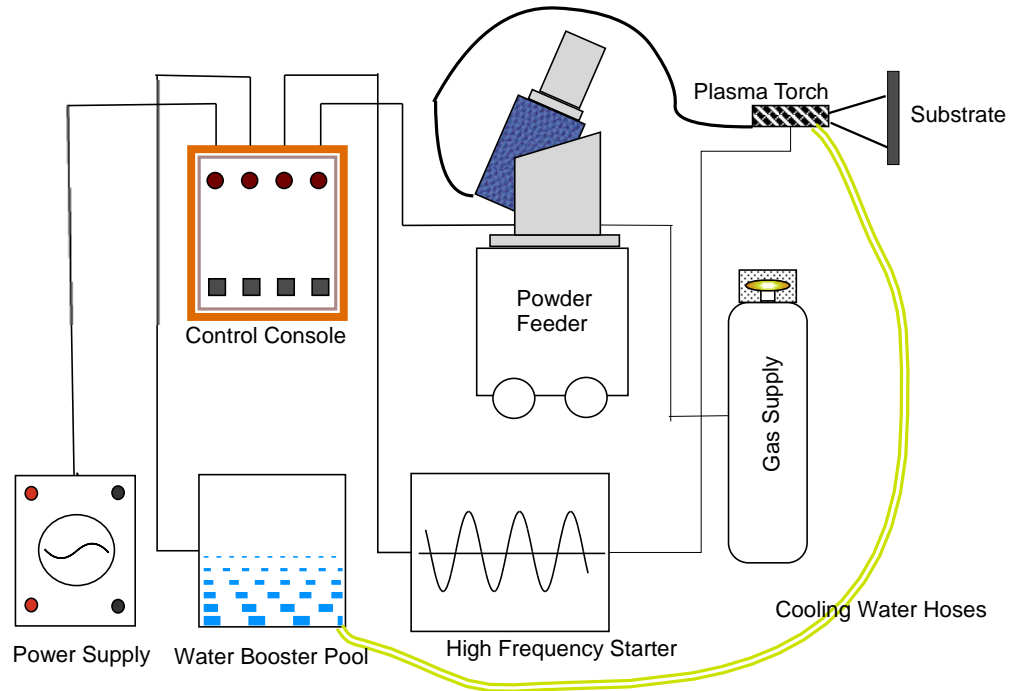


Fig. 2.1 A typical configuration of the plasma spraying system.

2.2.1 Facilities of the plasma spraying system

The core facilities (or components) of the plasma spray system consist of a plasma torch and a powder feeder.

2.2.1.1 Spray torch

The spray torch is one of the most essential parts of the entire spraying system. The basic design of plasma spray torches for the various spray processes has been essentially the same, based on producing a plasma jet by an arc discharge operated between a stick-type cathode and a nozzle-shaped anode [7]. There are two typical types of spray torches: radio frequency (RF) torches and direct current (DC) arc plasma torches. In the current work, DC plasma torch is employed to carry out the spray process.

Fig. 2.2 shows a typical DC plasma torch design, taking Praxair and TAFA's Model SG-100 plasma spray gun as the example, which is also the model used in the current work. The cathode is made of thoriated tungsten and a high purity oxygen-free copper anode as the arc plasma components, and gas injector, powder injector, nozzle and some other auxiliary components.

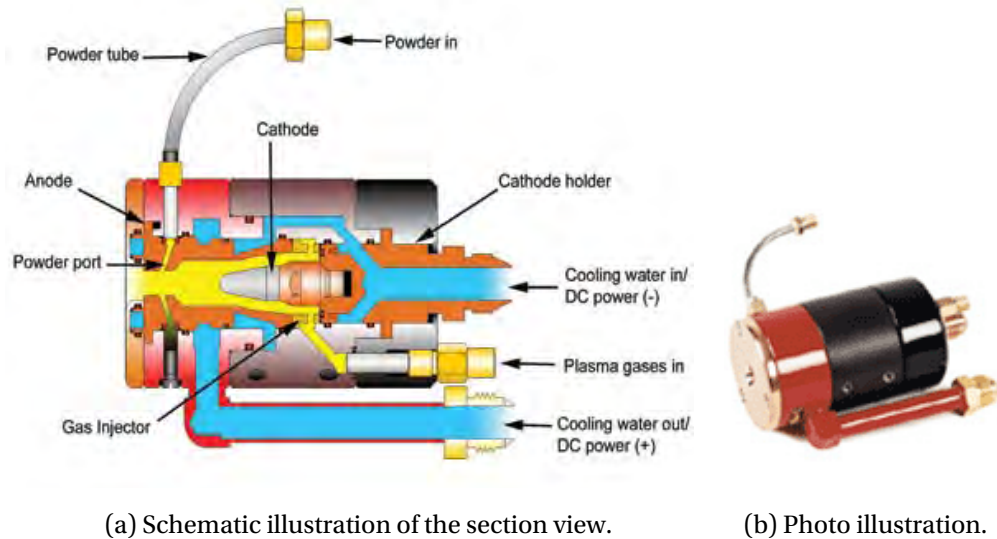


Fig. 2.2 Illustration of a DC plasma torch design, taking SG-100 as an example (Praxair Surface Technologies Inc., 1998).

A high-current arc is struck between the anode and cathode, ionizing and accelerating the plasma gas. The arc attachment to the anode wall [1 and 8] fluctuates continuously in length and position. For a given nozzle id, the fluctuations may be partially controlled by the gas composition, mass flow rate and arc current.

The electric arc produces high energy plasma, which leaves the nozzle with high velocities (600-2200 m/s) and temperatures (10000-15000 K). The high velocity jet induces vortex rings which coalesce and entrain cold surrounding atmospheric gases.

2.2.1.2 Powder feeder

Power feeder enables automatically feeding of powders into the plasma jet, with preset feed rate adjustment and temperature and quantity control. **Fig. 2.3** shows an illustration of the volumetric powder feeder[9], which is the type used in the current work.

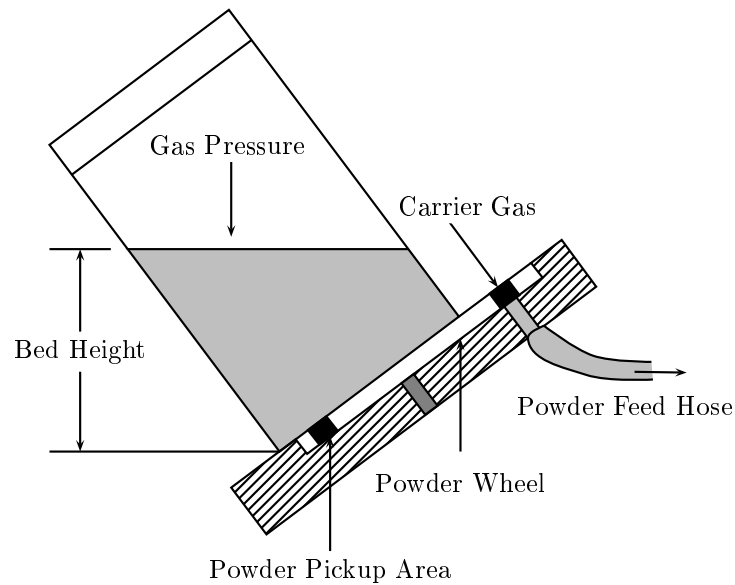


Fig. 2.3 Design of a common volumetric feeder (reproduced after [9]).

The volumetric powder feeder uses screws, slotted or drilled powder wheels as the controlling powder unit. The screw or powder wheel picks up the powders and delivers them to the canister exit in a controllable flow rate. This powder feed rate can be adjusted by controlling the wheel spinning speed. The relationship between them for different types of powder materials is shown in **Fig. 2.4**. The powders are then suspended in an inert carrier gas, which also provides a positive pressure to deliver these powder particles to the plasma torch through a powder-feed hose.

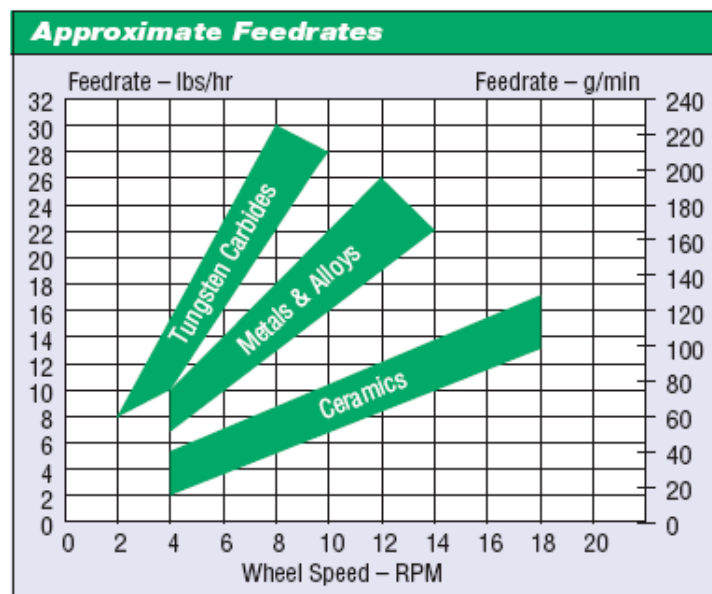


Fig. 2.4 Relation between the powder feed rate and the wheel spinning speed for different types of materials [10].

2.2.1.3 Control console and cooling system

The control console is the master and front-end of the whole system. It controls the power supply to the plasma torch, powder feeder, gas feeder and water cooling system. The gas flow rates, including those of the carrier gas and the (primary and secondary) plasma gases, can also be adjusted on the console panel.

Because the plasma torch suffers from high temperature of the plasma jet during operation, it is necessary to integrate a cooling system to prevent overheat damage and prolong the electrodes' service life as much as possible. A cooling circuit comprises a water tank, two water cooling hoses and guiding channels in the torch. A water booster pump guarantees proper pressure to drive the water through the cooling circuit.

2.2.2 Powder

The quality of the plasma sprayed coating depends very much on the feedstock material[11]. The enhanced quality and variety of feedstock powders contribute significantly to the advancement of thermal-spray technology. Either metals, metallic alloys, ceramics, or even glasses can be used as feedstock. Because yttria-stabilized zirconia (YSZ) is selected to be the feedstock in current work, this review mainly focuses on the zirconia based material.

Scientists and engineers have an exceptional interest in zirconia because of its unique and excellent properties: high refractoriness and corrosion resistance, mechanical strength, fracture toughness and some more[12]. The mechanical properties of zirconia is a function of phase structure and composition. It has three polymorphs stable at different temperatures: monoclinic when $T < 1170^{\circ}\text{C}$, tetragonal when $1170^{\circ}\text{C} < T < 2300^{\circ}\text{C}$, and cubic when $T > 2370^{\circ}\text{C}$ [13 and 14]. **Fig. 2.5** shows the equilibrium zirconia-yttria phase diagram[15]. By the addition of stabilizing agents such as ceria or yttria, it is possible to stabilize the high-temperature phase at room temperature. It is known as fully stabilized zirconia (FSZ) if all the high-temperature phase is stabilized; partially stabilized zirconia (PSZ) if a fraction of the high-temperature phase is stabilized.

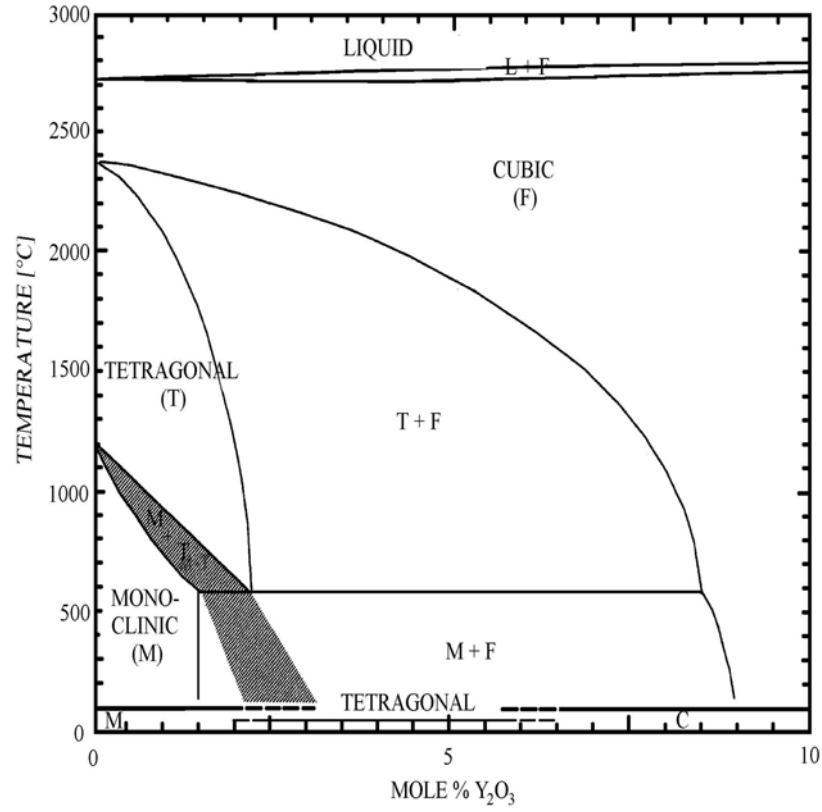


Fig. 2.5 Equilibrium zirconia-yttria phase diagram[15].

As a refractory material, at present it is very difficult to measure the thermo-physical properties of zirconia based ceramic, especially at high temperature ranges. However, a review is done to collect the the properties for YSZ. If unavailable, zirconia properties are used as the alternative values. Selected properties are tabulated in **Table 2.1**, including density ρ , melting point T_m , boiling point T_b , liquidus temperature T_l , solidus temperature T_s , latent heat of fusion H_f , latent heat of vaporization H_v , thermal conductivity k , surface tension σ , specific heat C_p and viscosity μ . These data are the source of the properties of YSZ properties for the numerical work. “Deduced” means the values of liquidus and solidus temperature are deduced from the phase diagram[15], the procedure of which is narrated in **Appendix E**.

Table 2.1 Collection of zirconia properties from the literature.

Property (Unit)	Magnitude	Researcher	Remarks
ρ (kg/m ³)	5890	Shackelford and Alexander[16]	-
T_m (K)	2988	Shackelford and Alexander[16]	-
T_b (K)	5273	Shackelford and Alexander[17]	-
T_l (K)	3031	Scott[15]	Deduced
T_s (K)	2978	Scott[15]	Deduced
H_f (J/kg)	7.06×10^5	Simon et al.[18]	-
H_v (J/kg)	6×10^6	Zhang et al.[6]	-
k (W/mK)	2.4	Ahmed and Bergman[19]	-
σ (N/m)	0.43	Shinoda et al.[20]	-
C_p (J/kgK)	Equation ¹	Shackelford and Alexander[16]	-
μ (Pas)	Equation ²	Shinoda et al.[21]	Theoretical

¹ $C_p = 1.06343E^{-6}T_p^3 - 2.188953E^{-3}T_p^2 + 1.709671T_p + 1.466367E^2, 273 \text{ K} < T_p < 873 \text{ K}; C_p = 678.5, T_p > 873 \text{ K}$

² $\mu = 0.0037 \exp(6100/T)$

2.3 Investigations on Plasma Flow Field and In-flight Particle Behavior

2.3.1 Numerical investigations

2.3.1.1 Plasma flow Field

This section focuses more on numerical modeling and simulation of the plasma flow field, especially on the velocity and temperature distribution in the plasma plume. Relative experimental facts are reviewed to assist understanding the modeling processes.

In the field of plasma modeling, the most prevalent method is self-developed tools by different groups. Ramshaw and Chang[22] developed a Computational Fluid Dynamics Code named LAVA, containing a very complete description of the high temperature plasma jets with entrained particles. Mostaghimi and Boulos[23] in the Plasma Technology Research Center (CRTP) set up a model of axi-symmetric ICP torches, including non-LTE effects. Computational methods for DC torches are established by many research groups, such as Rat et al.[24], Moreau et al.[25], and Trelles et al.[26 and 27].

Selezneva et al.[28] and Kang et al.[29] developed simulation models respectively by using a commercial CFD code FLUENT[30]. Eichert et al.[31] took another CFD code Phoenix to simulate an Ar-H₂ gas mixture inside and outside a DC plasma torch. Although these commercial softwares are not designed specially for plasma modeling, their flexible modular structures and powerful built-in solvers make them promising candidates for plasma modeling and further spray research.

2.3.1.1.1 Heat generation modeling

The transformations of initial chemical substances and electric energy into products and thermal energy is usually referred to as the mechanism of the plasma-chemical process[32]. In this process, the heat generation is one of the basic principles. The modeling of heat transfer can be categorized into such three methodologies:

(a) Magnetohydrodynamic (MHD) model

In magnetohydrodynamic (MHD) model, the simulation proceeds by solving numerically the magnetohydrodynamic (MHD) equations of a plasma. It generally applies to large-scale problems directly related to the behavior of experimental devices and facilities[33], including plasma spray process.

A distinguishing feature of the MHD model is that it can make a prediction of both the electromagnetic field and hydrodynamic field. Another advantage over other methods is that this approach is independent on any arbitrary assumptions or adjustable parameters. Westhoff and Szekely[34 and 35] found that the electromagnetic force has significant effect on the hydrodynamic field. As shown in **Fig. 2.6**, the calculated exit velocity was four times higher with the existence of electromagnetic force than that without the electromagnetic force.

(b) Inlet profiles for temperature and velocity

Ramshaw and Chang[22 and 36] described a model, wherein only the external flow into the ambient flow was cared about, thus ignoring the complicated plasma generation. Both two- and three-dimensional models were applied to calculate velocity, enthalpy, and temperature distributions at the nozzle exit, matching with the plasma gas flow rate and enthalpy. These properties were generally written as:

$$\frac{\phi(r) - \phi_w}{\phi_c - \phi_w} = 1 - \left(\frac{r}{R}\right)^n \quad (2.1)$$

where $\phi(r)$ represents the variable – temperature, flow velocity, or enthalpy – at the distance r from the torch axis; ϕ_c and ϕ_w are values of the variables on the torch axis and at the wall respectively; R is the torch radius and n a fitting parameter. However, the researchers found that this modeling method is restricted to the application of external injection scheme because there are two experiment-dependent variables ϕ_c and n measured at the torch exit.

(c) Constant heat source model

To simplify the plasma heat generation, Eichert et al.[31] replaced the local arc phenomena by a source term which considers only the thermal effect of the arc on

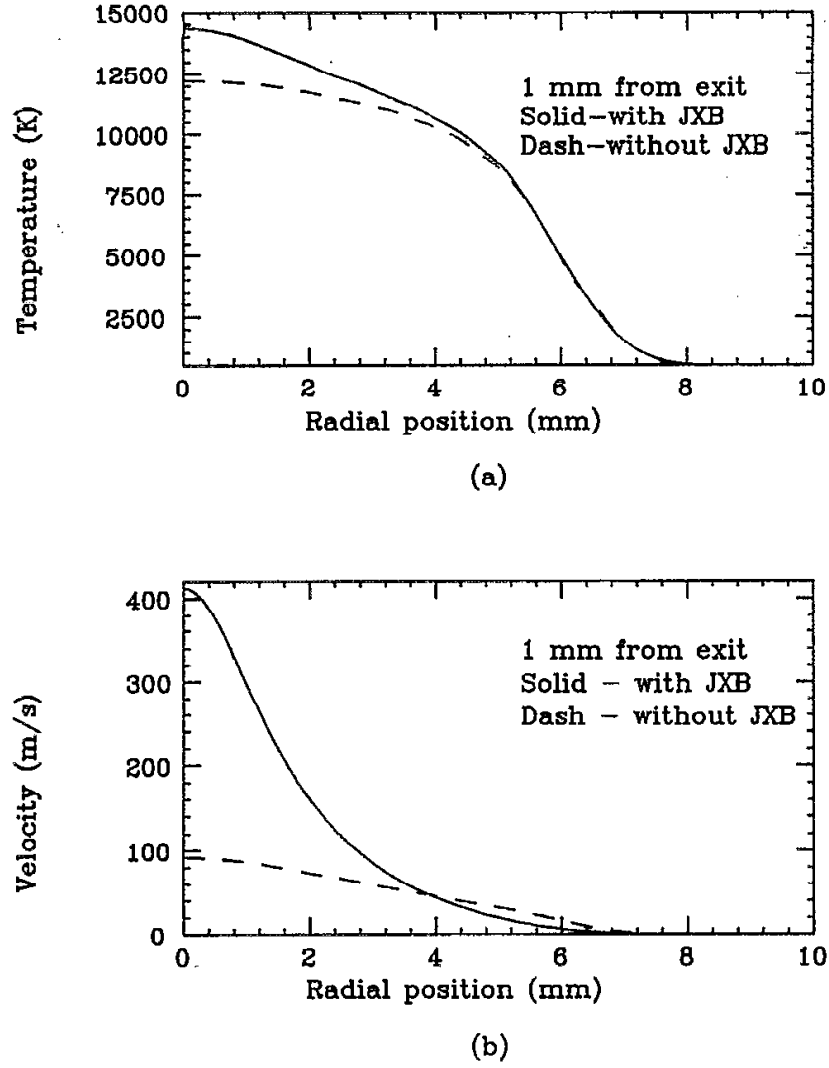


Fig. 2.6 Effect of electromagnetic force on the radial (a) plasma temperature and (b) velocity at the torch exit. Current $I = 750$ A; Ar (0.59 scmh)[34].

the gas flow on an averaged basis. This source term was defined as a total volumetric power input expressed as

$$P'''_{in} = \frac{UI}{V} \quad (2.2)$$

where P'''_{in} is the volume-averaged heat source, U the voltage, and I , the arc current, V is the torch volume.

Remesh et al.[37 and 38] and Kang et al.[29] introduced a reduction factor η_t , which was called “torch efficiency”, to account for the energy loss by the water cooling. It is measured based on the difference of temperatures between in the atmospheric environment and in the cooling water. The value is usually in the range of 60% – 70%. The energy source term became

$$P_{in}''' = \frac{\eta_t E(t) I}{V} \quad (2.3)$$

where $E(t)$ is the fluctuating arc voltage, which makes it possible to account for the time-dependent plasma conditions. However, Park et al.[39] found that the time averaged plasma conditions over the axial fluctuations were very close to the steady-state conditions. This makes the computations during a period of time much easier and less expensive than solving for time fluctuations.

In the present work, the constant heat source model is adopted with constant voltage. This approach is relatively easy and is proven to be sufficient by Kang et al.[29]

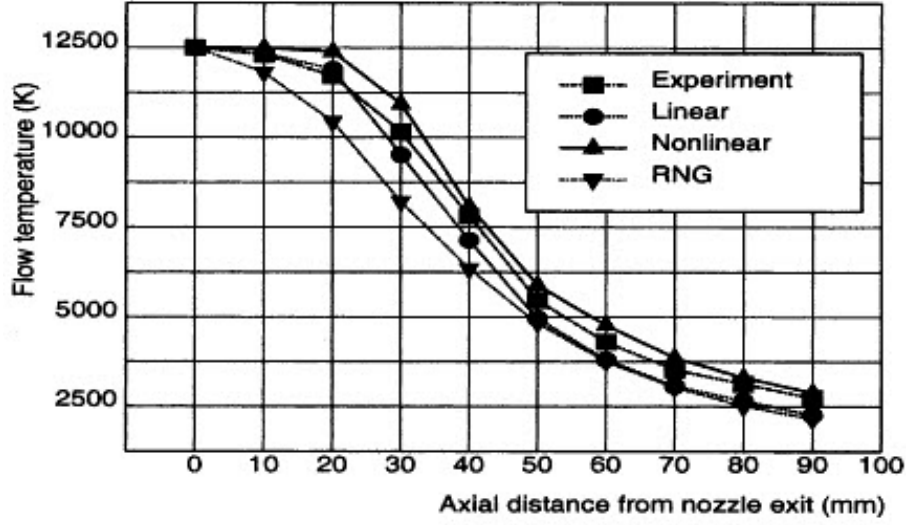
2.3.1.1.2 Turbulence modeling

The plasma flow in plasma spray is an intensively turbulent jet flow, due to high velocity magnitude (1000-2000 m/s) and Reynolds number (approximately 15000). Although some of the numerical studies were based on the laminar flow assumption, it is more accurate for researchers to include turbulence effect in their models.

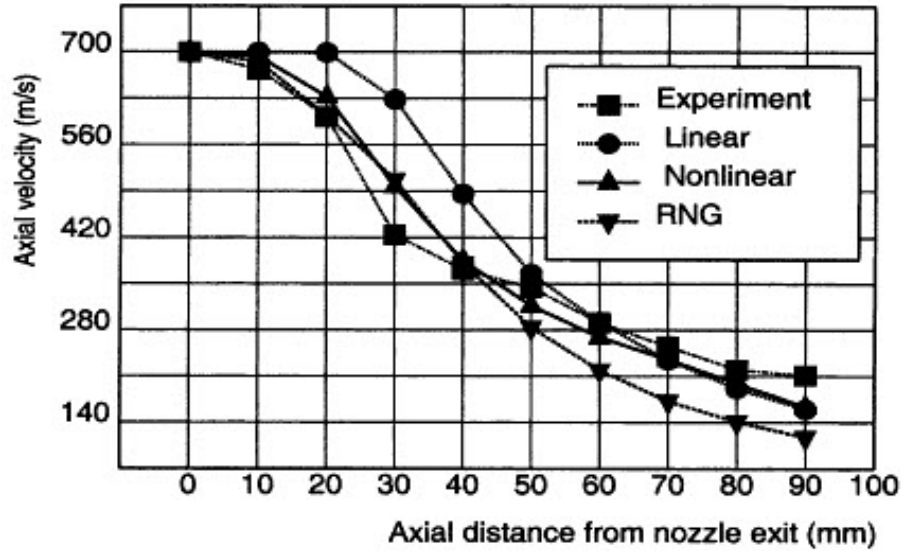
For the purpose of comparing the influence of different $k - \epsilon$ models on plasma flow, Liu et al.[40] applied linear (standard), non-linear and RNG (Re-normalization Group) $k - \epsilon$ models to investigate the process parameters effect. It was noted that there was not much discrepancy between all the models for temperature profiles. However, the non-linear model gave a velocity profile closer to the experimental data, as shown in **Fig. 2.7**.

It was observed that at 30 mm downstream of the nozzle exit, the standard $k - \epsilon$ also agreed well with the experiments. Moreover, there were multiple examples and precedents successfully simulating the plasma flow fields by using the standard $k - \epsilon$ model, such as the works by Chen and Boulos[41–47]. Their formulation, which took into account the coil-plasma interaction and coil geometry, gave more realistic results for the electromagnetic field and fluid dynamics aspects of the flow. It implied that the standard $k - \epsilon$ fulfilled the objects of modeling turbulence effect in the plasma spraying process, including our present work. The detailed standard

$k - \epsilon$ model for turbulent effect in plasma flow will be described in the simulation methodology on the plasma field and in-flight particle.



(a)



(b)

Fig. 2.7 Influence of different $k - \epsilon$ turbulence models on the computed flow (a) temperatures and (b) velocities in the axial torch axis. 17.7 KW, 85 l/min Ar-H₂[40].

2.3.1.2 Particle behavior

In plasma spray, feedstock powders are injected into, suspended and accelerated by the plasma jet, eventually sprayed onto the substrate. Complicated physical and chemical interactions occur between the in-flight particles and plasma flow. Numerical investigations on in-flight particle behavior are essentially the process

to establish a model to simulate the plasma-particle interactions, which can be considered as the case where discrete particles are transported by continuous turbulent flows.

2.3.1.2.1 Classification of particle behavior modeling

There are three basic approaches for plasma-particle interaction modeling: one-way coupling, two-way coupling and four-way coupling[48].

One-way coupling is the simplest approach, in which only the effect of the plasma flow on the particles is taken into account. Traditionally, a one-way coupling between the phases is employed for dilute systems. However, when the particles mass loading ratio increases, they will influence the plasma turbulence. In this situation, a two-way coupling problem needs to be solved: the particle behavior in turn affects the flow behavior. It may be considered as the consequence of a micro-turbulence produced by extra gradients around the particles.

More difficulties arises when additional heat and mass transfers between particles and plasma flow are concerned, especially when there are simultaneous occurrence of chemical reactions and radiative transfer. The prevalent methods used in most of the in-flight particle behavior modeling are one-way[42, 49 and 50] and two-way coupling[45, 47 and 51].

The work done by some researchers, such as Crowe[52] and Sobolev et al.[53] suggested that the coupling effect would be insignificant when the particle loading ratio (the ratio of particle mass flow rate to plasma mass flow rate) was less than 0.3. In our work, the particle loading ratio is 0.08, therefore it is appropriate to take “one-way coupling” approach in the modeling.

2.3.1.2.2 Momentum transfer in particles behavior modeling

The most important part of particle behavior modeling is the prediction of particle trajectory and in-flight parameters such as velocities and temperatures. The trajectory and velocities are determined mostly by the momentum transfer between the plasma and particles.

There are various factors affecting the momentum transfer between plasma and particles, such as viscous drag force, Basset history term, turbulent dispersion, evaporation and non-continuum effects[54].

The motion of a particle in a plasma field is determined by force balance, which can be written as

$$\vec{F} = m\vec{a} = \vec{F}_D + \vec{F}_p + \vec{F}_B + \vec{F}_e \quad (2.4)$$

where \vec{F} is the total force vector, \vec{F}_D the viscous drag force vector, \vec{F}_p the pressure gradient term, \vec{F}_B the Basset history term, and \vec{F}_e represents the sum of additional forces vector (gravitational, electric, etc.).

Clift et al.[55] suggests that as the plasma flow has a rather low density comparing with that of the injected particle, all terms except the viscous drag force and potential forces are typically neglected.

2.3.1.2.3 Heat and mass transfer modeling

In thermal plasma processing, heat and mass transfer between the plasma and the injected particles plays a crucial role. Particles injected into the plasma phase experience various effects, some of which are not present in ordinary gases. Waldie[56] summarized the most important effects that should be under considered, such as heat transfer associated with strongly varied plasma properties, vaporization, radiation, and noncontinuum situations. Many efforts have been spent in modeling one or several of these effects. Wan et al.[57] developed a model considering the heat conduction within a particle. They treated the phase-change interface as a boundary between the two different phase domains. The number of such phase-change interfaces depends on the temperature distribution inside the particle. All of these phase-change interfaces are moving boundaries. The boundary conditions for a partially melted particle (with one internal interface) is shown in **Fig. 2.8**.

Internal conduction within a particle may lead to a large differences between the surface and the inner temperature. The Biot number determines the relative

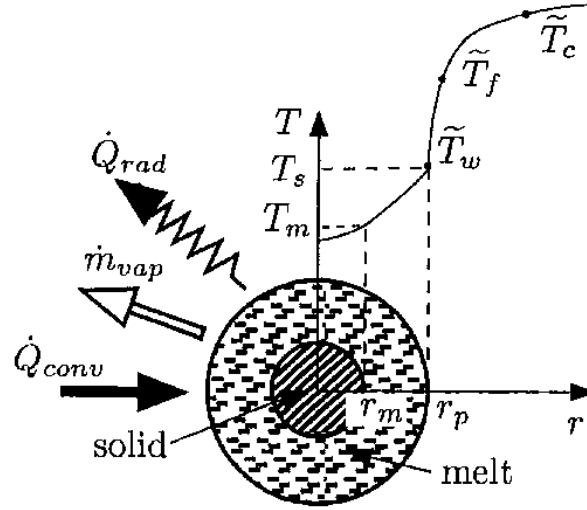


Fig. 2.8 Schematic of the particle geometry and heating model[57].

importance of heat conduction within a particle. It is defined as the ratio of convective to conductive heat transfer as below:

$$Bi = \frac{hd_p}{k_p} \quad (2.5)$$

where h is the convective heat transfer coefficient, k_p the thermal conductivity of the particle, and d_p the particle diameter.

Bourdin et al.[58] assumed that the conduction is the governing heat transfer mechanism (small Reynolds numbers) for particle heating in the plasma, thus developed such an equation:

$$Bi = \frac{k_\infty}{k_p} \quad (2.6)$$

where k_∞ is the average thermal conductivity of the plasma gas. They found when the $Bi > 0.3$, there will be substantial difference between the temperature at the surface and the center of a particle.

Xiong et al.[59] developed a model, introducing two dimensionless parameters – melting index M.I. and oxidation index O.I. to indicate the particle melting and oxidation state. The melting index M.I. is calculated as

$$M.I. = \frac{\Delta_{fly}}{\Delta_{melt}} \quad (2.7)$$

where Δ_{fly} and Δ_{melt} are respectively the time for particle in-flight and for particles to become fully melted. While the oxidation index O.I. is defined as the ratio of the oxide weight m_{oxide} to the particle weight $m_{particle}$.

They investigated the melting index of ZrO_2 . As shown in Fig. 2.9, all particles start melting virtually at the same location of 0.8 cm standoff distance, regardless of the size. The flight distance required for fully melting is different for particles of different sizes: 1.1, 1.8, 3 and 5.5 cm for particles with initial diameters of 20, 30, 40, and 50 μm respectively.

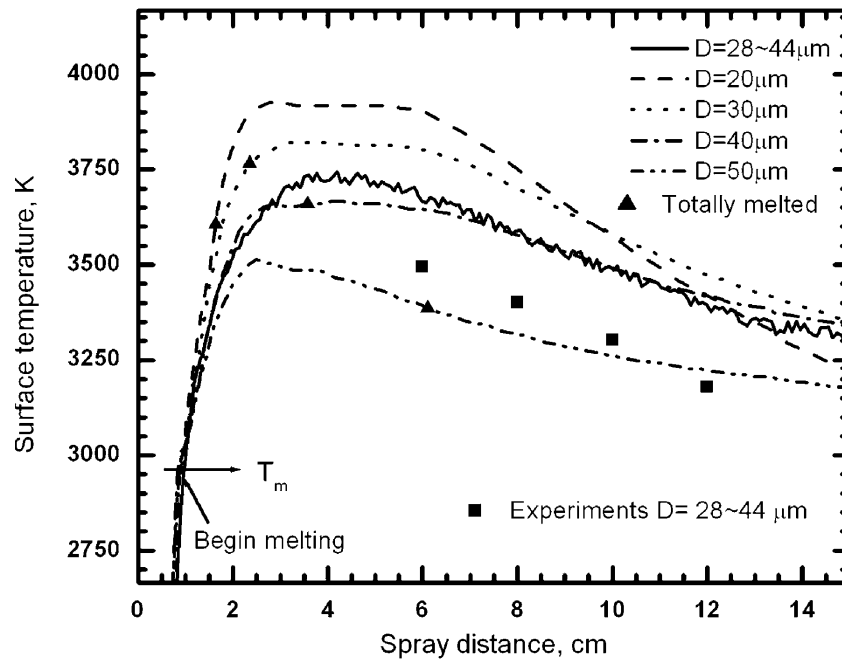


Fig. 2.9 Particle surface temperature and melting state for different sizes of ZrO_2 particles, comparing with experimental data[59].

In the present work, the substrate is positioned at a standoff distance of about 80 mm, which is sufficiently distant to for most of the particles to reach a fully-molten state. In the present work, we assume the particles have a uniform temperature, which means every single particle stays in a simple physical state, either “fully melted” or “unmelted”.

2.3.2 Experimental Observations

2.3.2.1 Plasma field observation

Singh et al.[60] employed Fast Fourier Transform (FFT) in the form of a long time series of multi-channel records of the plasma jet optical emission along and across the jet. Besides the arc current (**Fig. 2.10(a)**), they also investigated the effect of the mass flow rate on the plasma velocity profile, which was shown in **Fig. 2.10(b)**. The plasma velocity also increased with the increase of the mass flow rate. Furthermore, it was noticed that the plasma velocity decreased when it traveled further downstream. The reason was the entrainment of the atmospheric air into the plasma jet retarded the flow of the plasma jets.

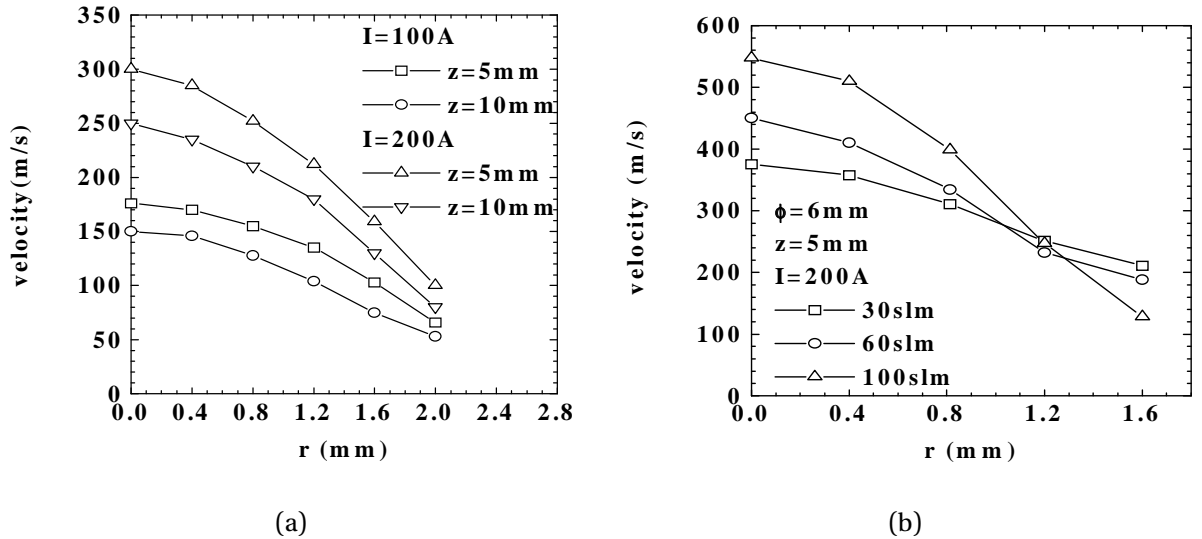


Fig. 2.10 The influence of (a) arc current and (b) gas flow rate on an argon plasma jet ($I = 200$ A)[60].

2.3.2.2 Particle behavior observation

Vardelle et al.[61] investigated the particle velocity, surface temperature and number flux distribution in a DC plasma jet by using a time-of-flight laser anemometer. A typical particle trajectory in “radial injection” scheme, with illustrations of particle flux number density distribution, is shown in **Fig. 2.11**. The particles spread over a large region of the plasma, although injected powder had a rather narrow size distribution. In the plane of injection, the particles present an asymmetrical profile, but a symmetrical one in the orthogonal plane (Y direction).

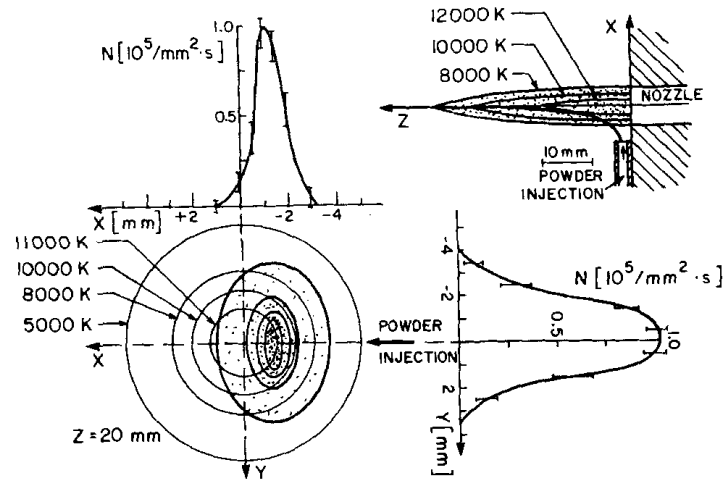


Fig. 2.11 Particle trajectories and number flux distributions. Alumina powder diameter $=18.0 \pm 3 \mu\text{m}$; carrier gas flow rate 5.5 l/min[61].

The distance of the injection port is also important to the particle trajectory. As shown in **Fig. 2.12**, by advancing the point of injection of the powder, even by only 4 mm, the particles penetrated deeper into the plasma jet and may have more chance to get heated and melted than when they are injected further away.

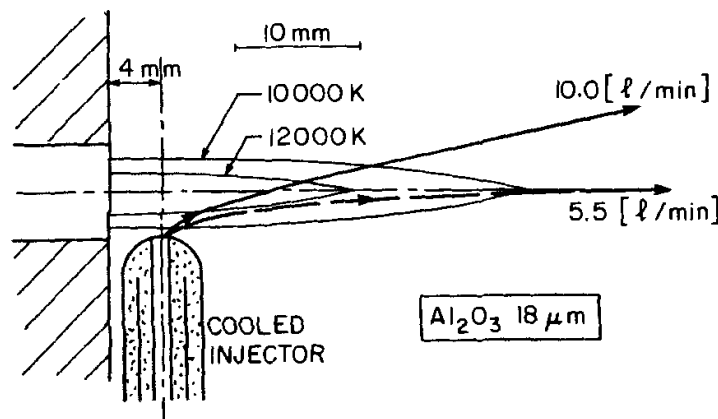


Fig. 2.12 Particle trajectories with water-cooled powder injection probe at jet fringe[61].

The increase of the plasma gas flow rate resulted in a substantial increase of the particle velocity (almost 40%) and a slight drop of the particle surface temperature (about 100 K). The particle flux number distribution were more uniform when the plasma gas flow rate increased (**Fig. 2.13**). The higher particle velocity and the more uniform particle flux number distribution due to the higher plasma gas flow rate are favorable conditions for an improved coating properties.

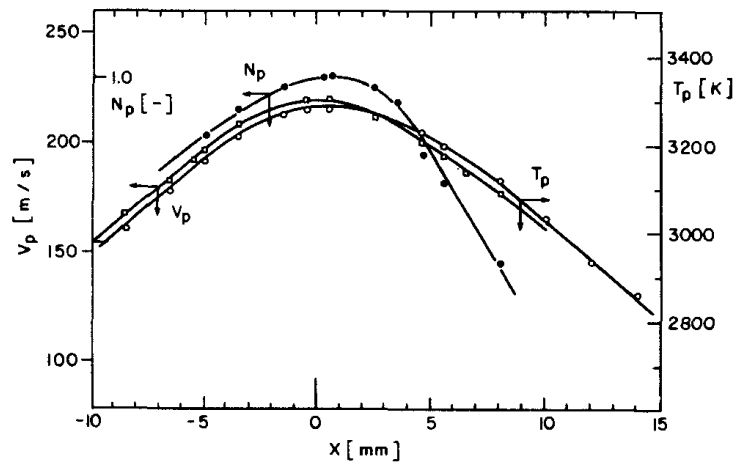


Fig. 2.13 Particle number flux, velocity, and surface temperature profiles at $Z = 75$ mm. Alumina powder diameter $= 18.0 \pm 3 \mu\text{m}$; carrier gas flow rate 5.5 l/min; Ar- H_2 90 l/min; 29.2 kW[61].

Zhang et al.[6] investigated the influence of particle injection angle (90° – tilting angle) on YSZ particle in-flight behavior and characteristics by using Accuraspray and DPV2000. The particle surface temperature monotonically decreased with the increase of injection angle from 0 to 20° . As the carrier gas flow rate increased, both the particle temperature and velocity initially increased and then decreased, giving a bell shape. These temperature and velocity profile are shown in **Fig. 2.14**. The mean particle size in the “flux center” (a total scanned area of $30 \times 30 \text{ mm}^2$ with the maximal particle flux) decreased when carrier gas flow increased or injection angle decreased.

As a non-destructive measurement technology, Phase Doppler Anemometry (PDA) system was used by Ma et al.[62 and 63] and Wang et al.[64] to monitor the in-flight metal (nickel) particle velocity and size simultaneously. The technology is based on the relationship of signal phase difference of the same particle measured at two different angles by two different detectors. The refractive and reflective light scattered from the particles are difficult to be distinguished by the fiber PDA system, which is known as Gaussian and slit effects. As a consequence, there may be significant size measurement error. However, the nickel particle to be measured has strong light absorption properties and strong light reflection. Thus by using reflective mode for the measurement of the the plasma spray process, the Gaussian and slit effects should have little influence. In addition, the fiber PDA system is also

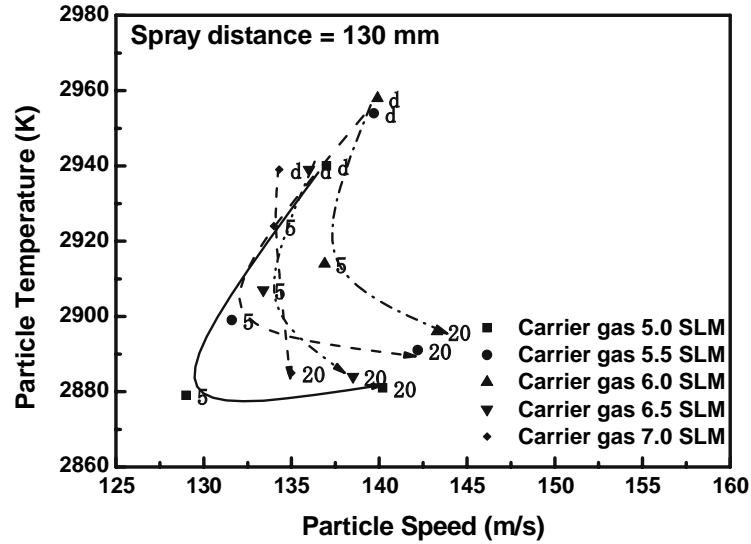


Fig. 2.14 YSZ particle temperature and velocity at the spray distance of 130 mm[6].

modified to be a dual mode PDA system to eliminate the errors caused by these two effects. **Fig. 2.15** shows the optical arrangements of (a) fiber PDA and (b) dual mode PDA.

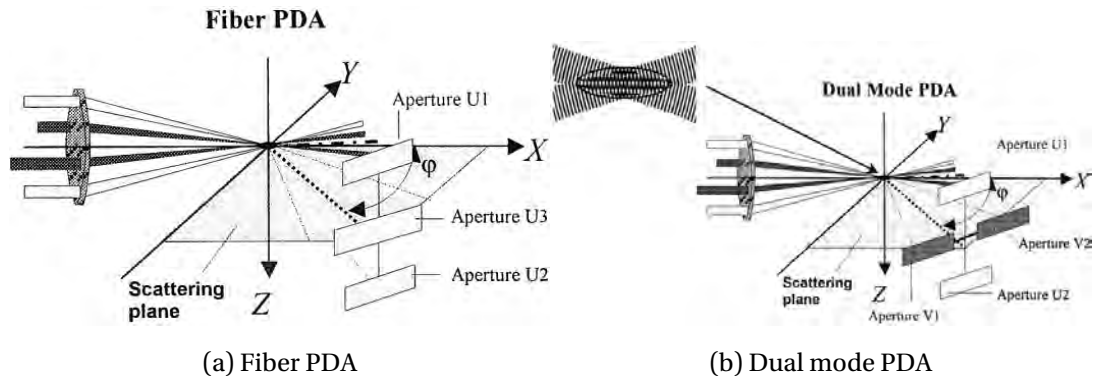


Fig. 2.15 The optical layout of PDA system[62].

In the fiber PDA system, there are three apertures U1, U2 and U3. The phase difference between the signals by detector pair U1 and U2 and by detector pair U1 and U3 are used for particle size measurement systems. The comparison of the results by the two pairs is used for checking the particle sphericity. The particle curvature is checked at the same plane. In the dual mode PDA system, two pairs of apertures U1-U2 and V1-V2 mounted orthogonally to each other are used for particle size measurement and sphericity checking. The particle curvatures are checked at two planes orthogonal to each other. Therefore, the dual mode PDA system

has more stringent sphericity tolerance than the fiber PDA. It was found that the refractive index of the particle will not change the phase factors involved in the particle diameter. The perpendicular polarization would be a better optical setting.

2.4 Investigations on Droplet Impacting Behavior

The elementary process of thermal spraying deposition is the impact of an individual droplet (or particle) onto the substrate to form a lenticular and lamellar splat. Explained in a simplified way, thermal spray deposition is a process during which the coating part builds up layer by layer from such solidified splats, as in **Fig. 2.16**. The final coating quality and thermal spray process performance are influenced greatly by this phenomenon. To optimize the thermal spray coating efficiency, it is essential to investigate the droplet impact behavior during thermal spray process. This section will review the current research status in droplet impact behavior in the thermal spray. The general knowledge and research on droplet impact in other applications are also introduced to portray a comprehensive picture of the droplet impact dynamics.

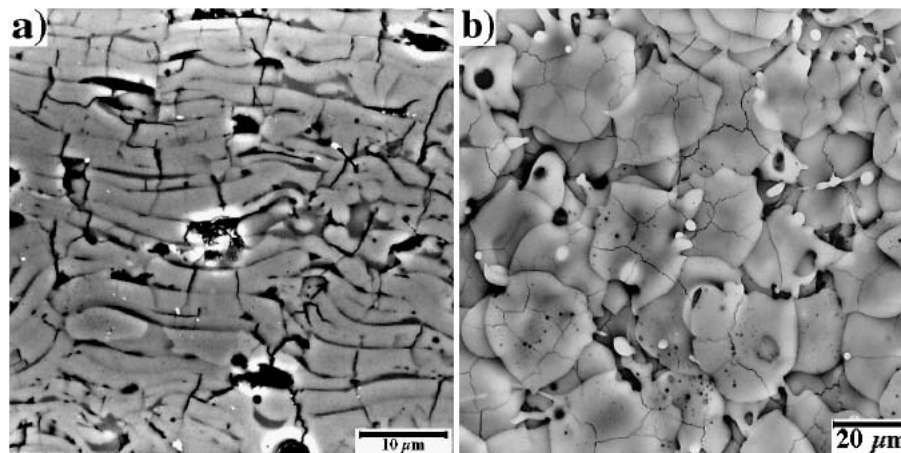


Fig. 2.16 SEM of typical morphologies of sprayed alumina in (a) cross-section view and (b) a top view[65], showing the accumulated layer structure of the coating.

2.4.1 Parameters affecting droplet impact outcome

The accompanying phenomena during droplet impact are extremely diverse, depending on the circumstances under which the impact occurs, as shown in **Fig. 2.17**. These circumstances are dictated by properties or conditions of the impacted surface, the droplet and the fluid medium between them.

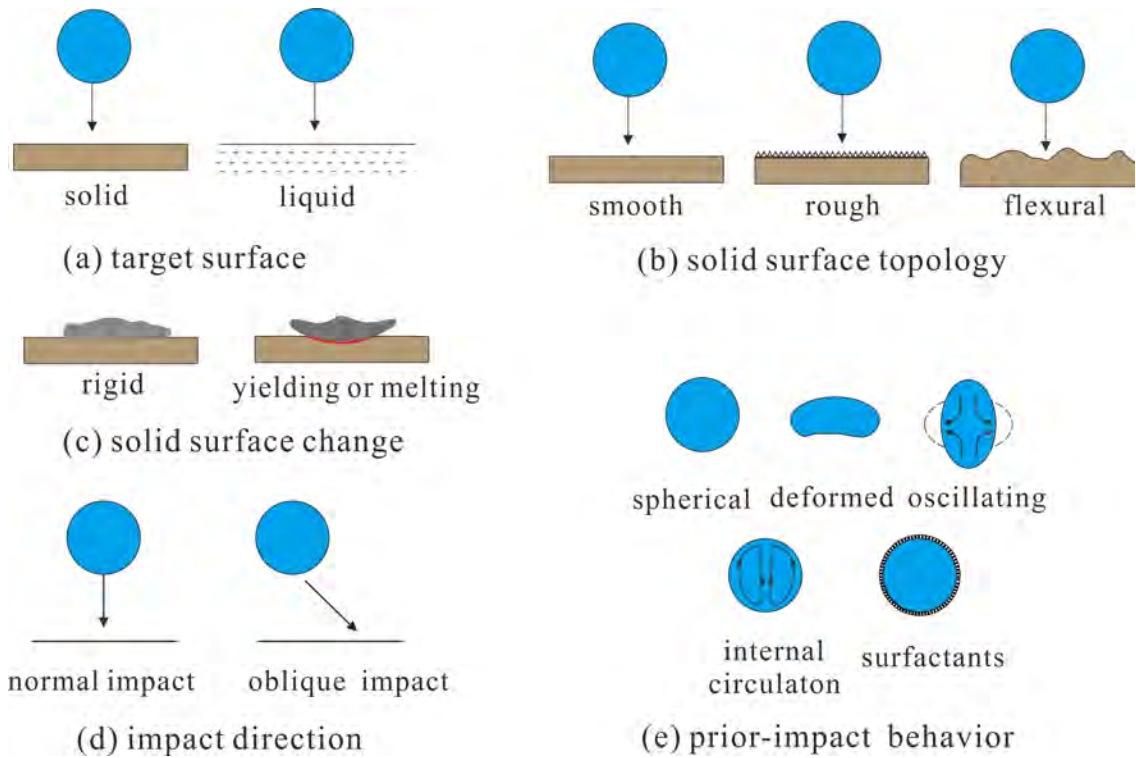


Fig. 2.17 Illustration of parameters affecting droplet impact phenomena.

2.4.1.1 Properties of the impacted surface

The impacted surface could be either solid or liquid (**Fig. 2.17(a)**). For thermal spraying technology, the impacted surface is solid, thus in the following texts only solid surface is discussed.

Illustrated in **Fig. 2.17(b)**, the simplest solid surface is a smooth plane. But it is just an ideal assumption in the analytical analysis or numerical simulation. Mostly the surfaces have microscopic roughness, even if they are polished by various methods. It is reported that splashing was reduced when highly polished surface were used[66]. In some cases, the surface is not a plane but with flexural areas. Levin and Hobbs[67] used a copper hemisphere as the impacted surface. Gunjal et al.[68] studied liquid droplet impacting on flat and spherical surfaces of pellets of trickle bed reactors with a low velocity (~ 0.2 m/s).

Fig. 2.17(c) shows the substrate change caused by the droplet impact. In many problems, the surface is considered as rigid body, which means the elastic response of the surface is insignificant. However, some researchers focused on this phenomena. Field et al.[69] took the elasticity of the surface into account. It is found that as the compliance of the surface increased, the critical angle β_c at which

the shock envelope overtakes the contact line also increased. The surface may also experience shape change due to substrate melting. Liu et al. investigated [70] the substrate melting phenomenon during thermal spraying. Flower-shaped splats are observed for molybdenum on stainless steel, brass and aluminum. The simulation carried out revealed that the splat solidification and substrate melting happened at the same time scale and interact with each other. Both particle and substrate materials played an important role on the melting behavior and consequently on the bond strength. The same phenomena was simulated by Zhang et al. [71], who applied SPH formulations of the Navier-Stokes equations and conservation equations of continuum mechanics to the motion of the liquid and the substrate respectively. The results revealed that the crater formed when the substrate melted substantially, which induced the splat splashing.

2.4.1.2 Properties of the droplet

Fig. 2.17(e) shows the shape change of the droplet prior to impact. The droplet is usually assumed to be homogeneous liquid and spherical prior to impact. However, some factors may change the droplet shape. The fluid between the droplet and the solid surface, usually is in gas phase, will slightly render the droplet to ellipsoidal shape by aerodynamic forces. Internal oscillation and circulation also deforms the droplet. In thermal spraying, the particles sometimes are not fully melted, resulting in inhomogeneous properties (melting state, viscosity and temperature etc.). Wu et al. [72] developed a model to simulate the droplet with a solid core impacting on a solid surface. It is revealed that the maximum spread factor ξ_m decreased as the solid core size increased.

The fluid surrounding the droplet prior to impact also affects the droplet shape to some extent. Engel [73] reduced the gas pressure to obtain larger impact velocities. If taking the droplet impact direction with respect to the solid surface into account, it could be divided into “normal impact” and “oblique impact” (or “off-angle impact”), as **Fig. 2.17(d)**. Mathematically, an oblique impact with a stationary surface is equal to a normal impact onto a surface moving perpendicularly to the impact direction.

However, due to the fluid existing between the droplet and the impacted surface, these two cases do not necessarily produce the same results[74].

2.4.2 Experimental investigations

Yarin[75] reviewed the droplet impact dynamics in the Annual Review of Fluid Mechanics in 2006, dealing with droplet impacting on thin liquid layers and dry surfaces. Worthington (1852-1916) was represented as one of the pioneers to investigate the droplet impacts systematically.

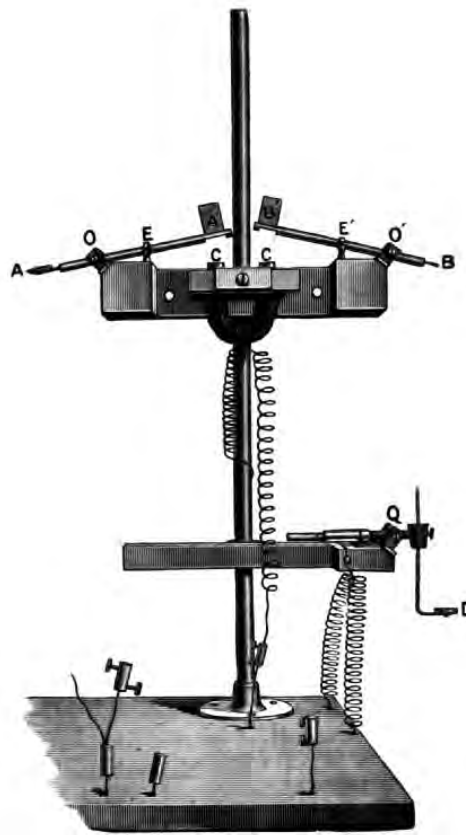


Fig. 2.18 Diagram of the apparatus designed by Worthington to view droplet impact behavior[76].

The droplet splash can not be satisfactorily seen with ordinary continuous light, because the changes are so rapid that the image of the later stage superpose upon a previous one before it has faded from the eye. The resulting impression of that is a confused assemblage of all the stages. Worthington[76] designed an exquisite apparatus to trigger a bright self-induction spark to view various stages of a liquid droplet splashing.

The apparatus used by Worthington was shown in **Fig. 2.18**. AA' and BB' were light rods pivoted on the horizontal axles O and O' respectively. The rod bore at the end A a small smoked watch-glass so that a drop of water lay on it without adhesion. An ivory timing sphere was at B. An electro-magnet CC' are used to hold down the iron ends A' and B'. On cutting off the current of the electro-magnet the ends A' and B' were simultaneously tossed up by the catapult, and thus the drop and sphere fell at the same moment. Before the drop reached the surface, the timing sphere struck a plate D and produced at the surface of the mercury a bright self-induction spark in the neighborhood of the splash via some mechanical and electrical setup. The flash of exceedingly short duration at any desired stage excluded all the stages previous and subsequent to the one thus picked out. By combining different stages of droplets with the same size and velocity, the whole course of the phenomenon was studied. **Fig. 2.19** shows the splash of a milk droplet falling on to a smoked glass plate captured by this apparatus. The droplet shape evolution with time could be viewed, including droplet splashing and secondary droplets generation.

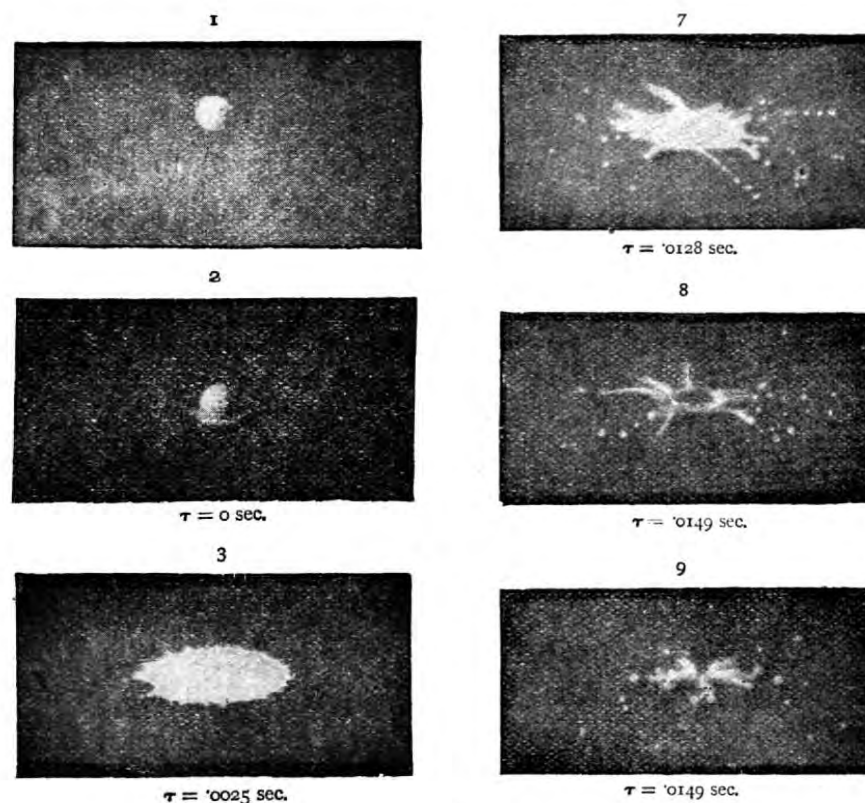


Fig. 2.19 Engravings of instantaneous photographs of the splash of a milk droplet falling 20 cm on to smoked glass by Worthington[76].

Thanks to the development of shutter speed technique, many researchers employed syringe-like droplet generator and CCD camera to investigate the impact behavior of liquid droplet with a low velocity[77–80]. The droplet is formed at the tip of the needle and detached from the syringe under its own weight. Similar to Worthington’s method, droplet impact dynamics are constructed from an ensemble of photographs of individual droplets impacting on the surface at different times. **Fig. 2.20** shows the apparatus used by Bussmann et al.[77] to capture water droplet impact behavior on inclined substrate. Although all the techniques had developed significantly, the basic design idea was similar to that of Worthington. A flash unit took the same function of the light spark; while the time delay circuit was the electronic alternative to the timing sphere.

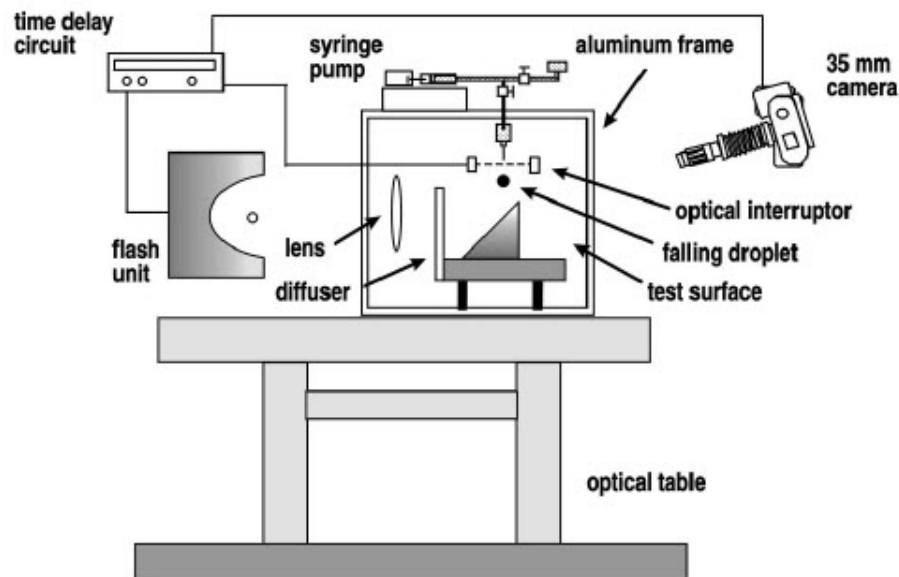


Fig. 2.20 Experimental apparatus used to capture droplet impact behavior[77].

However, when the application discipline is narrowed down to thermal spray, heat transfer and solidification complicate the droplet impacting behavior. The small size (typically tens or hundreds of μm in diameter) and high impact velocity ($> 100 \text{ m/s}$) of the droplet makes the splatting finish within a very short time on the order of microseconds. Therefore, it is difficult to observe the splatting behavior experimentally. A fast-response optical sensor was used by Vardelle et al.[81] to measure the radiation intensity of droplets sprayed onto a glass surface. Mehdizadeh et al.[82] developed a radiation triggered laser illumination technique to photograph the impact of molten molybdenum droplets on a glass substrate.

McDonald et al.[83 and 84] improved this technique by using two mirrors to reflect the splat image, as shown **Fig. 2.21**. A V-shaped shield and two additional barriers with holes of different size are used to reduce the number of particles landing on the substrate. The thermal radiation of the particles was measured with a fast two-color pyrometry system (D_1 and D_2). The optical sensor head focused the collected radiation onto an optical fiber with three slits. Two of the slits were used to detect the in-flight particles temperature and velocity; while the largest one was used to collect thermal radiation of the particle when it impacted and spread on the substrate. D_4 sensor was used to produce signal to trigger the electronic shutter of a CCD camera. By this means, no laser flash was used and it was not necessary for the substrate to be transparent. However, the experimental apparatus setup was very complicated and the photographs were not clear. The photographing was still not continuous, but was taken single, integrated image per impact. The advancement of photography technology is the key to the excellent on-line diagnostics of such a high speed droplet impact.

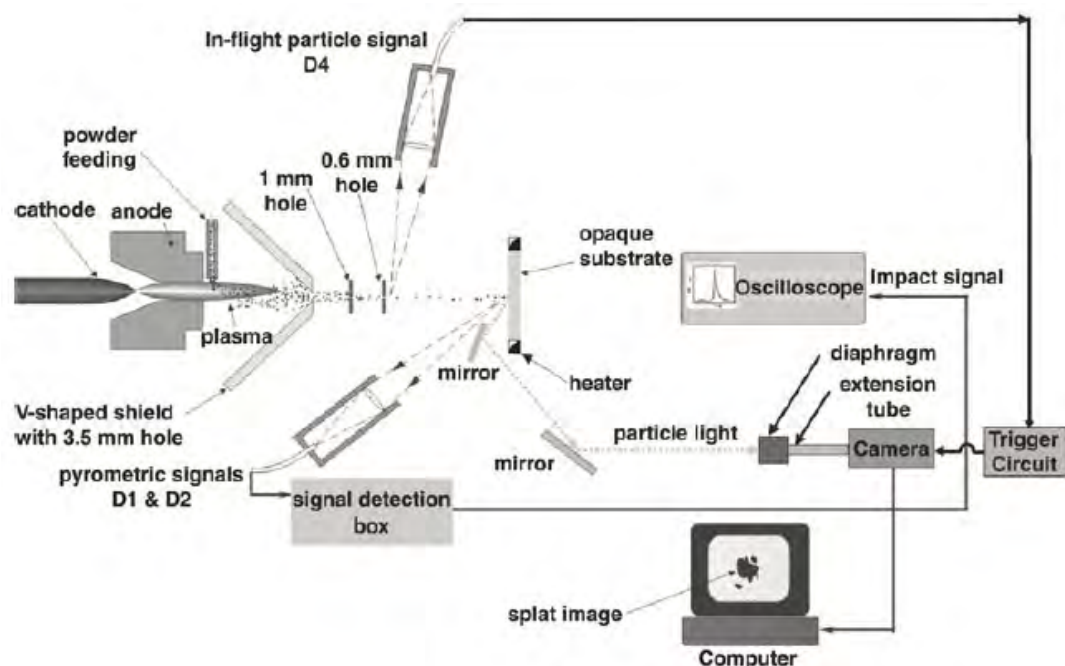


Fig. 2.21 Schematic of radiation images capturing system for plasma spray particles designed by McDonald et al.[84]

2.4.3 Theoretical and numerical methods for droplet impacting

Theoretical analysis and numerical simulations offer insights into the phenomena occurring during a droplet impacts onto the solid substrate. A plethora of efforts

have been devoted to the numerical modeling of droplet impacting on solid surfaces. Most of the numerical modeling is based on VOF (volume of fluid) algorithm. RIPPLE[85 and 86] and SOLA-VOF[87–89] are two representatives of VOF algorithm.

2.4.3.1 The Madejski model

As early as in 1976, Madejski set up a simple two-dimensional model to determine the flattening degree[90], in which inertia and viscous effect were considered.

Fig. 2.22 shows an illustration of this model, reproduced from Madejski's original work.

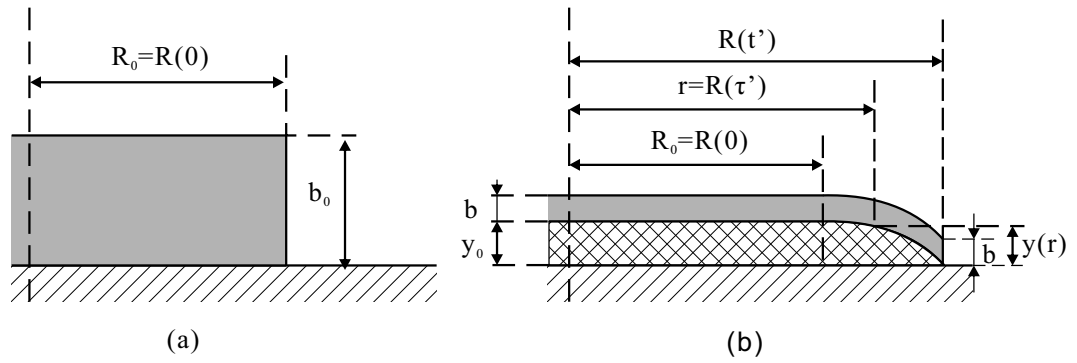


Fig. 2.22 Coordinate system definition (reproduced after Madejski). (a) $t' = 0$, (b) $t' > 0$ (reproduced after Madejski[90]).

A droplet of diameter D impinging perpendicularly on the surface flattens to form a cylinder. The radius $R(t')$ changes with time t' .

The thickness of the solidified layer y expressed below as:

$$y = U\sqrt{a(t' - \tau')} \quad (2.8)$$

where a is the thermal diffusivity of the solidified layer, U is a constant. The freezing begins at the moment τ' when the radius is $r = R(\tau')$.

The liquid layer thickness b depends only on time t' , and could be derived as a formula of densities of the solid ρ and the liquid ρ' ;

$$b' = \frac{\frac{\pi}{6}D^3\rho' - \rho V_s}{\pi R^2\rho'} \quad (2.9)$$

where V_s is the volume of the solid layer. By a series of calculations involving the energy equation and friction forces, the maximum flattening ratio ξ is expressed as a

function of three parameters k , Reynolds number Re and Weber number We , where k is a self-defined parameter. When $k = We^{-1} = 0$,

$$\xi_m = 1.2941(Re + 0.9517)^{1/5} \quad (2.10)$$

where the flattening ratio ξ is the ratio of the instantaneous radius R and the initial radius R_0 : $\xi = R/R_0$. The experimental investigation by Vardelle et al.[81] on zirconia particles sprayed perpendicularly on stainless steel substrate largely supported the Madejski's model.

When $Re > 100$, Equation 2.10 is simplified into

$$\xi_m = 1.294Re^{1/5} \quad (2.11)$$

Analytical and numerical investigations by other groups also concluded their results in such a format

$$\xi = aRe^b \quad (2.12)$$

where a and b are constants. Reynolds number $Re = \frac{\rho V D}{\mu}$, where ρ , V , D and μ are droplet density, velocity, diameter and viscosity respectively. But different with Madejski's model, the flattening ratio is defined as the ratio between the splat diameter d to the initial droplet diameter D (Fig. 2.23), which is called "spread factor". Table 2.2 listed the values of a and b in these researches.

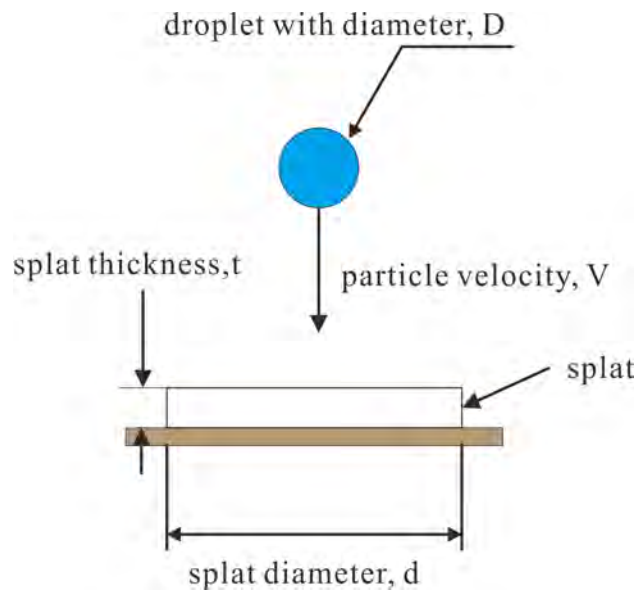


Fig. 2.23 Perfect formation of disk-shaped splat from a spherical molten droplet.

Table 2.2 A collection of spread factor ξ related constants a and b obtained from the literature.

a	b	Researcher	Methodology
1.2941	0.20	Madejski[90]	Analytical
1.0000	0.20	Trapaga and Szekeley[91]	Numerical
0.8300	0.21	Yoshida et al.[92]	Numerical
0.8200	0.21	Watanable et al.[93]	Numerical
1.0400	0.20	Liu et al.[85]	Numerical
1.0600	0.17	Fukanuma et al.[94]	Analytical
1.1626	0.20	Delplanque and Rangel[95]	Analytical
0.5000	0.25	Pasandideh-Fard et al.[88]	Analytical

From **Table 2.3**, it is noticed that no significant difference in spread factor between substrate materials of steel and steel pre-coated with zirconia. This implies that the splat flattening degree on the bare substrate and previously formed zirconia deposit is almost the same. It justifies the assumption that splat spread factor on the as-sprayed deposit is the same as on stainless steel substrate in the author's code for deposit growth simulation. Moreover, the splat is observed to be larger on smoother substrate. This may be attributed to that less energy is consumed by viscous dissipation during the flattening.

Table 2.3 A collection of spread factor ξ obtained by plasma-sprayed zirconia on various substrates. Surface roughness is denoted by R_a , substrate temperature T_s . The spread factor ξ is average value, while the range is in the braces.

ξ	Substrate material	T_s (K)	R_a (μm)	Researcher
4.90	Steel	573–773	0.05, 0.40, 9.00	Leger et al.[96]
4.70	Steel coated with zirconia	573–773	0.20,0.40	Leger et al.[96]
(3.50–5.50)	Polished stainless steel	474–573	0.10	Vardelle et al.[81]
5.50 (4.80–6.20)	Glass slide	–	0.02	Kucuk et al.[97]

Pasandideh and Mostaghimi[98] solved the full Navier-Stokes equations based on a modified SOLA-VOF method to predict the deformation and simultaneous solidification process of a droplet impinging on a flat surface. The solidification

caused a reduction in the final splat diameter. Bussmann et al.[77] developed a 3D model based on RIPPLE to find the 2 mm diameter water droplet impact phenomena onto a 45°inclined steel surface at a velocity of 1 m/s, imposing measured values of contact angles. The simulation predicted the droplet deformation and breakup well, comparing with the serial photographs taken by camera. Shinoda et al.[99] used the same model to predict the YSZ droplet splashing on dimple-patterned substrate, which is a special case of substrate roughness characteristics. The droplet velocity was set as 43 m/s, close to the thermal spray range. The micro-scale (8 μm in diameter and 1 μm in depth) dimple patterns caused splashing of droplets. Shumizu et al.[100] proposed a three-dimensional molecular dynamics model in Fortran 77 to simulate an aluminum droplet impacting onto an aluminum substrate. It is an innovative way to do droplet simulation, because it is in an atomic scale, and do not need to calculate the free-surface movement. The droplet velocity and diameter influences on the flattening behavior were analyzed. However, it requires a significant computational resource. Even for nano-sized particles, the calculation time for a simulation in a period of 60 ps was about 200 h in a Pentium IV 3GHz CPU and 1GB memory.

2.4.3.2 Heat transfer and solidification

Droplet and substrate thermal properties, such as temperature, specific heat and thermal conductivity and the interface thermal contact conditions affect the droplet and substrate heat transfer and droplet solidification, which are essential factors in the thermal spray droplet impact analysis.

The splat shapes change from a distorted shape with splashes characteristics to relatively well-formed disk shape when the substrate temperature increases. This transition occurs over a narrow temperature range. Fukumoto et al.[101] defined the transition temperature T_t , which was the critical substrate temperature above which 50% of the splats are well-formed disk shaped (**Fig. 2.24**). It is found that the substrate transition temperature is different for different substrate materials. The thermal conductivity of the substrate and the transition temperatures were related[102 and 103], as shown in **Fig. 2.25**. The figure indicated that higher

substrate thermal conductivity resulted in higher transition temperature. The transition temperature for YSZ particles on AISI304 stainless steel was evaluated as 345 K. Possible reasons of the splashing were proposed, including rapid solidification at the bottom surface of the splat, the presence of adsorbates and condensates on the substrate surface and poor substrate surface wettability.

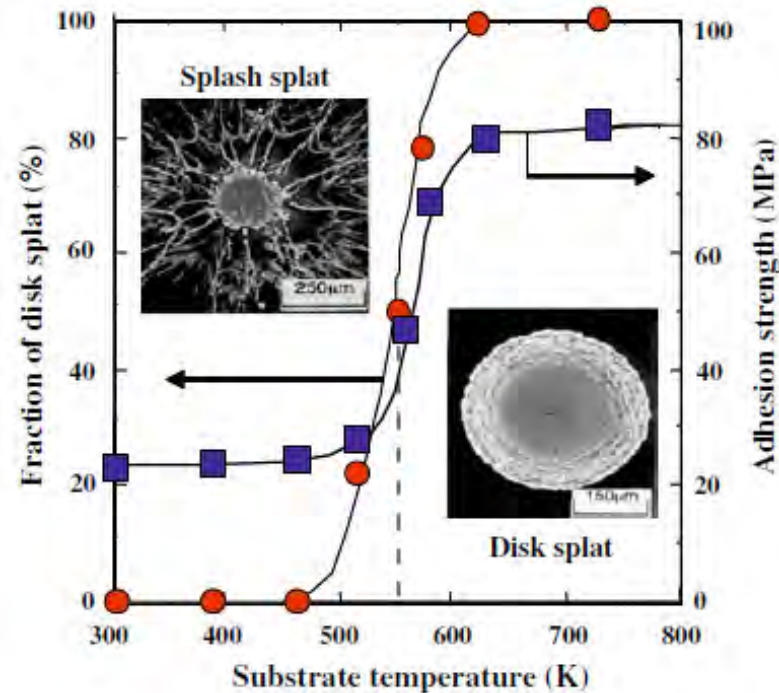


Fig. 2.24 Dependence of fraction of disk splat and coating adhesion strength on substrate temperature[103].

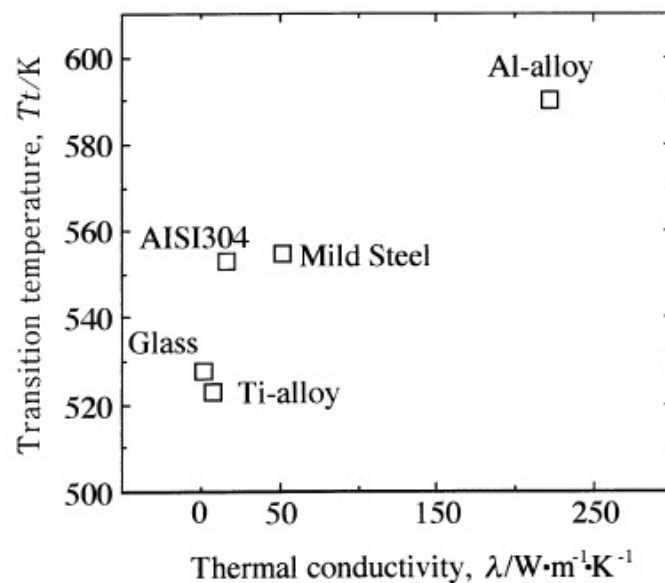


Fig. 2.25 Relationship between thermal conductivity of substrate and transition temperature[102].

Thermal contact resistance was employed to explain the splat splashing. It was defined as the temperature difference between the droplet (T) and substrate (T_s) divided by the heat flux (q) between them[104]:

$$R_c = \frac{\Delta T}{q} = \frac{T - T_s}{q} \quad (2.13)$$

R_c could be considered as the resistance of the thermal energy transfer between the droplet and the substrate.

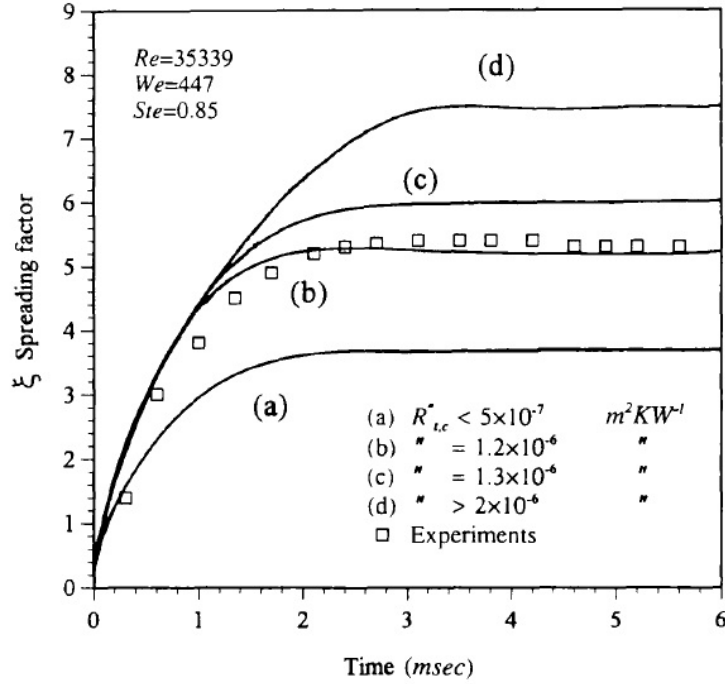


Fig. 2.26 Comparison between experimental observations and simulation results for the spreading and simultaneous solidification of a tin droplet on an alumina substrate[98].

Preheat treatment of the substrate was found to improve the possibility to get well-formed splats. It could be related to the presence of the adsorbates and condensates. The adsorbates and condensates, including water molecules, vaporize rapidly when a hot droplet approaches the substrate surface, creating high pressure under the flattening liquid, thus presenting high thermal contact resistance. Pasandideh-Fard and Mostaghimi[98] used a modified SOLA-VOF method to predict the molten tin particles spreading and solidification onto an alumina substrate, featuring different thermal contact resistance. The final spreading factor increases with the thermal contact resistance, as shown in **Fig. 2.26**. For the case under consideration, a contact resistance of $1.2 \times$

$10^{-6} \text{ m}^2 \text{ KW}^{-1}$ produced a result which agreed well with the experiments. Simultaneous solidification caused a final splat diameter reduction, which was more pronounced for high Re and Ste values. It was also found that the solidified splats in DC plasma spraying had larger diameters and were of uniform thickness compared to RF plasma spraying.

A simple 1D heat transfer model was employed by Wang et al.[64] to predict the splat quenching, considering the heat conduction in both the splat and the substrate, as well as the thermal contact resistance between them. The thermal contact resistance was represented by an interfacial heat transfer coefficient h . Solidification was simplified as a planar solid/liquid interface growing into the melt. This interface growing velocity V_i is a function of the interface location, affected by the thermal contact conditions, as in Fig. 2.27. A higher h lead to a higher interface velocity. When h was larger than $10^7 \text{ W/m}^2 \text{ K}$, only a minor interface velocity increase could be found by increasing h , except during the early stage of solidification.

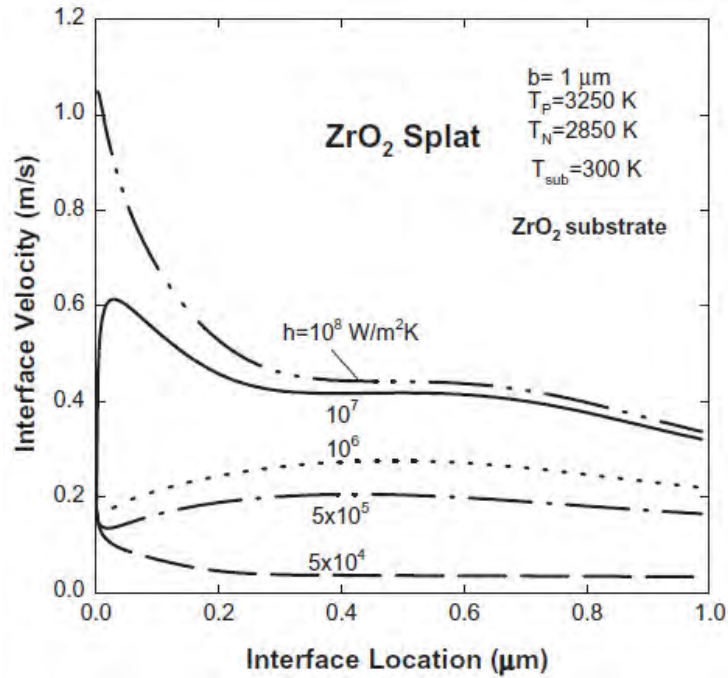


Fig. 2.27 Interface velocity as a function of the interface location from the contact surface for a 1 μm thick pure zirconia splat quenched on a zirconia substrate: effect of the thermal contact[64].

2.4.3.3 Effects of viscosity, surface tension and wettability

At the fluid dynamics aspect, viscosity, surface tension and wettability are important factors affecting the droplet impact and spreading dynamics. Surfactants and

wetting agents were used to make solutions with different viscosities and surface tensions. The surface tension decreased with increasing surfactant concentration to asymptotically attain a minimum constant value beyond the CMC (critical micelle concentration)[105 and 106]. Gatne et al.[106] conducted experiments with drops of aqueous solutions of three surfactants on glass (hydrophilic) and Teflon (hydrophobic) substrates. It was found that lower surface tension had a dual effect: a larger and thinner spread and more pronounced energy dissipation through viscous effects, even though the viscosities for the surfactant solutions were essentially the same. The maximum and final spreads on the hydrophobic surface (Teflon) were much smaller than those on a hydrophilic surface (glass).

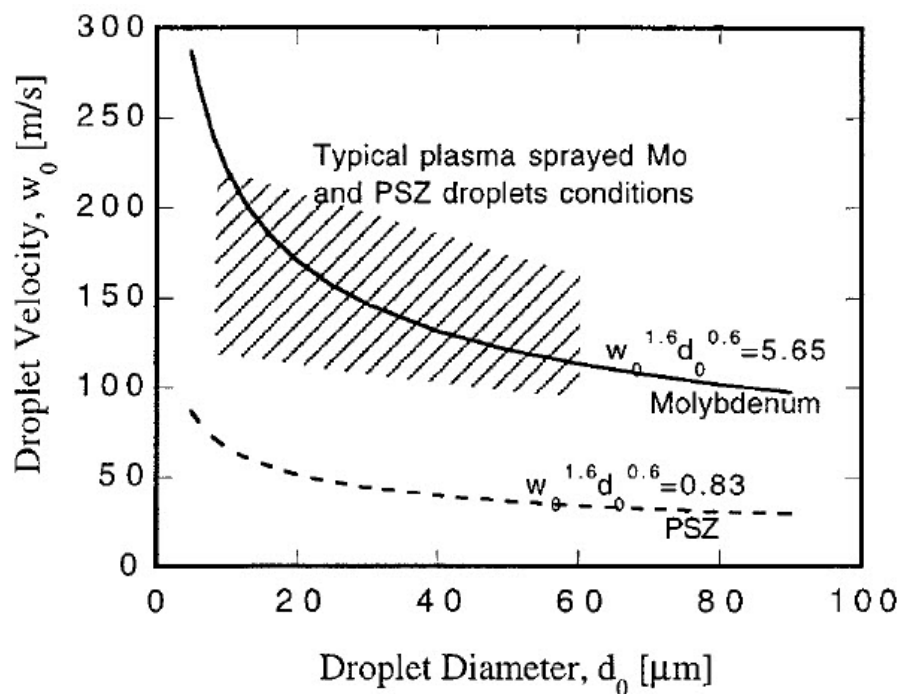


Fig. 2.28 Viscous dissipation dominating region was above the lines representing the criteria for different materials. The shadowed area represented the typical conditions in plasma spraying[107].

For thermal spraying, Wan et al.[107] performed analysis to reveal the effects of surface tension and wettability on the splat spreading. **Fig. 2.28** shows two criteria lines above which the viscous dissipation dominates the spreading. The typical process values of droplet diameter and velocity ranges for molybdenum (Mo) and zirconia (PSZ) were indicated by a shadowed area. The typical zirconia droplets were in the viscous dissipation dominant region, implying that the surface tension

and wetting contact angle effects could be ignored in the case of plasma spraying of zirconia. For Mo droplet, the effect of surface tension might be comparable to the effect of viscous dissipation. But the influence of wettability on spread factor was not as significant as that of the viscous dissipation. Generally, the droplet spreading under lower velocity depends more on the surface tension and wettability. It is because a particle with lower velocity has a higher ratio of Re to We ($Re/We = \sigma/(\mu V)$, where σ , μ and V are the surface tension, viscosity and velocity respectively). A higher value of this ratio implies that the effect of the surface tension is more significant than viscous dissipation in the droplet spreading. Pasandidehfar and Mostaghimi[98] also reported that the contact angle did not affect the splat spreading if the droplet impact velocity was larger than 1 m/s.

2.4.3.4 Effect of oblique impact

Some studies investigated the effect of the oblique impact on the splat morphology and coating characteristics. Montavon et al.[108] used image analysis techniques to examine the shape of individual Astroloy (nickel based alloy) splats on smooth copper substrates. The gun was displaced to achieve different spray angles. The spray angle was defined as the angle between the axis of the plasma gun and the substrate surface, in the plane orthogonal to the gun displacement, as shown in **Fig. 2.29**. The particles were assumed to fly along the torch axis, therefore, the spray angle was the angle between the droplet velocity and the substrate surface. The splat elongated from circular to elliptical shape when the spray angle changed from 90° to 30° . Several geometric quantities were introduced to characterize the splat:

$$\text{Equivalent diameter } ED = 2 \sqrt{\frac{A}{\pi}} \quad (2.14)$$

$$\text{Elongation factor } EF = \frac{\pi L^2}{4A} \quad (2.15)$$

$$\text{Degree of splashing } DS = \frac{P^2}{4\pi A} \quad (2.16)$$

where A refers to the splat area, L the longest dimension of the splat, P the perimeter of the splat.

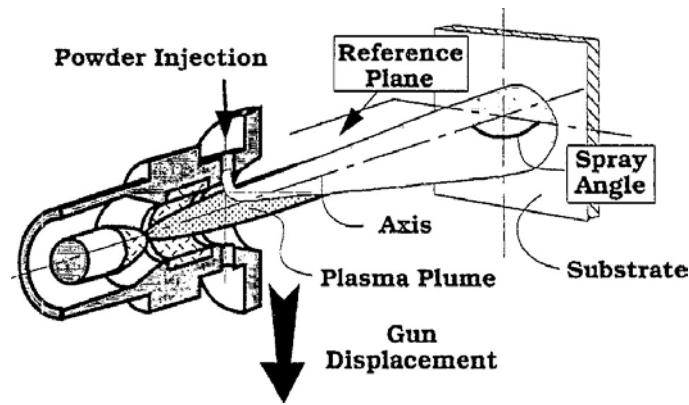


Fig. 2.29 Experimental set-up to perform the tests by Montavon et al., showing spray angle definition[108].

Results revealed that the elongation factor increased with a decrease of the spray angle. But the spread factor was not significantly affected.

Based on RIPPLE, Bussmann et al.[77] developed two numerical models, of water droplet impacting onto an inclined stainless steel plane at 45° , and a sharp edge where surfaces intersecting at right angles, as shown in **Fig. 2.30**. In their models, the initial phase of the impact was dominated by inertial effects; while viscous and surface tension also played important role in the successive spreading scenario. The liquid viscosity and surface tension in this model was assumed to be constant, and fluid flow was assumed to be Newtonian and laminar.

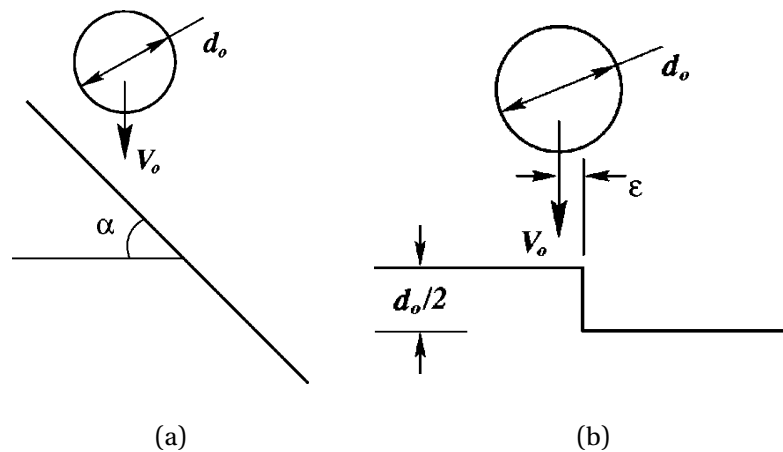


Fig. 2.30 Water droplet impact onto a stainless steel (a) inclined surface (b) edge with right angle surfaces[77].

Fig. 2.31 shows the photographs and corresponding numerical views of the droplet spreading and breakup conditions of both impact scenarios. There was good agreement between the simulation result and the experiment. However, the impact

conditions were not in the range of thermal spray parameters, and solidification physics was not taken into considerations.

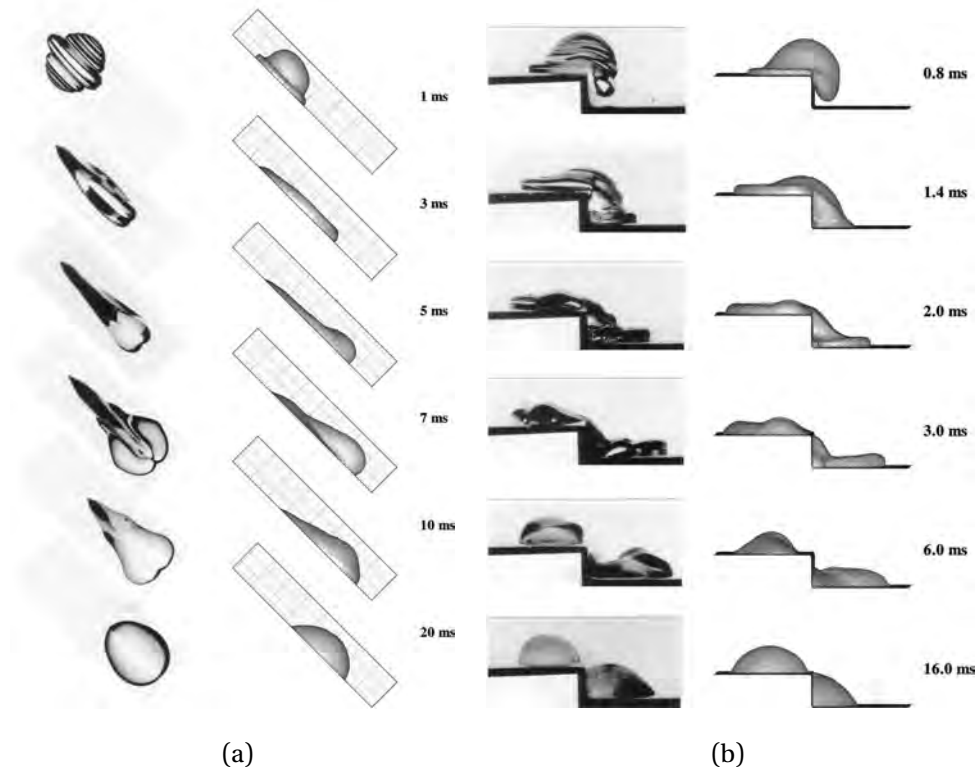


Fig. 2.31 Profile of side view of a 2 mm diameter water droplet at 1 m/s onto (a) a 45° stainless steel inclined surface and (b) 1 mm high stainless steel edge. Photographs at left, simulation results at right[77].

Bussmann et al.[109] improved this model to simulate molten nickel particle impact onto the substrate obliquely under DC plasma spraying conditions, with spray angle 30°, 45° and 90°. An additional quantity f was introduced to characterize the location of the splat, defined as the fraction of material at upstream of the impact point. The value of f decreased with the increase of spray angle, which corresponds to the larger elongation factor EF . However, substrate roughness and solidification physics were still not included in the model.

Some other studies focused on the role of the spray angle on coating characteristics. Leigh and Berndt[110] revealed the porosity and roughness increase and mechanical properties decrease (such as hardness, tensile adhesion strength and interfacial fracture toughness) at lower spray angle. Kanouff et al.[111] developed a model to predict surface roughness as a function of the spray angle, assuming simple models

of splat characteristics. A simple linear relationship between f and spray angle θ is conjectured:

$$f = \frac{\theta}{180^\circ} \quad (2.17)$$

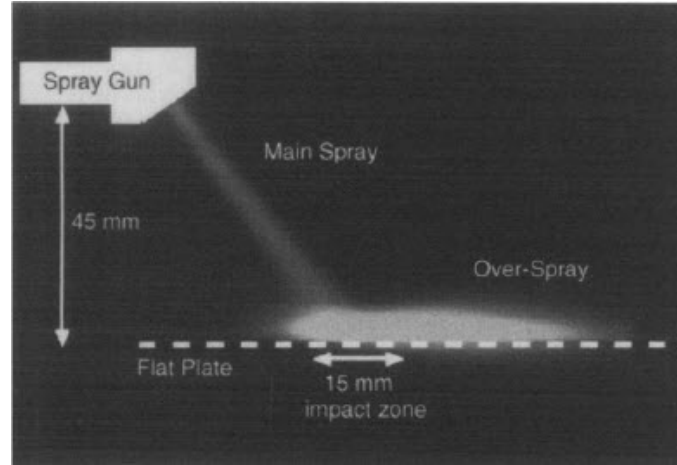


Fig. 2.32 Infrared image of the HVOF thermal spray impinging on a flat plate[111].

This model correctly predicted the increase trend of roughness with the spray angle decrease, but over-predicted the surface roughness observed experimentally.

An overspray phenomena was also observed. As shown in **Fig. 2.32**, the area over which the main spray impacted the target plate was approximately 15 mm long. Starting from the main spray impact zone, a 70 mm long bright elongated area parallel to the plate could be seen. It appeared to be caused by the thermal spray droplets ejected off the plate surface and was swept downstream parallel to the plate by the gas flow.

2.5 Deposit Formation

2.5.1 Simulation work on Deposit Formation

Not too much research focused on the coating build-up by thermal spraying. Beauvais et al.[112] developed a 3-D random building-up model to simulate the porosity formation by a few hundred of alumina particles during plasma spraying and HPPS. Random splats with diameters ranged between 10 and 80 μm and thickness between 1 and 3 μm were accumulated in MATLAB software. Splats were simplified as groups of bricks, as illustrated in **Fig. 2.33(a) and (b)**. The build-up of the splats was a “brick-by-brick” accumulation with a capability for deformation (**Fig. 2.33(c)**).

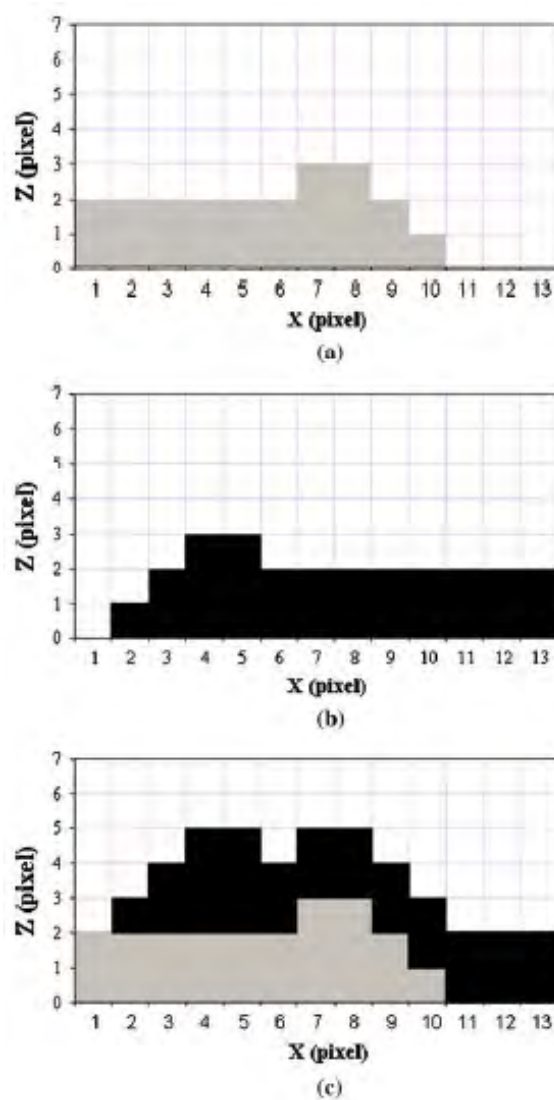


Fig. 2.33 Build up of two splats: (a) and (b) two distinct splats, (c) build up of these two splats[112].

Porosities were fed randomly with spheroids, the distribution of which was determined by the QIA (quantitative image analysis). Interlamella and intralamella cracks were added to the splats with 1 pixel thickness, the distribution of which were also determined by the QIA. The resulted cross sections of coatings were shown in Fig. 2.34. It was found that 13.6% of the APS coating consisted of connected pixels/pores, for an overall porosity of 14.6%, while the HPPS coating consisted of 8.98% connected pixels/pores, for an overall porosity of 9.5%.

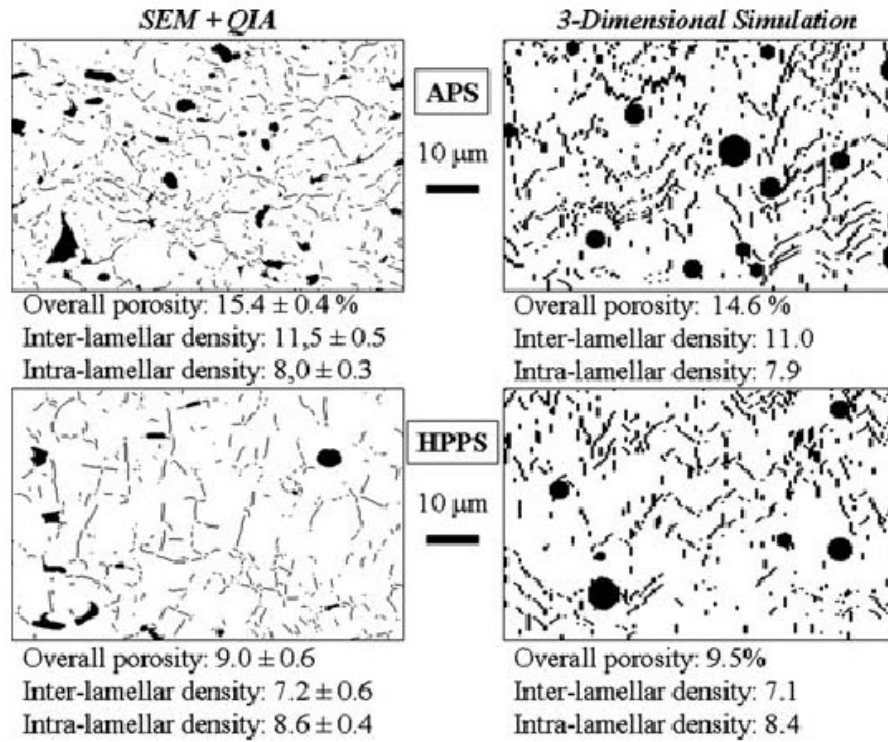


Fig. 2.34 Actual and simulated cross sections of porous APS and HPPS coatings[112].

Kang et al.[113] developed a similar model SCM (Substrate Cell Model). The calculation area is subdivided into a matrix of square grid cells of microscopic dimensions. The residual error sensitivity to the grid cell size is calculated and listed in Table 2.4. This residual error is defined as the difference between the total size area under coverage and the splat area, as given below:

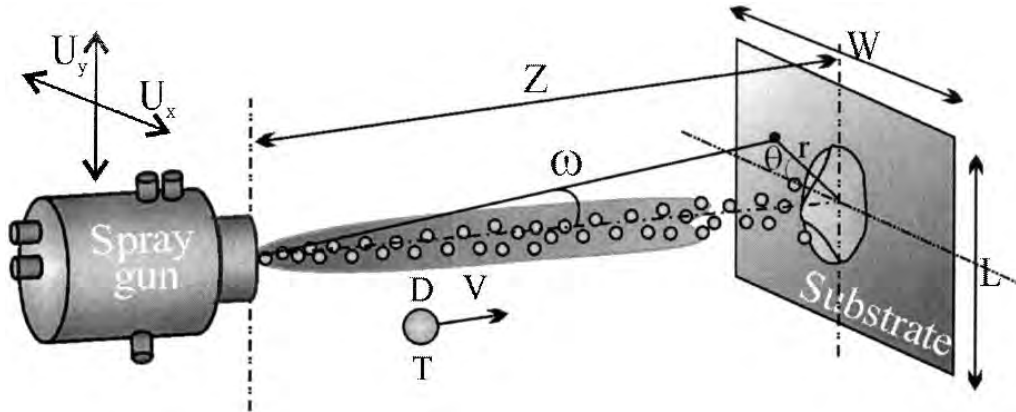
$$Error(\%) = 100 \times ABS\left(\frac{\frac{\pi d^2}{4} - (n_c \times A_c)}{\frac{\pi d^2}{4}}\right) \quad (2.18)$$

where d is the splat equivalent diameter, n_c is the number of cells accounted for calculation, A_c is the area of single cell.

Table 2.4 The maximal residual errors resulting from different cell sizes.

Cell Size (μm)	Error (%)
6×6	1
8×8	2
10×10	6
12×12	9

Ghafouri-Azar et al.[114] and Xue et al.[115] developed a three-dimensional stochastic model based on the Monte Carlo method. As shown in Fig. 2.35, the landing positions of particles is defined in a spherical coordinates by the gun/substrate distance Z , disperse angle ω and azimuthal angle θ . The process parameters such as particle size D , velocity V , temperature T , disperse angle ω were generated by following known distributions measured experimentally by diagnostic instruments such as the DPV-2000. In addition, all values of θ were considered equally probable.

**Fig. 2.35** Schematic diagram of a thermal spray process[114].

The coating build-up was simulated in a three-dimensional Cartesian grid. The x and y coordinate were in the plane of the substrate and the z axis was perpendicular to this plane. The single splat shape is a cylindrical splat with maximum spread factor ξ and thickness h_s .

$$\xi_{max} = \sqrt{\frac{We + 12}{3(1 - \cos\theta_{ls}) + 4(We/\sqrt{Re}) + We\sqrt{3Ste/4Pe}}} \quad (2.19)$$

$$h_s = \frac{2D}{3\xi_{max}^2} \quad (2.20)$$

where $\xi_{max} = d_{max}/D$, We is the Weber number, Re is the Reynolds number, Ste is the Stefan number, Pe is the Peclet number and θ_{ls} is the liquid-solid contact angle.

The overlapped splat was postulated based on observations from experiments. The splat shape formed by a droplet lands over a previously formed splat will not spread into a disk-shaped splat but assume a shape that depends on the distance between them. This distance is denoted as l . The different splat shape is shown in **Fig. 2.36** and the corresponding formulae were concluded in **Table 2.5**, where D_n is the diameter of the splat under consideration and D_m is the diameter of the nearest previously deposited splat. The surface area of non-circular splats was assumed to be the same as it remained circular.

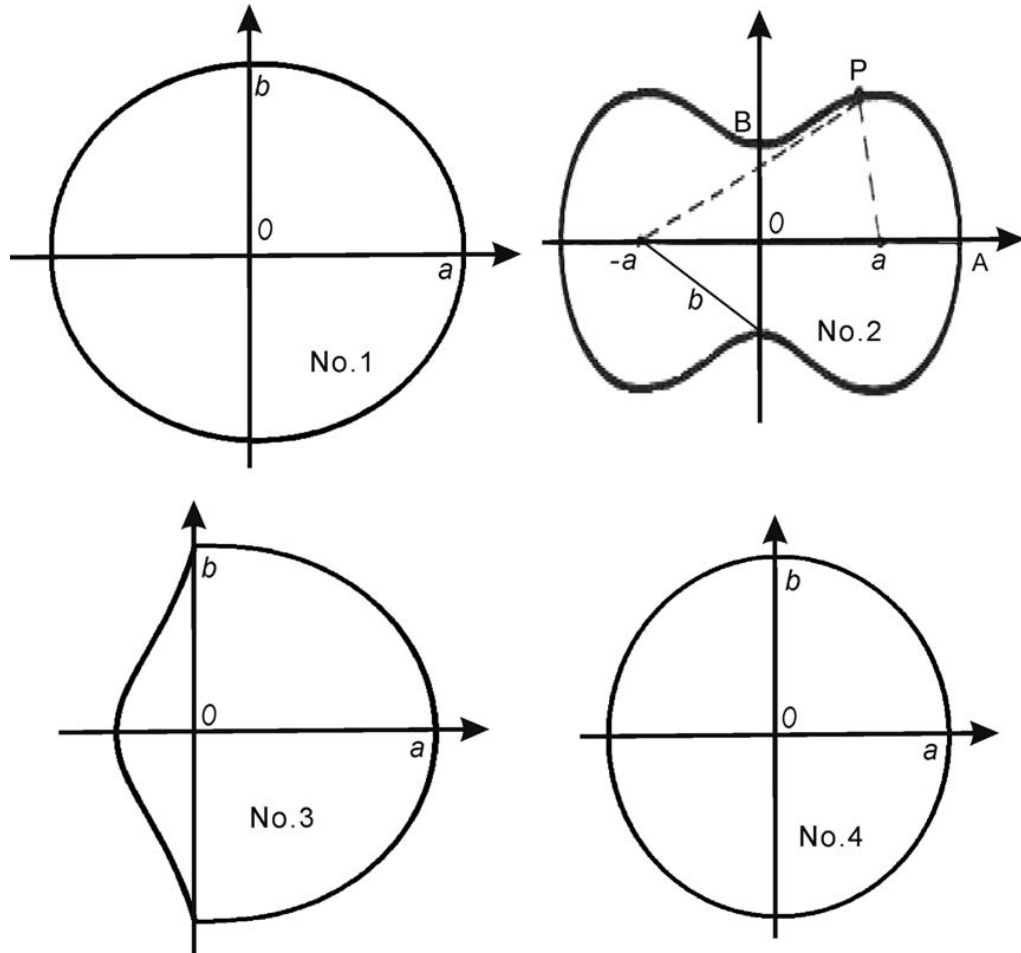


Fig. 2.36 Schematic diagram of the impact splat shapes when overlapping with the other splats[115].

The porosity in the coating is due to curl-up of splats caused by residual stresses for metal coatings[114] and incomplete filling of interstices in previously deposited material for ceramic coatings[115]. They assumed the pores evenly distributed over

Table 2.5 Equations to describe splat shapes in the Ghafouri-Azar[114] and Xue[115] model.

Shape	l	Equation	a/b
1	$0 \leq l \leq \frac{3}{8}D_m$	$\frac{x^2}{a^2} + \frac{y^2}{b^2} = 1$	$\frac{a}{b} \approx 0.8386(\frac{l}{D_m}) + 0.6878$
2	$\frac{3}{8}D_m < l \leq \frac{l}{2}D_m$	$r^4 + a^4 - 2a^2r^2 \cos 2\theta = b^4$	$\frac{a}{b} \approx -1.2842(\frac{l}{D_m}) + 1.2338$
3	$\frac{1}{2}D_m < l \leq \frac{7}{8}D_m$	$\begin{cases} y = \frac{R}{e^{2x/R} + e^{-2x/R}} & y > 0 \\ \frac{x^2}{a^2} + \frac{y^2}{b^2} = 1 & y < 0 \end{cases}$	1.0
4	$\frac{7}{8}D_m < l \leq \frac{D_n + D_m}{2}$	$\frac{x^2}{a^2} + \frac{y^2}{b^2} = 1$	1.1

the area between $0.6R$ and the edge of the splat, where R was the splat radius. The void height under a splat was represented by

$$h_g(x_i, y_j) = \begin{cases} \frac{\sum r_i V_{in}(i)}{0.4R\lambda} & , |(x_i, y_j) - (x_c, y_c)| > 0.6R \\ 0 & , |(x_i, y_j) - (x_c, y_c)| \leq 0.6R \end{cases} \quad (2.21)$$

where (x_c, y_c) are the coordinates of the splat center, $\sum V_{in}$ is the total volume of pores, λ is the width of the asperity row.

Then the coating is built-up by a method similar to Volume-of-Fluid (VOF), i.e.,

$$f_{i,j,k} = \frac{V_{mat}}{V_{cell}} \quad (2.22)$$

where $f = 1$ if the cell is inside the splat and $f = 0$ if the cell is outside the splat. For a partially filled cell, $0 < f_{i,j,k} < 1$. The profile of the deposit is updated with the splats building up with others. The predictions from the model showed that the porosity, thickness and roughness decrease with increasing particle velocity. The model also predicted the reduction in porosity with particle size.

The model developed in this work was inherited from Kang's SCM code. The difference is that the splat formation was implemented on the pre-deposited surface, i.e., the surface to be deposited is changed with time and not a flat surface. The deposit is computed from accumulation of approximately 300,000 splats for each time interval. Porosity is not included in the current model, since the computing hardware is not enough for the pores calculation involved in so many splats accumulation. Besides, the overlapping mechanism between splats is still not clear on an inclined surface or a curve surface. Thus a simple thickness accumulation

method, which essentially is the same as that by Beauvais et al.[112] and Kang et al.[113] are employed.

2.5.2 Particle Rebound and Deposition Efficiency

During the deposition, some material mass will be lost, due to various reasons such as particle evaporation, particle diversion by the gas flow and splats peel-off. Particle rebound is the one of the most significant reasons. Shinoda et al.[116] noticed that during the plasma spraying of the YSZ particles, secondary particles were ejected and flew in the radial direction at the periphery of the deposit, which is considered as the rebound phenomena of solid particles, as shown in Fig. 2.37. Kang et al.[117] investigated the plasma spray deposit on inclined substrates. It could be seen that the particles rebound toward the upper region of the substrate with the increase of the substrate inclination angle. In addition, more particles rebounded toward the upper region of the substrate.

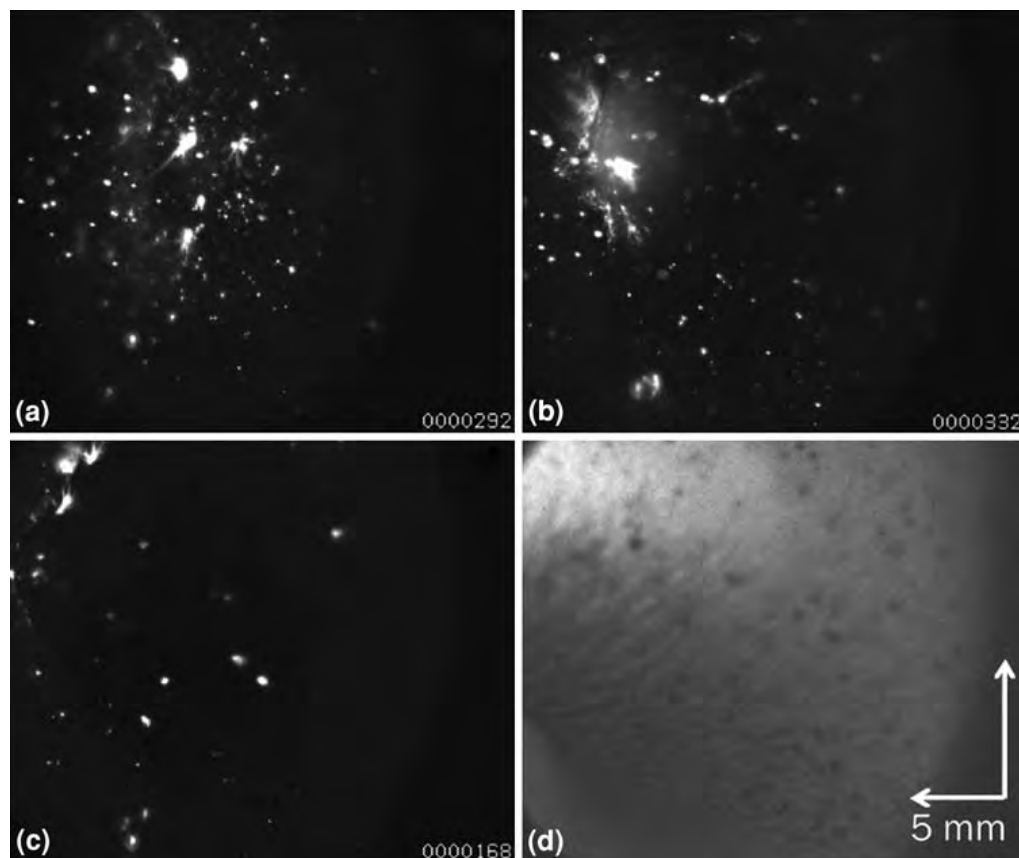


Fig. 2.37 In situ observation of deposit formation by Shinoda et al. (a) 12s, (b) 43s, (c) 64s after powder injection. (d) after deposition.

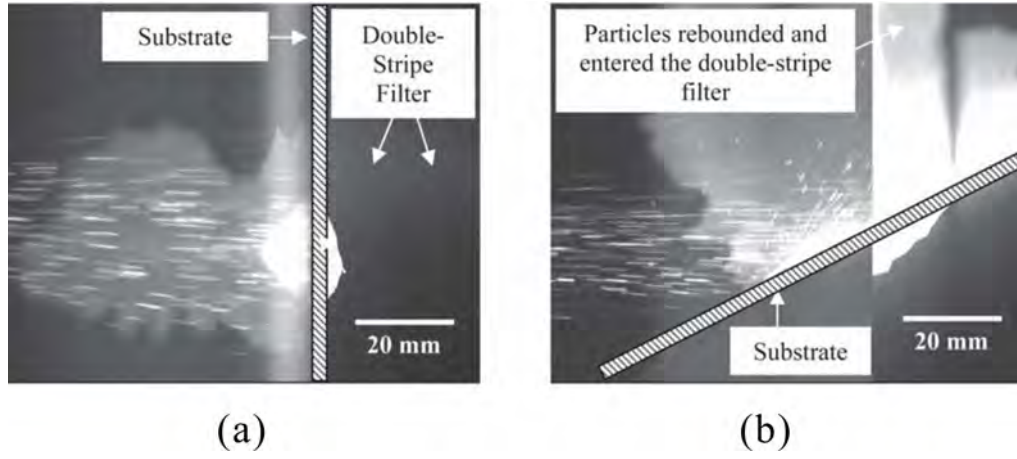


Fig. 2.38 Images of particles (a) impacting on the perpendicular substrate, (b) deflected by the substrate in an inclination angle 60° .

To evaluate the mass loss during the deposition, deposition efficiency is introduced. Essentially deposition efficiency is the fraction of the material which is deposited. It is calculated from **Equation 2.23**:

$$DE = \frac{W_D}{W_I} \times 100\% \quad (2.23)$$

where W_D is the mass of deposit on the substrate and W_I is the mass of the powders injected.

Values of deposition efficiency obtained from the work conducted under different process conditions are collected as in **Table 2.6**. The lowest deposition efficiency was on the substrate glass slide, which was relatively smooth. It is because a smoother surface has a weaker mechanical adhesion between the splats and the substrate, thus reduces the deposition efficiency. Kucuk et al.[97] summarized that the deposition efficiency was lower for the deposit sprayed with (1) lower torch power (2) higher powder feed rate (3) larger stand-off distance (4) irregular powder morphology and (5) a worn torch electrode.

Table 2.6 Collection of deposition efficiencies from the literature.

Powder	Substrate material	Deposition efficiency (%)	Operating condition	Researcher
Zirconia (Al-1075)	–	40–65	900A, 34V, Ar-He	Fincke and Swank[118]
Fused YSZ	Grit-blasted mild steel	55	800A, 34–32V, Ar-H ₂	Leblanc et al.[119]
Crushed YSZ	Grit-blasted mild steel	48–51	500–600A, Ar-H ₂	Jewett et al.[120]
YSZ	Glass slide	7–25	600A, 70V, Ar-H ₂	Kucuk et al.[97]

Chapter 3

Experiments on the Plasma Spray Process

3.1 Introduction

This chapter describes the experimental procedure of the plasma spray process in the work, including in-flight particle diagnostics, single splat capture and characterization and deposit formation and characterization. The purpose of this work is to provide data for the input parameters selection for the droplet impact behavior simulation and validation of the simulation work on the in-flight particles, droplet impact behavior and deposit formation.

The workflow of the experiment procedure is shown in **Fig. 3.1**. Different substrates are included in the plasma plume for different purposes:

- a. Online-diagnostics of the in-flight particles by SprayWatch© with no substrate included. The measurement distance is set as 80 mm, which is the stand-off distance of the substrates in other cases. The purpose of this configuration is to measure the in-flight particle parameters prior to their impact on the substrates.
- b. Single splat capture by flat substrates (stainless steel sheets) for the droplet impact behavior analysis under normal impact conditions.
- c. Single splat capture by curved substrate (stainless steel sheets) for the droplet morphology evaluation on curved surfaces.
- d. Deposit formation on the curved shape substrates (grit-blasted mild steel). SprayWatch© is employed to monitor the deposit growth with time.

The stand-off distance is defined as the distance between the plasma torch front face and the vertical plane where the substrate front surface center resides. It is set as 80 mm for all the experiments consistently. A shutter system is introduced into the spray system for increasing the possibility of getting relatively perfect splats.

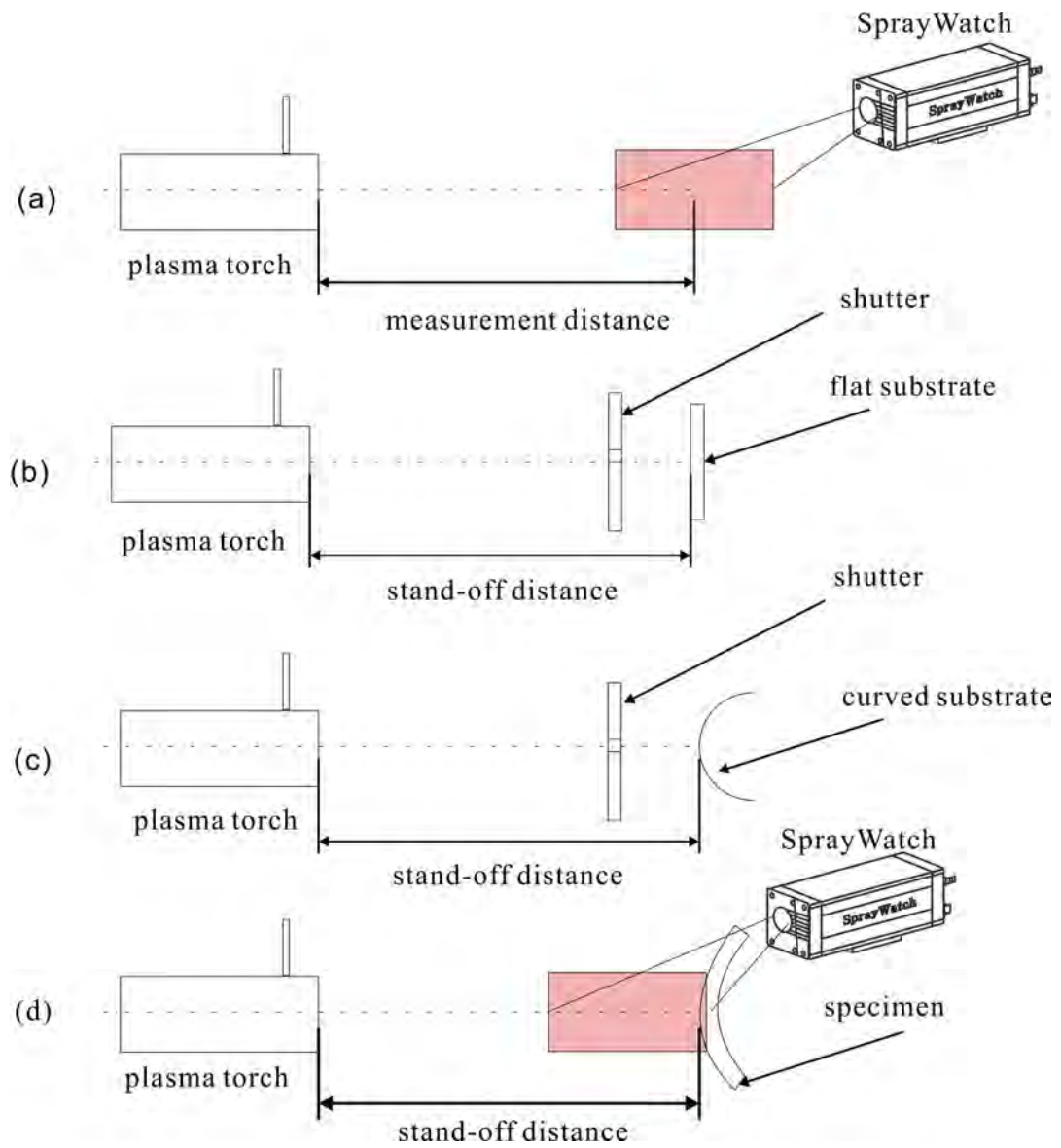


Fig. 3.1 Schematic illustration of the workflow of the experiments. The shaded square area represents the measurement area of the SprayWatch®.

3.2 Spray facilities and parameters

General plasma spray operating conditions is described in this section. The plasma spraying is performed by the SG-100© torch (Praxair Surface Technologies Inc., N670 Communication Drive, Appleton, Wisconsin 54915, USA). A schematic illustration of the plasma torch is shown in **Fig. 3.2**. A roto-feed powder hopper (Miller) model 1264© (also from the above supplier) is used to introduce the powder into the plasma torch via an internal powder injector with a 2 mm internal diameter. The primary gas and carrier gas used in this study is argon. The other detail plasma spray operating parameters are listed in **Table 3.1**.

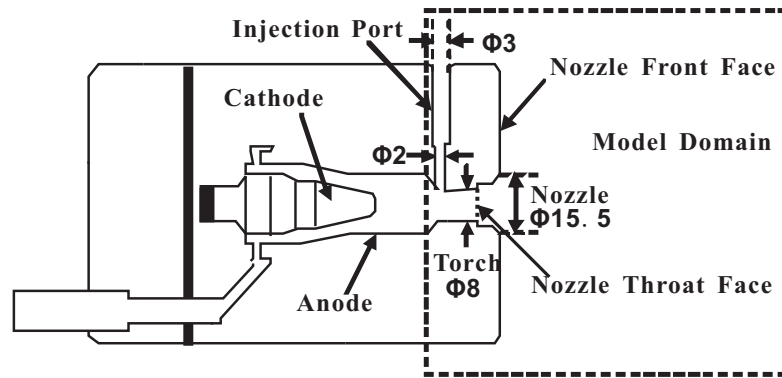


Fig. 3.2 Schematic illustration of the SG-100 torch gun.

Table 3.1 Experimental spray parameters.

Parameter (Unit)	Magnitude
Substrate standoff distance (mm)	80
Current (A)	900
Voltage (V)	35
Primary gas (Argon) flow rate (slm)	72
Carrier gas (Argon) flow rate (slm)	4.2

The feedstock powder in the experiment throughout the entire work is a commercially available 8wt% yttria partially stabilized zirconia (YSZ), product code: 204NS (Saint-Gobain Coating Solutions, Northampton, Massachusetts, USA). The powder size is in the range of 22 to 125 μm in diameter with a mode of 37 μm . The powder is characterized by near-perfect spherical shape, as the SEM photograph shown in **Fig. 3.3**.

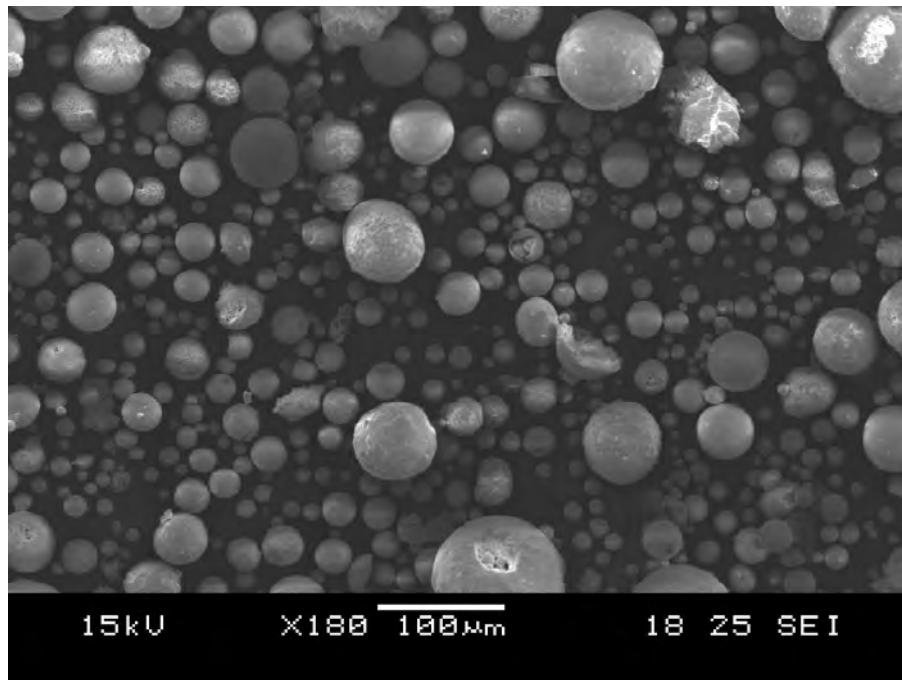


Fig. 3.3 SEM photograph of yttria partially stabilized (8wt%) zirconia (YSZ) powder showing near-perfect spherical particles.

These spray conditions and feedstock powders are used throughout the entire work in the thesis. In the following texts, the three spray experiment sets are described, including in-flight particle behavior diagnostics by SprayWatch®, single splat capture experiment and deposit formation on the curved shape substrates.

3.3 In-flight particle behavior diagnostics by SprayWatch©

SprayWatch2i© from Oseir (Hermiankatu, 6A, 33720 Tampere, Finland) is used to acquire the in-flight particle parameters prior to impact, such as velocity, temperature and flight angle. These values serve as validation data for the in-flight particle parameters simulation by FLUENT© and as the basis of input parameters selection for the droplet impact behavior simulation.

SprayWatch© is an advanced monitoring system for diagnostics and process control of various thermal spray processes. The image capturing function is achieved by a digital CCD camera unit. Digital images of in-flight particles are taken with short exposure time, and transferred to a dedicated computer instantly for “on-line” processing. Special algorithms developed by Oseir Ltd. are used to control the camera, and calculate the particle in-flight parameters. Principles of these algorithms are narrated in the succeeding paragraphs. A dust-proof industrial cabinet is used to prevent the computer from damages caused by dust and high-temperature environment.

3.3.1 Measurement Volume and Focus Distance

The CCD camera consists of an array of tiny detectors. Therefore, the measurement volume is very large compared to that of a point-measurement system. It can be adjusted by setting the focus distance through the SprayWatch© software. Definition of the measurement volume and some related terms are illustrated in **Fig. 3.4** and described below:

- Measurement volume, the volume in which the particles can be detected.
- DoF (Depth of Field) is the depth of the measurement volume. It depends on the aperture of the imaging optics, which is automatically selected on the basis of brightness of the process under monitoring. Small value (1-50) of aperture is suitable for bright process, while larger (80-100) value is typical for lower temperature processes.
- FOV X, width of the measurement volume.
- FOV Y, height of the measurement volume.

- Focus distance is the distance between the spray and the camera unit.
- Stand-off distance, distance between the spray torch and the substrate being sprayed.
- Measurement distance, distance between the spray torch and the center of the imaged volume.

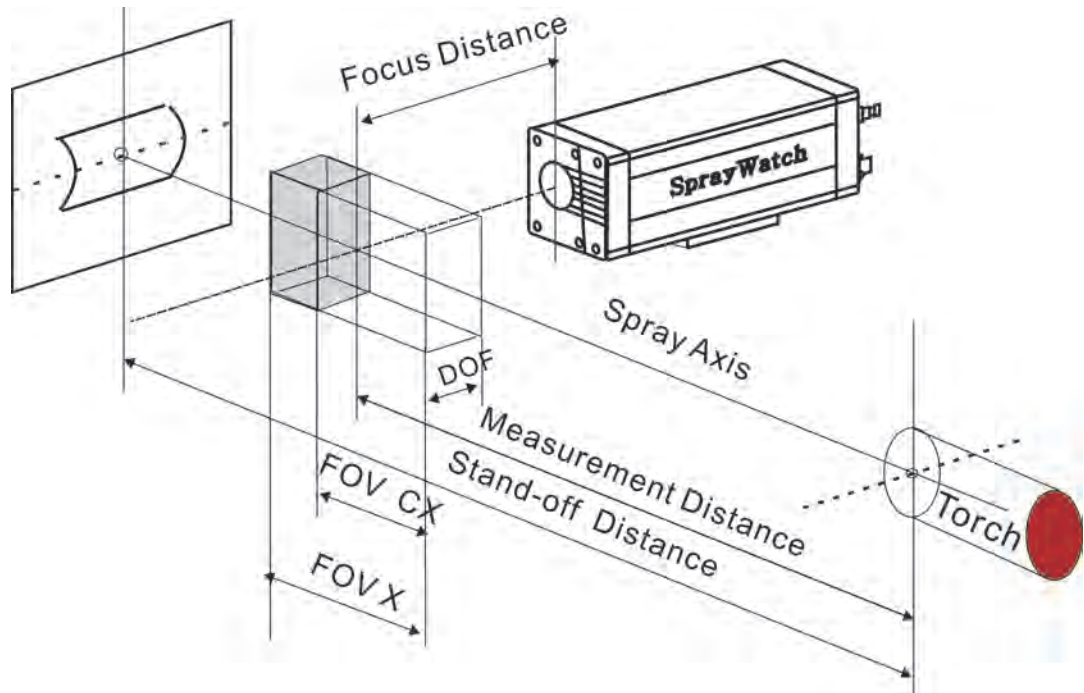


Fig. 3.4 SprayWatch setting for particle in-flight parameters diagnostics and definition of some measurement terms.

Fig. 3.5 shows the imaged area, which is the side view of the measurement volume of the SprayWatch® in the plasma spray plume. It is divided into two sections by the spectrally resolving optics: Section A is imaged by clear optics, while Section B is blur, because it is covered by two optical filters. The purpose of this design is to measure the average particle temperature, which will be elaborated later in this section.

In the experiment of the in-flight particle diagnostics, no substrate is included. The measurement distance is the same as the stand-off distance value when substrates are included. By this means, the obtained in-flight particle parameters can be considered as those values prior to their impact to the substrates. The focus distance is set as 270 mm. The monitoring lasted for 30s, capturing around 300 particles for each repetition.

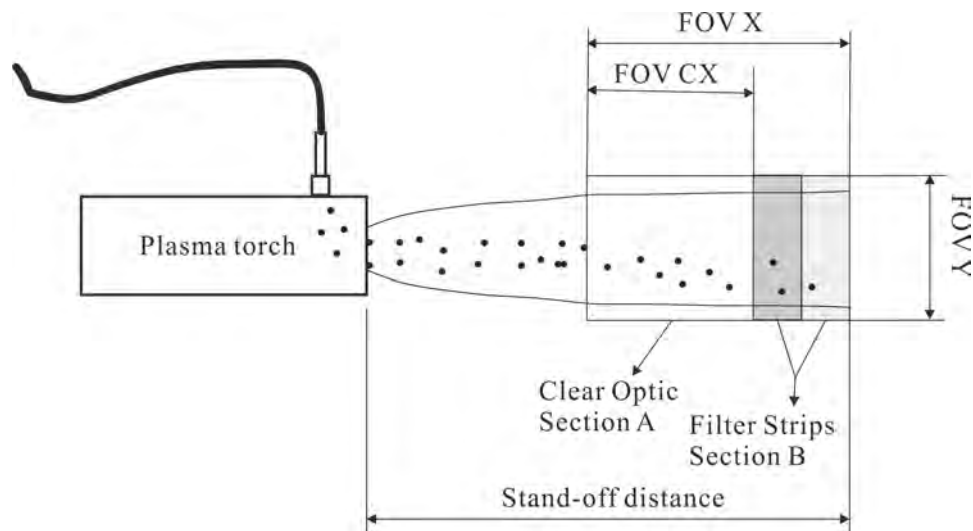


Fig. 3.5 Side view of the measurement volume in the plasma spray plume.

3.3.2 Particle Velocity Measurement

Particle velocity is measured by the “time-of-flight” method. The camera takes images with short exposure time, during which the particle travels to the next position. A special image processing algorithm enable the software to construct the particle trace. Thereafter, the in-flight angle and travel distance could be measured, and the particle velocity is computed from the travel distance and the exposure time. The accuracy of this method is 0.1 to 1 m/s depending on the velocity range.

3.3.3 Particle Temperature measurement

Particle temperature is measured by two-color pyrometry. In order to use two-color pyrometry, two images in two wavelength ranges need to be captured. Conventionally, it is accomplished by two cameras, or a special, complicated and expensive optical setup for one camera. In SprayWatch®, the CCD camera is partly covered by a special optical double-stripe filter, as Section B shown in **Fig. 3.5**. The filter combination allows measurement of the radiation intensity of the particle flow in two narrow wavelength ranges centered at 680 and 870 nm. The lateral distribution of the average particle temperature in the spray can be calculated by the two-color pyrometry method. No further calibration is needed because the two signals in different wavelength range are detected by the same, monolithic detector array and amplified by the same circuit. The temperature detection will not

disturb the in-flight particle velocity and trajectory detection, because this function is accomplished by the remaining, clear part of the CCD camera.

3.3.4 Observation by SprayWatch©

Fig. 3.6 shows the example image of plasma spray process captured by SprayWatch©, showing in-flight particles traversing the image area.

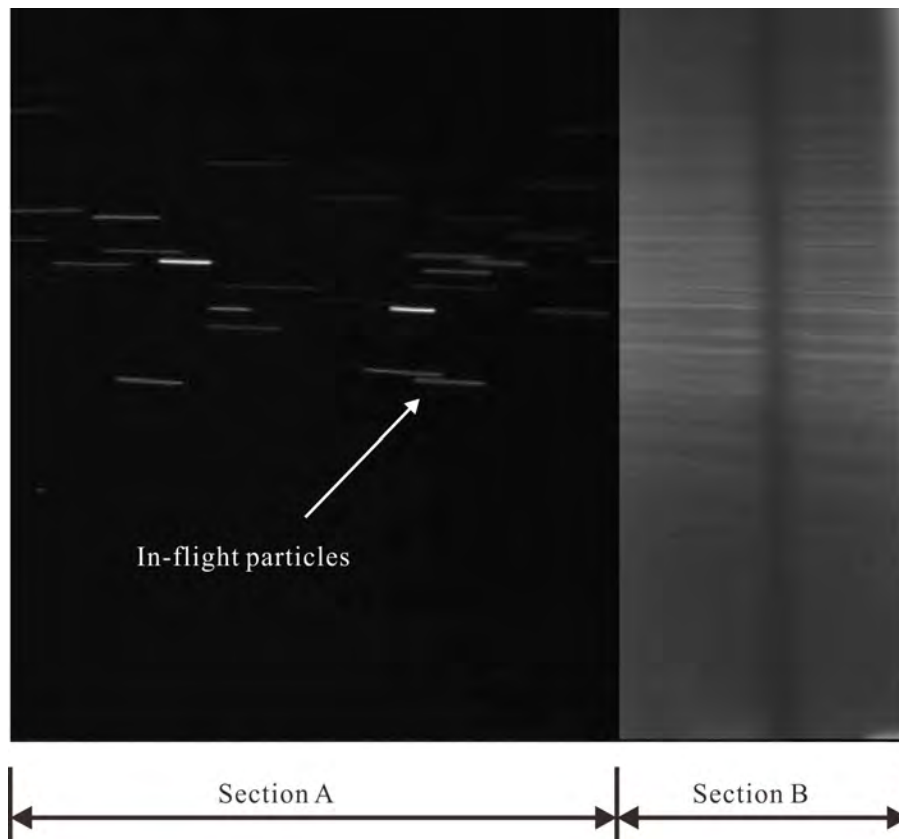


Fig. 3.6 Example of the captured image of plasma spray process by SprayWatch©.

The velocity and flight angle distribution from the SprayWatch© measurement are shown in **Fig. 3.7**. It can be noticed that the distribution is in a “bell” shape. The flight angle of most of the particles ranges from 0° to 8° (with the mean value 2.22° and a standard deviation 3.09°), which eventually justify the assumption in the author’s deposition code that all the particles impact to the a virtual vertical plane perpendicularly.

Although the particle temperature measured by SprayWatch© is not as accurate as velocities, it is still post-processed to evaluate the upper boundary, median values and lower boundaries at every time frame, as in **Fig. 3.8**. The range of

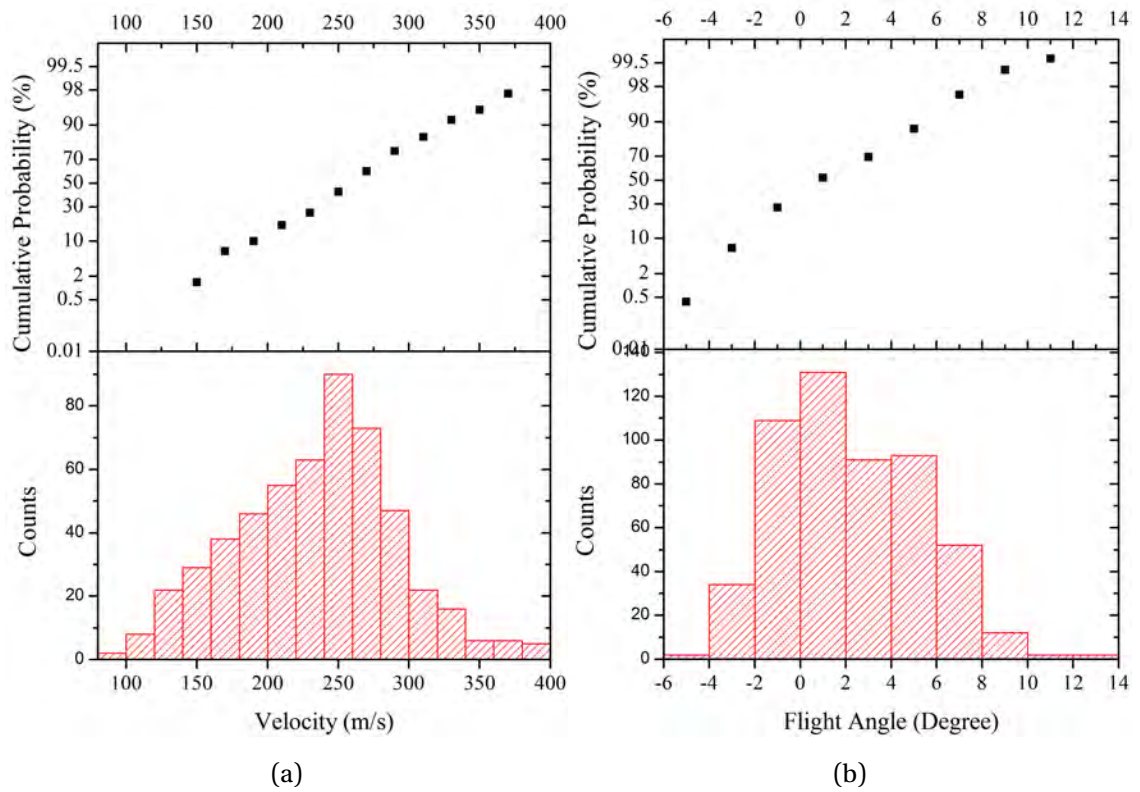


Fig. 3.7 Particle (a) velocity magnitude and (b) flight angle distribution histogram and probability plot from SprayWatch© diagnostics.

the temperature is used to select droplet temperature for droplet impact behavior simulations.

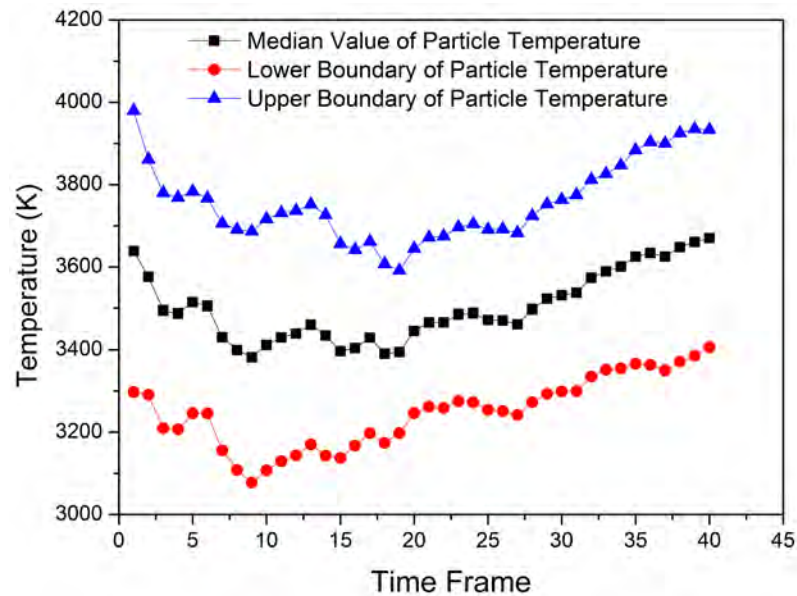


Fig. 3.8 Particle temperature measured by SprayWatch©. Median values, upper boundary and lower boundary values are shown respectively with the time frame.

3.4 Single splat capture experiments

Single splats are captured by flat and curved stainless steel sheets and then characterized by microscopes. The stainless steel sheets are pretreated and a “shutter system” is designed and built to increase the possibility of getting near-perfect splats. The mass flow rate is set as 1 g/s to avoid excessive particles impacting on the substrate.

3.4.1 The substrate preparation

The target substrates are stainless steel sheets with size of $20 \times 20 \times 0.3$ thick mm for flat substrate and $85 \times 22 \times 0.3$ thick mm for curved substrate. It is a compromise to choose the thickness of the substrate. A too thin substrate will experience a severe surface melting and shape change under the high temperature of the plasma plume. But the substrate also cannot be very thick for the following reasons:

- The substrate sheet has enough flexibility to wrap around the substrate holder without any damage to the sheet surface.
- It is also easy to be flattened, for the purpose of microscope inspection. It is found that the splats have sufficient adhesion not to spall from the substrate.
- It is easy to cut the splat distribution region off with a low possibility of splats peeling off.

Elemental analysis is carried out using Energy Dispersive Spectroscopy (JEOL JSM-5600LV). The EDS spectrum is shown in **Fig. 3.9**. The weight fraction of elements are: Fe 83.19%, Cr 16.81%. From the specification table of stainless steel¹, it could be concluded that the material of the substrate is stainless steel AI 430.

A polishing procedure is carried out to remove the scratches and produce a relatively uniform roughness. Grit papers with ascending order of grid numbers (180→400→800→1200) are used in the polishing process. The resulting surface roughness is approximate $0.2 \mu\text{m}$. After polishing, the substrates are stored in a desiccant chamber to prevent them from absorbing water moisture.

¹ http://www.machinist-materials.com/stainless_table.htm

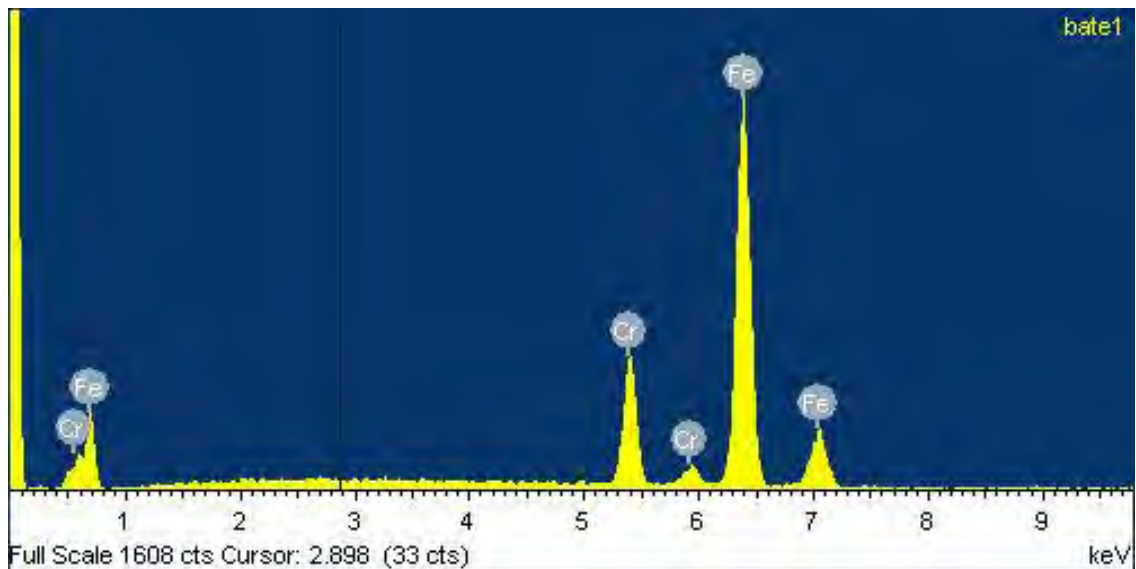


Fig. 3.9 EDS analysis spectrum of the substrate surface.

Different substrate preheat temperatures have been found[121] to affect the splat morphology by their influence on the thermal contact resistance of the substrate. Therefore, in order to increase the possibility of obtaining perfect or relatively perfect splat forming, the substrate sheets have to be preheated before spraying.



Fig. 3.10 Quartz tube heater used for substrate sheets preheating.

A self-made quartz tube heater (**Fig. 3.10**) is used to preheat the substrate sheet overnight before spraying. Resistance wire is spirally wound around a quartz tube. Glass wool cloth and aluminum foil are wrapped for heat preservation. The input voltage is adjusted by an electric transformer to ensure the internal temperature is 350°C.

After preheating, the substrate sheets are mounted. For the flat substrate case, the substrate sheet is fixed on a fixture in front of the plasma torch by a magnetic bar on the back of the fixture. The substrate center is in the centerline of the plasma torch and the substrate surface is perpendicular to this centerline. For the curved substrate case, the substrate sheet is wrapped around the substrate holder made from the aluminum cylindrical holder and tightly fixed on it by two screws (separation angle 90°), as in **Fig. 3.11**. This substrate holder has the radius 13.5 mm.

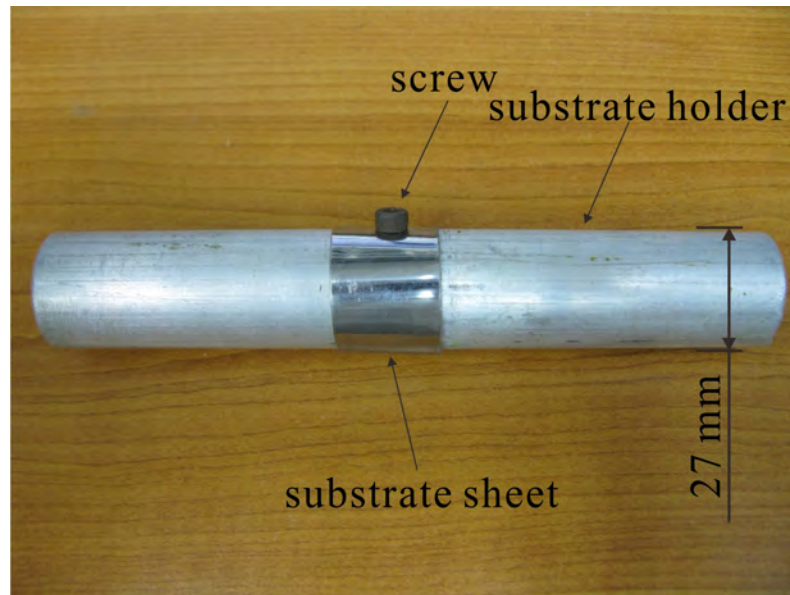


Fig. 3.11 The fixing of substrate sheet around the cylindrical holder

3.4.2 Experimental setup

The experimental setup is shown in **Fig. 3.12**. The substrate is placed in front of the torch, with a standoff distance of 80 mm. A “shutter system” consisting of a plate with a slit cut in it controls the in-flight particle flux to reduce excessive splat overlapping. The shutter will block the spray plume and particle flux when it is at rest on the bottom bar of the frame. A steel wire rope is used to lift the shutter plate to move it up and down, so the particles may pass through the slit on the shutter plate within a very short time.

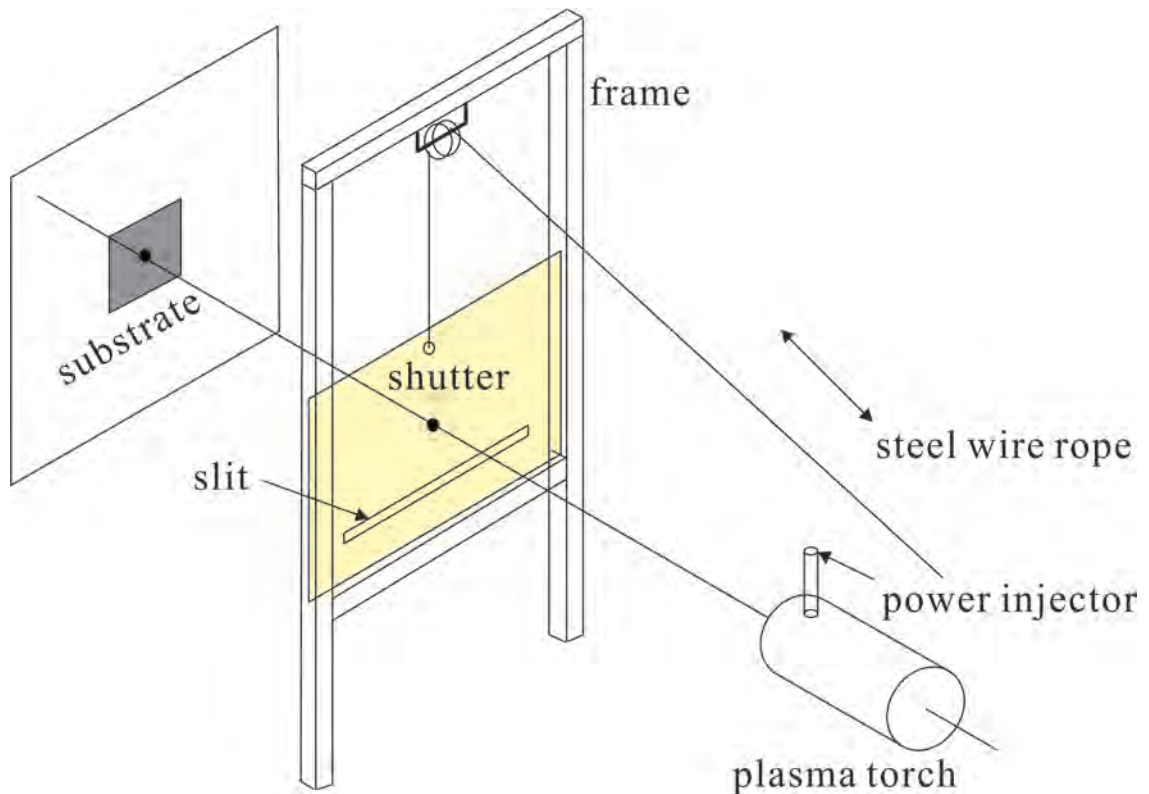


Fig. 3.12 Plasma spray system setting for the single splat capturing, showing the “shutter system”.

3.4.3 Substrate temperature evolution evaluation

Before the single splat capturing experiment, a test of the substrate temperature evolution behavior has been carried out. The purpose of this test is to monitor substrate sheet temperature, in case the substrate sheet is overheated to distort its shape. If possible, this surface temperature will be held in a relatively stable value, which will be set as the input value in the simulation. A simple temperature acquisition system is designed, as shown in **Fig. 3.13** and **3.14**.

This test is done by using the curved substrate. A K-type thermocouple is twisted and spot welded and rested between the substrate sheet and the cylinder substrate holder. **Fig. 3.14** shows the view under the substrate sheet. The temperature reading is the average value of those at several contact points. To protect the thermocouples outer sheath from the plasma plume, a protection sheet also surrounds around the cylinder holder, at one side of the substrate sheet. The thermocouples extend under the substrate sheet, the protection sheet, and then is connected to a Portable Data Logger (TDS-302, Tokyo Sokki Kenkyujo Co., Ltd), as in **Fig. 3.15**. The temperature

acquisition interval is set as 1s, the minimal time interval that the data logger can achieve.

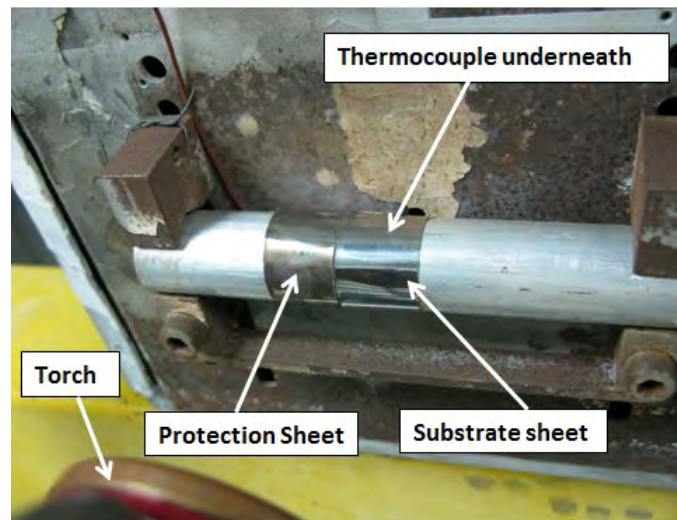


Fig. 3.13 Substrate sheet surface temperature measurement system.

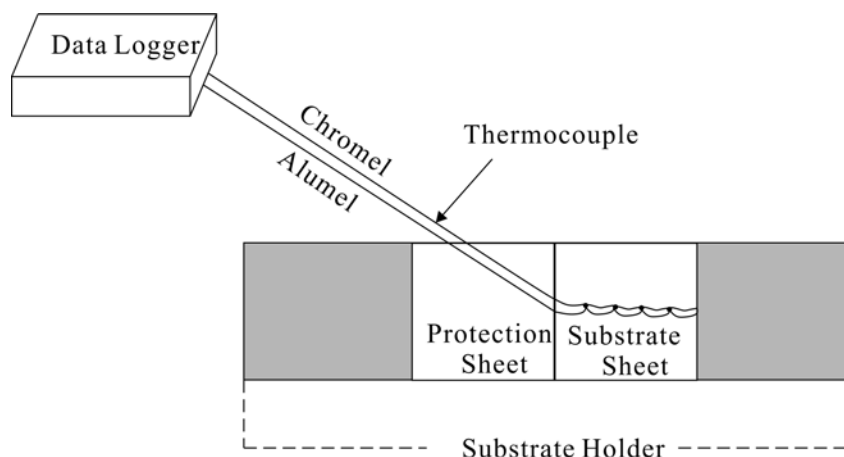


Fig. 3.14 The thermocouple attachment under the substrate sheet.



Fig. 3.15 Data logger used to record the temperature data from the thermocouples.

In the splat capture experiment, there are three stages, as in **Fig. 3.16**. In the beginning, the shutter is totally lifted, so the plasma plume impinged on the substrate sheet. The substrate sheet is preheated during this period, which is called “plasma heating phase”(a). After that, the shutter is moved up and down by releasing and pulling the steel wire. When the particles are fully blocked by this shutter, it is called “block phase”(b); when some of the particles pass through the slit, it is called “splat capture phase” (c). Three tests are made to find an appropriate plasma heat time. In the first test, the shutter is lifted throughout the spray period without particle injection. In the second test, the preheat phase is set as about 4 s. In the third test, it is set as about 2 s), shorter than the second test. In both of the second and third tests, particles are injected after the preheat phase.

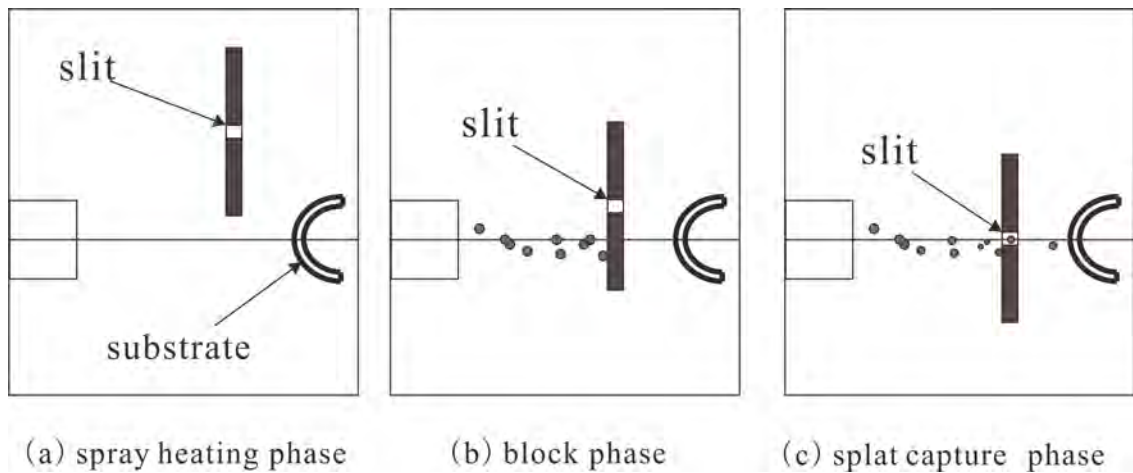


Fig. 3.16 The three phases during splat capture experiment

The first test, the temperature development without a shutter blockage is shown in **Fig. 3.17**. It is noticed that the temperature increases rapidly with spray time, until the power is switched off. Subsequently, the temperature is relatively stable for about 13 s, then decreases with a higher cooling rate. Because the substrate sheet is very thin (0.3 mm), a continuous spray heating is not preferred. The temperature development with the shutter moving is monitored in the second test.

As is evident from **Fig. 3.18**, the temperature increases to 930 K in 4 s after the spray start during the “plasma heating phase”. After this period, the shutter is moved up and down, the temperature fluctuates because the slit allows intermittent heating. The temperature starts to drop since the spray torch is switched off. The lower

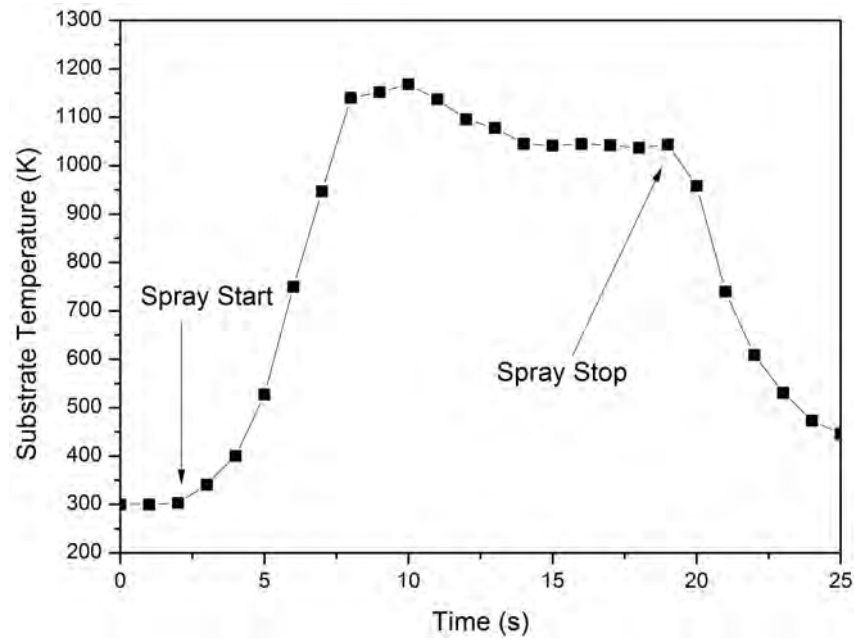


Fig. 3.17 Substrate sheet surface temperature development behavior during and after spraying without a shutter blockage.

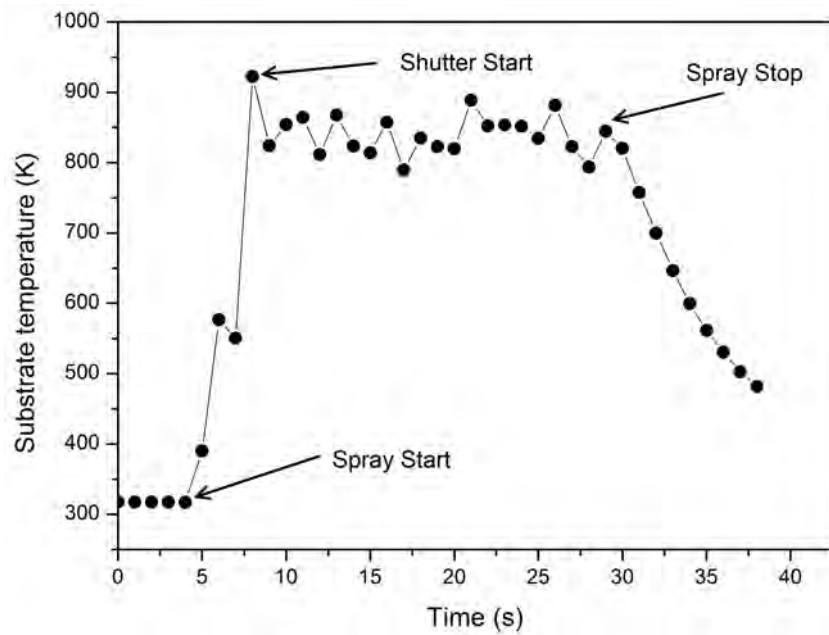


Fig. 3.18 Substrate sheet surface temperature development behavior with 4 s preheat phase.

temperature (850°C in the plateau part) compared with the temperature in **Fig. 3.17** (1100°C in the plateau part) may be attributed to the shutter intervention. To protect the substrate surface from damage, another test is done. The plasma heat phase is set as 2 s. The resulting temperature development is shown in **Fig. 3.19**. The

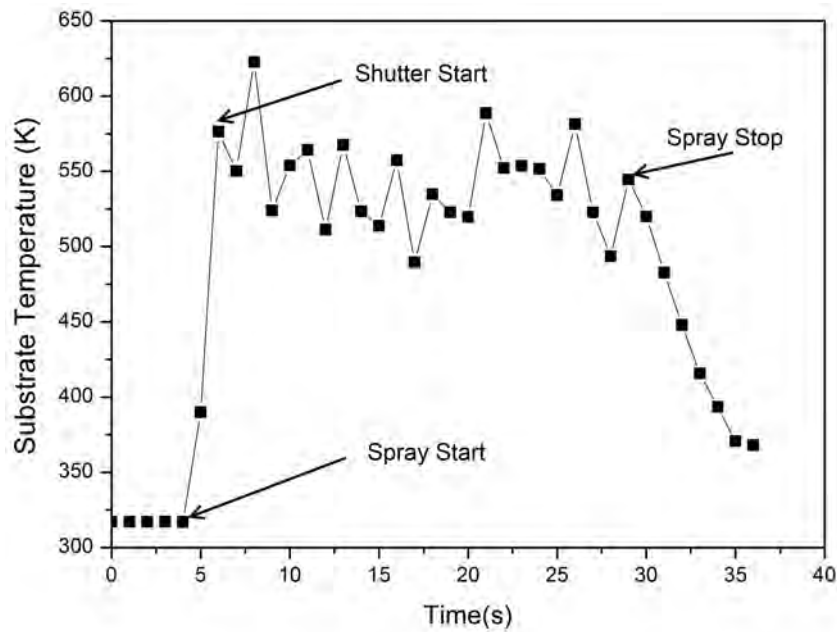


Fig. 3.19 Substrate sheet surface temperature evolution behavior with 2 s preheat phase.

temperature is lower as expected. In the experiments after this set of tests, the plasma heat phase is set as 2 s consistently, as deduced from the plot in **Fig. 3.19**.

3.4.4 Experimental image analysis

In order to inspect the morphologies of the splats, the substrates are examined by the scanning electron microscope (FE-SEM, Quanta 200 FEG System, FEI Company, USA) and the confocal imaging profiler (Eclipse L150 PL μ , Nikon, Tokyo, Japan). The substrates are sputter-coated with gold prior to the SEM inspection, as zirconia is non-conducting material. The splat three-dimensional profiles are measured by the confocal imaging profiler. For the convenience of determining the position of an individual splat on the curve substrate, an Olympus BX51WI optical microscope (Olympus, Japan) equipped with CCD camera (QICAM, QImaging, Canada) is employed to analyze the splats geometries, instead of SEM used for characterize the splats on flat substrates.

3.4.4.1 Types of splats on the flat substrate.

Fig. 3.20 shows a broad view of many splats on the flat substrate under the the scanning electron microscope. Inspection of individual splat reveals different types of splats, as shown in **Fig. 3.21**. **Fig. 3.21(a)** presents an example of a perfect splat

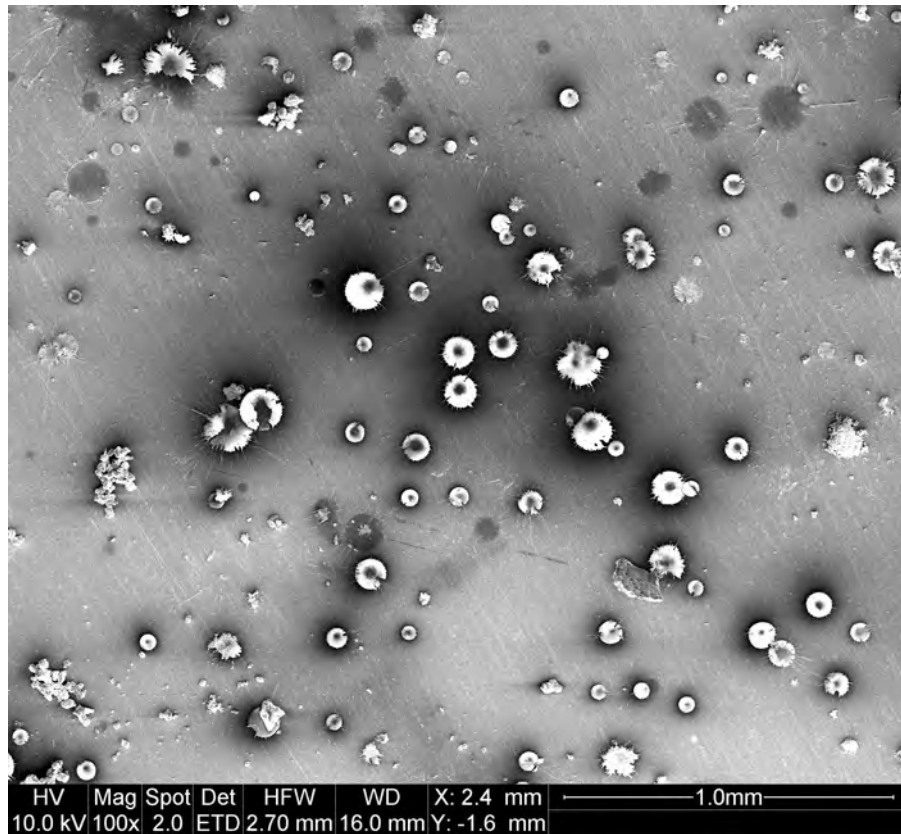


Fig. 3.20 A broad view of the substrate with many splats on it.

on the substrate. The splat remains intact with almost no splashing characteristics. **Fig. 3.21(b)** shows partially breakup in the splat mainbody with protruding fingers surrounding the splat. It is obvious that in **Fig. 3.21(c)**, the splat is in a flower-like shape. The splashing becomes severe, characterized by the large extent of jets and fingers. Most of the splats captured in this experiments belong to type (a) and (b), which are digitalized in this research to serve as validation of the simulation.

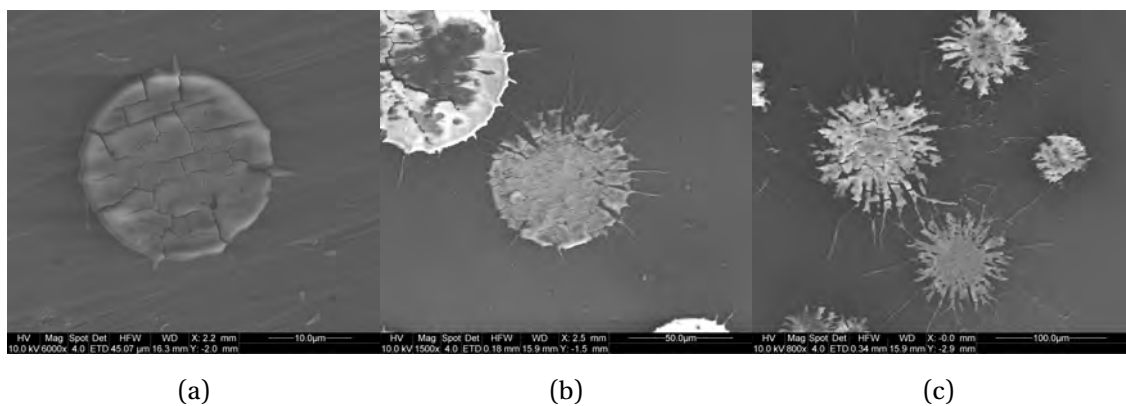


Fig. 3.21 Typical splats found on the flat substrate.

3.4.4.2 Splat shape on the curved substrate

For curved substrate, the substrate sheet is unwrapped and taken off from the cylinder substrate holder after spraying. The sheet is flattened for observation under microscopes. The flattening procedure results in a coordinate transformation, as shown in Fig. 3.22, which is called “development”.

The curve surface (semicircle) represents the front face of the substrate sheet. O' is the middle point of the semicircle, at the angular position 0° . S' is a point where a splat resides. On the developed surface, the corresponding point becomes S , which is at a location with the distance OS equals to the arc length $O'S'$.

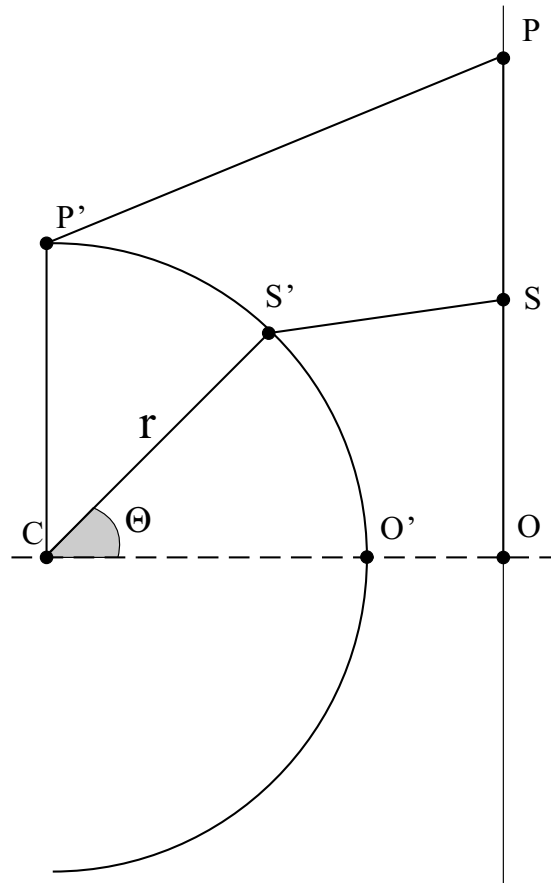


Fig. 3.22 The conversion between splat location on curved substrate sheet and the flatten sheet.

The splat locating idea is presented in Fig. 3.23. The microscope projects a light spot on the substrate sheet. The middle point of the developed surface (flattened substrate sheet) O is set as the reference point. Therefore, the distance between the light spot, S and the middle point of the flattened sheet O , is the position of the splat

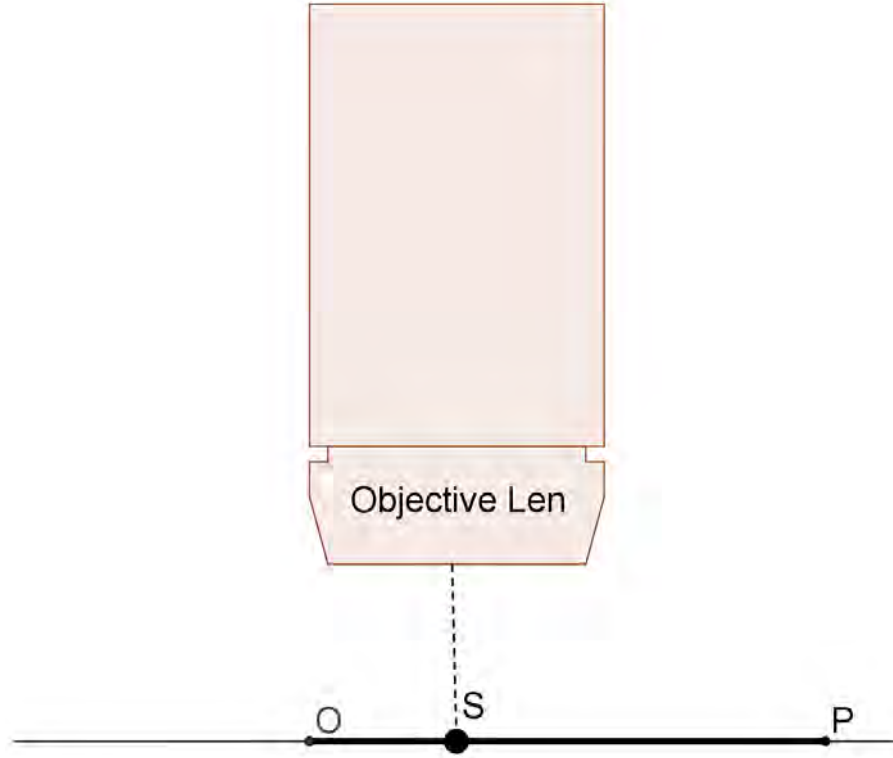


Fig. 3.23 The locating of the splat under microscope.

under inspection. This position is then converted back to the angular position on the original curved substrate. As shown in **Fig. 3.22**, the splat location S is converted to the angular location θ by the following way:

Since $OS = O'S'$, which means

$$OS = r_s \theta \quad (3.1)$$

therefore,

$$\theta = \frac{OS}{r_s} = \frac{OS}{r_h + t_s} \quad (3.2)$$

where r_s is the radius of the stainless steel sheet surface, r_h the radius of the substrate holder, t_s the thickness of the stainless steel sheet.

By the way mentioned above, splats at different impact angles are inspected. **Fig. 3.24** shows examples of the captured splats at different impact angles on the curve-shape substrate. It is noticed that under normal impact, the splat presents a circular shape. When the impact angle increases (the location of the splat gets away from the center of the curve substrate), the splat elongates and appears as

an ellipse shape. Some area of the images are darker due to out of focus since the substrate sheet cannot be perfectly flattened. **Fig. 3.25** shows examples of snapshots of the splats at different angles under confocal imaging profiler. To extract the splat morphology, the ascii data are postprocessed, which will be discussed in the results and discussion part of this thesis.

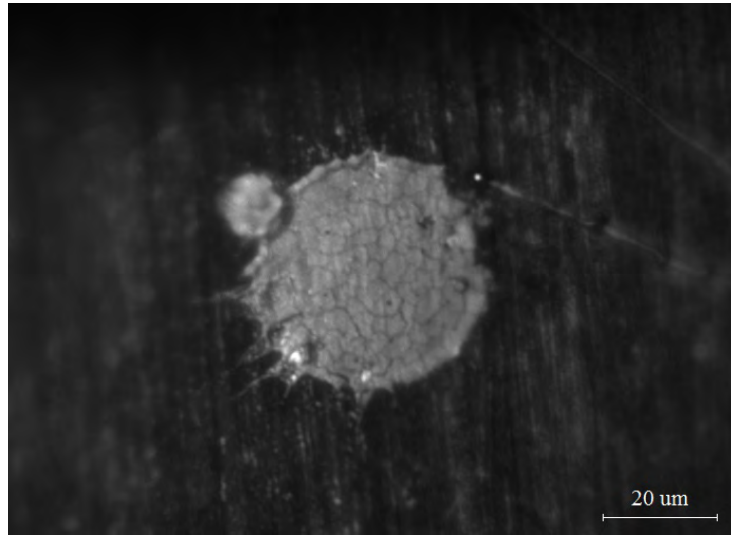
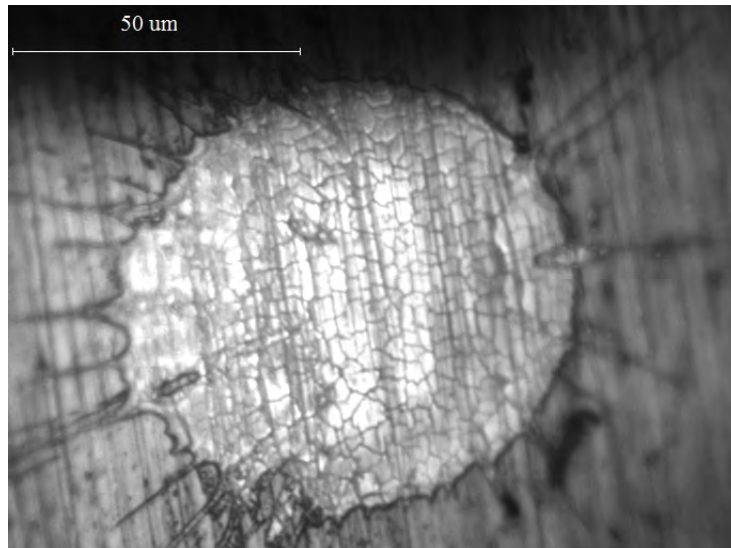
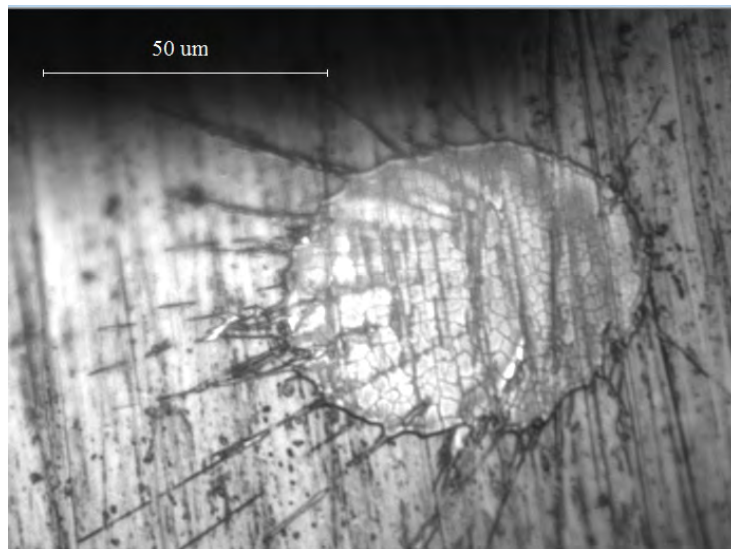
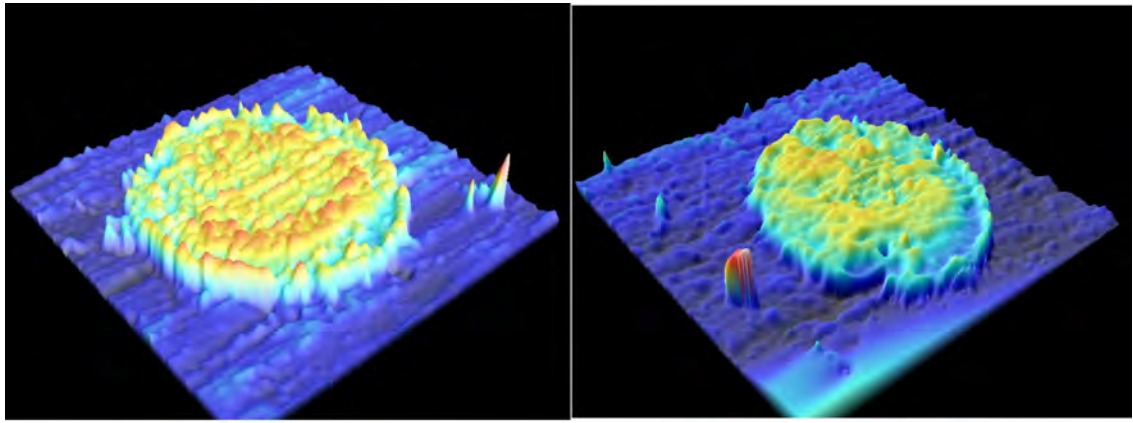
(a) 4° (b) 31° (c) 46°

Fig. 3.24 Optical micrographs of splats produced at different impact angles.



(a) impact angle of 20°

(b) impact angle of 43°

Fig. 3.25 Example of snapshots of splats at different impact angles under confocal imaging profiler.

3.5 Experiments on Deposit Formation

3.5.1 Experimental setup

In the deposit formation experiment, specimen are grit-blasted mild steel substrates as shown in **Fig. 3.26**. The mean arithmetic surface roughness is $50\ \mu\text{m}$. The radius of the convex surface is $R_1 = 85.7\ \text{mm}$. The substrate is placed in front of the plasma torch, with the convex surface facing to the torch. The stand-off distance is 80 mm.



Fig. 3.26 Curved specimen used in the deposit formation experiment.

Three cases are carried out, with the substrate in different vertical positions, achieving deposit at different locations on the substrate. As shown in **Fig. 3.27**, the resulting deposits are respectively on the upper, middle and lower part of the substrate surface in case 1, 2 and 3.

The exact spray durations are calculated from the SprayWatch© diagnostics images. Because the images are captured 3 frames per second, the spray time can be evaluated from the number of images since the depositing started. It is calculated that the substrate in each case is sprayed around 5 s for case 2, 10 s for case 1 and 3.

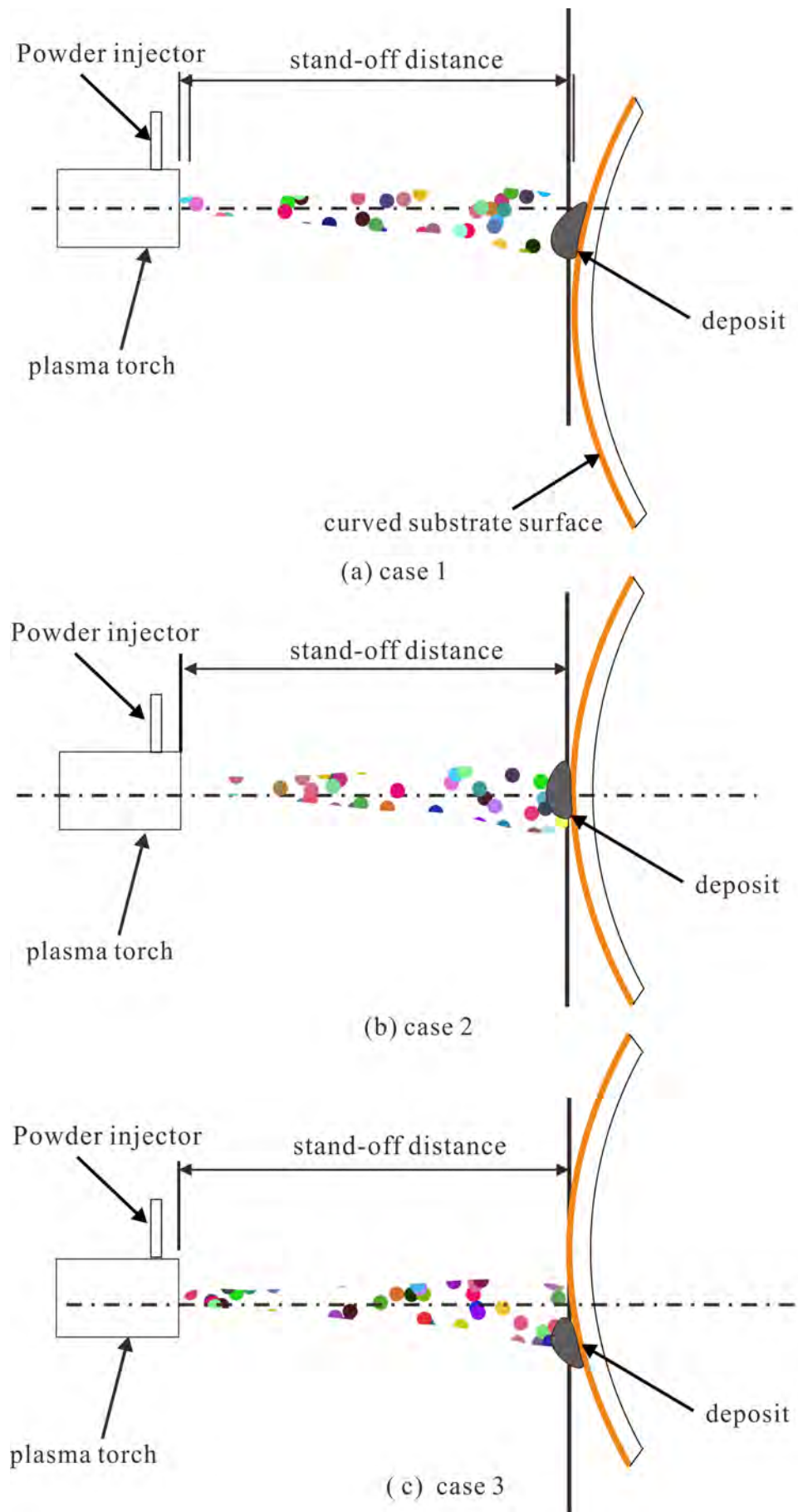


Fig. 3.27 Illustration of three experimental cases being carried out. The deposit resides on (a) case 1, the upper part of the substrate surface; (b) case 2, the middle part of the substrate surface; (c) case 3, the lower part of the substrate surface.

3.5.2 Deposition Efficiency

In experiments not all the incident particles adhere onto the substrate. Rebounding, peeling and some other factors, such as material vaporization may result in a low deposition efficiency. Therefore, it is necessary to take deposition efficiency into account in the modeling. Deposition efficiency is defined as the ratio of the weight of powder deposited on the substrate to that of powder injected into the torch per unit time, as shown in the equation below:

$$DE = \frac{W_D}{W_I} \times 100\% \quad (3.3)$$

where W_D is the deposit mass, while W_I is the mass of powder injected into the torch. The substrates are weighed before and after spraying respectively by a digital balance. Thus the net masses of the deposits (W_D) can be evaluated by subtraction method. The mass of feedstock powders injected into the torch are calculated from the powder feed rate (g/s) and the spray time (s). The powder feed rate is obtained by taking the injector off from the plasma torch and collecting the powders over a fixed collection time, in a bottle with known mass under thermal spray condition of carrier gas pressure and powder feeder rpm setting. The mass of collected powder per unit time is considered as the powder feed rate.

The deposition efficiency for the three cases is 37.5%, 37.1% and 41.4% respectively. These values are not considered very accurate, due to the large difference between the weight of deposit (~ 0.8 g) and the substrate weight (~ 700 g) and the fluctuation of the powder injection rate. However, the deposition efficiency is an acceptable value to take the mass loss caused by many factors into account.

3.5.3 Calibration of the dimensions of images from SprayWatch©

In order to monitor the deposit growing procedure, SprayWatch© on-line diagnostics system is employed. The part of substrate front face to be deposited is included in the clear area of the SprayWatch© view.

To set a reference for the dimensions of the images captured by SprayWatch©, a series of tests are carried out to find the relationship between the focus distance

(fd) and the width of field of view (FOV X) and height of field of view (FOV Y) of the measurement volume. The focus distance is adjusted between 215 mm and 390 mm. A metal ruler is mounted on the substrate holder as the reference marker for focus adjustment and dimension calibration. **Fig. 3.28** shows the image captured by SprayWatch® with the reference ruler when the focus distance is 215 mm. From the images, FOV X and FOV Y are calculated.

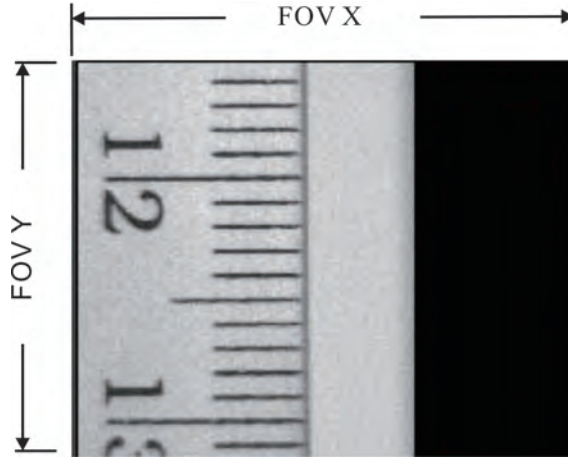


Fig. 3.28 An example of image at the focus distance 215 mm by SprayWatch® for dimensions calibration. A metal ruler is included for reference purpose.

The relationships between focus distance and FOV X, FOV Y are concluded in **Fig. 3.29**. As expected, linear relationships are found. The fitted formula are

$$\begin{cases} FOV X = 0.039913 + 0.09735 \times fd \\ FOV Y = 0.87418 + 0.07162 \times fd \end{cases} \quad (3.4)$$

where fd is the focus distance.

3.5.4 3D profile measurement of sprayed deposit

To provide a more detailed realization of the deposit shape, TalyScan 150 (Taylor Hobson Ltd, Leicester, England) is employed to construct the 3D profile, as shown in **Fig. 3.30**. It is a scanning system designed for 3D measurement, which has contact and non-contact scanning capabilities. A temporary platform is used to bear the specimen because the built-in platform is very small.

The non-contact method uses laser to detect the specimen topology. The starting point is set to the machine origin (0,0,0). The scanning laser is then moved in a zigzag pattern to measure the coordinates of the deposit surface points with constant

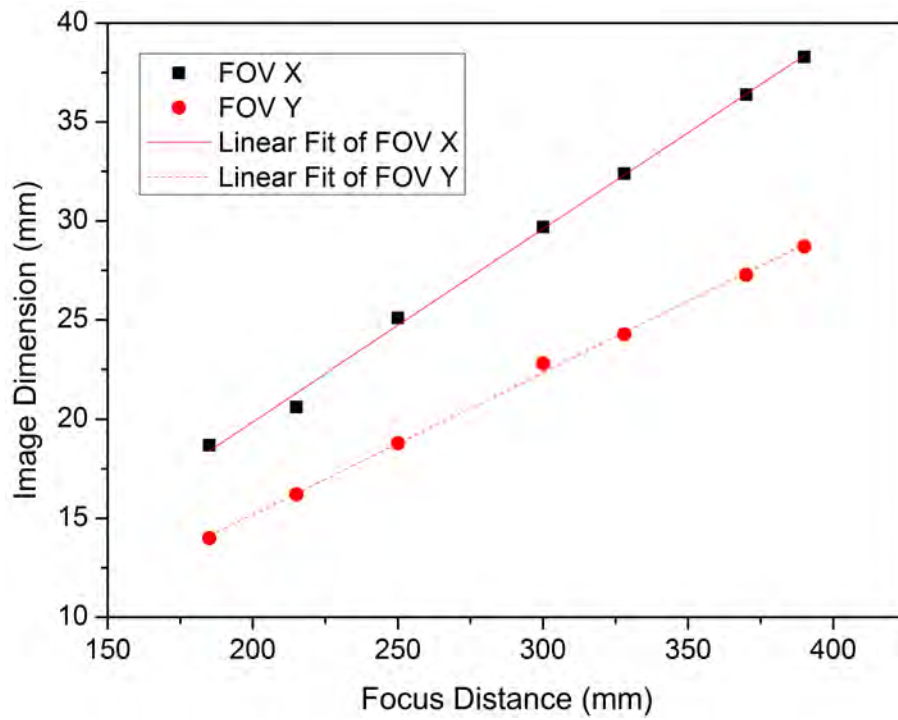
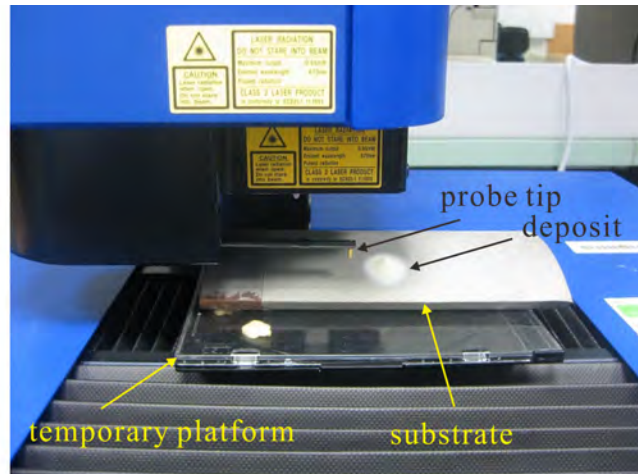


Fig. 3.29 The measurement volume length and height correlate with the focus distance.



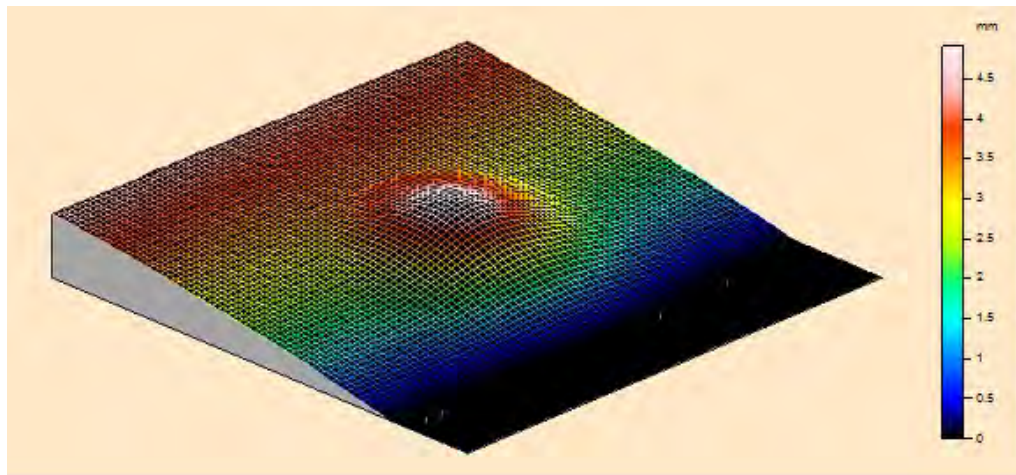
(a) Talyscan equipment



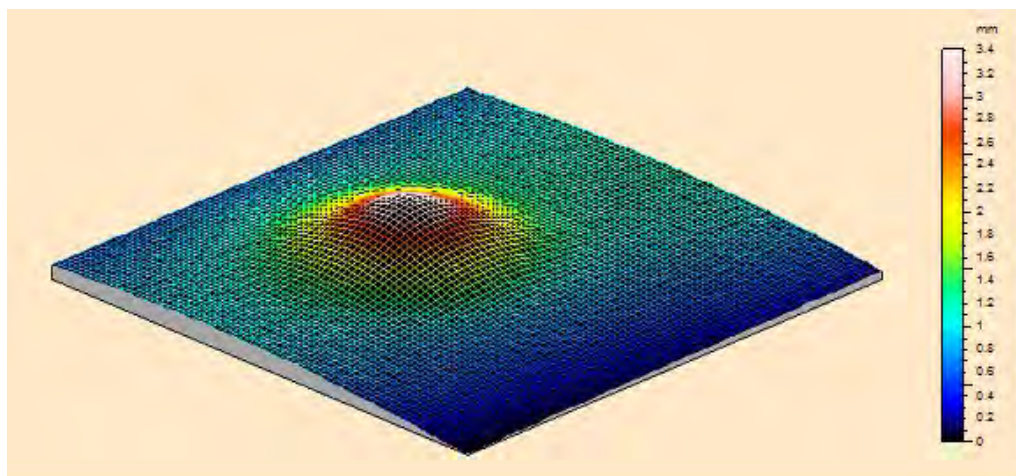
(b) Talyscan working area

Fig. 3.30 TalyScan 150 3D scanning system.

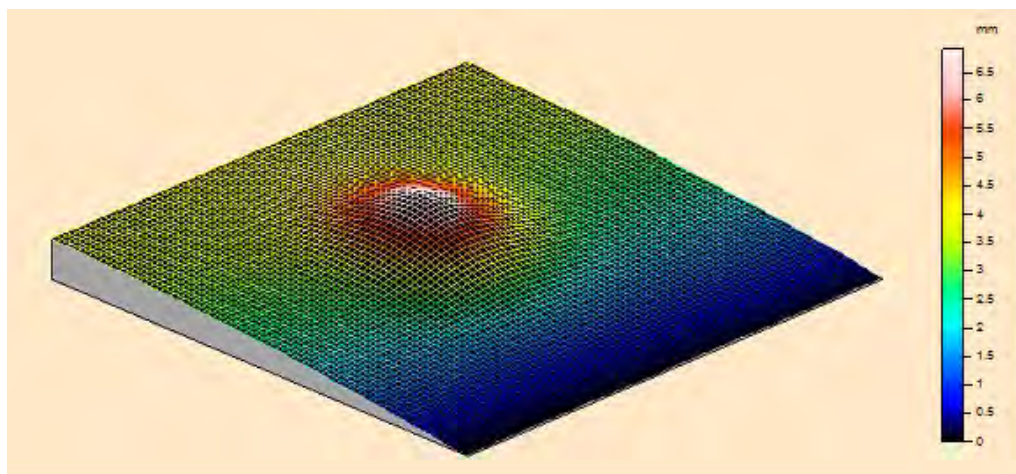
step size of $25\ \mu\text{m}$. The total scanning distances are 20 mm along x and y directions respectively. Thus the profile of the deposits are obtained. **Fig. 3.31** shows the deposit profiles from TalyScan measurements for case 1–3.



(a) case 1



(b) case 2



(c) case 3

Fig. 3.31 Deposit profiles from TalyScan measurements.

Chapter 4

Simulation Methodologies

4.1 Introduction

This chapter provides a specification of the simulation methodologies for the three different aspects of the plasma spray procedure: plasma flow field and in-flight particle behavior, droplet impact behavior and deposit growth.

Particle size, velocity, temperature, spatial distribution and melting state are the basic input parameters for the modeling of coating formation. A three dimensional Computational Fluid Dynamics (CFD) model based on FLUENT® is developed to determine the in-flight particles behavior in the plasma flame.

The droplet impact is the elementary process for the deposit formation in thermal spray process. A numerical model based on the computational fluid dynamics (CFD) Flow-3D® is made, including the physics of heat transfer and solidification. In-flight particle parameters from the online diagnostic system SprayWatch® are used as the initial conditions of the droplet for the modeling. The purpose is to find correlations between the impact parameters and the final splat morphology on both flat and curved surfaces. The underlying mechanisms determine the droplet impact phenomena are also the scope of the research.

Based on the splat morphologies correlation with the impact parameters, a semi-empirical methodology has been developed to predict the deposit growth with time in the thermal spray process. Time segmentation and coordinate transformation constitute the frame of the code.

4.2 Modeling and Simulation Methodology on Plasma Field and In-flight Particles

The CFD model includes the plasma heat generation and plasma and particle interaction. The three dimensional CFD domain of the model encompasses the torch and a cylindrical atmosphere region in front of the torch. Constant volumetric heat source model is used to model the plasma heat generation. The heat transfer from plasma to particles is modeled by the one-way coupling method.

The turbulent and cooling effects by the entrainment of ambient air into the plasma jet was found to affect the particle trajectories and the corresponding temperature and velocities. It is expected that these effects become more severe when the jet impinges on the substrate, leading to flow stagnation and reversals around the obstacles in the plasma plume. In order to investigate the effects of substrate inclusion on plasma flow and particles behavior, five cases are carried out by numerical simulations.

4.2.1 Geometry Design

As shown in **Fig. 4.1**, a part of the plasma torch (black line) is extracted to represent the entire torch gun, named upstream computational domain; adjacent to it, a downstream computational domain is created (dashed line), in a cylindrical shape with the dimensions of $\phi 160$ mm (diameter) \times 250 mm (length). The entire computational domain is presented in **Fig. 4.2**.

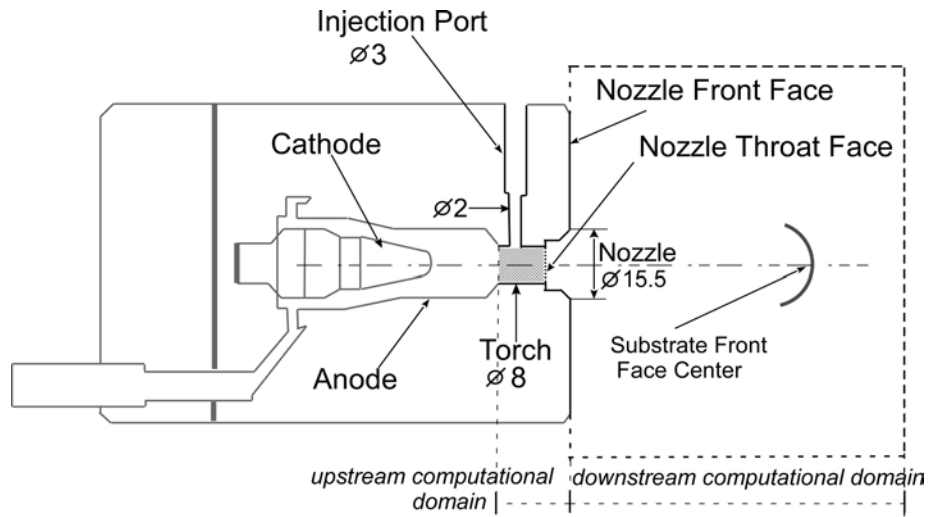


Fig. 4.1 Model of computational domain of plasma spray.

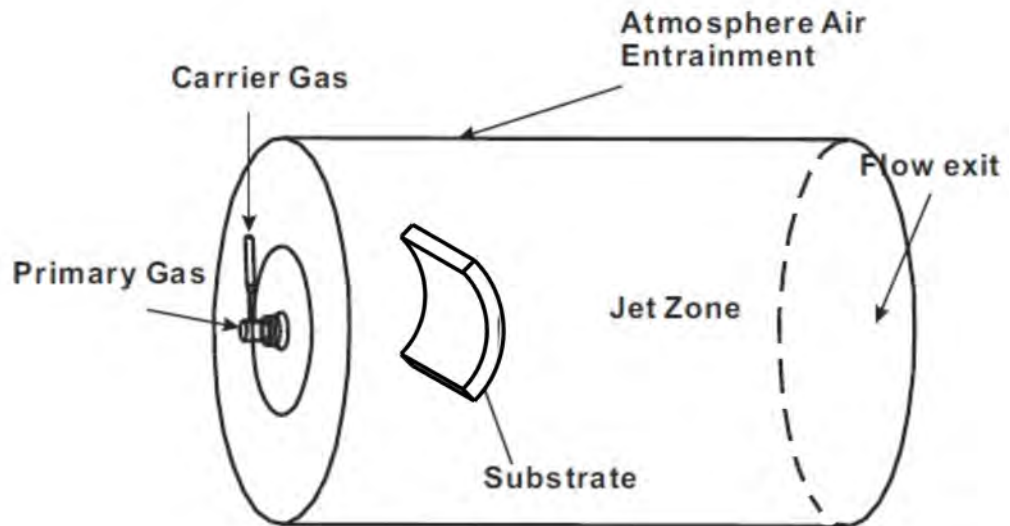


Fig. 4.2 3D view of computational domain of plasma spray.

The geometrical shape of the curved substrates is illustrated in **Fig. 4.3**, with dimensions of width W , length L , inner radius $R1$ and outer radius $R2$. The axes of curvature are positioned orthogonally with respect to the carrier gas injection direction (shown as dashed line), as shown in **Fig. 4.4** – the model with concave surface of the substrate facing to the torch exit is labeled as “C”; when the convex surface facing to the torch exit, it is labeled as “V”.

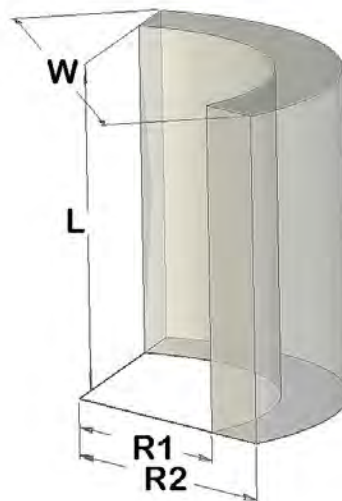


Fig. 4.3 Schematic illustration of substrate shape.

Together with the case without substrate inclusion (referred to as Freestream case), five cases are conducted to assess the effect of shape and orientation on plasma field

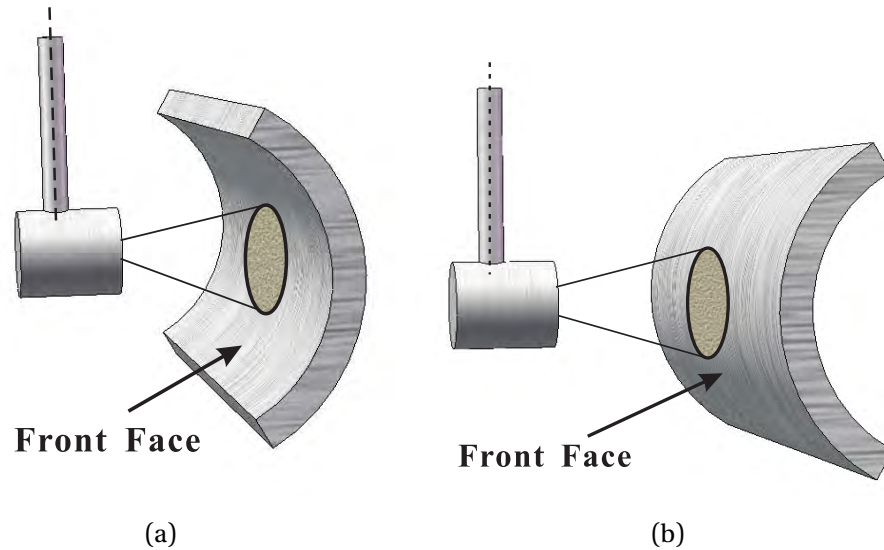


Fig. 4.4 Schematic Illustrations of substrate orientation: (a) concave case
(b) convex case.

temperature and velocity: Freestream (Fr), two concave and two convex cases as in **Table 4.1**. These substrates have the same length (L) 50 mm, other specifications in these cases are also listed in the table. In addition, these substrates are placed at a distance of 80 mm between the nozzle front face and the center of substrate front face.

Table 4.1 Dimensional specifications and orientation of substrates in five model cases.

Case	W(mm)	R1(mm)	R2(mm)	Curvature (mm^{-1})
Fr	–	–	–	0
S1-C	25	11	13	0.0909
S1-V	25	11	13	0.0769
S2-C	55	51	57	0.0196
S2-V	55	51	57	0.0175

4.2.2 Computing Strategy for Plasma Field

Integration of structured and unstructured schemes is utilized to generate elements throughout the whole geometry by using Gambit V2.3.16©; the model is further solved by FLUENT V6.3.26©. The adopted total grid size here is around 70,000 cells for the Freestream case. The number increases with the inclusion of the substrate.

Moreover, several assumptions are adopted to established this model:

- The torch is equipped with a straight gas injector; therefore, primary gas is injected normally from gas injector into the torch, and no swirl is present in the plasma heat generation.
- The plasma is considered as optically thin, i.e., transparent to radiative heat transfer.
- As the lateral boundary of the external domain is a distance far away from the nozzle exit, an atmospheric boundary is imposed there.
- Because of the high velocity of the plasma flow, the inertia force is the dominant force compared with the buoyancy force or the gravity effect. Therefore, no other sources than the inertia is included.
- The plasma fluid flow is assumed as incompressible and in a steady-state.
- The argon gas is chemically inert with temperature-dependent thermodynamic and transport properties in local thermodynamics equilibrium (LTE) assumption. Properties of argon and air are adopted from literature[122] and fitted into a piecewise linear profile in FLUENT®.
- Because of the small sizes and high velocity of the in-flight particles, gravitational force is negligible compared with the viscous drag force.
- Because of the high temperature of the plasma field (about 12,000 K) and small size of the feedstock particles, the particles are assumed to be liquid droplets once they enter the plasma field. This liquid form is a pseudo-liquid, which means the particles are in a “quasi-liquid” phase, even when the temperature is much lower than the melting point of the material.

4.2.3 Plasma Flow Modeling

4.2.3.1 Governing equations

The general governing equation for plasma flow can be written as a differential form as in **Equation 4.1**.

$$\nabla \cdot (\rho \vec{V} \phi) = \nabla \cdot (\Gamma_{\phi} \nabla \phi) + S_{\phi} \quad (4.1)$$

where ϕ is the process variable and \vec{V} the velocity factor. Process variables ϕ , diffusion coefficients Γ_ϕ , and the source terms represent different combinations of variables in different conservation equations, which are clearly shown in **Table 4.2**.

Table 4.2 The process variables, diffusion coefficients and source terms for Equation 4.1.

Equation	Mass	Momentum	Energy	Species	Turbulence
Variable (ϕ)	1	u, v, w	h	Y_n	κ, ε
Diffusion coefficient (Γ_ϕ)	0	$\mu_l + \mu_t$	$k_l + k_t$	$D_l + D_t$	$\mu_l + \frac{\mu_t}{P_{r_{t,\kappa}}}, \mu_l + \frac{\mu_t}{P_{r_{t,\varepsilon}}}$
Source term (S_ϕ)	0	$-\nabla p$	P'''_{in}	0	$G_\kappa - \rho\varepsilon, C_{1\varepsilon}\frac{\varepsilon}{\kappa}G_\kappa - C_{1\varepsilon}\rho\frac{\varepsilon^2}{\kappa}$

4.2.3.2 Plasma heat generation

Argon gas is used as primary and carrier gases. A volumetric heat source defined by source term P'''_{in} is included in the governing energy equation to approximately represent the arc heating:

$$P'''_{in} = \frac{\eta EI_A}{V_a} \quad (4.2)$$

where P'''_{in} is the volume – averaged heat source, E the arc voltage, I_A the arc current and V_a the volume of the anode. Torch efficiency, η , is set as 67% [123], which takes heat energy loss to the circulating cooling water into account.

4.2.3.3 Wall functions

The flow behavior and turbulence structure of turbulent flow may be significantly affected by the inclusion of the solid substrate, especially the position and shape of substrate. Velocity decreases sharply in the near-wall region. Large velocity gradients result in high turbulence area around the substrate. In order to make the simulation closer to reality, a series of semi-empirical formulas are utilized to associate the viscosity-affected region with the wall and the fully turbulent region.

Based on Launder and Spalding's proposal[124], U_E , τ_w , T_E , T_w , \dot{q} and y are respectively defined as the time-average plasma velocity at adjacent element E along the wall[124], the shear stress along the velocity direction, the time-average

temperatures at points E and W , the heat flux to the wall, and the distance from the wall. E represents an element point adjacent to the wall. The following equation, which is called the “law-of-the-wall” for mean velocity, is used as the wall function [30].

$$U^* = \begin{cases} \frac{1}{K} \ln(a * y^*), & y^* > 11.225 \\ y^*, & y^* < 11.225 \end{cases} \quad (4.3)$$

where U^* , dimensionless velocity, and y^* , distance from the element to the wall are defined as below:

$$U^* = \frac{U_E C_\mu^{1/4} \kappa_E^{1/2}}{\tau_w / \rho} \quad (4.4)$$

$$y^* = \frac{\rho C_\mu^{1/4} \kappa_E^{1/2} y_E}{\mu} \quad (4.5)$$

C_μ has a empirical constant value 0.09, κ_E is the turbulence kinetic energy at point E , while y_E is the distance from point E to the wall.

The logarithmic law for mean temperature is similar to that for mean velocity, according to Reynolds’ analogy between momentum and energy transport. The law-of-the-wall for temperature employed in FLUENT© comprises the following two different laws:

$$T^* \equiv \frac{(T_W - T_E) \rho C_\infty C_\mu^{1/4} \kappa_E^{1/2}}{\dot{q}} = \begin{cases} Pr y^*, & y^* < y_T^* \\ Pr_t \left[\frac{1}{K} \ln(a y^*) + P \right], & y^* > y_T^* \end{cases} \quad (4.6)$$

where C_∞ is the plasma specific heat capacity, \dot{q} the flux heat to the substrate, y_T^* the non-dimensional thermal sublayer thickness. The value of P is given by **Equation 4.7**[125].

$$P = 9.24 \left[\left(\frac{Pr}{Pr_t} \right)^{3/4} - 1 \right] (1 + 0.28 e^{-0.007 Pr / Pr_t}) \quad (4.7)$$

where Pr is the Prandtl number $Pr = \mu / \alpha$. When $y^* < y_T^*$, the equation is the linear law for the thermal conduction sublayer where conduction is important; while when $y^* > y_T^*$, it becomes the logarithmic law for the turbulent region where effects of turbulence dominate conduction[30].

4.2.4 Operating Parameters and Boundary Conditions

The operating parameters are listed in **Table 4.3**. Inlets of the torch and injector are both modeled as a mass flow inlet in order to achieve a better convergence rate comparing to that of a pressure inlet. The mass flow rates of primary gas and carrier gas are respectively assigned to torch and injector port. All the torch gun walls are set at a constant temperature of 300 K, which is the ambient temperature. Boundaries of downstream computational domain are set as pressure outlet, where atmospheric condition is imposed. Turbulence model at inlets of the torch and injectors are characterized by turbulent intensity and hydraulic diameter. The turbulent intensities at arc gas and carries gas inlets can be calculated by Equation **Equation 4.8**.

$$I_t = 0.16Re^{-1/8} \quad (4.8)$$

Table 4.3 Operating parameters for plasma simulation

Operating parameter (Unit)	Magnitude
Torch diameter (mm)	8
Nozzle diameter (mm)	15.5
Injection port diameter (mm)	3
Substrate standoff distance (mm)	80
Powder size (μm)	22-125
Current input (A)	900
Voltage (V)	35
Torch efficiency (%)	67
Heat Source (W/m^3)	4.4178×10^{10}
Arc gas (Argon) flow rate (kg/s)	1.9474×10^{-3}
Carrier gas (Argon) flow rate (kg/s)	1.136×10^{-4}
TI at arc gas inlet (%)	4.83
TI at carrier gas inlet (%)	6.09

The thermodynamic and transport properties of gases vary with temperature drastically. Therefore, it is better to involve the temperature-dependent properties in the modeling of atmospheric plasma spraying. There are two types of gas – argon and air – in this CFD model. Their temperature-dependent properties were

adopted from literature[122] and fitted as piecewise linear profiles with respect to temperatures. These profiles are the input data for gas properties in FLUENT®, shown in **Appendix C**.

However, in atmospheric plasma spraying, when the plasma gas gets out of the nozzle, the air will be entrained and mixed with the plasma gas. Therefore, the mixing properties are necessary for modeling. Volume-weighted mixing law was employed for density calculation, while mass-weighted mixing law was adopted for the other properties, which is also described in **Appendix C**. Some other input data are calculated and elaborated in **Appendix D**.

4.2.5 Particle dynamics and heat transfer modeling

On the basis of the obtained converged plasma field, zirconia particles are injected axially through an internal injection port. The flow of particles is modeled by FLUENT® using the discrete phase model in a Lagrangian frame of reference. A fundamental assumption made in this model is that the dispersed second phase occupies a low volume fraction, which means the second phase is sufficiently dilute that particle-particle interactions and the effects of the particle volume fraction on the gas phase are negligible. Motion of a particle is defined as a function of its velocity:

$$\frac{d\vec{X}_p}{dt} = \vec{V}_p \quad (4.9)$$

where the particle velocity \vec{V}_p can be determined from a momentum balance for the particle by

$$m_p \frac{d\vec{V}_p}{dt} = \vec{F}_D \quad (4.10)$$

m_p is the mass of single particle, while \vec{F}_D , is defined as following:

$$\vec{F}_D = \frac{18\mu}{\rho_p D_p^2} \frac{C_D Re}{24} (\vec{V} - \vec{V}_p) \quad (4.11)$$

where Re is the local relative Reynolds number with the following definition:

$$Re = \frac{\rho D_p |\vec{V} - \vec{V}_p|}{\mu} \quad (4.12)$$

while the drag coefficient C_D , typically is given as a function of Reynolds number:

$$C_D = a_1 + \frac{a_2}{Re} + \frac{a_3}{Re^2} \quad (4.13)$$

where a_1 , a_2 and a_3 are constant coefficients over several ranges of Reynolds number[126].

For the comparison purpose, turbulence flow effect on the particle trajectories is ignored for the inaugural cases of the in-flight particle simulation. In such a case, the trajectory is computed based on the mean continuous phase velocity field (**Equation 4.10**). After that, a stochastic tracking method, “Random Walk Model”, is utilized to predict the dispersion of particles due to turbulence. In this approach, the instantaneous value of the fluctuating gas flow velocity is included:

$$\vec{V} = \vec{\bar{V}} + \vec{V}' \quad (4.14)$$

where $\vec{\bar{V}}$ is the mean velocity vector, \vec{V}' the velocity vector fluctuation. The trajectory equations are integrated along the particle path by using the instantaneous flow velocity. By computing the trajectory in this manner for a sufficient number of representative particles, the random effects of turbulence on the particle turbulence may be accounted for. In the plasma spray process, the radiative heat losses from the particle are negligible comparing with the conductive heat flux from the plasma to the particle[58]. Therefore,

$$m_p C_p \frac{dT_p}{dt} = h A_p (T_\infty - T_p) + \frac{dm_p}{dt} h_{lt} \quad (4.15)$$

where m_p is the mass of the particle, C_p the specific heat capacity of the particle, T_p the particle temperature, T_∞ the local temperature of the continuous phase, A_p the surface area of the particle, h_{lt} the latent heat. The heat transfer coefficient, h , is defined by using the correlation of Ranz and Marshall[127]:

$$h = \frac{k_\infty}{D_p} (2.0 + 0.6 Re_d^{1/2} Pr^{1/3}) \quad (4.16)$$

where k_∞ is the thermal conductivity of the plasma phase, Re_d means the Reynolds number based on the particle diameter and the relative velocity, Pr the Prandtl number of the continuous phase. The first term on the right hand of **Equation 4.15** is

the convective heat transfer; while the second one is the latent heat transfer through evaporation and condensation. When the particle temperature is below the particle melting point, i.e., $T_p < T_m$, the second term can be omitted, which means the process is considered as an inert heating or cooling process.

4.3 Modeling and Simulation Methodology on Droplet Impact Behavior

In this section the impact behavior of YSZ droplet on the flat surface and curved surface is simulated using Flow-3D®. The same methodology is used except that they have different coordinate system: for flat substrate, the model is based on Cartesian coordinate system, while for curved substrate, the model is based on cylindrical coordinate conforming to the curved surface.

Several terms are defined to make the discussion of droplet impact behavior more clearly and easily, which is shown as below:

- **Flattening** When the droplet impacts onto the substrate, the fluid flows outward parallel to the substrate surface; while the height of the fluid decrease continuously.
- **Splashing** The phenomena in which the fluid disintegrates from the splat, or jets out from the splat.
- **Splattting** A general term refers to the phenomenon including droplet flattening, solidification and splashing.

4.3.1 Computing Strategy

The Flow3D® solves the Navier-Stokes equation by the finite difference method. Volume of Fluid (VOF) and Fractional and Volume Obstacle Representation (FAVOR™) method are the basis of this code.

4.3.1.1 Volume of Fluid (VOF) and Fractional and Volume Obstacle Representation (FAVOR™) method

VOF and FAVOR™ essentially are both using volume-fraction methods. The VOF function, defined as $F(x,y,z)$, is introduced to identify the presence of fluid in space. The value is 1 when the point (x,y,z) is located in the fluid, but 0 when the point is outside the fluid. The computational domain to be modeled is divided into a set of control volumes, or cells. In the computational cells, F is a step function, the F value

is unity at any cell filled with fluid but zero at an empty cell. The cell partially filled with fluid presents a F value between 0 and 1 and is referred as an “interface cell”. Therefore, F records the volume fraction of the control volume filled with fluid.

Similarly, the obstacle geometry surfaces are defined by another fractional volume quantity V_F . It is defined as the open volume fraction of a control volume that is not blocked by a solid. By this way the geometry interface is residing in a control volume with $0 < V_F < 1$. This technique is used to model complex geometry in the computational domain and is named as Fractional and Volume Obstacle Representation (FAVOR™) method.

Combining of VOF and FAVOR, the actual volume of fluid in each control volume is $FV_F\Gamma$, if Γ is the volume of a control volume. The VOF function satisfies the equation

$$\frac{\partial F}{\partial t} + \frac{1}{V_F} \left[\frac{\partial}{\partial x}(FA_x u) + \frac{\partial}{\partial y}(FA_y v) + \frac{\partial}{\partial z}(FA_z w) \right] = 0 \quad (4.17)$$

where (u,v,w) is the fluid velocity vectors in the three directions (x,y,z) in the Cartesian coordinate. A_x , A_y and A_z are respectively the area open to the flow in x , y and z directions in a control volume.

Knowing the fluid fractional values F and the fluid moving direction, it is possible to construct the general location and orientation of a free surface within a control volume. As the liquid moves, the VOF function is updated at different time steps by the governing transport equations.

4.3.1.2 The transport equations

The governing equations that describe the transport of the fluid are represented by the mass continuity equation, the momentum equation and the energy equation. The mass continuity equation is given as:

$$V_F \frac{\partial \rho}{\partial t} + \mathbf{A} \nabla \cdot \rho \vec{V} = 0 \quad (4.18)$$

where ρ is the fluid density and \vec{V} is the velocity vector (u,v,w) in the Cartesian coordinates. \mathbf{A} is the triangle matrix of A_x , A_y and A_z :

$$\mathbf{A} = \text{diag}[A_x, A_y, A_z] \quad (4.19)$$

The equations of momentum are the Navier-Stokes equations with some additional terms:

$$V_F \frac{\partial}{\partial t} \rho \vec{V} + \mathbf{A} \nabla \cdot \rho \vec{V} \vec{V} = -\nabla p - \mathbf{A} \nabla \cdot \tau \quad (4.20)$$

where p is the pressure, τ the stress tensor.

Fluid energy equation is expressed as below:

$$V_F \frac{\partial}{\partial t} (\rho I) + \mathbf{A} \nabla \cdot \rho I \vec{V} = \mathbf{A} p \nabla \cdot \vec{V} + T_{dif} \quad (4.21)$$

where I is the macroscopic mixture internal energy, which is assumed as a linear function of temperature

$$I = C_l \cdot T + (1 - F_s) \cdot h_f \quad (4.22)$$

C_l is the specific heat of fluid, F_s the solid fraction, h_f the latent heat of fusion. T_{dif} is the heat conduction diffusion term, which is given by

$$T_{dif} = \mathbf{A} \nabla \cdot (k \nabla T) \quad (4.23)$$

where k is the thermal conductivity of the fluid and T the temperature of the fluid.

The heat transfer between the fluid and the substrate is also included, as in the following equation:

$$\begin{aligned} (1 - V_F) \rho_w C_w \frac{\partial T_w}{\partial t} - \frac{\partial}{\partial x} \left[k_w (1 - A_x) \frac{\partial T_w}{\partial x} \right] - \frac{\partial}{\partial y} \left[k_w (1 - A_y) \frac{\partial T_w}{\partial y} \right] \\ - \frac{\partial}{\partial z} \left[k_w (1 - A_z) \frac{\partial T_w}{\partial z} \right] = T_{sor} \end{aligned} \quad (4.24)$$

where T_w is the substrate temperature, ρ_w , C_w and k_w are the substrate density, specific heat and thermal conductivity respectively. T_{sor} is the liquid-substrate heat transfer. This heat transfer through a specific surface in a control volume is defined as:

$$q = h A_w (T_w - T) \quad (4.25)$$

where h is the heat transfer coefficient between the droplet fluid and the substrate, A_w is the interface area within the cell, T and T_w are the fluid and wall surface temperature respectively.

4.3.2 Model Setup

A few assumptions are made to simplify the problem. The ambient air is considered as void, which applies uniform pressure (101325 Pa) on the fluid (the droplet). The convective and radiative heat transfer between the fluid and the ambient air are neglected. The droplet is assumed to be fully-melted and spherical at the moment of impact.

4.3.2.1 Normal impact

For the normal impact, the droplet is modeled to impact on the substrate perpendicularly. Due to the symmetry of the geometry, only a quarter of the droplet and the corresponding substrate beneath this part are modeled, as illustrated in Fig. 4.5.

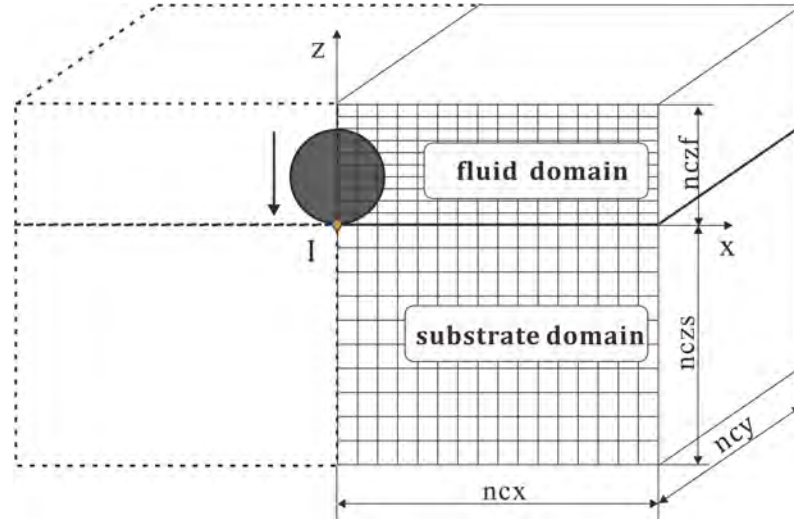


Fig. 4.5 Illustration of computational domain and mesh setup for droplet impacting perpendicularly on the substrate. The computational domain includes a quarter of the droplet and part of the substrate beneath it.

The computational domain size is adjusted according to the droplet size and impact velocity so that the entire splatting phenomenon occurs within this domain. The computational domain is divided into two subdomains: the “fluid domain” above the substrate surface, where the droplet fluid spreads, splashes and solidifies; and the “substrate domain”, where part of the substrate is included. Since the droplet deformation is very drastic, the grids are finer along z direction in the “fluid domain” than in the “substrate domain” in order to capture the droplet deformation

and final splat thickness. The grid size is uniform along x and y directions. For comparison purpose, the grid size along x and y direction are uniform in all the cases of different droplet size and impact velocity, i.e. $dx = dy = 1 \mu\text{m}$. The runtime of the simulations is varied for different cases. For the case of highest velocity, the simulation time is 24 h.

The thermophysical properties of YSZ and of the stainless steel substrate and the interface parameters between the droplet and the substrate are summarized in **Table 4.4**. The thermalphysical properties of YSZ have been reviewed in **Chapter 2**, but for convenience, they are also included in the table. Specific heat values of the liquidus and solidus YSZ are the average value between the temperature ranges in the simulation, because in Flow-3D® only constant value is accepted.

Table 4.4 Thermophysical properties of YSZ, stainless steel substrate and interface parameters between droplet and substrate.

Parameter (Unit)	Magnitude
Melting Point (K)	2988
Liquidus Temperature (K)	3031
Solidus Temperature (K)	2978
Latent heat of fusion (kJ/kg)	706.3
Density (kg/m^3)	5890
Viscosity (Pas)	$0.0037 \exp(6100/T)$
Thermal Conductivity (W/mK)	2.4
Specific heat of solid (J/kgK)	872
Specific heat of liquid (J/kgK)	1364
Surface Tension (N/m)	0.43
Contact angle (Degree)	90
Thermal conductivity of substrate (W/mK)	32.9
Specific heat of substrate (J/kgK)	570
Density of substrate (kg/m^3)	7700
Roughness of substrate (μm)	0.2

The initial conditions of the droplet and substrate at the moment of impact are summarized in **Table 4.5**. The droplet velocities and temperatures are representative values from the experimental diagnostics by SprayWatch®.

Table 4.5 Initial conditions for numerical simulation.

Parameter (Unit)	Magnitude
Velocity (m/s)	120,200,300,400
Temperature (K)	3200,3500,3800
Convective heat transfer coefficient (W/m ² K)	10 ⁵ ,10 ⁶ ,10 ⁷
Substrate temperature (K)	823,1573

As illustrated in **Fig. 4.6**, the velocity selection is based on the particle velocity distribution from SprayWatch© diagnostics. $v_5 = 200$ m/s is a value close to the median value q_2 , $v_4 = 120$ m/s and $v_6 = 300$ m/s are the values between the minimum value min and the first quartile q_1 and between the third quartile q_3 and the maximum value max . The values close to the minimum value min ($v_3=80$ m/s) and the maximum value max ($v_4 = 400$ m/s) are also included to investigate the splatting behavior under extreme conditions. In order to see a full picture of the relationship between the spread factor and the impact velocity, another two velocity values in the small range are introduced ($v_1 = 50$ m/s and $v_3 = 100$ m/s), although the velocity $v_1 = 50$ m/s is not in the range of a typical plasma spray.

The droplet temperature measured by SprayWatch© is not as accurate as the velocity. The values are median values at different time step. Meanwhile the standard deviations at these time steps are also evaluated. Based on these data, the median value, the upper and lower boundary values are plotted versus the time frame number. The selected temperature values are the approximate lowest boundary value, the median and upper boundary value of the plot respectively: 3200 K, 3500 K and 3800 K. The substrate temperature is set as 823 K, which is approximated from the thermocouple measurement of the substrate. Moreover, since the value from the thermocouple measurement is the mean value between different points on the substrate, it is believed that some area of the substrate has a higher value. In the current simulation, a value close to the melting temperature of the stainless steel is adopted, which is 1573 K. To investigate the effect of heat contact resistance, different values of heat transfer coefficient between the substrate and the droplet are set: 10^5 , 10^6 and 10^7 W/m²K, following the instructions by Pasandideh-Fard and Mostaghimi[98 and 128] . Different cases are carried

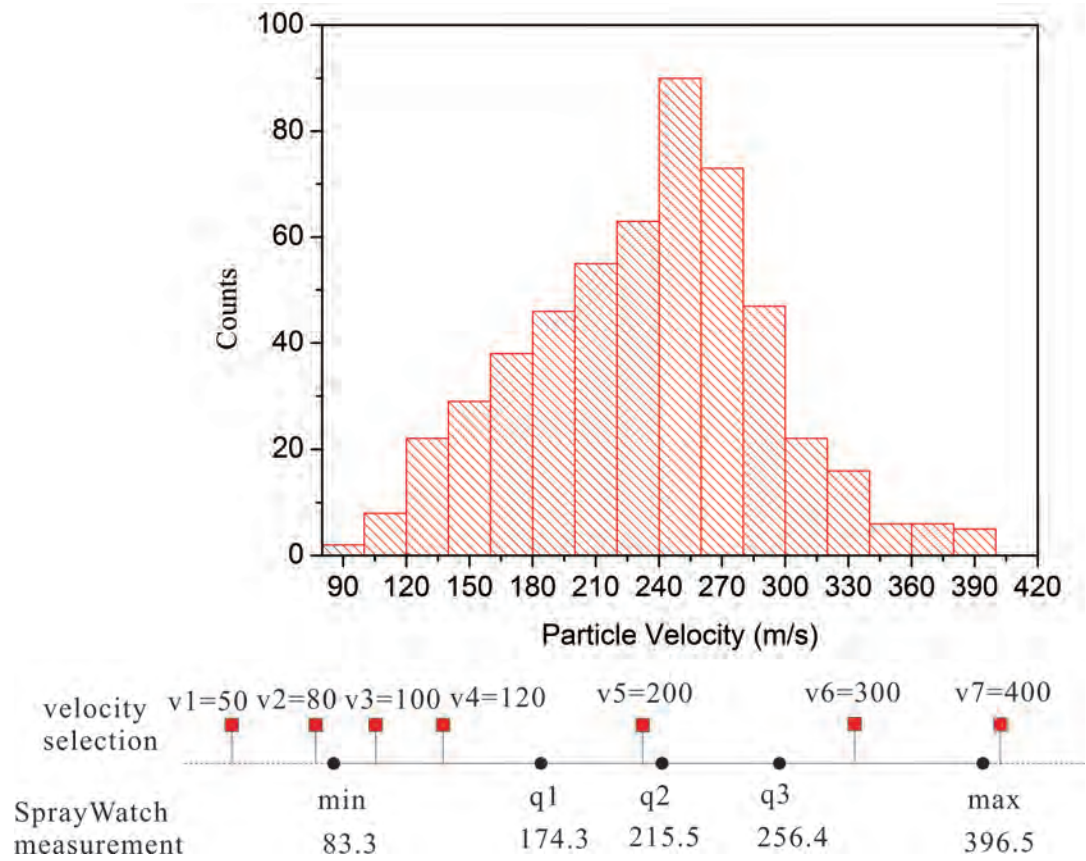


Fig. 4.6 Illustration of velocity selection based on the particle velocity distribution from SprayWatch® diagnostics.

out by combining these parameters, which are listed in **Table 4.6**. Not all the possible combinations of these parameters, but those may give obvious tendency or correlation have been presented. The cases are sorted by droplet velocity (V) firstly, then in the sequence of droplet temperature (T), interface heat transfer coefficient (h) and substrate surface temperature (T_s).

Table 4.6 Simulation cases implemented for the normal impact.

Case	T (K)	V (m/s)	h (W/m ² K)	T _s (K)
1	3200	200	1×10^6	823
2		400	1×10^6	823
3		400	1×10^6	1573
4		50	1×10^6	823
5		80	1×10^6	823
6		100	1×10^6	823
7		120	1×10^6	823
8	3500	200	2×10^5	823
9		200	1×10^6	300
10		200	1×10^6	823
11		200	1×10^6	1573
12		200	1×10^7	823
13		300	1×10^6	823
14		400	1×10^6	823
15	3800	200	1×10^6	823
16		400	1×10^7	823
17		400	1×10^6	823

4.3.2.2 Droplet impact on curved surfaces

In order to simulate the particle splatting on curved substrate, the coordinate system setting should be reconsidered. The splat is expected to conform to the curved surface. Therefore, to demonstrate the splat topology, it is more appropriate to describe the splat thickness normal to the surface and the spreading behavior along the curved surface, as illustrated in Fig. 4.7. The curve represents the substrate surface. R is the radius of the surface. The splat thickness t can be evaluated by the dimension along the radial direction.

A cylinder with the same radius as the substrate in the experiment is modeled as solid obstacle in the computational domain. A cylindrical coordinate conformed to the cylinder is created, as in Fig. 4.8. The z direction is the radial axis in the cylindrical coordinate system, the x' direction actually is the angular direction in the model, which is different with the x axis in the Cartesian coordinate. The droplet impacts onto the substrate surface at a position with angular coordinate θ .

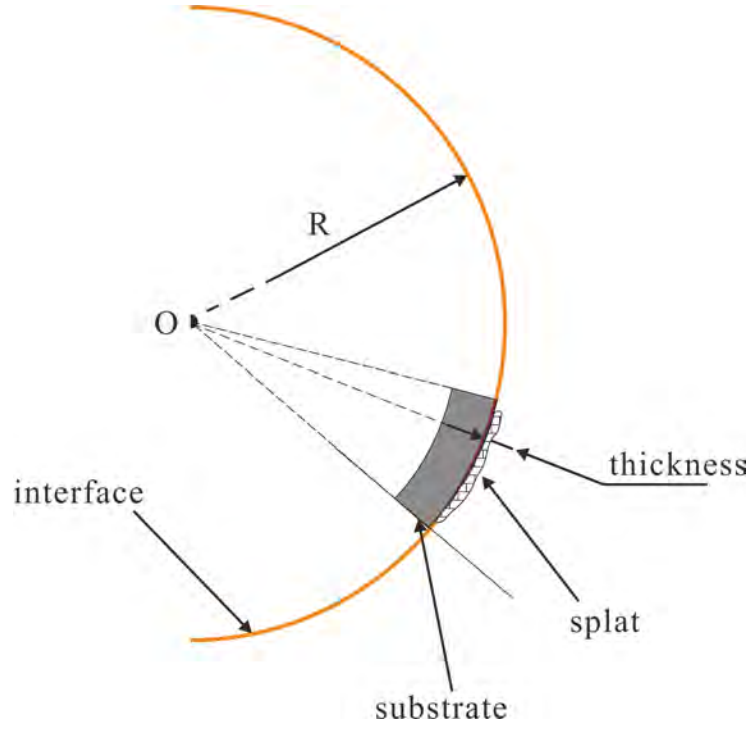


Fig. 4.7 Illustration of splat thickness evaluation on a curve surface.

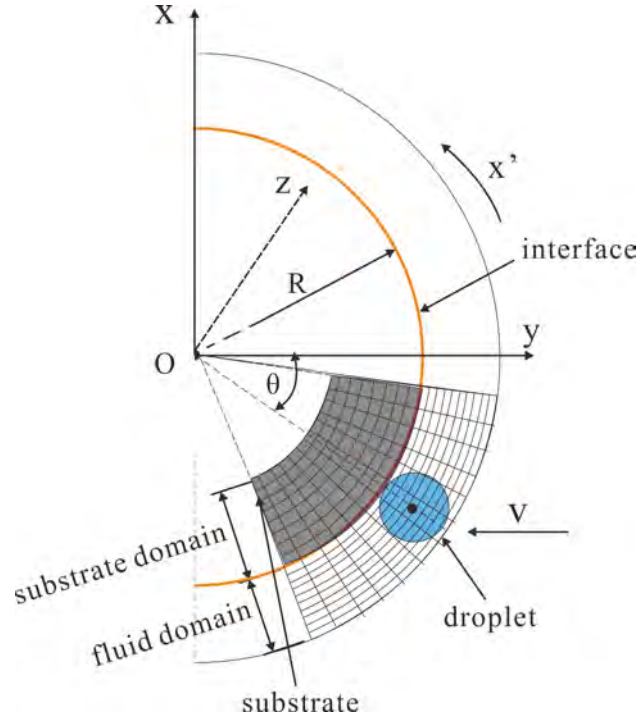


Fig. 4.8 Illustration of computational domain and meshing in the cylindrical coordinate (conformed to the substrate).

This angle actually is the droplet impact angle, which is obvious in geometry considerations. Therefore, in the following context, this term is called “impact angle” consistently. The impact point is set as the origin in the curved plane $x' - y'$. For the cases with impact angle $\theta = 0^\circ$, a quarter of the droplet and the substrate

underneath is modeled. For the other cases, half of the droplet and the substrate under it is modeled, in order to investigate the shape change along the substrate curved surface. In the cartesian coordinate, the fluid domain has a finer mesh than the substrate domain. The dimensions are adjusted according to the case to be modeled, i.e., larger domain is required to simulate the case with a larger impact angle. But the grid size along x' and y directions remain the same through all the cases as $1\ \mu\text{m}$ in order to evaluate the splat geometry consistently.

The droplet temperature is 3500 K, substrate temperature 873 K, interface heat transfer coefficient is $1 \times 10^6\ \text{W/m}^2\text{K}$. Different cases are simulated with combinations of different impact angle (0° , 20° , 40° , 60°) with different velocity (120 m/s, 200m/s, 300m/s). The purpose is to investigate the effect of the impact angle on the splat final morphology.

4.3.3 Slices and lines for splat geometry evaluation

For convenience, some slices and lines in the fluid domain (**Fig. 4.5**) are defined to analyze the splat geometry, as illustrated in **Fig. 4.9**. A slice that cuts through the cells closest to the substrate surface is defined as “bottom surface”, which is at $z = 0.17\ \mu\text{m}$. Another slice that cuts through the cells closest to the center-plane ($y = 0$) is defined as “center surface”, which is at $y = 0.17\ \mu\text{m}$. Similarly, a line parallel to the centerline ($x = y = 0$) is defined as “centerline”, which is at $x = y = 0.17\ \mu\text{m}$.

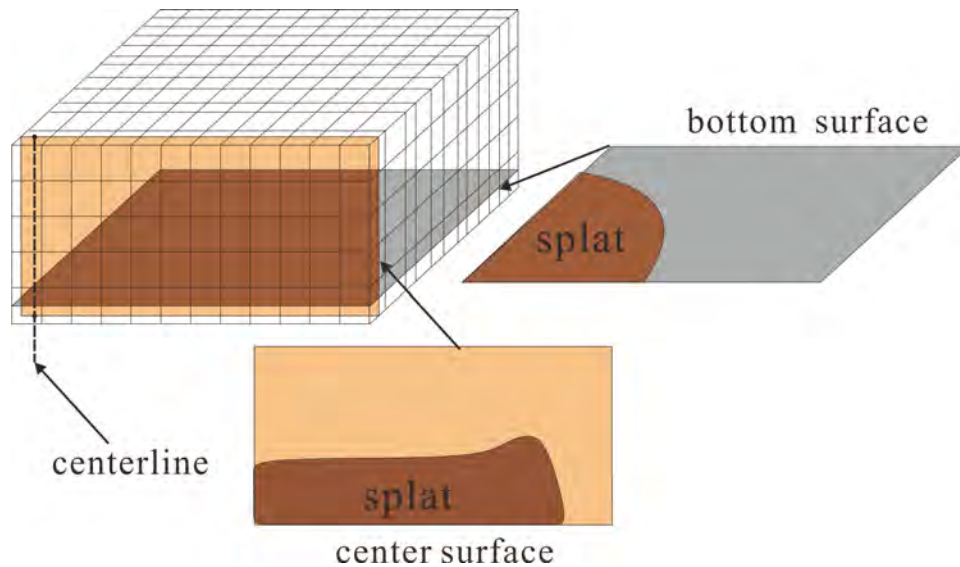


Fig. 4.9 Lines and sections definition to extract simulation variables and splat morphology dimensions.

The definition of these slices and lines are the same for droplet impacting on curved substrate, except that the “bottom surface” conforms to the curved shape of the substrate surface, as shown in **Fig. 4.10**. x represents the azimuthal coordinate, but with a length dimension (μm), while z represents the dimension along the radius, by which the thickness of the splat can be evaluated.

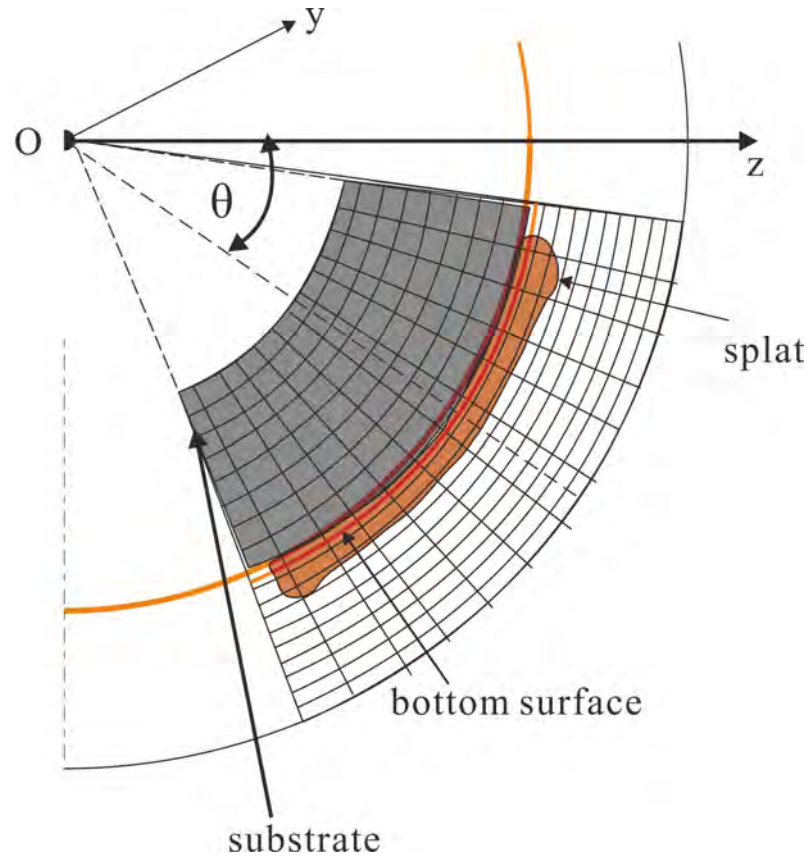


Fig. 4.10 Center surface of the computational domain, showing the bottom surface (side view) conformed to the curved shape of the substrate.

4.4 Numerical Methodology of Deposition Formation

In the deposition code, the approach uses combined simulation and empirical results. The former part consists of Computational Fluid Dynamics (CFD) model in FLUENT® to solve the plasma field as well as the in-flight behavior of the particles. Flow-3D® is used to simulate the droplet impact behavior on the flat and curved surfaces to find the relationship between the splat geometrical factors and the particle in-flight parameters. The empirical part of the approach validates the Flow-3D® results and provides the fitted polynomial equation for the aspect ratio for the splat geometry. For convenience, brief review on the geometrical relations obtained from the experiments and simulation are provided before describing the concept of the deposition code.

4.4.1 Review on the geometrical relations

From the results from experiments and simulation on droplet impact behavior, the morphologies of splats are simplified and related to the impact angle θ and velocity V . Some of these correlations are in the results and discussion part, but as prerequisites of the deposit model, they are summarized in this section.

The droplet with diameter D deforms into a splat with the equivalent diameter d :

$$d = \xi D \quad (4.26)$$

where the spread factor ξ is a power function of the impact velocity V

$$\xi = 1.1532V^{0.24} \quad (4.27)$$

As shown in **Fig. 4.11**, under normal impact, the splat presents a circular disk shape, while under oblique impact, the splat presents an elliptical splat. The major radius a and minor radius b could be derived from

$$\begin{cases} a &= \frac{d}{2}\sqrt{\zeta} \\ b &= \frac{d}{2\sqrt{\zeta}} \end{cases} \quad (4.28)$$

where ζ is the aspect ratio of the splat and has the following relationship with the impact angle θ :

$$\zeta = 0.93146 + 0.01684\theta - 2.70151E - 4\theta^2 + 4.30331E - 6\theta^3 \quad (4.29)$$

The splat center resides in the downstream of the impact point I with an elongation distance l :

$$l = \chi D \quad (4.30)$$

where χ is the elongation factor of the splat, which is given by

$$\chi = 0.04147\theta - 0.096 \quad (4.31)$$

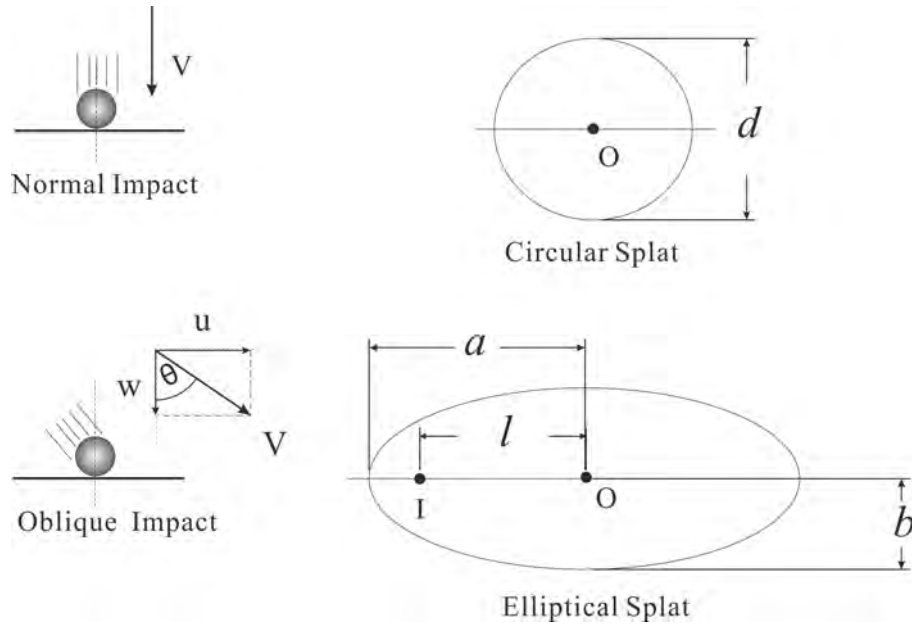


Fig. 4.11 Illustration of simplified splat morphology under normal impact and oblique impact.

4.4.2 Modeling assumptions

Several assumptions are made to simplify the simulation, which are listed belows.

- The deposit profile is smooth, i.e. there is no abrupt protrusion or crater on the deposit surface. Therefore, approximately every single splat spans over an area with the same normal directions.
- During the deposition, porosity or voids tend to form between overlapping splats. It is admitted that the porosity formation will affect the deposit morphology and quality, but currently the inter-splat microstructure has not been investigated in the work. In addition, the pores or voids consideration

will significantly complicate the model if every interface is considered. In this simplified model, porosity formation is not considered. This assumption will lower the prediction of the deposit thickness and make the deposit not smooth as it naturally be. The consideration of porosity will be necessary in the future development.

- Particles are assumed to be fully molten spheres prior to impact.
- The final shape will be a perfect circular disks when impact angle is 0° , but an elliptical disk when the impact angle is between 0° and 90° .

4.4.3 Data acquisition and manipulation

The incoming particles data are acquired from the FLUENT© simulation. As shown in Fig. 4.12, a virtual plane placed to the plasma torch front face is created at the stand-off distance 80 mm to “capture” the particles. In-flight parameters such as velocity, temperature and size of the particles passing through this plane are collected and processed into the input data of particles for deposit simulation.

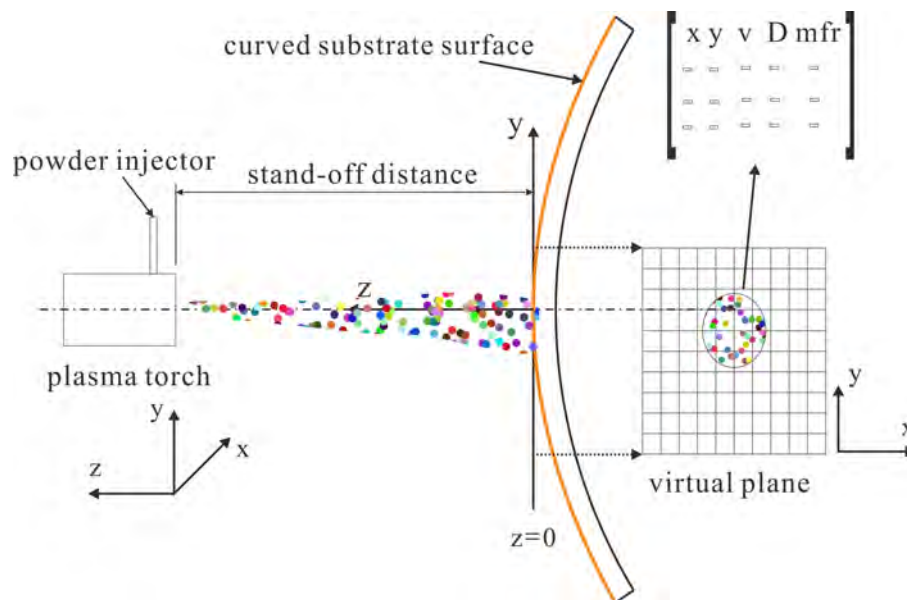


Fig. 4.12 Illustration of acquisition of particles in-flight parameters used for deposit simulation at the virtual plane.

The FLUENT© particles output gives the following information:

$x \quad y \quad z \quad V_x \quad V_y \quad V_z \quad D \quad T \quad mfr$

where (x,y,z) are the location where particle passes through the virtual plane in the three-dimensional space, (V_x,V_y,V_z) are the particle velocity components along the three coordinate axes, D , T and mfr are the particle diameter, temperature and mass flow rate respectively. Because the virtual plane is aligned at the stand-off distance, the column z is eliminated from the input data. In addition, the velocity components V_x and V_y are much smaller than V_z , the column V_x and V_y are also eliminated from the input data. This means that the particles are assumed to impact onto the virtual plane perpendicularly. The particle flux mass flow rate is scaled by the deposition efficiency DE , for the purpose of excluding the mass loss due to particle rebound, material evaporation and etc. Moreover, the particle temperature data are not included in the simulation. Therefore, the input particles data for simulation input are the following particle parameters at the virtual plane that remains from the original data set.

$$x \quad y \quad V_z \quad D \quad mfr \times DE$$

For the convenience of expression, the velocity component V_z is termed as velocity V in the subsequent texts. The mass flow rate $mfr \times DE$ is used for the time segmentation in the model development, which is described in the following subsection.

4.4.4 Time segmentation and deposit update

As observed in the experiment, the deposit profile changes continuously during the plasma spraying. In other words, except in the very early stage, the particles are impacting onto the geometrically varying profile, not on the initial substrate surface. Since the particle flattening shape factors are influenced by the impact angle, it is better to update the deposit profile during the simulation.

The FLUENT® particles output essentially are particle streams at different positions. The mass flow rate for individual particle stream represents the total mass of particles passing through the fixed location per unit time (kg/s). The spraying time is divided into several sequential time segments of uniform length Δt , as illustrated in **Fig. 4.13**. At the preset time, the deposit profile is updated, which becomes the

calculation base for the depositing in the subsequent segment. Within one time segment Δt , all the particles are assumed to impact onto the previous deposit profile.

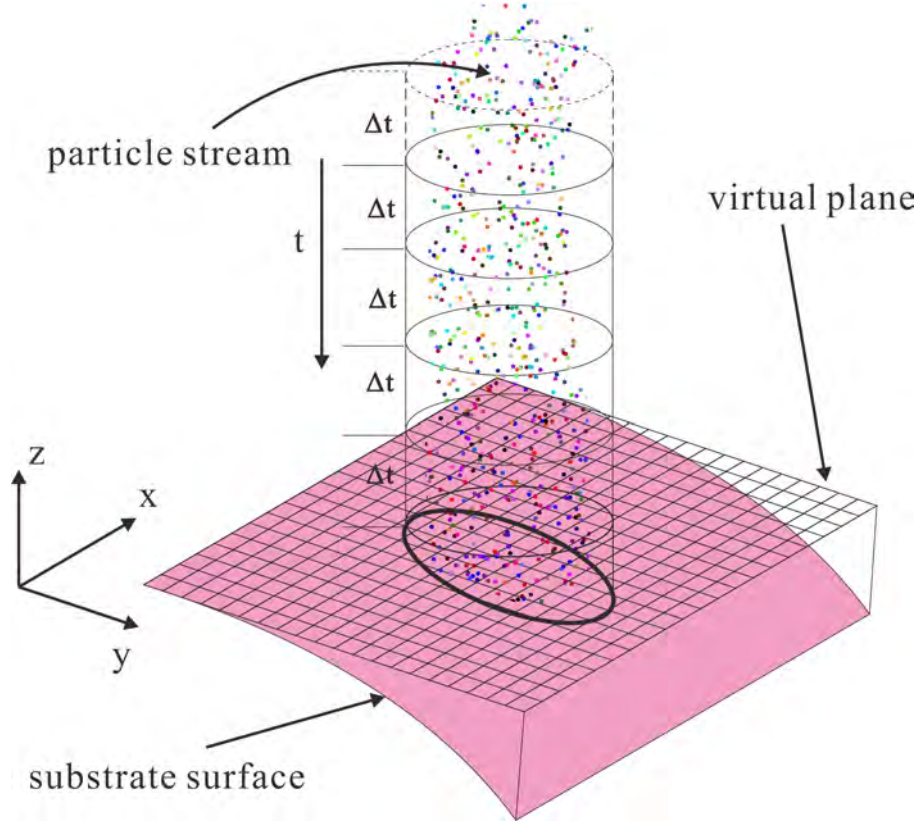


Fig. 4.13 Illustration of time segmentation of author's code for deposit simulation.

The initial substrate surface can be considered as the initial (at $t = 0$) deposit profile. As shown in **Fig. 4.12**, the virtual plane is the plane $z = 0$ in the author's code, the positive z direction is facing the plasma torch, which is the deposit growth direction. The summit (S) of the substrate surface coincides with the virtual plane, but moves along the vertical (y) direction for the 3 cases. **Fig. 4.14** shows the coordinate system and substrate alignment.

The circle center C of the arc-shape profile is $(y_0, -R)$, therefore, the substrate surface profile can be expressed as

$$z = -R + \sqrt{R^2 - (y - y_0)^2} \quad (4.32)$$

where $R = 85$ mm is the radius of the arc, $W = 84$ mm is the width of the substrate surface. y_0 is altered when the substrate is placed in different positions.

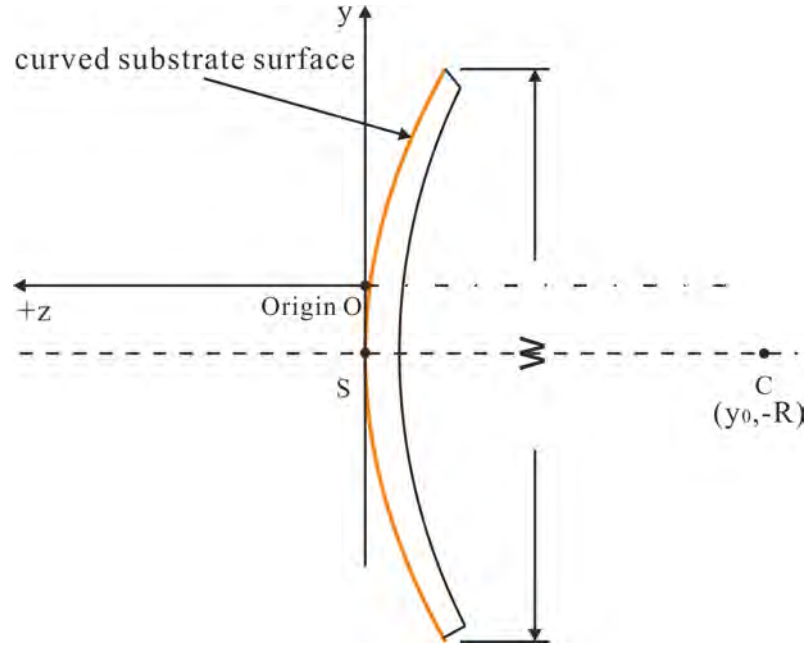


Fig. 4.14 Illustration of the coordinate system in the author's code and the alignment of the substrate.

4.4.5 Determination of computational domain and gridding considerations

From the out-of-plane view of the as-sprayed substrate as shown in **Fig. 4.15**, it is observed that the deposit has a hazy outer boundary, which is not clearly defined area with very low thickness, like a halo. Experimentally this characteristic, or halo phenomena is observed because the YSZ color is different with the substrate. However, in the simulation, it is very difficult to discriminate the thickness difference, especially when the substrate is curved-shape substrate. Therefore, the computation domain is selected according to the inner circle (diameter 13.2 mm) of the deposit. Referring to the contour of number of particles in the virtual plane, the computational domain is $-8 \text{ mm} \leq x \leq 8 \text{ mm}$ and $-18 \text{ mm} \leq y \leq -1 \text{ mm}$, slightly larger than the inner circle size evaluated from the deposit image.

As shown in **Fig. 4.16(a)**, the computational domain is divided into grids with uniform size $\Delta x = \Delta y = 5 \mu\text{m}$. This figure is just an illustration of the gridding strategy, but not using the real mesh size. The resulting nodes of the grids have their peculiar z values. The deposit profile is constructed from these nodes. Therefore, every cell in the two-dimensional plane represents a facet of the profile, which has

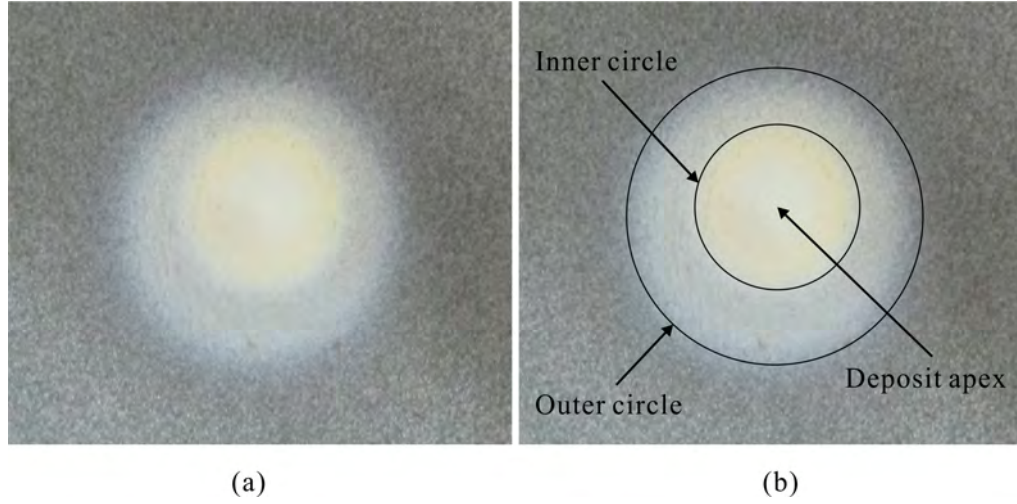


Fig. 4.15 Out-of-plane view of the deposit (a) without annotation (b) with annotation, showing the halo phenomena. The deposit is taken from case 2, the one formed in the middle part of the substrate.

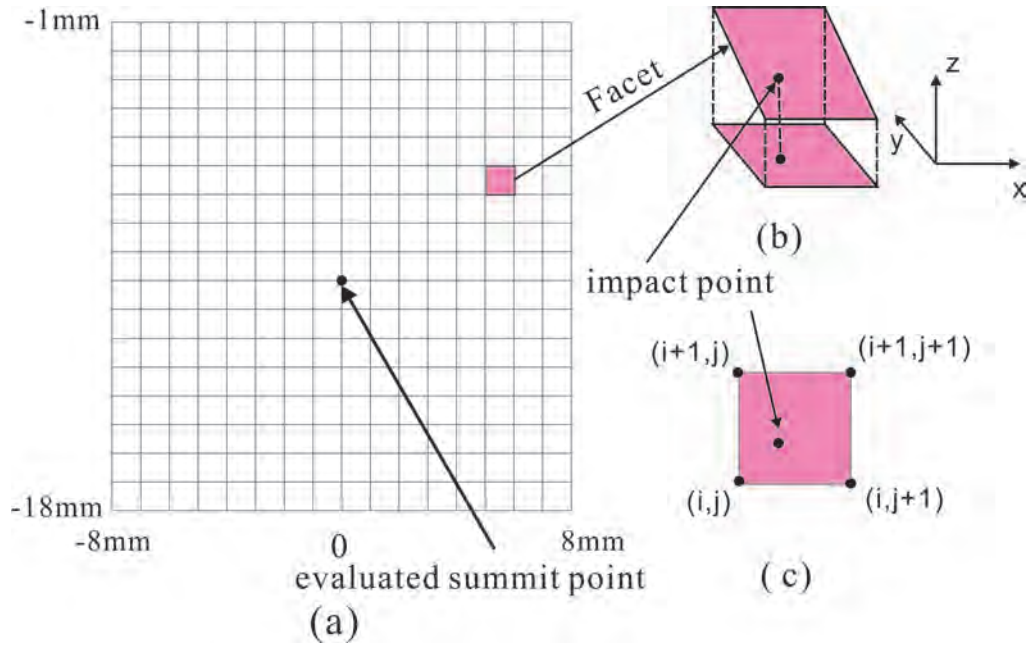


Fig. 4.16 The two-dimensional computational domain for deposit profile and its gridding.

its own normal direction. The projection of the facet to the $x - y$ two-dimensional plane is clearly shown in **Fig. 4.16(b) and (c)**.

4.4.6 Modeling of single splat geometry on the deposit profile

The particles deform to splats with different geometry in the space due to different impact velocity V , impact angle θ and some other parameters. The impact angle for

an individual particle is determined by the particle impact direction and the profile surface direction. The particle essentially impacts onto a facet of the deposit profile. Because the incoming particles are assumed to impact on the virtual plane perpendicularly, the x and y coordinates of the impact point on the deposit profile are the same as on the virtual plane. These coordinates (x,y) are converted to the grid coordinates (normalized by the grid size) by

$$x_g = \frac{x}{\Delta x}, y_g = \frac{y}{\Delta y} \quad (4.33)$$

where x_g and y_g are the grid coordinates of the impact point, Δx and Δy are the grid size along x and y directions respectively. The closest node ($P1$) to the impact point (I) is found by rounding these values, as shown in **Fig. 4.17(a)**.

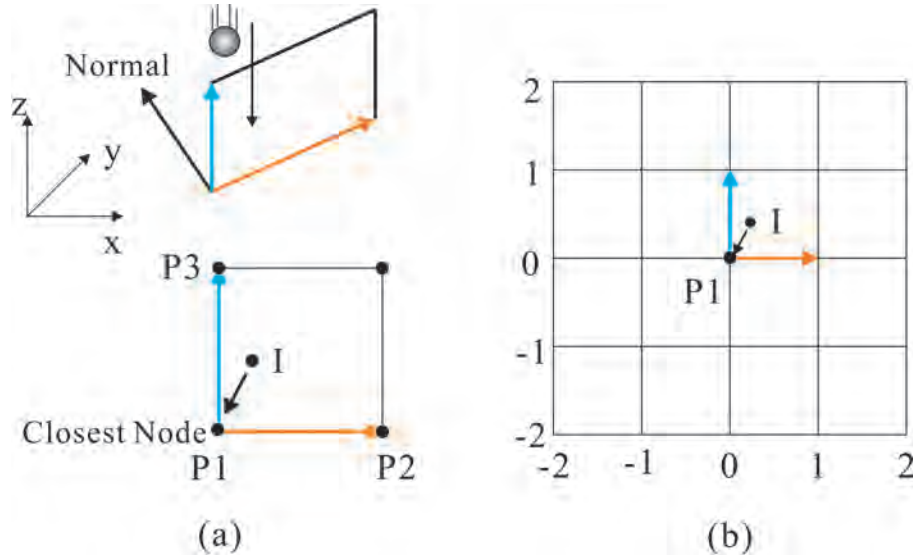


Fig. 4.17 Determination of (a) the impact surface facet vertex and (b) the computation of the surface normal at the impact point.

The normal of one facet is evaluated by the two vectors starting from the lower left corner of the facet. As in **Fig. 4.17(a)**, three points $P1$, $P2$ and $P3$ are in counter-clockwise order. The facet normal is

$$\vec{n} = \overrightarrow{P1P2} \times \overrightarrow{P1P3} \quad (4.34)$$

The surface normal \vec{n} at the impact point I is computed as the average value of the normals of the 16 facets around the node point $P1$. Shown in **Fig. 4.17(a)**, these facets are selected from the point $P1$, by selecting 2 grids to the four directions ($\pm x$ and $\pm y$).

As shown in **Fig. 4.18**, the surface normal \vec{n} can be expressed as $[u, v, w]$. Since the particles impact onto the virtual plane perpendicularly, which means they are parallel to the component w . Therefore the impact angle of an individual particle can be computed from the surface normal at the impact point I

$$\theta = \arctan\left(\frac{\sqrt{u^2 + v^2}}{w}\right) \quad (4.35)$$

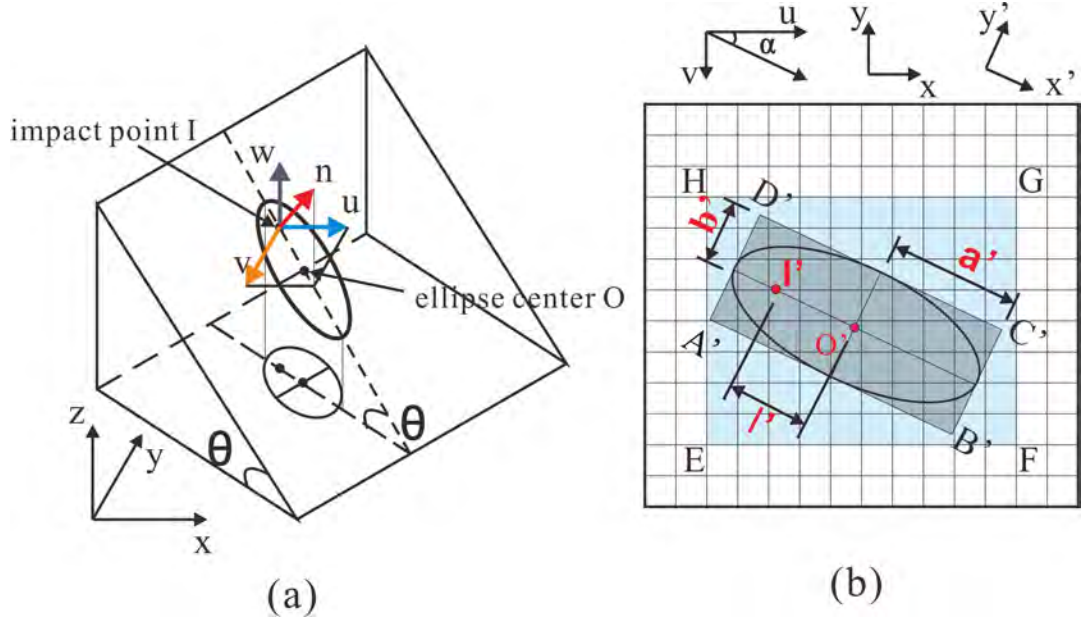


Fig. 4.18 Projection of a single elliptical splat on the deposit surface onto the $x - y$ two-dimensional plane and the transformation between the global coordinate system and the splat coordinate system.

The impact angle θ itself can not define the splat alignment in space. Another angle parameter, elongation angle α , is defined to describe the splat elongation direction in the $x - y$ two dimensional plane:

$$\alpha = \arctan\left(\frac{v}{w}\right) \quad (4.36)$$

The splat elongates into an ellipse on the deposit profile, then this ellipse is projected onto the $x - y$ two-dimensional plane. Therefore the major (a) and minor (b) radius can be calculated with respect to the aspect ratio ζ .

$$a = \frac{d\sqrt{\zeta}}{2} \quad (4.37)$$

$$b = \frac{d}{2\sqrt{\zeta}} \quad (4.38)$$

The focus distance c is expressed as

$$c = \sqrt{a^2 - b^2} \quad (4.39)$$

The projected major radius $a' = a \cos \theta$, while the projected minor radius $b' = b$ because the minor axis is parallel to the $x - y$ two-dimensional plane. The position of the projected ellipse center O' is found by extending the impact point I' along the elongation direction by the elongation distance l' .

$$x_{O'} = \begin{cases} x + l' \cos \alpha, & u \geq 0 \\ x - l' \cos \alpha, & u < 0 \end{cases} \quad (4.40)$$

$$y_{O'} = y + l' \sin \alpha \quad (4.41)$$

The elongation distance l' on the projected plane can be calculated from the elongation distance l of the splat on the deposit profile.

$$l' = l \cos \theta \quad (4.42)$$

where the elongation distance on the deposit profile can be evaluated by **Equation 4.30** and **Equation 4.31**.

$$l = (0.04147\theta - 0.096)D \quad (4.43)$$

where θ is the impact angle for individual impact particle, D is the initial particle diameter.

A local coordinate system is set up for every individual splat, which is called the splat coordinate system. The origin of this coordinate system is set at the projected ellipse center O' ($x_{O'}$, $y_{O'}$), the x' axis is aligned with the projected major axis, the y' axis is aligned with the projected minor axis. For the convenience of description, the original coordinate system is called global coordinate system. In the splat coordinate system, a boundary frame $A'B'C'D'$ is drawn encompassing this ellipse. The frame corner coordinates are respectively

$$\begin{cases} A'(-a', -b') \\ B'(a', -b') \\ C'(a', b') \\ D'(-a', b') \end{cases}$$

in the splat coordinate system.

The coordinates of these four points in the splat coordinate system are transformed to the coordinates in the global coordinate system. Then, a frame aligned on the grids encompassing this boundary frame is created, as a rectangle $EFGH$ in **Fig. 4.18(b)**. All the nodes inside this frame are evaluated iteratively if they should be included in the splat thickness calculation for this splat.

In the individual splat coordinate system, because the splat center is $O'(0,0)$, a point in the ellipse must satisfy the equation below:

$$\frac{x'^2}{a'^2} + \frac{y'^2}{b'^2} \leq 1 \quad (4.44)$$

where (x', y') are the point coordinates in the splat coordinate system, a' and b' are the splat major and minor radius respectively. Therefore, the variable

$$c_n = \frac{x'^2}{a'^2} + \frac{y'^2}{b'^2} \quad (4.45)$$

is considered as the criterion whether a point resides in the ellipse area.

Based on this algorithm, a method is established to determine if a node is included in the thickness calculation in a splat, as shown in **Fig. 4.19**. In subfigure (b), the ellipse represents the splat covering area. The red points are the nodes which are considered to be included in the splat thickness calculation for this splat. These nodes are determined by two criterion parameters r and s .

Fig. 4.19(a) shows an example node P in the boundary frame, assuming it is the grid node (m, n) . Firstly, the coordinates of this node are transformed from the global coordinate system (x_m, y_n) to the splat coordinate system (x'_m, y'_n) . Four midpoints of the grid line segments surrounding this node P are labeled as S_1 , S_2 , S_3 and S_4 . The coordinates of these points in the splat coordinate system are

$$\begin{cases} S_1 = (x'_{m+0.5}, y'_n) \\ S_2 = (x'_m, y'_{n+0.5}) \\ S_3 = (x'_{m-0.5}, y'_n) \\ S_4 = (x'_m, y'_{n-0.5}) \end{cases}$$

The criterion variable c_n is evaluated for node P and passed to parameter r

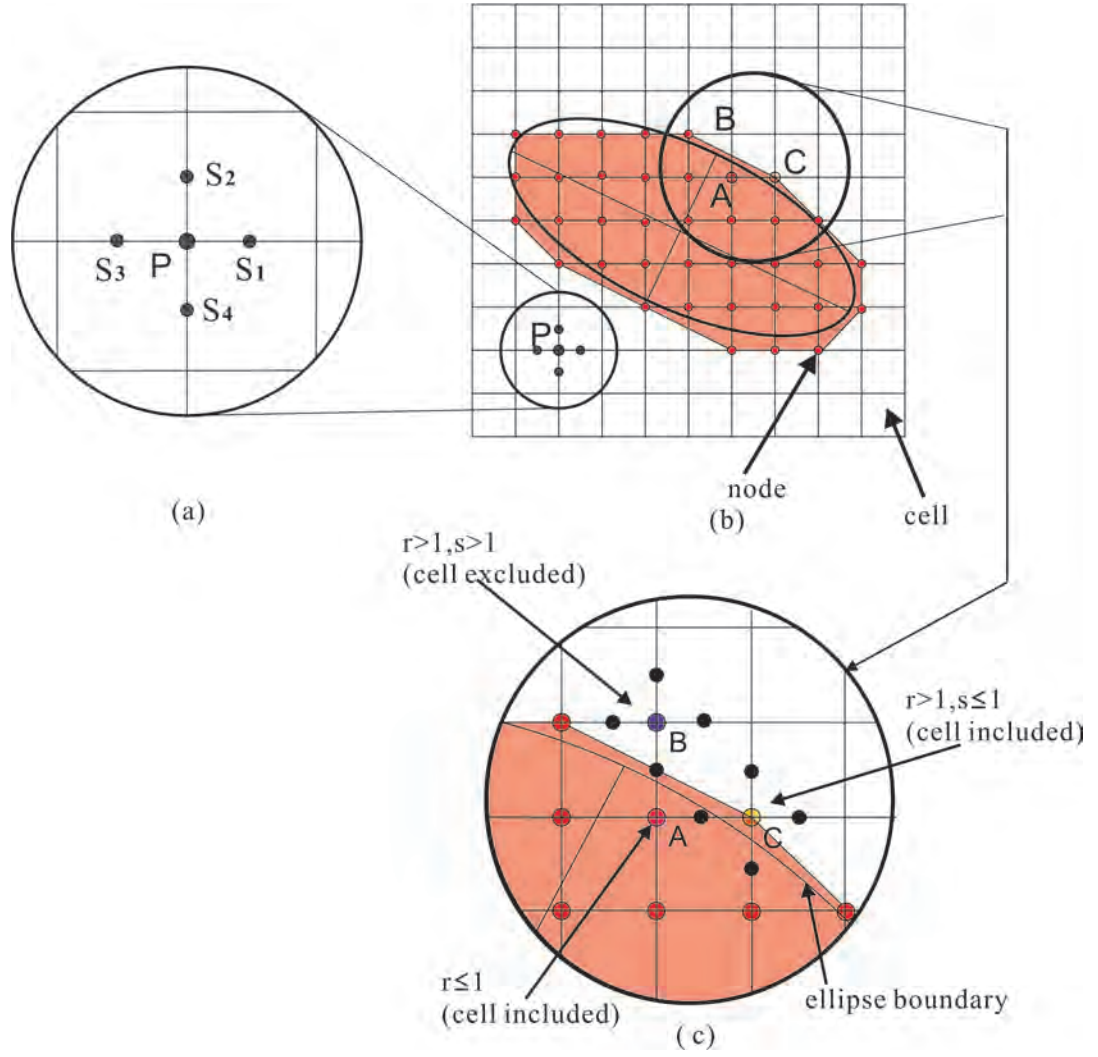


Fig. 4.19 Determination of nodes for an individual splat thickness calculation.

$$r = \frac{x'_m{}^2}{a'^2} + \frac{y'_n{}^2}{b'^2} \quad (4.46)$$

Another parameter s is defined as the average value of the criterion variable c_n for points S_1 to S_4 ,

$$\begin{cases} S_1 = \frac{x'_{m+0.5}{}^2}{a'^2} + \frac{y'_n{}^2}{b'^2} \\ S_2 = \frac{x'_m{}^2}{a'^2} + \frac{y'_{n+0.5}{}^2}{b'^2} \\ S_3 = \frac{x'_{m-0.5}{}^2}{a'^2} + \frac{y'_n{}^2}{b'^2} \\ S_4 = \frac{x'_m{}^2}{a'^2} + \frac{y'_{n-0.5}{}^2}{b'^2} \\ S = \frac{S_1 + S_2 + S_3 + S_4}{4} \end{cases} \quad (4.47)$$

As shown in **Fig. 4.19**, A , B and C represent three different types of nodes in the splat coordinate system. For node A , the criterion parameter r satisfies the condition

$r \leq 1$, i.e., the node falls inside the ellipse, it is considered as part of the splat and being assigned with a splat thickness t' .

It is observed that some nodes outside the ellipse are very close to the ellipse boundary. If they are excluded, the approximation error may be unsatisfactorily large. To reduce the approximation error, the criteria parameter s is introduced to determine if the node is very close to the ellipse.

Illustrated in **Fig. 4.19(c)**, if none of the four midpoints surrounding node (like node B) is inside the ellipse ($s > 1$), the node is excluded; if at least one of the four midpoints surrounding node (like node C) fall in the ellipse ($s \leq 1$), the node is included.

All the nodes included in the individual splat thickness calculation will be assigned with a thickness t' . From **Fig. 4.19(a)**, it can be seen that this is a good approximation of the splat covering area by this algorithm.

The splat thickness t' can be calculated from the impact particle diameter D , the impact velocity V and the impact angle θ . From **Equation 5.3, 5.5 and 5.6** the splat thickness t is

$$t = \frac{2}{3} \frac{D}{\xi^2} \quad (4.48)$$

Illustrated in **Fig. 4.20**, the distance t' thus can be calculated as

$$t' = \frac{t}{\cos \theta} \quad (4.49)$$

where θ is the angle between the impacted surface and the $x - y$ two-dimensional plane; it is also the impact angle of the impact particle with respect to the impacted surface.

4.4.7 Modeling of multiple overlapping splats

The particles impact onto the deposit surface at different time. In this work, simplified thickness accumulation is implemented for deposition formation. Upon impact, the subsequent droplet forms splat overlapping the previously deposited splats compactly.

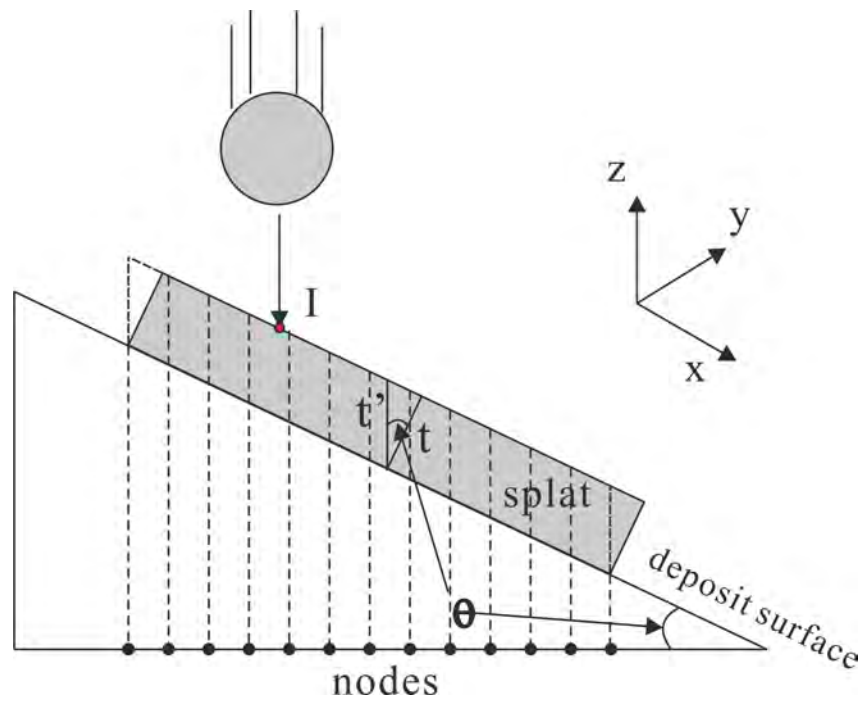


Fig. 4.20 Node advancement along z axis caused by single splat depositing.

Fig. 4.21 schematically shows the concept of two overlapping splats. The thickness of these two splats t_1 and t_2 are projected to the z direction as t'_1 and t'_2 . In the overlapping area, the thickness increase is the summation of the two projected thickness $t'_1 + t'_2$.

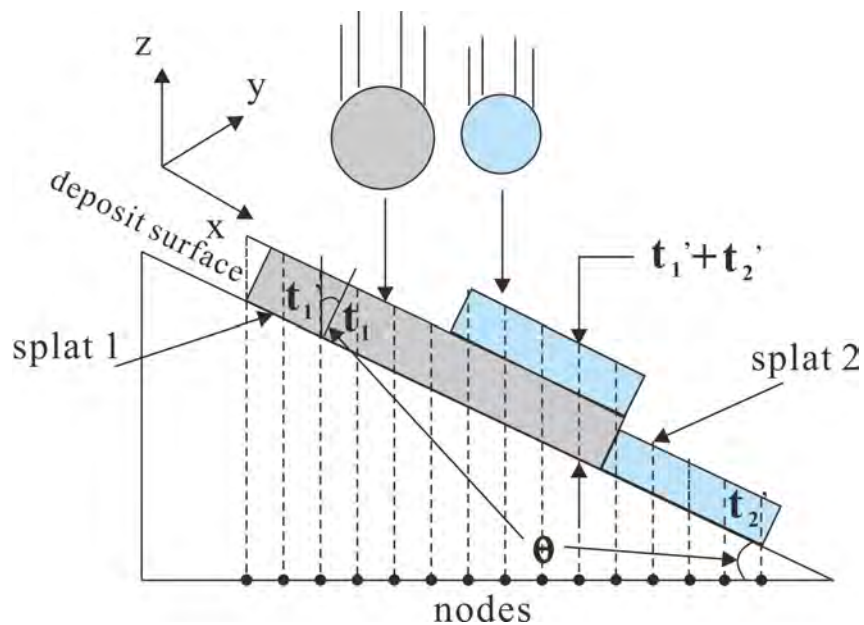


Fig. 4.21 Schematic illustration of the deposition model depicting the thickness build-up of two overlapping splats.

By this means, there is no pores or non-continuous part in the deposit. This will under-predict the deposit volume. More realistic inter-splat microstructure will be the consideration of this code in the future.

4.4.8 Overall model procedure and case implementation

The entire procedure for the model is clearly shown in the flow chart in **Fig. 4.22**. The code is written in C++ programming language and listed in **Appendix H**. When the code is implemented, the $x - y$ two-dimensional plane grid size is set as $5 \times 5 \mu\text{m}$.

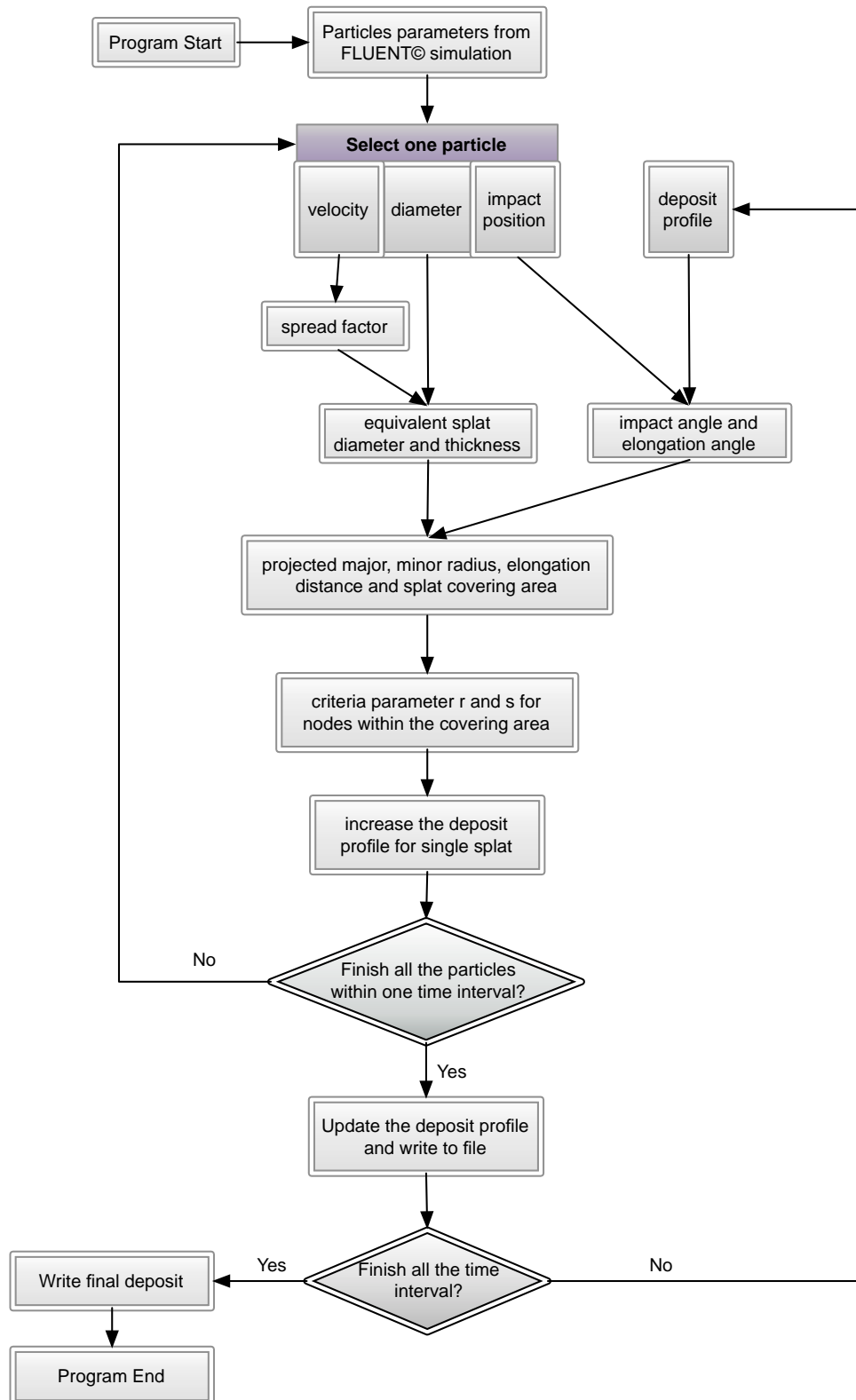


Fig. 4.22 Flowchart of the the deposit model implementation procedure.

Three cases are implemented by following the experiment cases. In addition, a complementary case is carried out by taking a flat surface as the targeted substrate, although there is no experimental counterpart for this case. However, it is a problem to decide the vertical position of the substrate. In the experiment, the vertical position is roughly set by observation. Moreover, the particles trajectory deviates from the spray torch axis to the downward ($-y$) direction. Therefore, it is impossible to set the deposit position exactly when carrying out the experiments. In order to determine the deposit position on the substrate surface, image analysis from the SprayWatch diagnostics are carried out.

The substrate position y_0 along y axis for the three cases are evaluated, as shown in **Fig. 4.23** to **Fig. 4.25**. The evaluation method is depicted below. Take case 1 as an example, **Fig. 4.23(a)** shows the SprayWatch® image before the deposition starts. FOV X is calculated from the focus distance fd .

$$\begin{aligned} FOV X &= 0.039913 + 0.09735 \times fd \\ &= 0.039913 + 0.09735 \times 276 = 26.9 \text{ mm} \end{aligned}$$

The image width is set as this calibrated FOV X value, keeping the width to height ratio unchanged. Then a profile with the substrate surface radius R is drawn and fitted to the surface arc in the image, which is brighter than the background. Then the substrate summit S is found, which is actually in the position $(y_0, 0)$ in the (y, z) coordinate. The deposit apex position is evaluated by its relative position to the point S . In case 1, the coordinate is $(y_0 + 16.7, 1.045)$ in the units of millimeter. In **Fig. 5.59**, the contour center for the number of particle is about $(0, -10)$ in the units of mm. The deposit apex is assumed to be at the contour center, thus $y_0 + 16.7 = -10$. By this means, the substrate position along y axis for case 1 can be determined as $y_0 = -26.7$ mm.

The results of the position y_0 are listed in **Table 4.7**. t_p is introduced to describe the thickness of the deposit, which is defined as the distance from one point on the profile surface to the corresponding substrate surface at the same x and y values. Peak deposit thickness t_{pm} is the peak value of the t_p . In the SprayWatch®

diagnostics images, it is evaluated as the distance from the deposit apex to the substrate surface.

Table 4.7 Image dimension calibration for cases 1 to 3 and the final maximal deposit projected thickness t_{pm} .

Case	Focus distance (mm)	FOV X (mm)	y_0 (mm)	t_{pm} (mm)
1	276	26.90	-26.70	2.99
2	270	26.32	-5.69	1.05
3	273	26.62	12.00	2.32

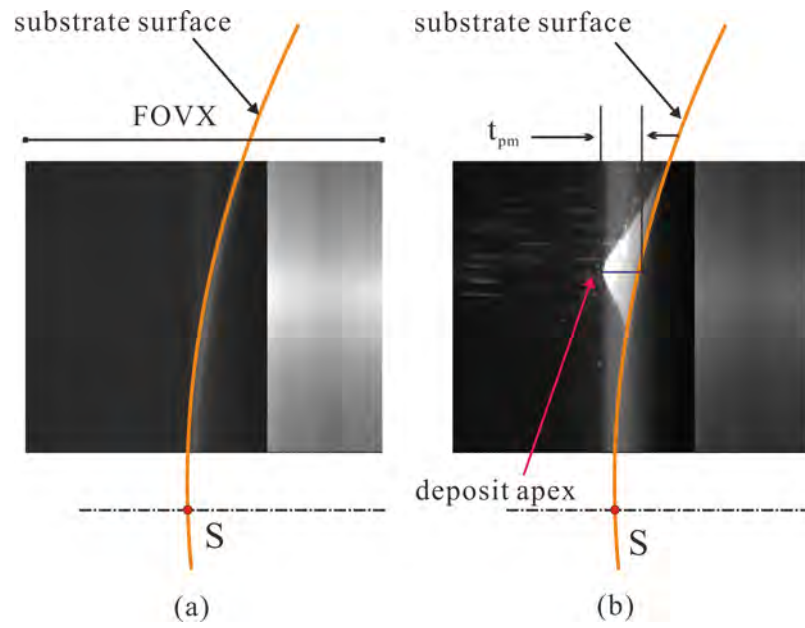


Fig. 4.23 Determination of the deposit position and apex height for case 1.

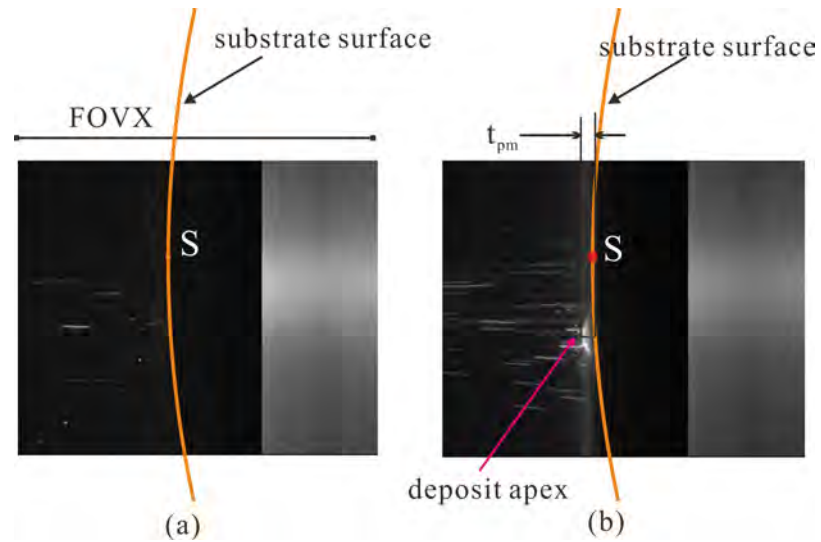


Fig. 4.24 Determination of the deposit position and apex height for case 2.

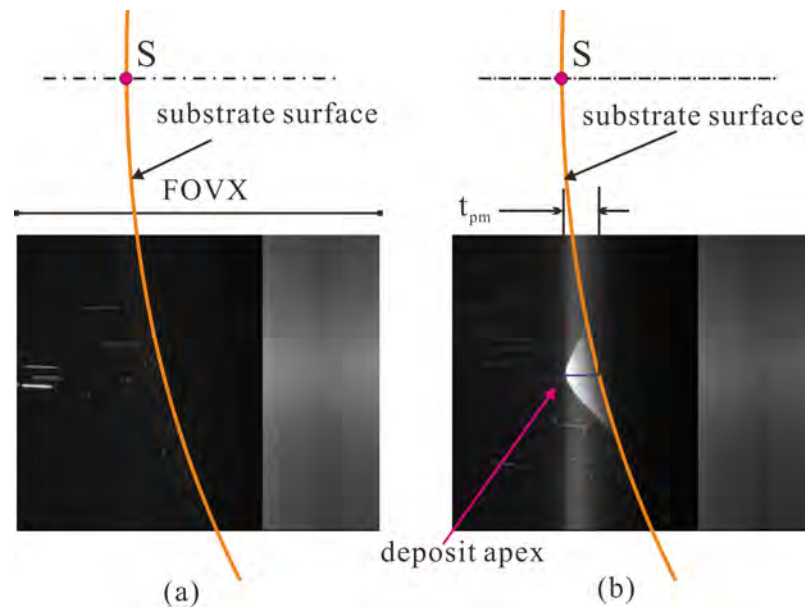


Fig. 4.25 Determination of the deposit position and apex height for case 3.

Chapter 5

Results and Discussion

5.1 Introduction

This chapter presents the results of experiments and simulations described in **Chapter 3** and **Chapter 4**. The experimental results are analyzed to validate the simulation results. Combining the experimental and simulation results, some interesting findings are made.

In the first section, the plasma plume temperature and velocity field are presented firstly. An axial centerline and two orthogonal slices are created to extract the data in the simulation results. The effect of the inclusion of the substrate on the plasma plume is investigated by the contour and vector stream plots. In simulation, the individual particle trajectory and temperature and velocity history are examined to investigate the effect of the particle sizes. The substrate inclusion effect on the particle distribution is also analyzed by comparing the case with substrate and the freestream case. The online-diagnostics of the in-flight particles in the experiment is used to validate the freestream case in the simulation. Although SprayWatch® cannot capture all the particles in the trajectory, the obtained data represent the in-flight particle parameters value and distribution.

The second section is divided into two subsections based on the analysis of splatting behavior on the flat substrate and curved substrate. The impact behavior is mainly discussed in the subsection for flat substrate, including the droplet flattening, jetting and fingering phenomena; while the splat morphology evaluation is carried out in both the two subsections. Splat morphology factors – spread factor, aspect ratio and elongation factor are evaluated and related to the impact parameters, such as droplet velocity and impact angle.

In the third section, the deposit growth and final morphology from experimental observation are analyzed. Simulation results are compared with the experiments both by the profile shape and the maximum peak thickness quantity.

5.2 Plasma Field Generation and In-flight Particle Behavior

The simulation results on plasma field generation and in-flight particle behavior are analyzed in this section. Lines and surfaces cutting through the computational domain are created to acquire the plasma temperature and velocity distribution. The in-flight particles are “captured” by plane at the position of 80 mm. To investigate the effect of particle size on the particle fate, single particles with different sizes are traced. The SprayWatch® on-line diagnostics are used to compare with the Freestream case of the simulation.

5.2.1 Data acquisition lines and surfaces

In order to analyze the simulation results, data of interest are extracted along several surfaces (or lines). As shown in **Fig. 5.1**, the line PQ along z-axis is referred to as Centerline; two plane-shape longitudinal sections at $x = 0$ and $y = 0$ are respectively referred to as YZ-plane (blue color) and XZ-plane (pink color).

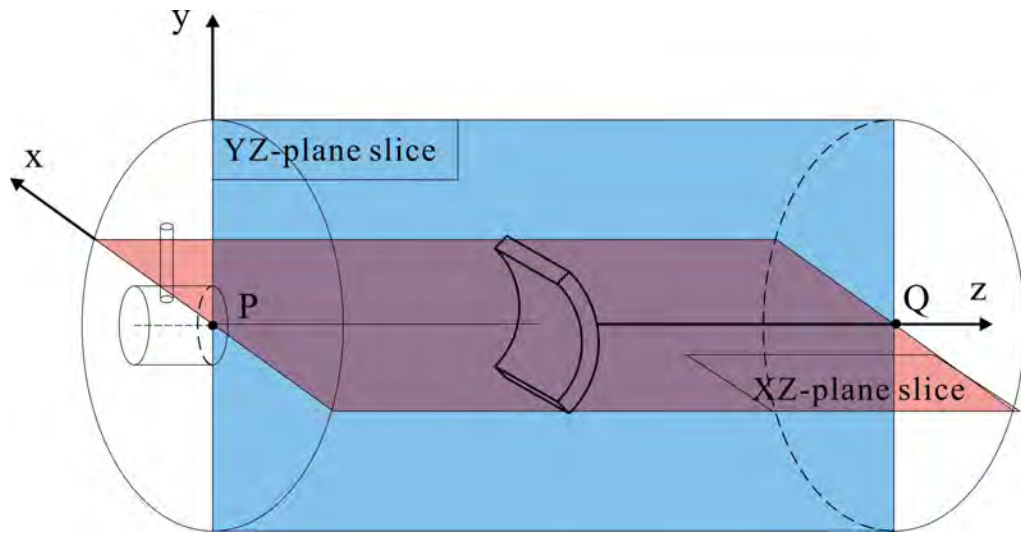


Fig. 5.1 Schematic Illustration of centerline and YZ- and XZ-plane slices.

Moreover, two parallel acquisition surfaces of the substrate front face are created to get the near-substrate-wall flow field behavior. **Fig. 5.2** illustrates the side view of parallel data acquisition surface, which has a distance D_w to the substrate front face. These two parallel surfaces are respectively referred to as near surface with

$D_w = 0.1mm$ and far surface with $D_w = 5$ mm. It is necessary to mention that the length of the parallel data acquisition surfaces extends in both directions within the downstream computational domain, while the substrate front face is of a length L , as shown in **Fig. 5.3**. The cross-hatched surface represents the substrate front face, while the surface in front of it is the data acquisition surface. The region on the data acquisition surface directly ahead of the substrate front face, is referred to as inner region; while the extended region at sides of the inner region is referred to as outer region.

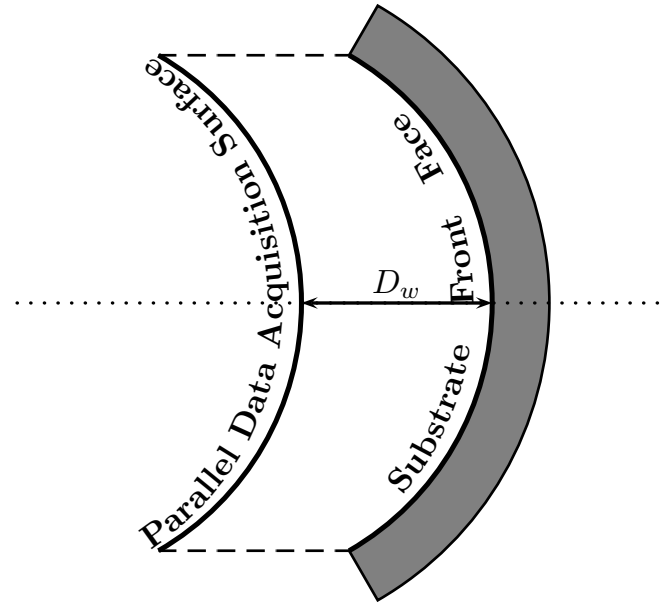


Fig. 5.2 Schematic illustration of side view of parallel data acquisition surface.

For visualization convenience, a flattening procedure maps specific curvilinear coordinates of the parallel data acquisition surface (near or far) (**Fig. 5.4(a)**) into a planar representation without distortion(**Fig. 5.4(b)**). The resultant surface is called Developed Surface, with a transformed Y coordinate $Y' = R\theta$.

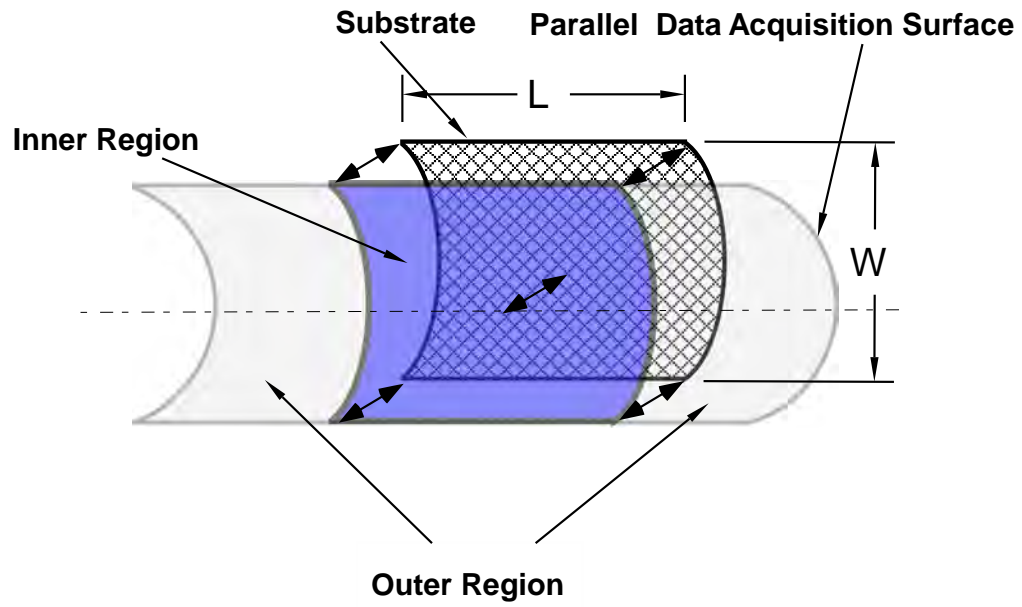


Fig. 5.3 Schematic illustration of inner region and outer region of the parallel data acquisition surface.

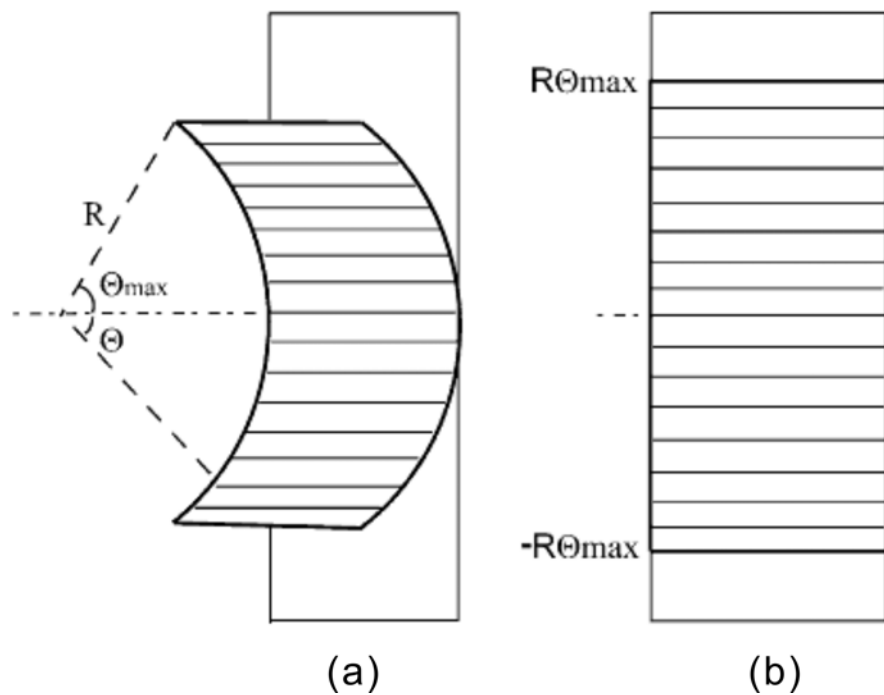


Fig. 5.4 Schematic Illustration of flattening parallel curved surface into developed surface: (a) original surface; (b) developed surface.

5.2.2 Grid independence tests and verification of simulation model

A grid independence test is conducted on the mesh models at the beginning of the simulation work to ensure an optimized mesh scheme was obtained. It is carried out for Freestream case with three levels of grid size: coarse with number of total grids as 715161, medium 1475949 and fine 2174076. The three levels are roughly in a ratio of $1\times$, $2\times$ and $3\times$ the number of grids of the coarse model respectively. The plasma temperature and velocity magnitude were extracted from XZ-plane to monitor the effects of the mesh refinement, which are shown in **Fig. 5.5**. The coarse, medium and fine model are illustrated respectively by solid, dashed and dotted lines. There is no much discrepancy between these three levels, and an average of about 3% difference is found between adjacent levels. Therefore, the coarse grid scheme is adopted for the following work because the less consumption of computing time and resource.

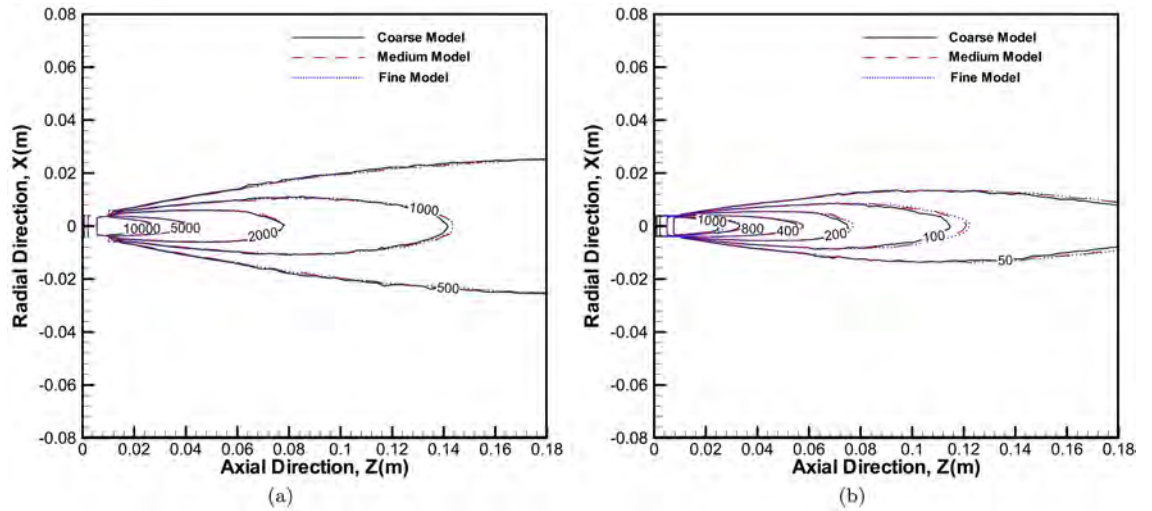


Fig. 5.5 Grid independence tests for Freestream by comparison of contours of (a) temperature and (b) velocity in XZ plane.

In order to verify the numerical model, it is modified to fit the experimental setup by Mckelliget et al.'s work[129]. This model was simulated based on the operating conditions of 7.4 kW power input and 35.4 l/min of argon gas flow rate. The mathematical models, the assumptions and boundary conditions setting remained as the author's model. Moreover, a comparison model is set up with turbulence correction advised by Bolot et al.[130]

Figure 5.6 (a) and (b) respectively shows the plasma temperature and axial velocity distribution along the Centerline. The square scatters, solid lines and dashed lines are the experimental data from McKelliget et al.[129], result of the model without turbulence correction and the model with turbulence correction respectively. It can be seen that plasma core of the current model is shorter than the turbulence correction model but closer to the experimental data at a relatively far distance away from the torch exit. Because the intention of our current work is to investigate the influence of curved substrates on the plasma field, especially the particle behavior far away from the plasma jet core, therefore, the current model without turbulence correction is adopted.

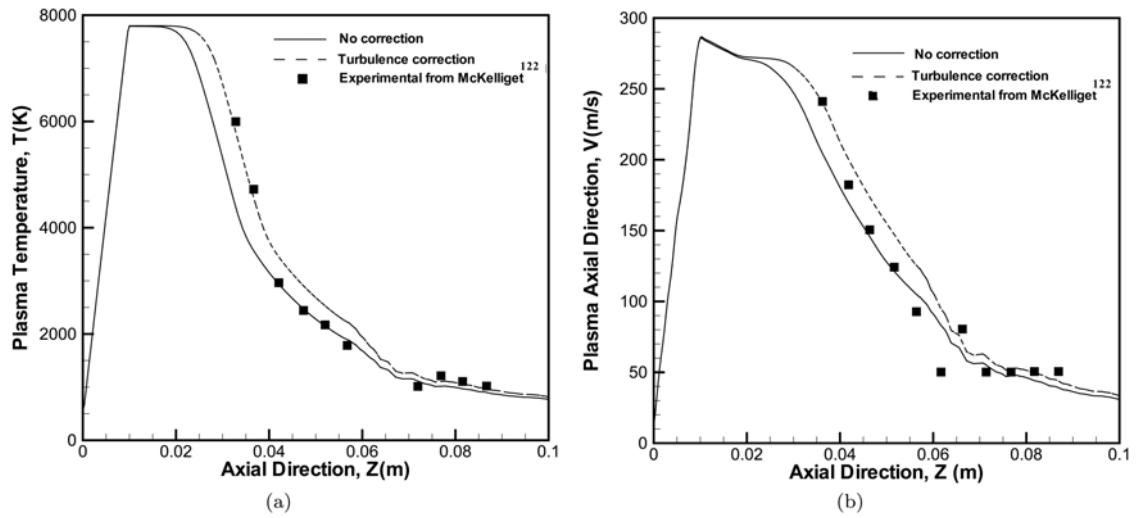
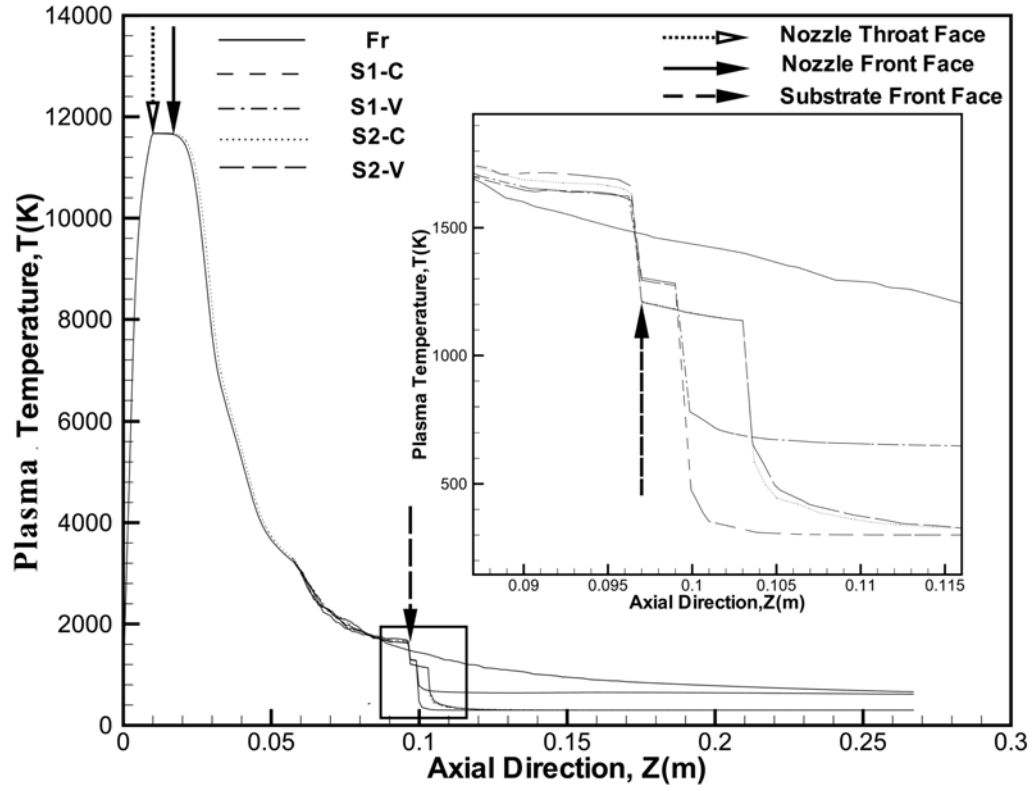


Fig. 5.6 Verification of simulation model by comparison with experimental data from McKelliget et al.[129] in (a) temperature and (b) axial velocity along centerline.

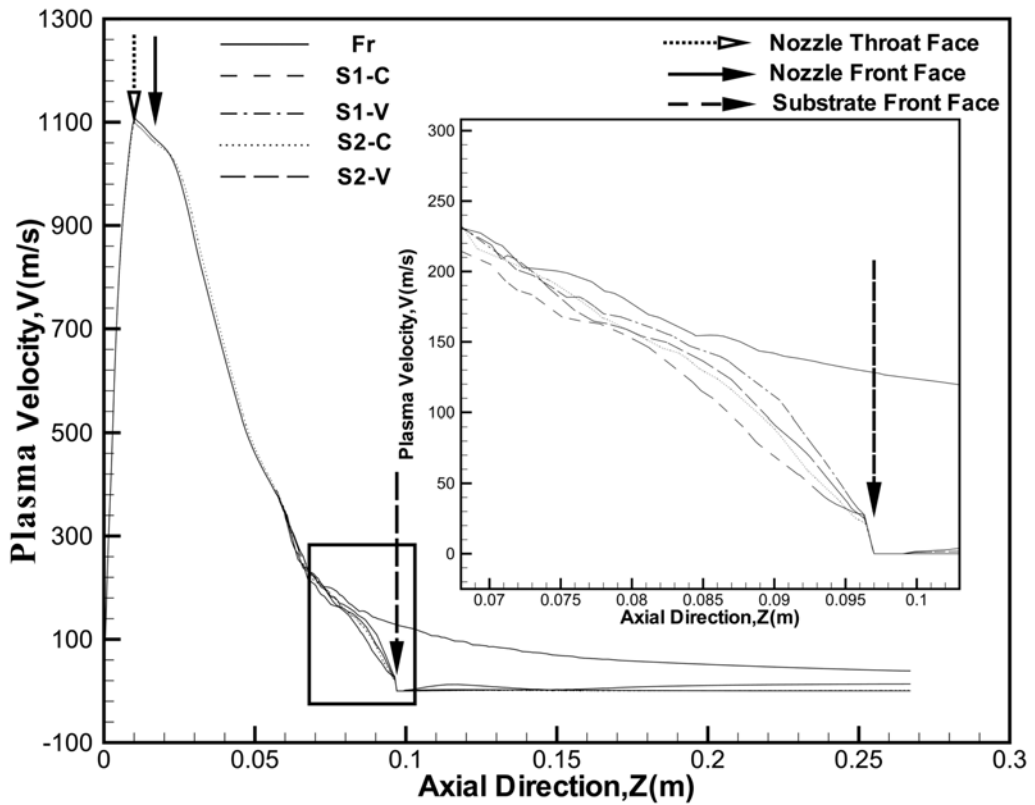
5.2.3 Temperature and velocity distributions along axial centerline

Fig. 5.7(a) shows the plasma temperature distribution along the centerline for the five cases. Fr stands for freestream case, S1 and S2 represent the two substrates with different shape, C and V represent concave and convex orientations respectively. The radius of the surface facing to the spray torch thus is 11, 13, 51, 57 mm for S1-C, S1-V, S2-C and S2-V case respectively. Because of the high intensity arc, the plasma temperature increases sharply at the upstream of nozzle throat face. The expansion effect of argon gas due to high temperature results in a similar plasma velocity profile (**Fig. 5.7(b)**).

Temperature and velocity start to drop immediately after the nozzle throat face, in a relatively small reduction rate. The temperature (also the velocity) decreases drastically to ambient condition after approximately 20 mm downstream of the nozzle front face. Plasma velocities of those cases with inclusion of substrates initially almost coincide with the freestream case up to nearly 20 mm upstream of the substrate front face, where they start deviating from the freestream cases due to the obstruction effect. Comparing with plasma velocity, the obstruction effect on the plasma temperature is relatively minor, until approximately 10mm upstream. The temperature drop across the substrate is more drastic than the upstream of the substrate front face. For different cases, the temperature drop intensity is nearly the same, but at different temperature decreasing rates, which varies inversely as the substrate thickness. This phenomena is shown clearly in **Fig. 5.7(b)**.



(a)



(b)

Fig. 5.7 Prediction of axial centerline distribution of (a) plasma temperature, (b) plasma velocity. Fr stands for freestream case, S1 and S2 represent the two substrates, C and V represent concave and convex orientations respectively.

5.2.4 Plasma plume thermal field

Fig. 5.8 and **Fig. 5.9** present plasma temperature contours for the substrate S1 and S2 respectively. The contours are symmetrical about the YZ-plane (as seen in XZ-plane view), but not about the XZ-plane (as seen in YZ-plane view). There is a deviation of the plasma plume to the negative Y direction due to the carrier gas injection. Temperature of the plasma core region with relatively higher value remains nearly the same shape, as a result of the far distance from the substrates; isothermal temperature contour lines follow the substrate shape to some extent. The concave substrate causes a more drastic divergence. When the width of the concave substrate exceeds a certain value, the plasma flow reverses; whilst there will be a vortex flow when the width of the convex substrate falls below a certain value.

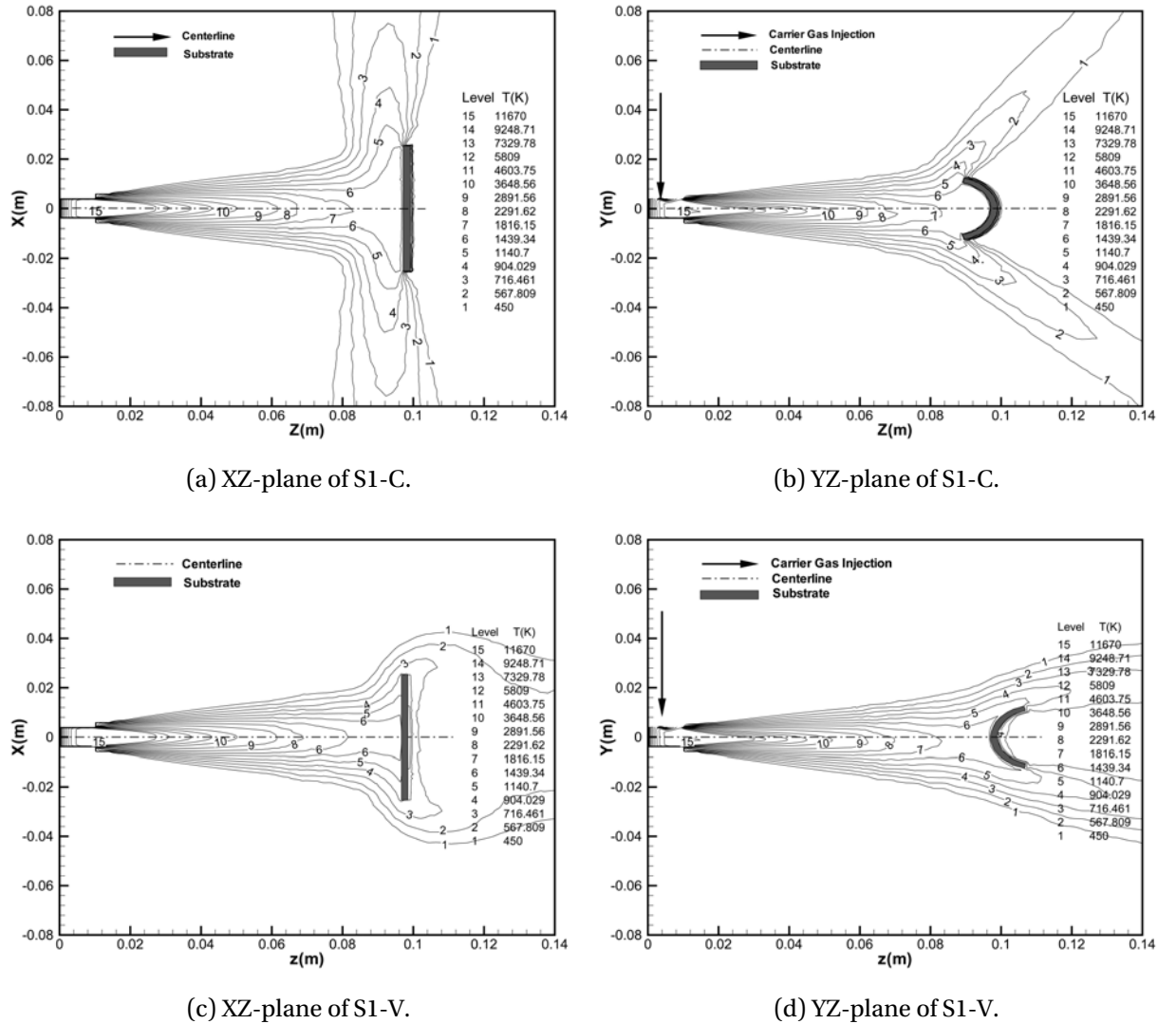
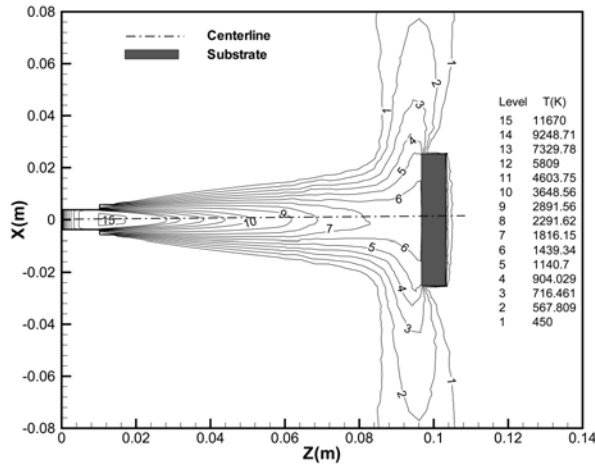
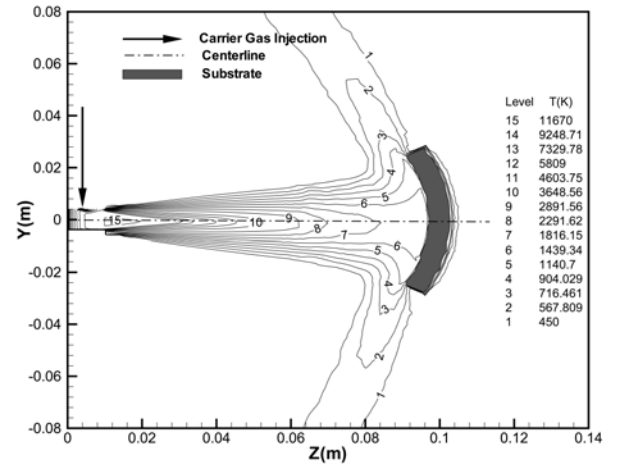


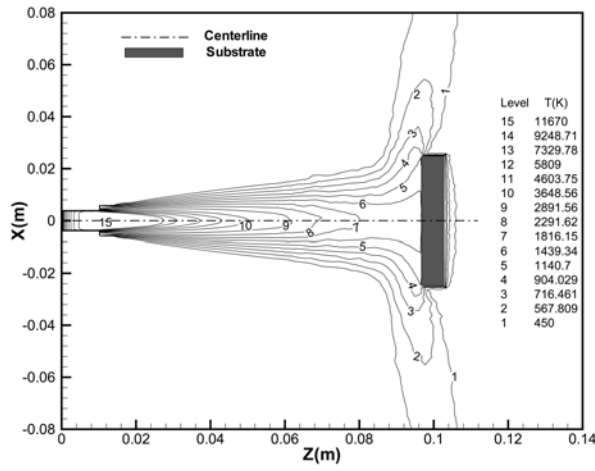
Fig. 5.8 Comparison of plasma temperature contours in XZ- and YZ-planes for the substrate S1 in the concave (C) and convex (V) orientations.



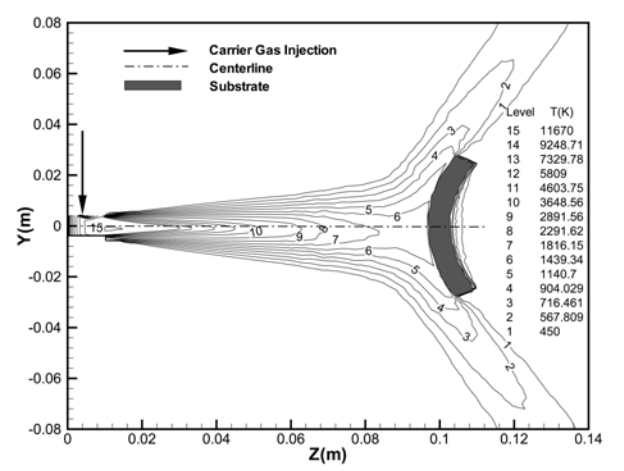
(a) XZ-plane of S2-C.



(b) YZ-plane of S2-C.



(c) XZ-plane of S2-V.



(d) YZ-plane of S2-V.

Fig. 5.9 Comparison of plasma temperature contours in XZ- and YZ-planes for the substrate S2 in the concave (C) and convex (V) orientations.

Temperature contours in the near surface and far surface are shown in **Fig. 5.10**. As claimed previously, near surface and far surface are two parallel surfaces with respect to the substrate front face, and with the distance to the substrate front face of 0.1 mm and 5 mm respectively. The contour seems more regular in far surface than that in near surface. There is a high temperature gradient across the shared borders of inner region and outer region (at nearly 25 mm along X direction) in near surface.

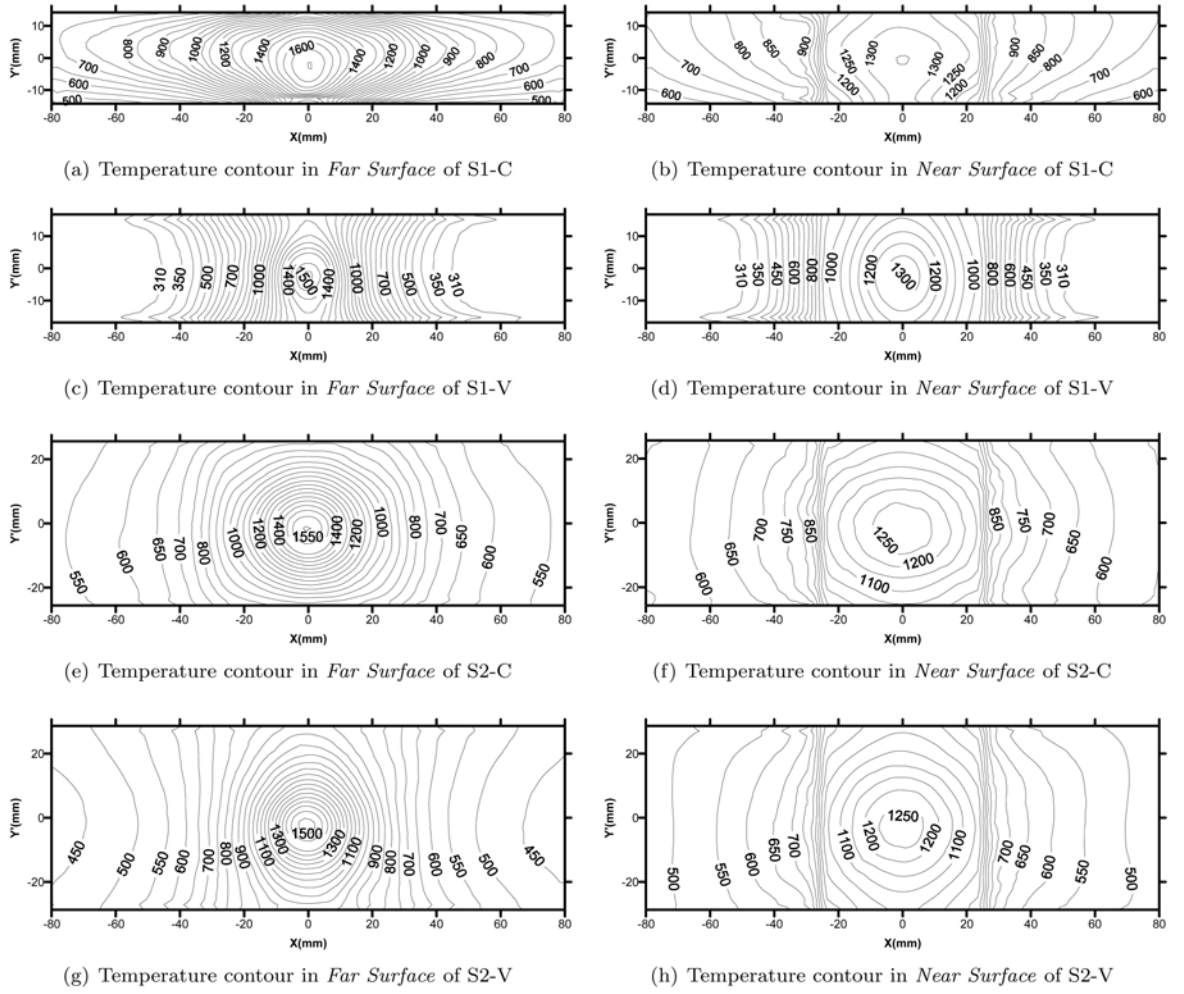
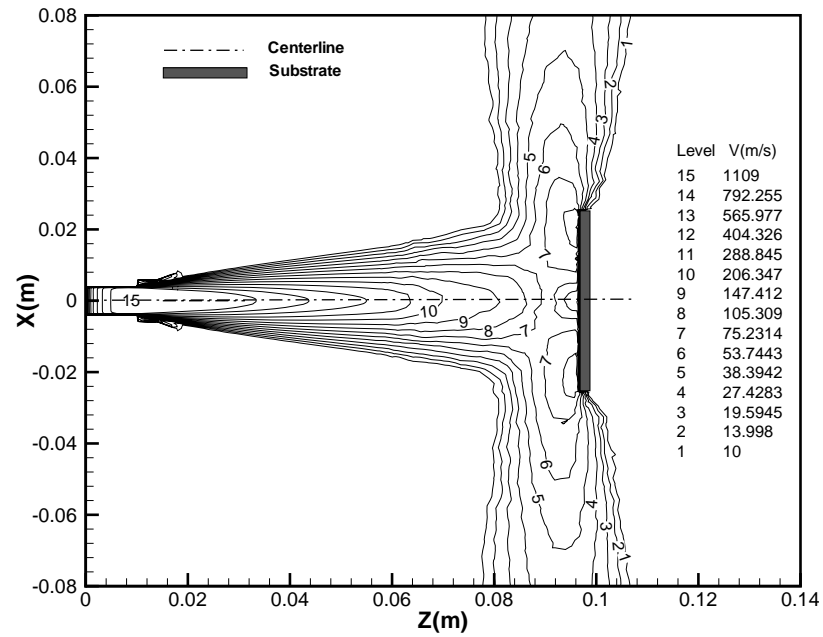


Fig. 5.10 Temperature contours in near and far surfaces for four different cases with substrates. S1 and S2 represent the two substrates, C and V represent concave and convex orientations respectively.

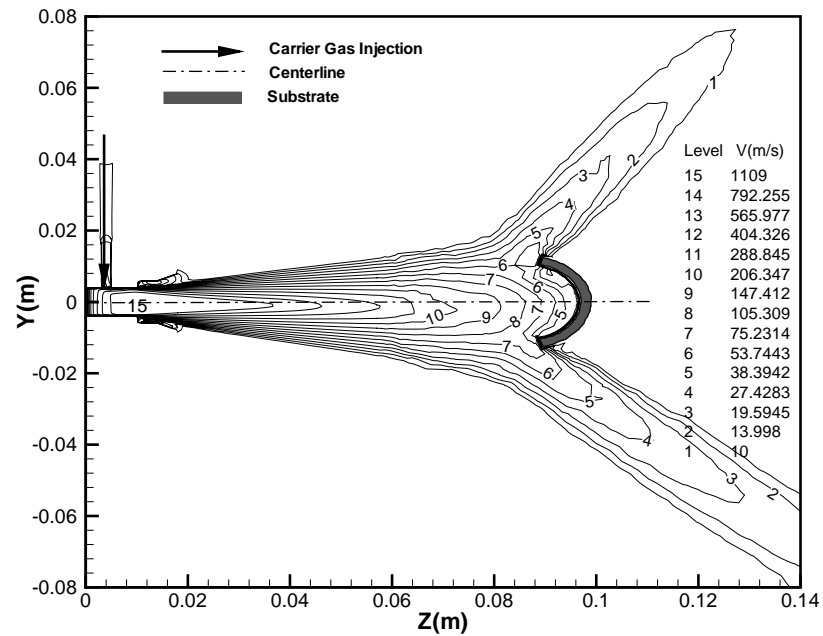
5.2.5 Plasma velocity field

As the velocity magnitude contours in XZ- and YZ- plane are quite similar to the temperature contours, only the velocity contour of S1-C case is shown, in **Fig. 5.11**. **Fig. 5.12** shows velocity contours in the near surface and far surface. In contrast to the plasma temperature, velocity is more affected by substrate obstruction. There is still a relatively high gradient across the shared borders of inner region and outer region in near surface. Contour shape and velocity magnitude at inner region of near surface are totally different from those at its counterpart area in far surface, caused by the stagnation effect. Whilst the contour shapes remains similar and velocity magnitude is changed little in the outer region of these two surfaces. The contours

are symmetric with respect to $X = 0$ but deviate to the negative Y direction with respect to $Y = 0$.



(a) Velocity contour in XZ-plane of S1-C case



(b) Velocity contour in YZ-plane of S1-C case

Fig. 5.11 Comparison of plasma velocity contours in XZ- and YZ-planes for S1-C case. C represents concave orientation.

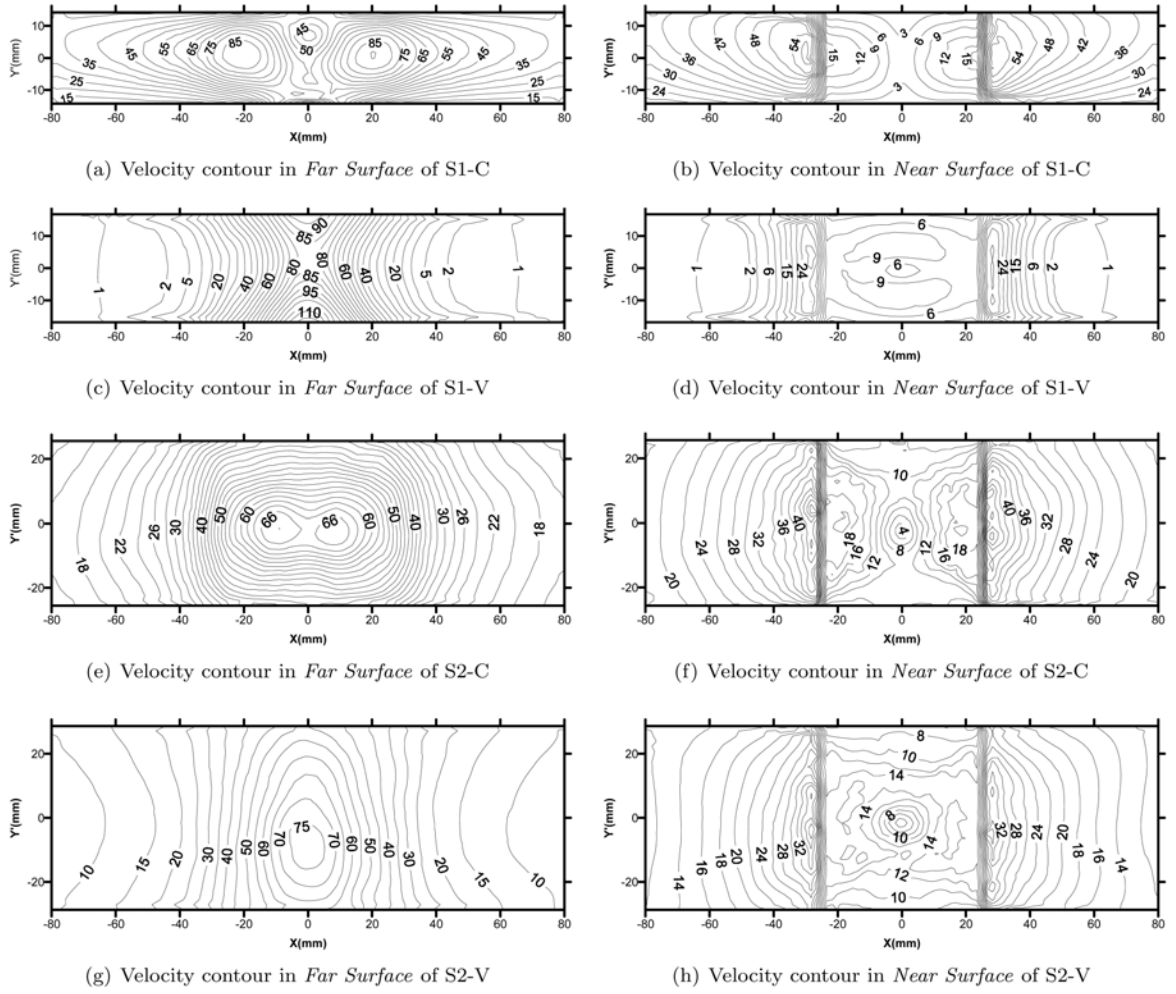


Fig. 5.12 Velocity contours in near and far surfaces for four different cases with substrates. S1 and S2 represent the two substrates, C and V represent concave and convex orientations respectively.

Fig. 5.13 shows clearly the plasma velocity streamlines in the longitudinal XZ- and YZ-planes. Velocity magnitude is indicated by grayscale (the darker the arrow, the larger the velocity magnitude). Initially the plasma flow develops freely after it exits from the nozzle; but at the near-wall region, the stream is drastically diverted due to the substrate obstruction and follows the substrate wall shape. The velocity vectors are shown in **Fig. 5.14**. The maximum velocity magnitude is observed at the shared borders of inner region and outer region (± 25 mm in X direction). Substrates placed in convex orientation provide an “easier way” for the stream to bypass around the substrates. Those with relatively large curvature (S1) will result in all upward-reversing flow (in Y direction) along the substrate front surface for concave case (**Fig. 5.13(b)**) or intensive turbulence at rear area of the substrate (**Fig. 5.14(d)**) for convex case, which is called “wave” phenomena. The velocity vectors which flow

towards substrate side edges from surrounding domain are also caused by such a turbulence effect, as shown in Fig. 5.14(d).

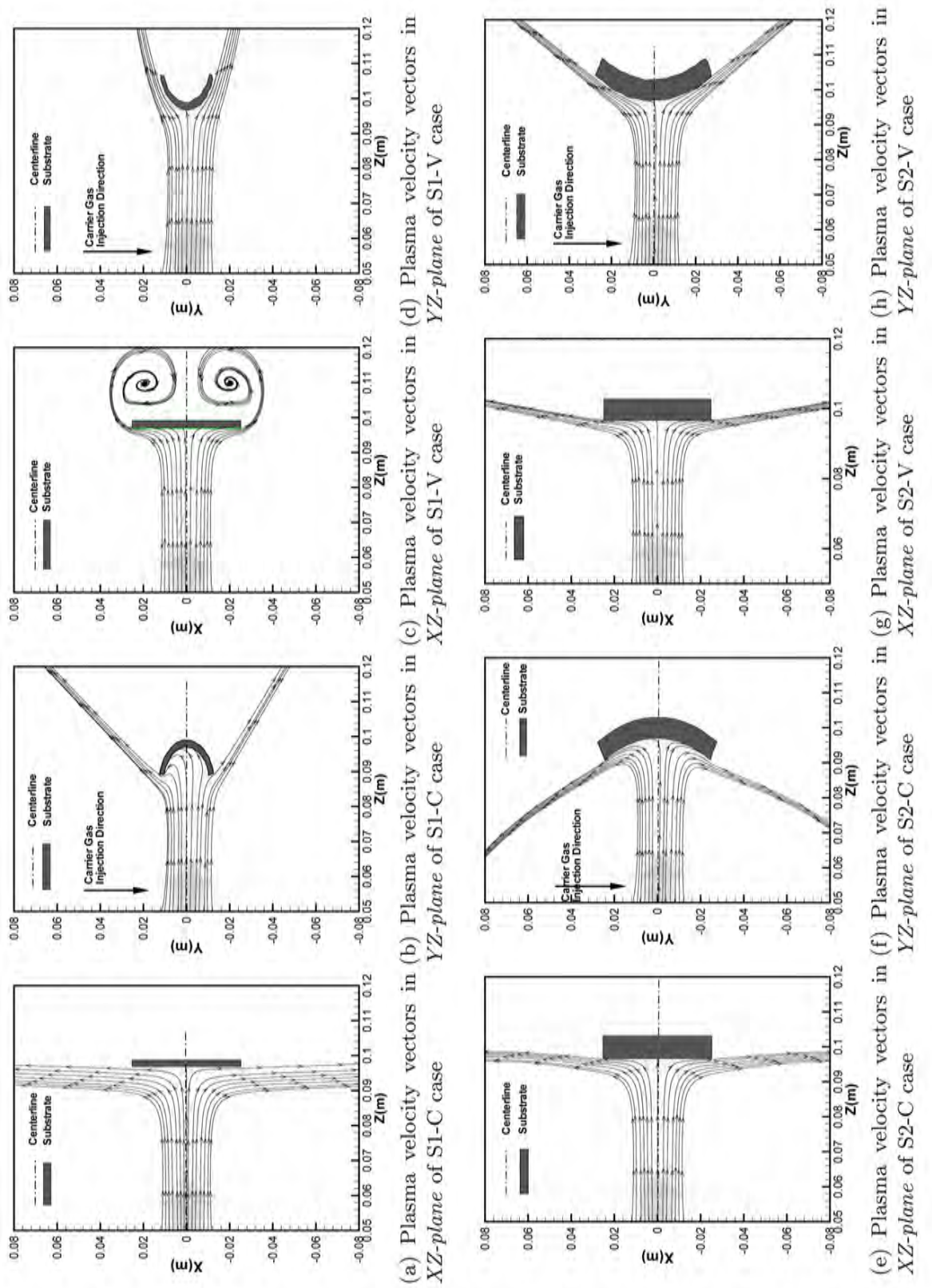


Fig. 5.13 Plasma velocity vectors in XZ- and YZ-planes of four cases with substrates. S1 and S2 represent the two substrates, C and V represent concave and convex orientations respectively.

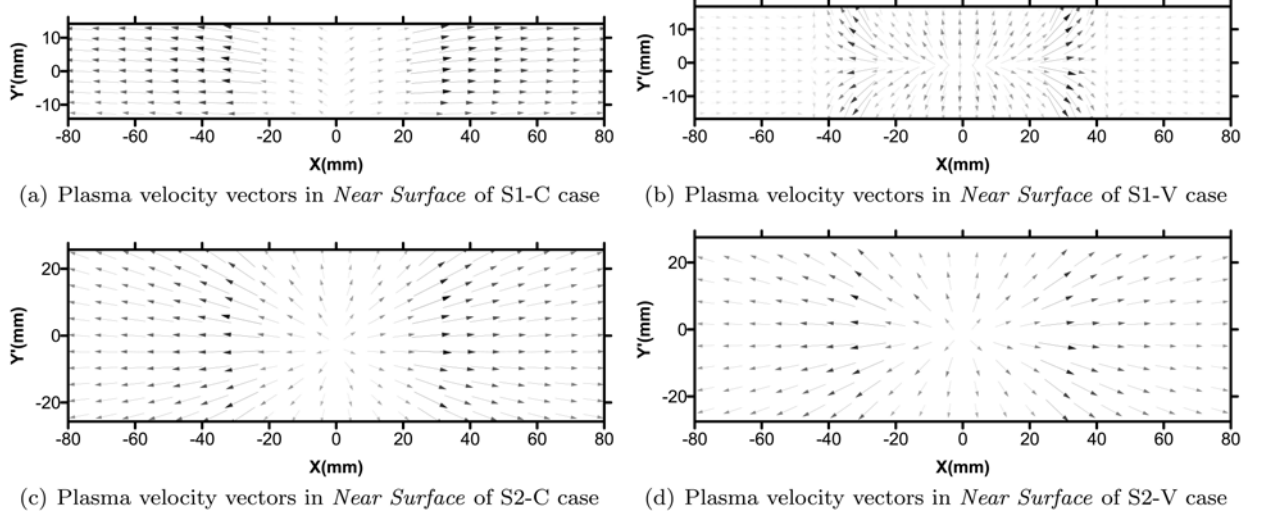


Fig. 5.14 Plasma velocity vectors in near surface of four cases with substrates. S1 and S2 represent the two substrates, C and V represent concave and convex orientations respectively.

5.2.6 Particles in-flight temperature, velocity and trajectory

In order to have a comprehensive understanding of the in-flight particles behavior, two different types of injections are utilized to set the initial particle injection position for the simulation, which is illustrated in **Fig. 5.15**.

In type (a), referred to as point injection, particles are injected at the center of the injection port of the plasma torch; in type (b), referred to as surface injection, particles are injected as a group from each cell of the mesh of the injection port. Point injection is for introducing a single particle to investigate its trajectories and in-flight behavior; while surface injection is for multiple particles injection, where the particles are distributed uniformly on the injection surface of the injection port. Combined with different particle size ranges, different injection methods are implemented to investigate the in-flight particle features.

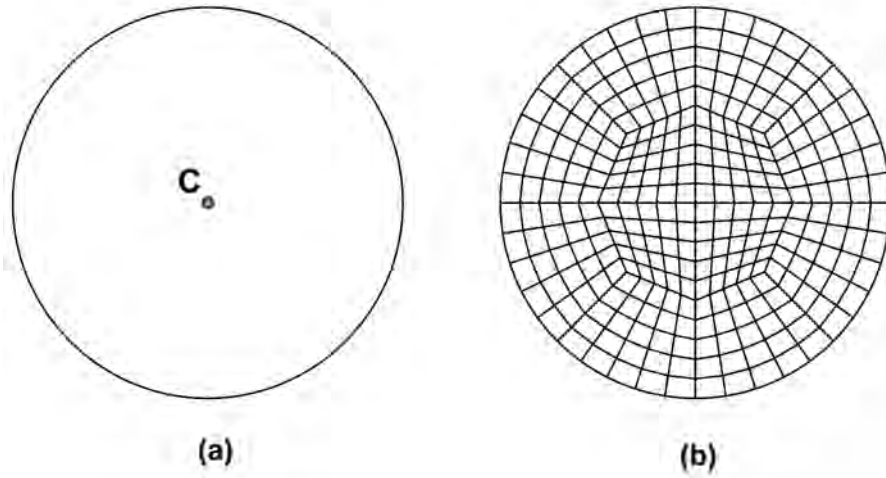


Fig. 5.15 Injection types: (a) point Injection; (b) surface Injection.

In order to investigate the particle size effect on the trajectory, a group of particles with discrete sizes of $22\ \mu\text{m}$, $47.8\ \mu\text{m}$, $73.5\ \mu\text{m}$, $99.5\ \mu\text{m}$ and $125\ \mu\text{m}$ are injected by point injection type in freestream case. These five particle sizes are selected from the particle size range, with uniform difference $\sim 26\ \mu\text{m}$. **Fig. 5.16** shows trajectories of these particles within the computing domain; an insert shows part of the trajectories magnified to illustrate more clearly the profiles. while part of the trajectories are magnified to illustrate more clearly the profiles.

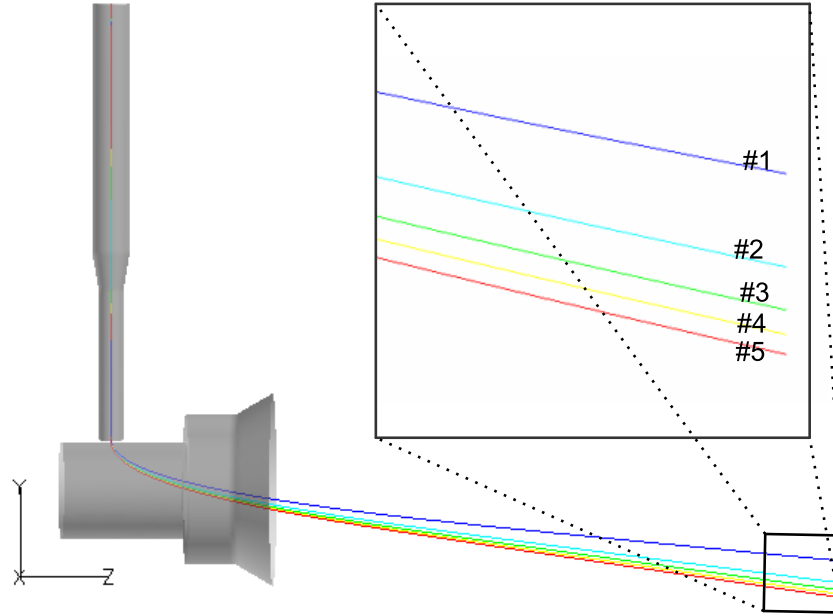


Fig. 5.16 Trajectories of particles injected from injection port center: #1, 2.20 μm ; #2, 4.78 μm ; #3, 7.35 μm ; #4, 9.95 μm ; #5, 12.5 μm .

Entrained by the same carrier gas, larger particles are imparted with higher inertia comparing with those with smaller sizes, which enables them to penetrate further across the plasma jet. So it can be noted that larger particles tend to have a lower trajectories.

At the same time, particles temperature and velocity profiles along their trajectories are respectively shown in **Fig. 5.17** and **Fig. 5.18**. Both the velocity and temperature of these particles increase drastically when they exit from the injector and immediately entrained by the plasma jet; and after reaching a peak value, start to decrease. Smaller particles have a steeper velocity/temperature gradient and a larger peak value, which is due to their lower inertia and heat capacity. It has to be mentioned that the particle is assumed to be introduced in a quasi-liquid state, thus the temperature starts at 300 K, which is not in conflict with the reality.

In the successive work, S2-C case (substrate 2, with concave orientation facing to the plasma torch) with particles loading is compared with freestream case to see if the inclusion of substrate will have effects on the particle trajectories, and further affect the particle distributions on the substrates. For the sake of investigating the effect of

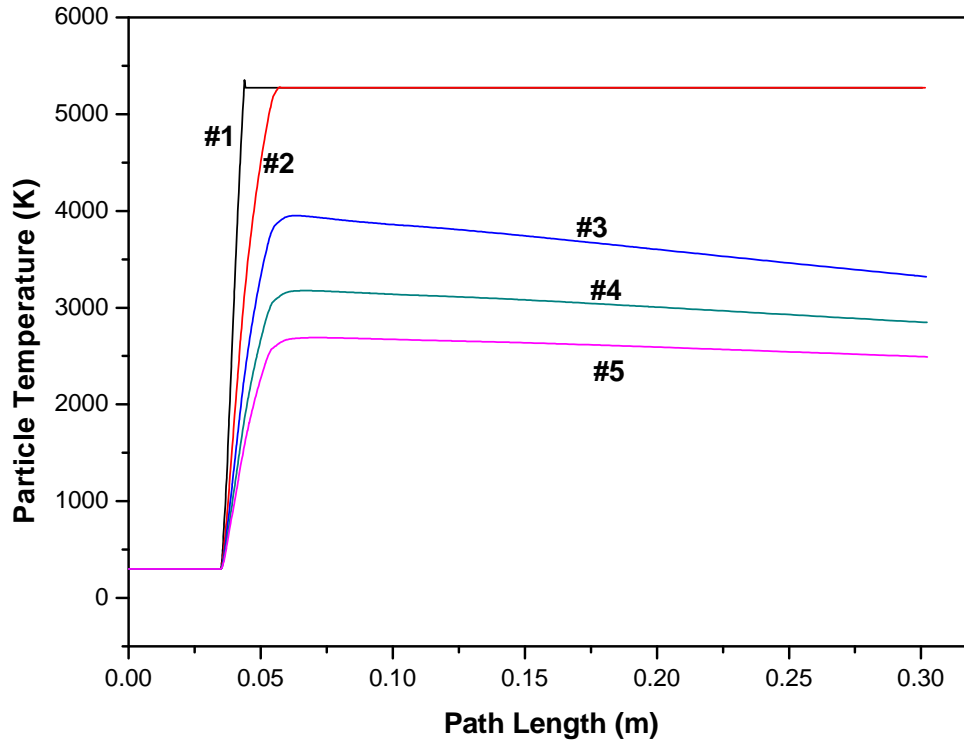


Fig. 5.17 Particles temperature profile along their trajectories. #1, $2.20\ \mu\text{m}$; #2, $4.78\ \mu\text{m}$; #3, $7.35\ \mu\text{m}$; #4, $9.95\ \mu\text{m}$; #5, $12.5\ \mu\text{m}$.

plasma flow on small particles with diameter down to several μm , vaporization and evaporation effect is deactivated to avoid their vanishing during the flight.

For each case, particles with the same diameters of $3\ \mu\text{m}$, $5\ \mu\text{m}$ and $10\ \mu\text{m}$ are injected by surface injection type respectively in freestream case and S2-C case. S2 represents the substrate 2, C represents concave orientation, thus the radius of the front face is 51 mm. All the particles are captured by the substrate, and then illustrated on the developed surface of the front face of the substrate. For the freestream case, a virtual substrate with exactly the same geometry as that in S2-C case is included to make sure the mesh conditions of these two cases are exactly the same. The virtual substrate is also used for particles capturing. Results are shown respectively in the figures from Fig. 5.19 to Fig. 5.21, it can be seen that smaller particles are more susceptible to the plasma flow deflection by the substrate obstruction. It is obvious that the diverging flow deviates the smaller particles from their freestream trajectories. For $3\ \mu\text{m}$ particles, the upward and sideways flow

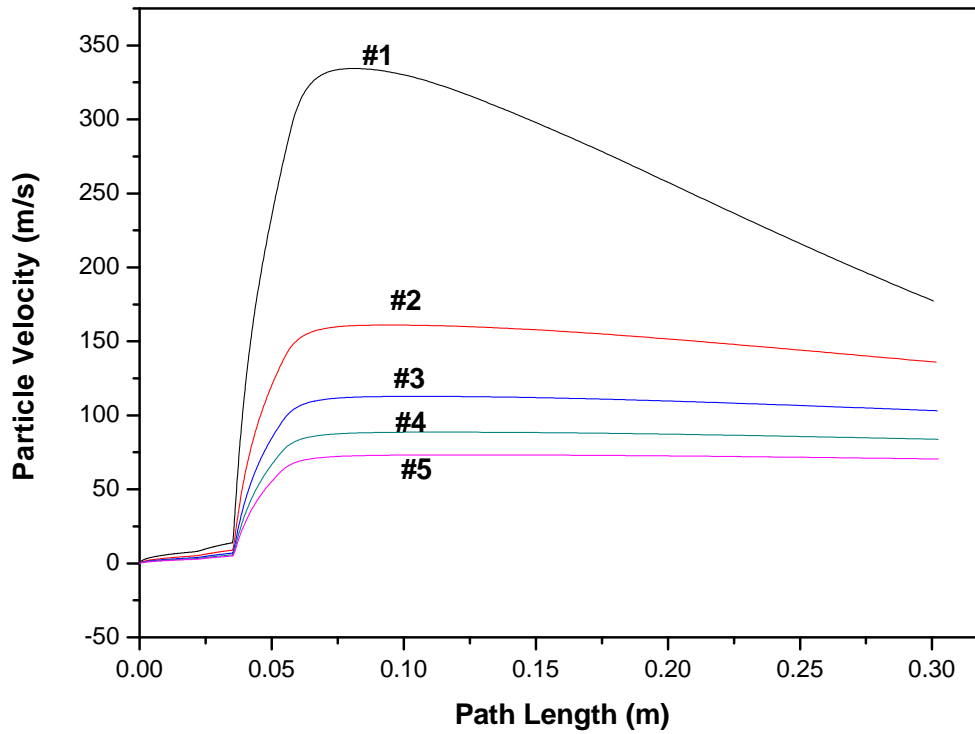


Fig. 5.18 Particles velocity profile along their trajectories. #1, $2.20\ \mu\text{m}$; #2, $4.78\ \mu\text{m}$; #3, $7.35\ \mu\text{m}$; #4, $9.95\ \mu\text{m}$; #5, $12.5\ \mu\text{m}$.

makes the distribution wider and higher than that in the freestream case; while for $5\ \mu\text{m}$ particles, the downward flow makes the distribution lower. When the particles diameter increases to $10\ \mu\text{m}$, the difference becomes insignificant.

From the study above, it can be concluded that there is a threshold of particle diameter, above which the particles are insusceptible to the flow deflection. In the combination of spray parameters (carrier gas flow rate, primary gas flow rate, energy source, injection position and method, etc.) in this work, the threshold is approximate $10\ \mu\text{m}$.

The dispersion of particles due to turbulence in the fluid phase is not taken into account in all the above work. The purpose is to investigate the effect of substrate inclusion on the particle trajectory shift. In the following work, stochastic tracking approach is used for particle dispersion prediction. The power feedstock which is the commercially available powder YSZ particles is defined for a range of diameters between 22 and $125\ \mu\text{m}$ with intervals $1\ \mu\text{m}$. These particles are injected by surface

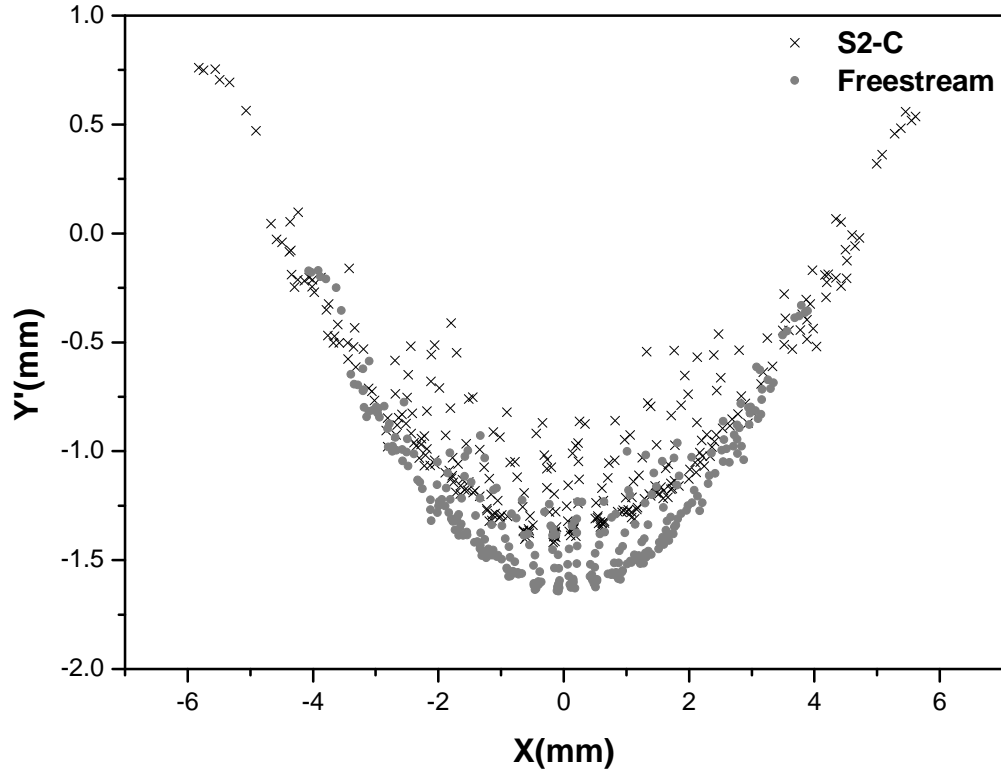


Fig. 5.19 Particle distribution comparison between freestream and S2-C with $3\ \mu\text{m}$ uniform particles injection. Y' scale is larger than the X axis for a better illustration.

injection type, and captured by the substrate. The resultant particle distribution data are post-processed by a Fortran code and then mapped onto the developed surface of the substrate in a contour form.

Fig. 5.22 shows the contour distributions of particles in terms of diameter, number of particles, temperature and velocity on the developed surface of the substrate in S2-C case, shown in the left column; while freestream case is compared, in the right column. No significant effect of the substrate on the dispersion of particles is observed. The result also confirms the conclusion above, despite of the consideration of particle dispersion. In addition, it is noticed that larger particles tend to accumulate at the lower part of the substrate, with lower velocity and temperature. However, it is noted that contour of the number of particles have a different contour shape (concentric circles) with those of the other parameters (temperature, velocity, diameter). By superimposing subfigure (a) and (f) together, it is found that the particles with the medium diameters have the highest concentration.

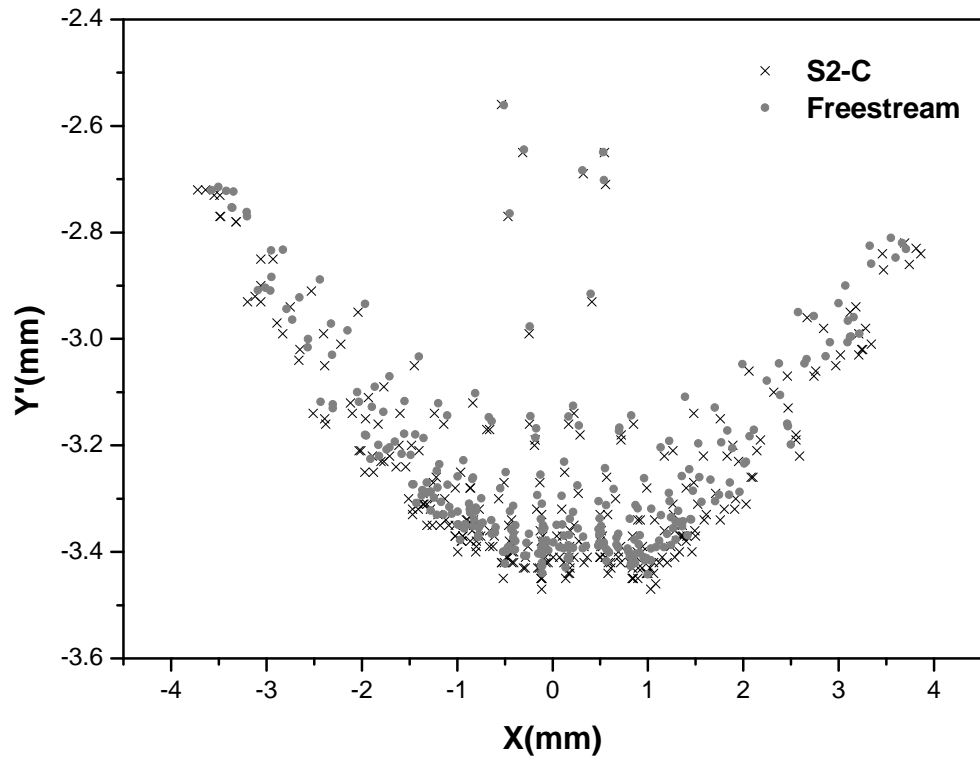


Fig. 5.20 Particle distribution comparison between freestream and S2-C with 5 μm uniform particles injection. Y' scale is larger than the X axis for a better illustration.

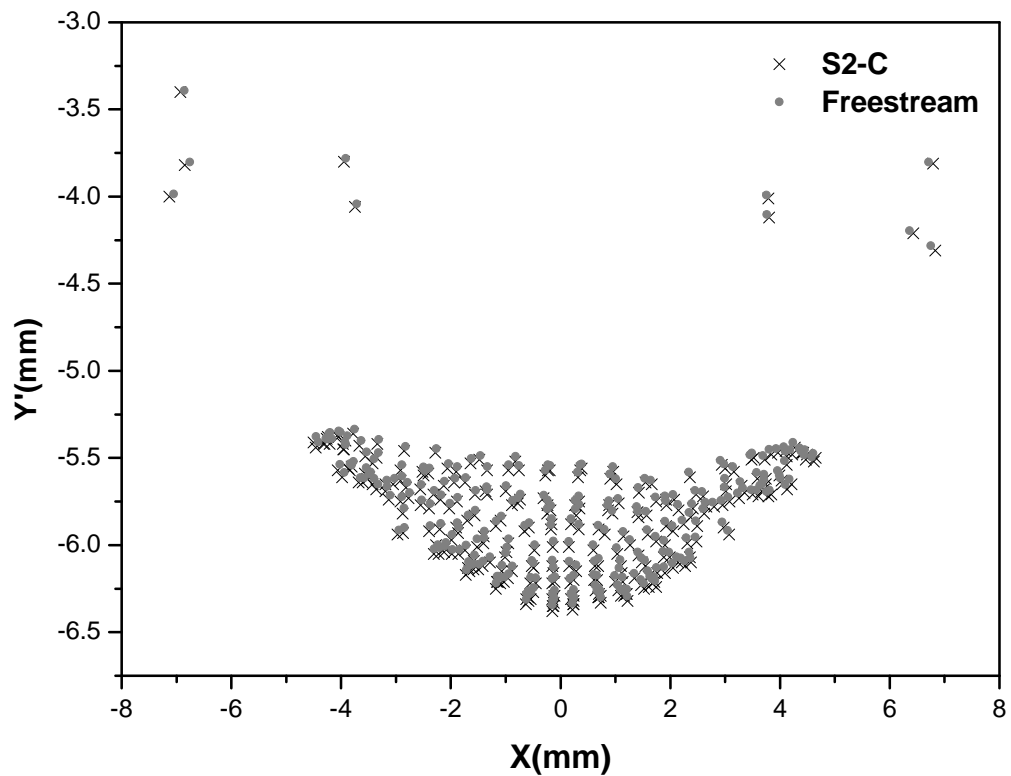


Fig. 5.21 Particle distribution comparison between freestream and S2-C with 10 μm uniform particles injection. Y' scale is larger than the X axis for a better illustration.

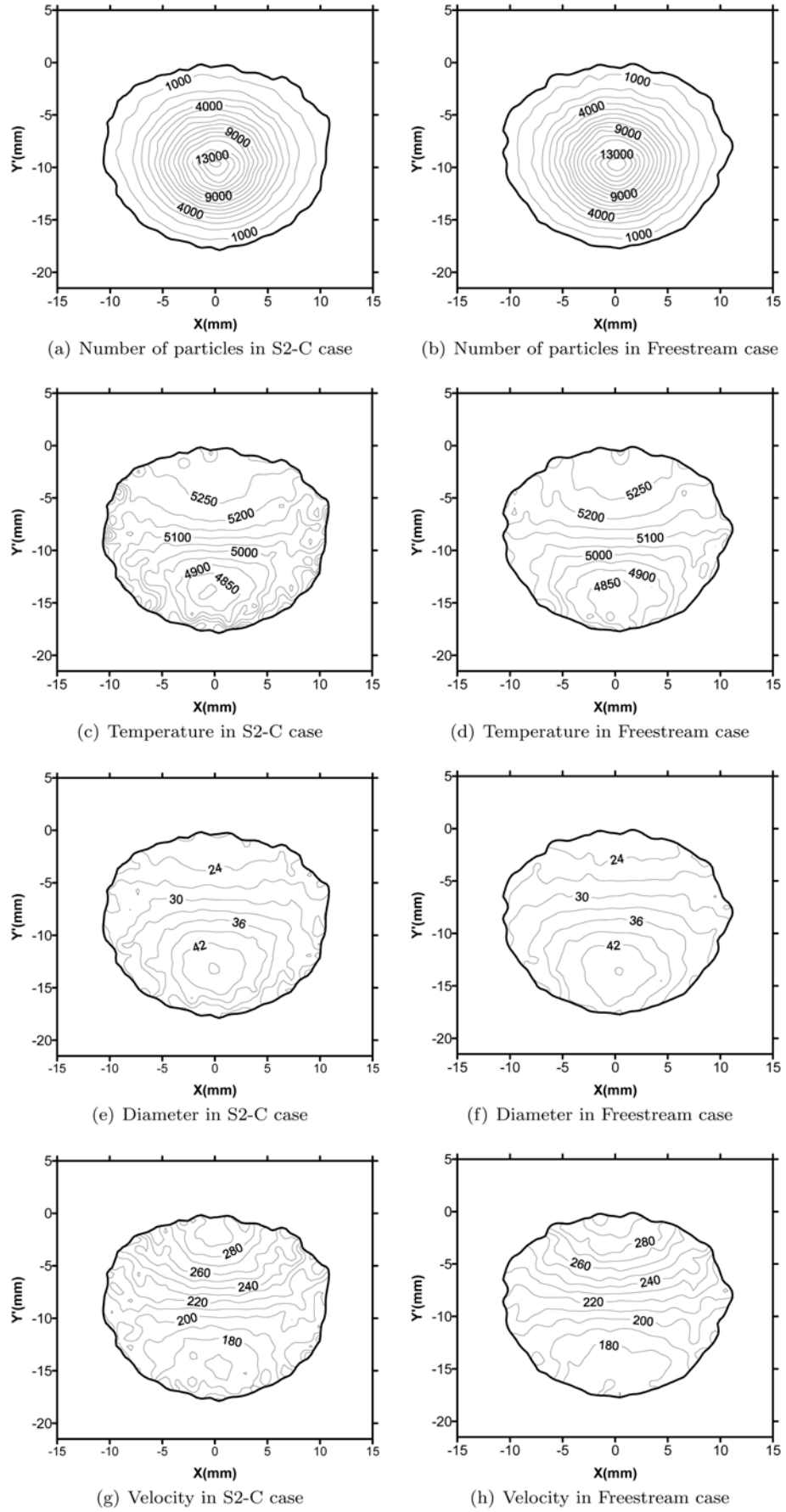


Fig. 5.22 Comparison of contours of particle in-flight parameters; results from the S2-C case is illustrated in the left column, while the corresponding freestream case in the right column.

Fig. 5.23 shows particle temperature distribution histogram and probability plot, which is obtained from the particles dispersion data of S2-C. Most of the particles range between the melting point of 2988 K and boiling point of 5273 K for zirconia, implying the majority of particles would have either melted or vaporized, which is the expected result for plasma spray coating. **Fig. 5.24** shows the particle temperature distribution over different particle sizes. Black points form a trend-line of mean particle temperatures within the entire particle size range. Smaller particles tend to acquire higher temperature comparing with their larger counterparts, which supports the result from **Fig. 5.17** and **Fig. 5.22**. This phenomenon is attributed to the relationship between heat transfer and temperature variation. The convective heat transfer equals the energy increase of the particle, $Q_c = W_p$, i.e.,

$$m_p C_p \Delta T_p = h A_p (T_l - T_p) \quad (5.1)$$

where Q_c and W_p are the convective heat transfer between plasma and particle and the energy increase of the particle respectively. T_l and T_p are respectively the temperature of plasma and particle, ΔT_p is the temperature change of the particle, $\Delta T_p = T_p - T_i$, where T_i is the initial particle temperature. By substituting the expressions of mass of the particle $m_p = \frac{1}{6} \pi \rho_p D_p^3$, and the surface area $A_p = \pi D_p^2$, an equation of the particle temperature variance is derived:

$$\Delta T_p = \frac{6h}{\rho_p D_p + 6h} (T_l - T_i) \quad (5.2)$$

Therefore, the smaller particles have the tendency to acquire higher temperature change. In other words, the smaller particles experience heat transfer per volume due to their larger ratio of surface area to the volume.

In **Fig. 5.24**, grey color scattered points represent each individual particle. The uppermost particles aligned to be in a nearly straight line, where the temperature reaches the boiling point and never goes up further. It is noted that some of the particles with relatively small sizes have lower temperature. This phenomenon may be understood by the following way: the small particles have lower initial momentum when they flush into the nozzle; therefore, they are unable to penetrate into the jet core, where the highest plasma temperature exists. In addition, the

smaller particles cool down faster at the lower temperature regions of the plasma plume.

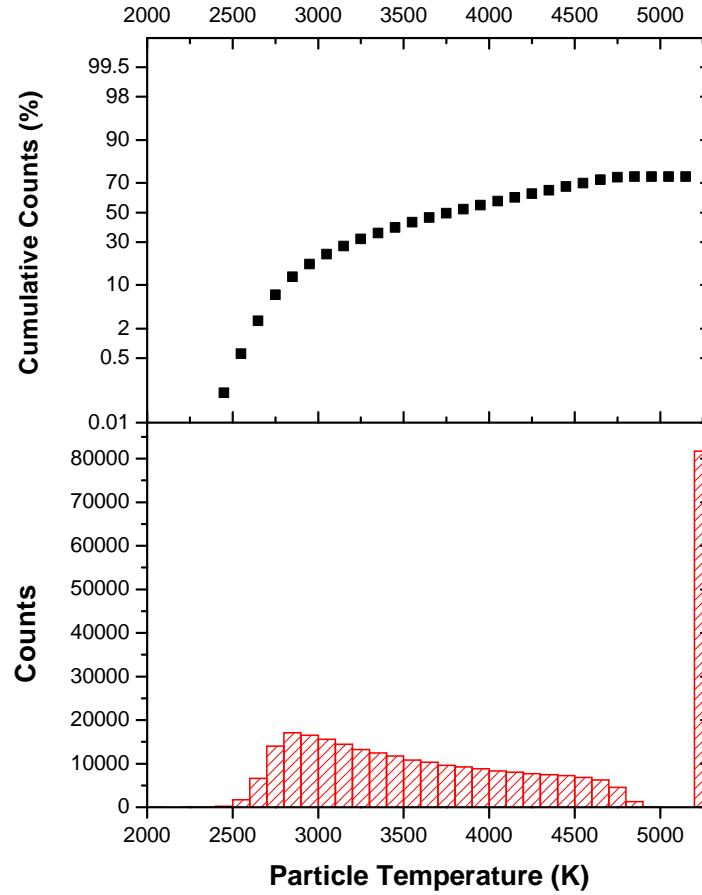


Fig. 5.23 Particle temperature distribution histogram (lower figure) and probability plot (upper figure) in S2-C case.

In this particle heat transport model, it is assumed that the Biot number is low ($\ll 1.0$), which means the particles have a nearly infinite thermal conduction. The instantaneous heat flow from the surface to the center of the particles gives it the uniform particle temperature. This assumption is more suitable for metallic particles, which have much larger thermal conduction than Zirconia.

Zirconia particles have poor heat conducting materials, which will result in a significant difference between the surface temperature and the internal temperature. In some cases, even when the surface temperature reaches the boiling point, its center may still be in solid state[58]. So particles will start evaporate

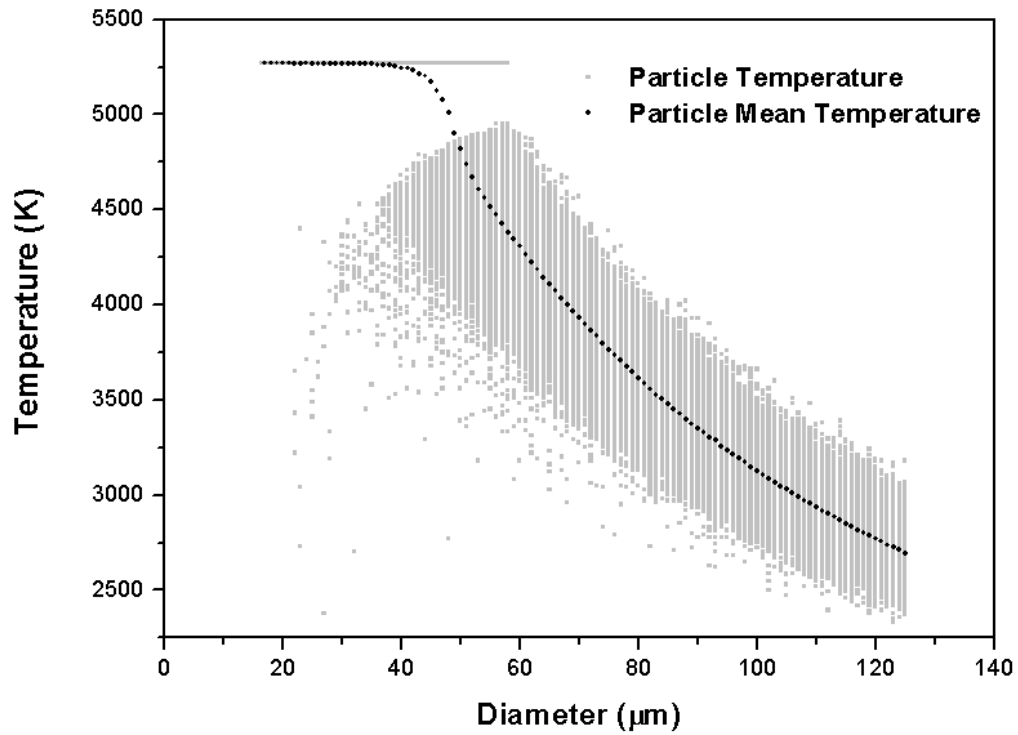


Fig. 5.24 Particle temperature and mean temperature distribution versus diameter.

earlier than the simulation data, which results in a more severe mass losses. So the distribution of particles diameter will drift towards the smaller value, which further makes the particles more susceptible to the flow change by the substrate. However, even though the internal conduction is considered, the conclusion that the substrate inclusion has insignificant effect on the particle in-flight parameters should also be valid. It is because of the small portion of the smaller particles and the relatively large initial size range ($22\ \mu\text{m}$ to $125\ \mu\text{m}$). Furthermore, the mass losses due to the evaporation, together with the particle rebound and overspray at substrate may be the dominant reasons for the rather low deposition efficiency ($\approx 40\%$)[29] in the actual spraying process using the same operating conditions.

5.2.7 Comparison between SprayWatch© diagnostics and the simulation

SprayWatch© diagnostics results are compared with the simulation results. Because the measurement distance by SprayWatch© is 80 mm, a virtual plane is created in front of the plasma torch to acquire the particles data in the Freestream model, at the stand-off position 80 mm. The velocity magnitude distribution (**Fig. 5.25**) and particle flight angle distribution (**Fig. 5.26**) are compared with the SprayWatch© results.

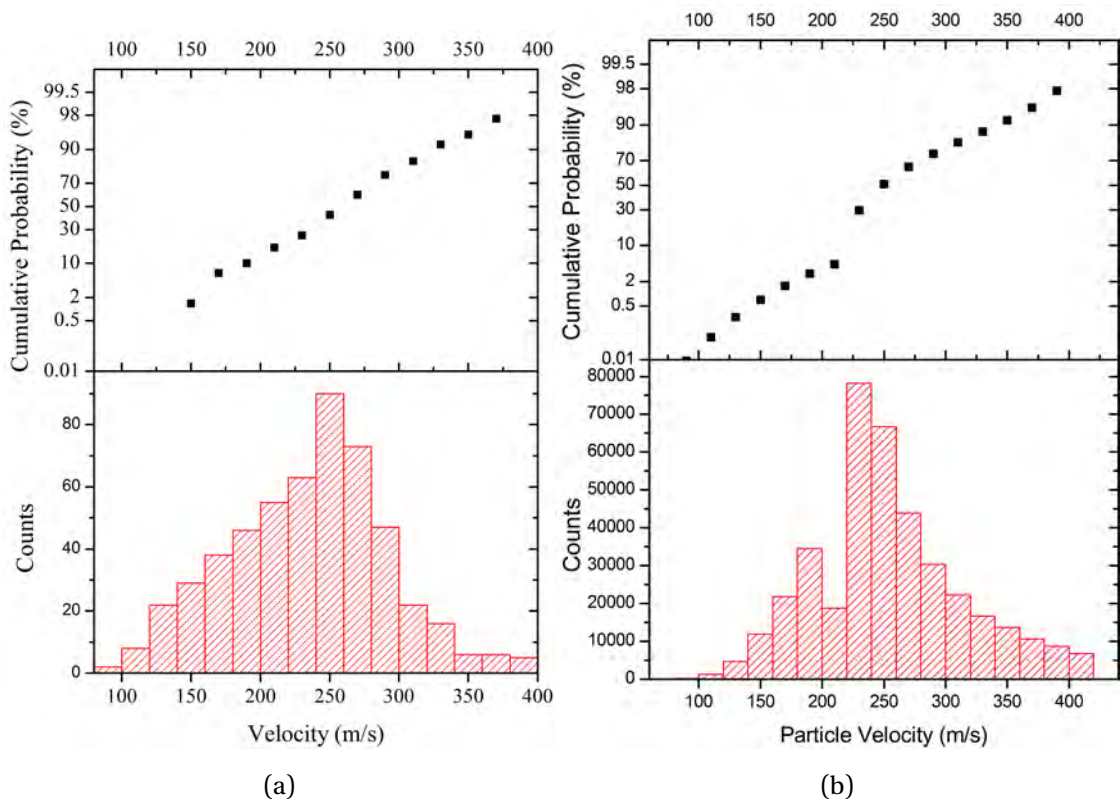


Fig. 5.25 Particle velocity magnitude distribution histogram and probability plot from (a) SprayWatch© diagnostics and (b) simulation.

The simulation predicts well the range of particle velocities and distributions. The velocity ranges from 70.9 m/s to 431.6 m/s in the simulation, while the velocity from SprayWatch© ranges from 83.3 m/s to 396.5 m/s. The simulation results are skewed to a lower velocity than their experimental counterparts, but generally present similar distribution shape.

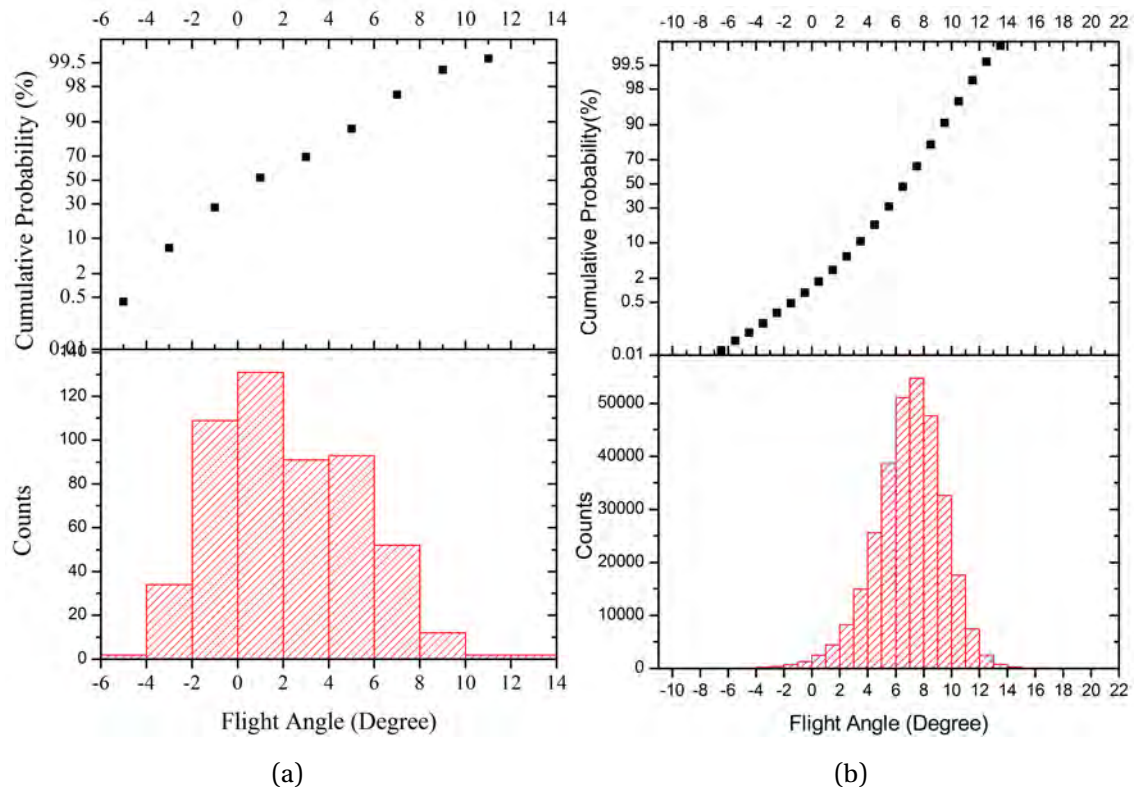


Fig. 5.26 Particle velocity magnitude distribution histogram and probability plot from (a) SprayWatch© diagnostics and (b) simulation.

From SprayWatch© results, most of the particles are in the range of -2° and 10° . The simulation histogram agrees well with the experiment, but with very few particles scattered with larger flight angles.

5.3 Droplet Impact Behavior and Splat Morphologies

This section discusses the droplet impact behavior under thermal spray conditions. It is mainly from the experiments and simulations on the flat substrate case under normal impact and on the curved substrate. Splat morphologies are analyzed to derive the splat shape in the space, which will further become the basis for the deposit formation simulation.

5.3.1 Geometric quantities definition

Several quantities are introduced in this work to characterize the geometry of the splats. A droplet with diameter D impacting on the substrate forms a disk-shape splat with a thickness t , as in Fig. 5.27.

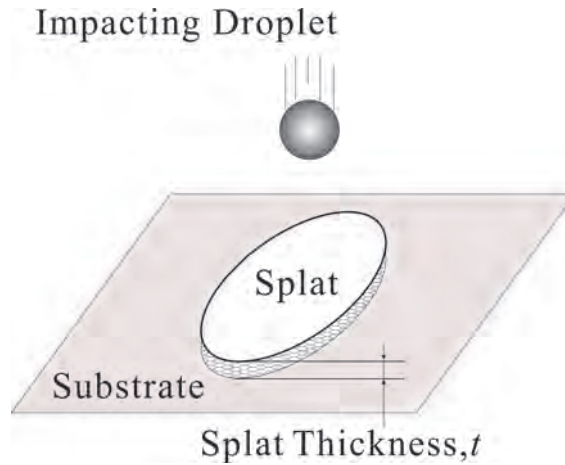


Fig. 5.27 Illustration of a molten droplet impacting on the substrate to form a disk-shape splat.

The thickness of the splat is denoted as t . In a simplified mode, the thickness is assumed to be uniform. Therefore, the thickness t can be deduced from the volume V_s and the area A_s of the splat.

$$t = \frac{V_s}{A_s} \quad (5.3)$$

In the case of normal impact, the cross section along the thickness direction of the splat takes a circular shape. Besides the thickness t , the diameter d is employed to describe the shape of the splat. The extent of the droplet flattening is described by

the spread factor ξ , defined as the ratio of the splat diameter d to the initial droplet diameter D .

$$\xi = \frac{d}{D} \quad (5.4)$$

If during the droplet impacting, the volume of the droplet remains unchanged, the volume of the droplet is the same as the volume of the splat V_s . Thus the initial droplet diameter can be derived as

$$D = \sqrt[3]{\frac{6V_s}{\pi}} \quad (5.5)$$

Since the splat diameter d can be derived from the splat area A as

$$d = 2\sqrt{\frac{A_s}{\pi}} \quad (5.6)$$

the spread factor can be expressed as

$$\xi = \frac{0.91\sqrt{A_s}}{\sqrt[3]{V_s}} \quad (5.7)$$

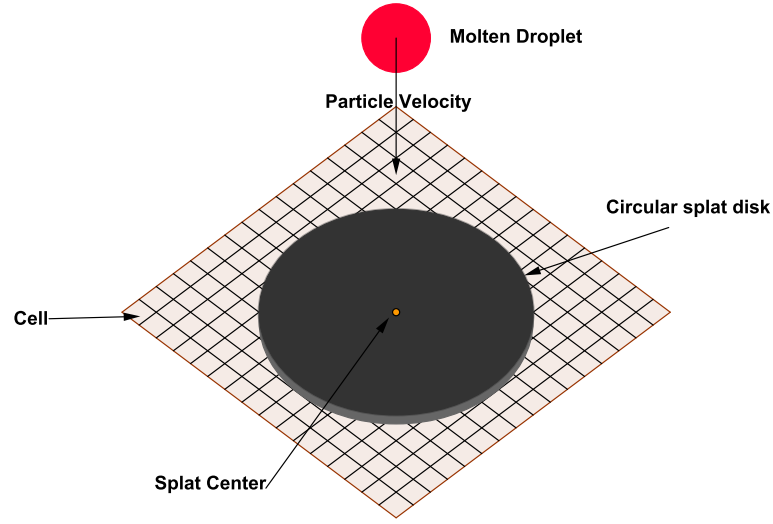
where V_s and A_s are the volume and area of the splat respectively.

Under normal impact, the splat approximates a circular disk with the diameter d . If the droplet impacts onto the surface obliquely, which is termed as “oblique impact”, resulting splat shape will elongates to an elliptical disk, as shown in **Fig. 5.28**.

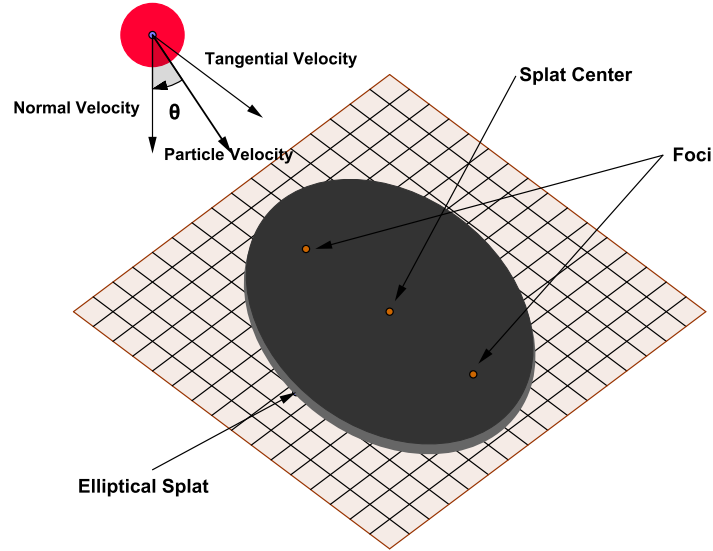
Impact angle θ is defined as the angle between the droplet velocity vector and its normal velocity (component perpendicular to the substrate surface). Under oblique impact, the diameter d is no longer appropriate to describe the splat shape. The major radius a and minor radius b are introduced to achieve this purpose, as shown in **Fig. 5.29**.

To describe the elongation degree of an elliptical splat, another shape factor, aspect ratio ζ is introduced, which is defined as the ratio between the major and minor radius

$$\zeta = \frac{a}{b} \quad (5.8)$$



(a) normal impact



(b) oblique impact

Fig. 5.28 Perfect formation of (a) a circular splat from normal impact and (b) an elliptical splat from oblique impact.

By such a definition, an elliptical splat can be converted mathematically into a circular splat with the same area. This circular splat with the same area is called an “equivalent splat”, the diameter of which is “equivalent diameter”.

Take the equivalent diameter d as an intermediate quantity, combining with the spread factor ξ and aspect ratio ζ , the splat morphology at different impact angles can be described.

The equivalent diameter of the splat can be expressed by the initial droplet diameter D and spread factor ξ :

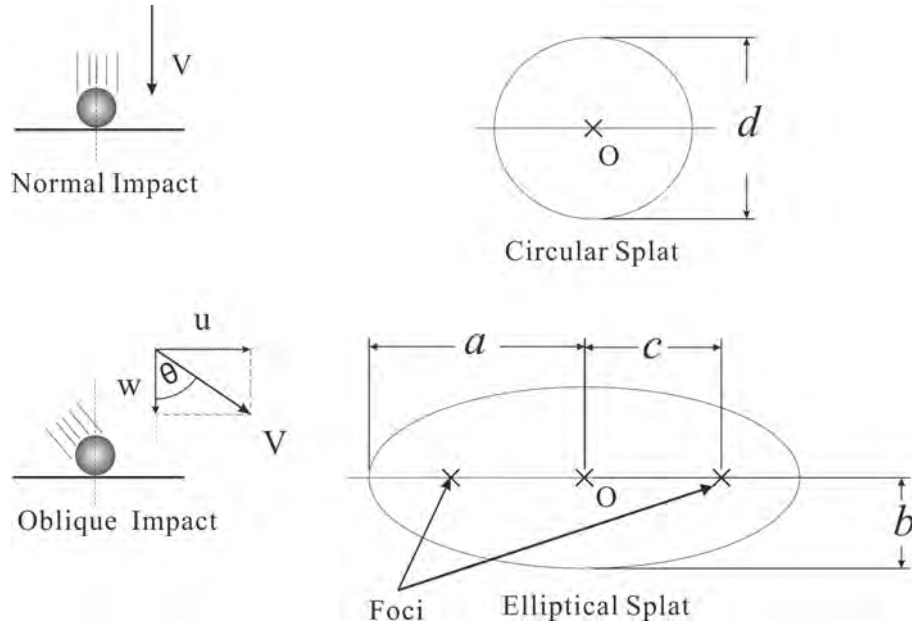


Fig. 5.29 Idealized illustration of the aerial view of the splat for the case of normal impact and oblique impact.

$$d = D\xi \quad (5.9)$$

In the case of normal impact, the equivalent diameter d is the geometry diameter of the splat; in the case of oblique impact, the major radius a and minor radius b can be derived by the area conservation method:

Area of circle = Area of ellipse

$$\frac{\pi d^2}{4} = \pi ab$$

Combining with **Equation 5.8**, the major and minor radius can be derived as:

$$a = \frac{d\zeta}{2} \quad (5.10)$$

$$b = \frac{d}{2\zeta} \quad (5.11)$$

5.3.2 Effect of impact parameters on the droplet impact behavior

5.3.2.1 Characterization of individual splats from confocal profiles on flat substrates.

A method is developed to derive the spread factor from the profiles acquired by confocal imaging profiler. Image maps and 3D shaded rendering images are

constructed by Surfer 8® (Golden Software, Inc., Golden, Colorado, USA) from the ascii data of the profile. Examples of the images are shown in **Fig. 5.30**. Surfer® is a 3D processing software used for terrain modeling, surface analysis, contour mapping, 3D surface mapping, volumetrics, and much more purposes.

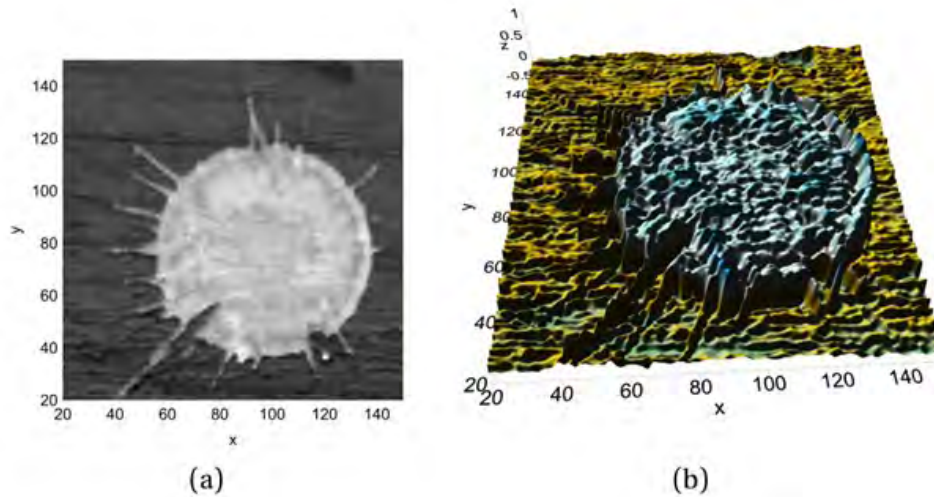


Fig. 5.30 (a) Image maps and (b) 3D shaded rendering images constructed from the profile data acquired by confocal imaging profiler.

The image map of the splat (a) is postprocessed by Image-Pro Plus 6® (Corporate Headquarters, Media Cybernetics, Inc., MD, USA). Image-Pro Plus is an image processing and analysis software, which is always deployed in the computer of a microscope system. Dimension analysis is a fundamental function of this software. In Image-Pro Plus, a boundary is defined carefully by tracing the points along the periphery of the splat. The encompassed area A is evaluated, with fingers characteristics included to obtain an accurate area measurement. The Surfer® calculation function is employed to evaluate the splat volume. A base surface elevation is evaluated by choosing an area with no splat material covered. By defining this elevation as lower surface, the splat volume V_s is evaluated by integration method.

5.3.2.2 Evolution of droplet morphology during impact

The evolution of droplet morphology during impacting for case 3 is shown in **Fig. 5.31**, which is colored by the variable “solid fraction”. The figures are adjusted in a perspective view to observe the morphology evolution more clearly.

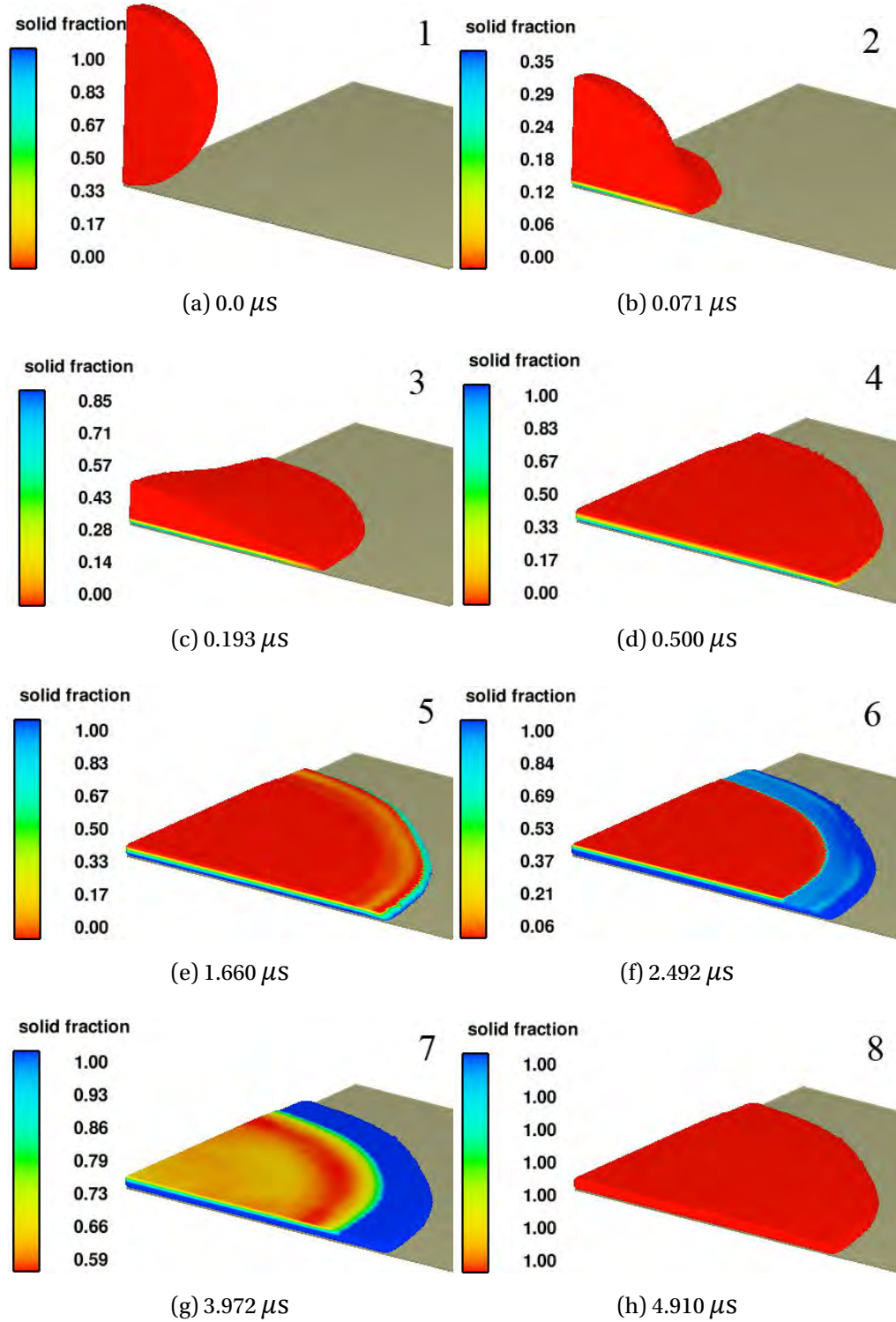


Fig. 5.31 Evolution of droplet morphology during its impact perpendicularly onto the substrate. The contour is based on the value of Volume of Fluid.

It is noticed that the droplet experiences a drastic change of state. The droplet flattens within a short time (approx. 0.500 μs as in Fig. 5.31(d)). Before the droplet flattening ceases, solidification occurs in the fluid layer close to the substrate surface and spreads upward to form a solidified layer. This characteristics is named as the “two-layer characteristic” in this work. After the droplet achieves the maximum

flattening extent, the fringe of the splat starts to solidify, while the remaining fluid on top of the solidified layer continues to expand outward, as in **Fig. 5.31(e)**. This fluid accumulates at the fringe and elevates the fringe to a higher level than the interior of the splats, presenting a “pizza-like” morphology. The corresponding center surface of the splat at the same time frames are shown in **Fig. 5.32**. The contour is colored by the VOF value F . The z-axis is scaled up by 5 times, in order to see the characteristics more clearly. The raised fringe characteristic is more clearly shown in these cross section view of the splats which is also seen in the constructed images from confocal image profiler data as in **Fig. 5.30**. The solidification expands to the interior (**Fig. 5.31(f) and (g)**) and finishes approx. $4.9 \mu\text{s}$ after the moment of impact (**Fig. 5.31(h)**).

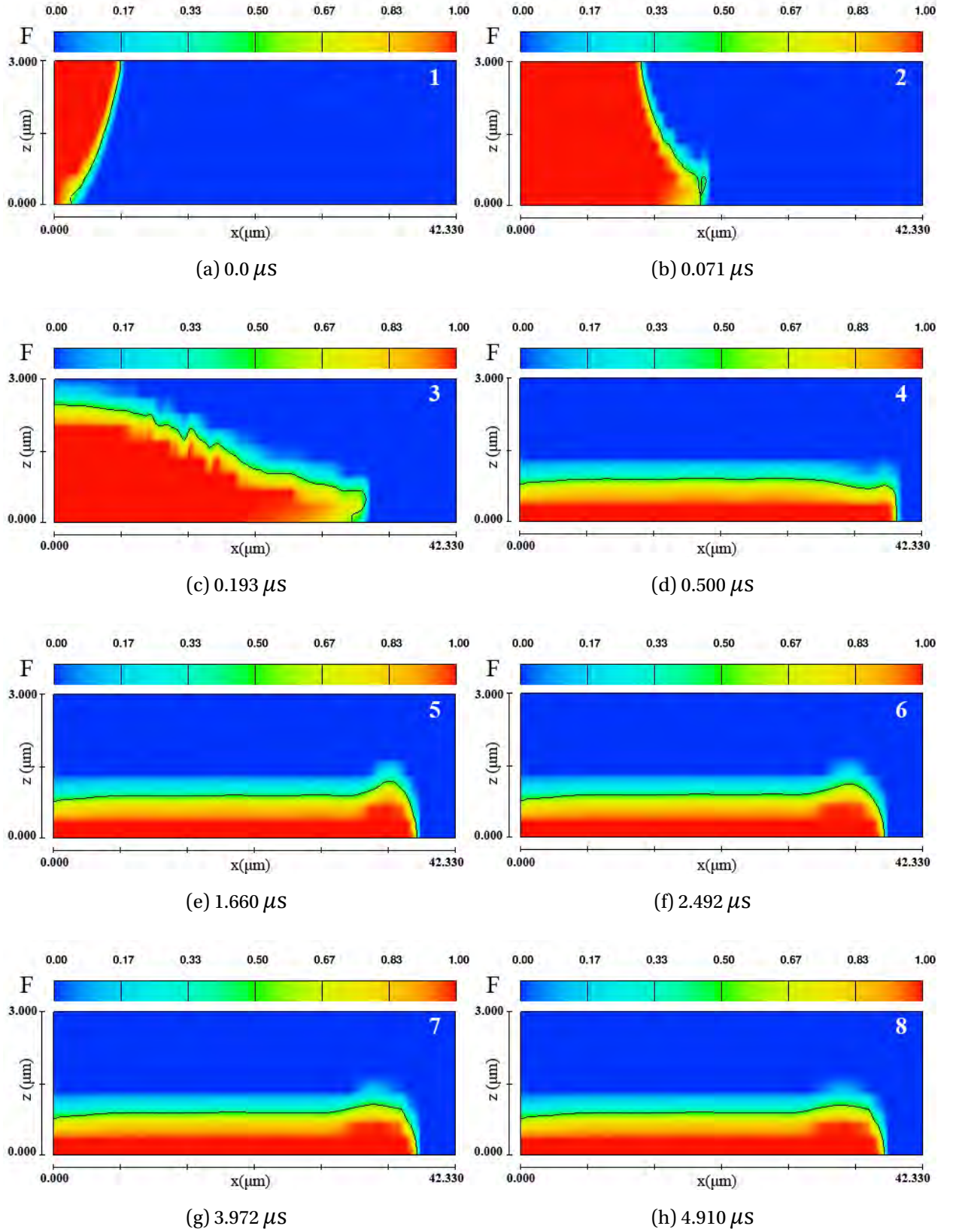


Fig. 5.32 Evolution of droplet morphology at the center surface during its impact perpendicularly onto the substrate. The contour is based on the value of Volume of Fluid.

5.3.2.3 Effects of thermal parameters on splatting behavior

At the fixed velocity 200 m/s, different cases with different other parameters are carried out to investigate their effects on the splatting behavior. A sub-table of **Table 4.6** is extracted as **Table 5.1**, including cases 1,8-12 and 15:

Table 5.1 Simulation cases implemented for the normal impact with fixed velocity 200 m/s.

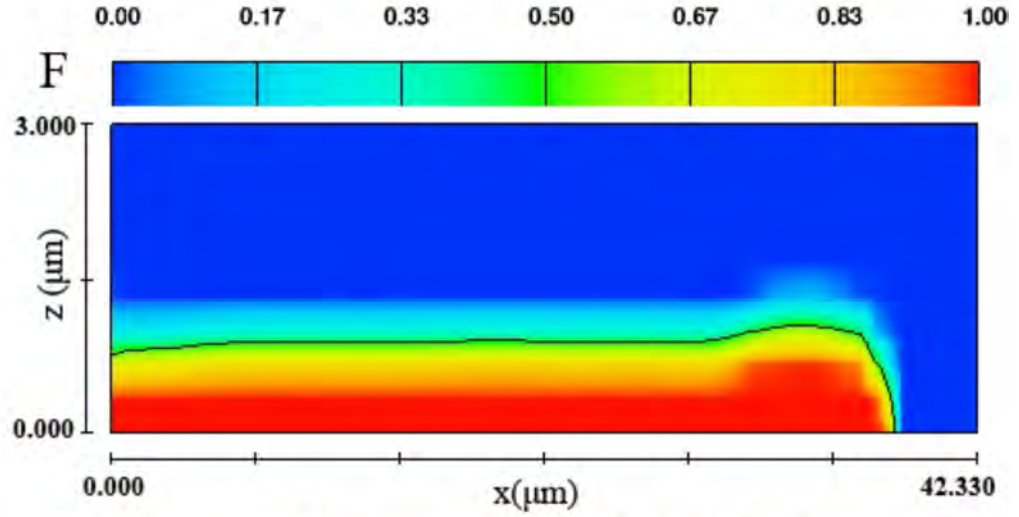
Case	T (K)	h (W/m ² K)	T_s (K)
1	3200	1×10^6	823
8	3500	2×10^5	823
9	3500	1×10^6	300
10	3500	1×10^6	823
11	3500	1×10^6	1573
12	3500	1×10^7	823
15	3800	1×10^6	823

Case 1, 10 and 15 have the same substrate temperature (823K) and the same heat transfer coefficient (1×10^6 W/m²K). The cross-section view of the splat at the center surface for these cases are shown in **Fig. 5.33**. It is found that the temperature increase ((a) 3200 K→(b) 3500 K→(c) 3800 K) makes the fringe elevation characteristic more obvious, which means that the higher temperature promotes the fringe elevation. It could be attributed to the more-pronounced delayed solidification of the fluid on top of the solid layer, which results more fluid accumulation at the fringe of the splat. It is also noticed that the droplet temperature does not affect the droplet flattening degree, which will be explained later in the summary part of this section.

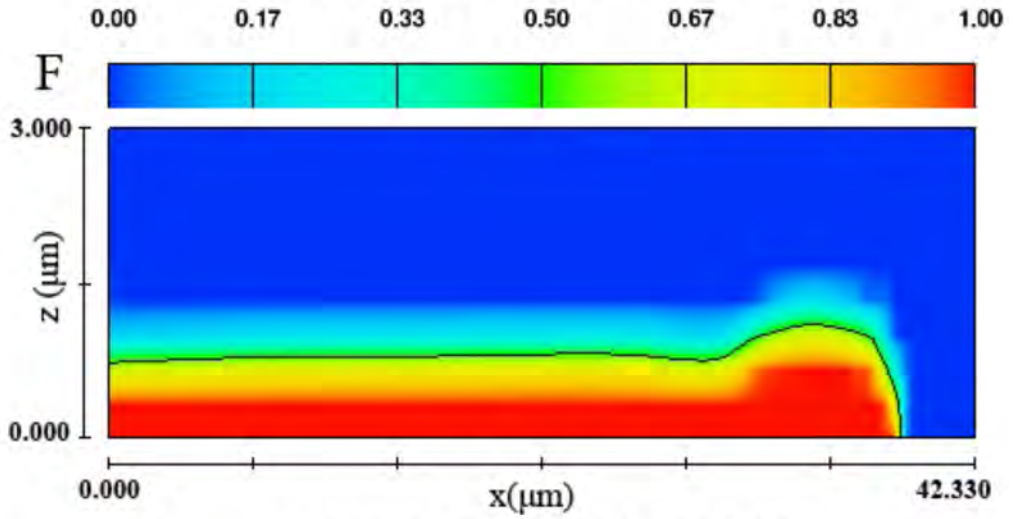
At the fixed temperature 3500 K and the substrate temperature 823 K (case 8, 10, 12), the lower heat transfer coefficient (2×10^5 W/m²K) results in a more pronounced fringe elevation, as in **Fig. 5.34(a)**. By observing the evolution procedure of the cross section of the splat (**Fig. 5.35**), it could be noticed that the droplet experiences a recoil procedure after the splat achieves its maximum spread. This is possibly caused by the surface tension effects, since the splat remains fluid state for a long time due to the slow heat transfer to the substrate. It is also the reason for the

larger fringe elevation. The higher heat transfer coefficient ($10^7 \text{W/m}^2\text{K}$) results in a faster solidification, which inhibits the recoil tendency and the fringe elevation, as noticed in **Fig. 5.34(a)-(c)**. Therefore, it is concluded that the higher the droplet temperature, or the lower the heat transfer coefficient both promotes the splat fringe elevation and the splat recoil.

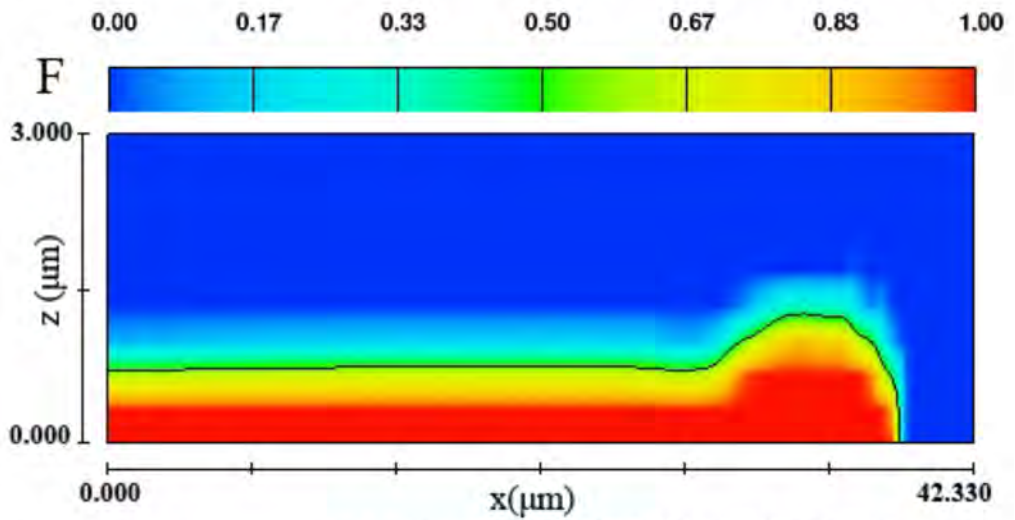
Because the substrate temperature 823 K in the simulation is just the approximate mean value of the averaged values at the measurement points of the substrate, it is believed that some areas of the substrate have higher temperature. In contrast to case 10, case 9 has a lower substrate temperature 300 K and case 11 has a higher one 1573 K. The resulting cross section of the splat of case 9-11 is shown in **Fig. 5.36**. It can be seen that the splat fringe elevation is more evident when the substrate temperature is at higher level. Combining the results of all these cases relevant to thermal parameters, it could be concluded that these parameters will affect the fringe elevation and recoil procedure after the splat achieves its maximum spread, by the surface tension effects.



(a) case 1, $T=3200\text{K}$, $t=4.91 \mu\text{s}$

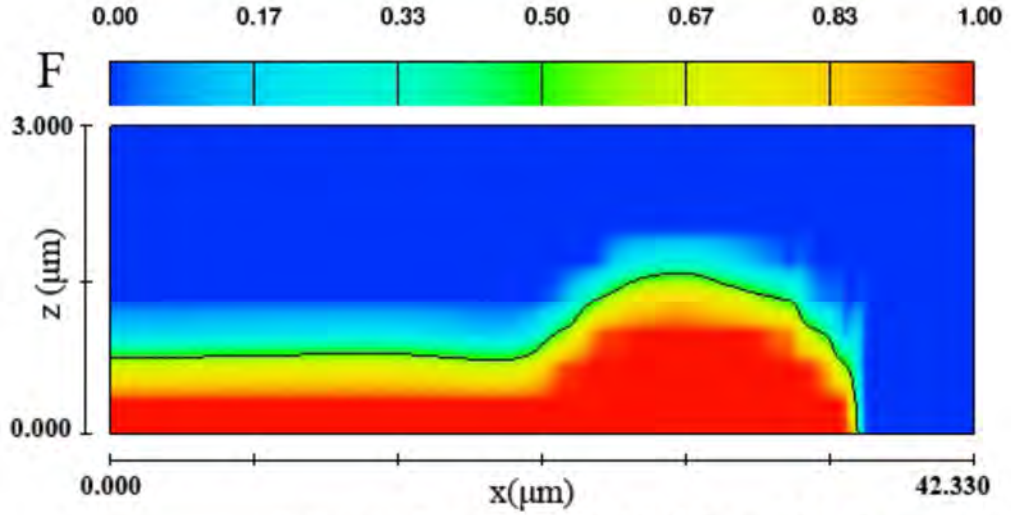


(b) case 10, $T=3500\text{K}$, $t=5.91 \mu\text{s}$

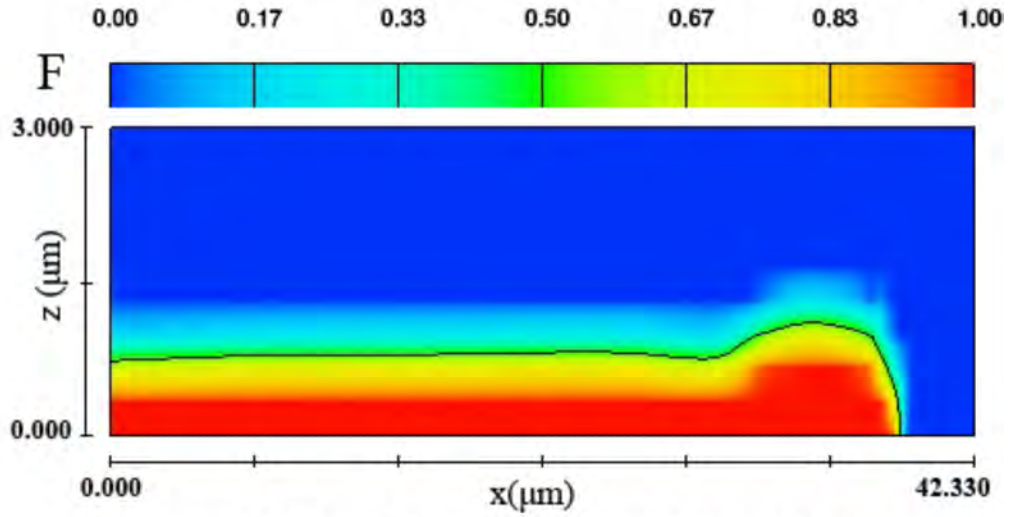


(c) case 15, $T=3800\text{K}$, $t=8.22 \mu\text{s}$

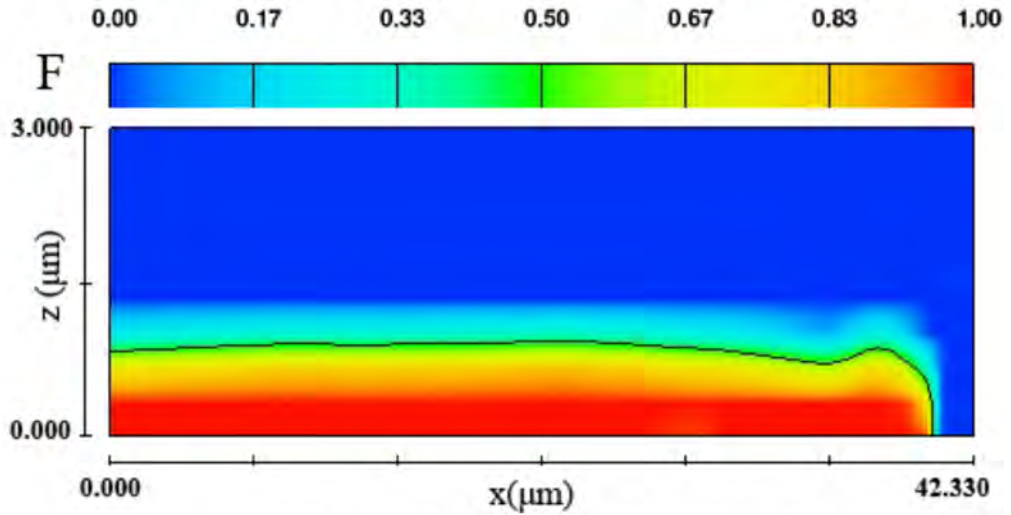
Fig. 5.33 Cross section view of a splat at the center surface, showing different extents of fringe elevation under different droplet temperature. The contour is based on the value of Volume of Fluid.



(a) case 8, $h=2 \times 10^5 \text{ W/m}^2\text{K}$, $t=27.10 \mu\text{s}$



(b) case 10, $h=1 \times 10^6 \text{ W/m}^2\text{K}$, $t=5.91 \mu\text{s}$



(c) case 12, $h=1 \times 10^7 \text{ W/m}^2\text{K}$, $t=2.00 \mu\text{s}$

Fig. 5.34 Cross section view of a splat at the center surface, showing different extents of fringe elevation under different heat transfer coefficient. The contour is based on the value of Volume of Fluid.

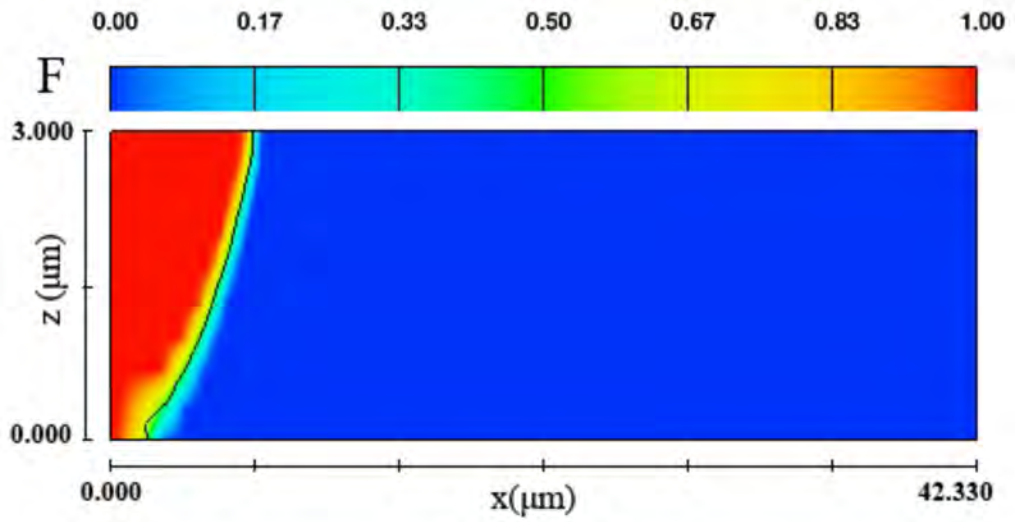
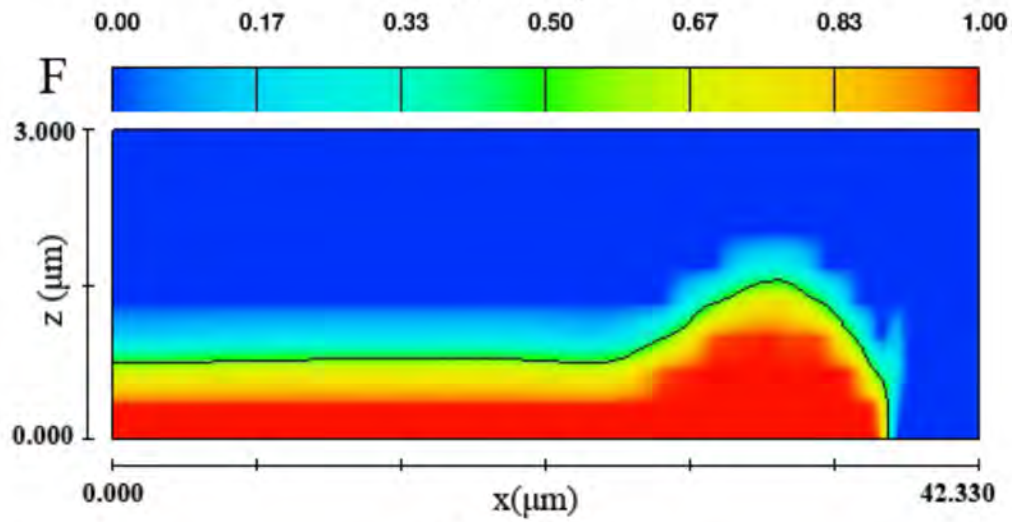
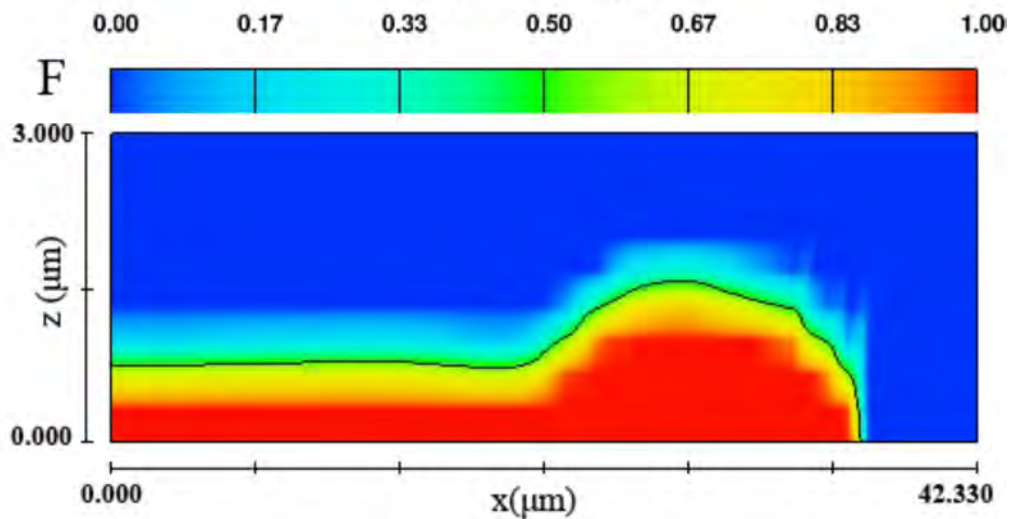
(a) $t = 0 \mu s$ (b) $t = 6.93 \mu s$ (c) $t = 27.10 \mu s$

Fig. 5.35 Cross section view of a splat at the center surface at different time frame, under a low heat transfer coefficient $2 \times 10^5 \text{ W/m}^2\text{K}$. The contour is based on the value of Volume of Fluid.

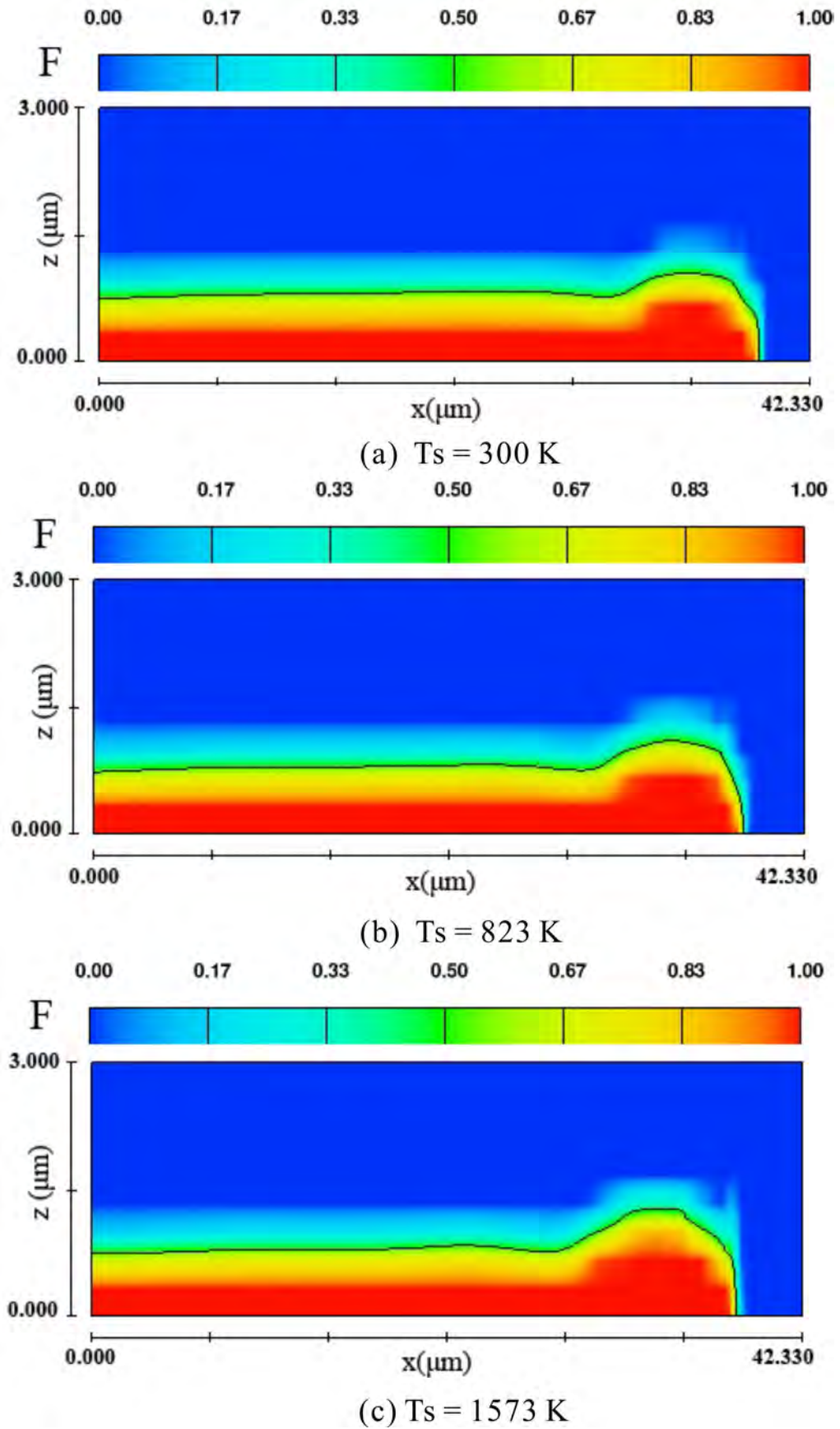


Fig. 5.36 Cross section view of a splat at the center surface, showing different extents of fringe elevation for different substrate surface temperature. The contour is based on the value of Volume of Fluid.

5.3.2.4 Effect of droplet velocity

The droplet velocity is varied to see its influence on the splat morphology. The velocity is set as 50 m/s (case 4), 80 m/s (case 5), 100 m/s (case 6) 120 m/s (case 7), 200 m/s (case 10), 300 m/s (case 13) and 400 m/s (case 14). These cases are shown in **Table 5.2**. From the analysis above, it is noticed that the difference between case 10 (10^6 W/m²K) and case 12 (10^7 W/m²K) is not significant. Therefore, in this section the heat transfer coefficient is fixed at 10^6 W/m²K, the droplet temperature at 3500 K, the substrate temperature at 823 K. The cross section of the splat bottom surface is shown in **Fig. 5.37**. For the convenience of forming, the case with velocity 100 m/s is not shown, but it is still involved in the spread factor calculation. It is noticed that the droplet spread degree increases with the velocity. At high velocity, splashing characteristic such as fingers appear to be obvious. By using Image-Pro Plus®, the radius of the splat is evaluated. Thus the splat spread factor ξ can be derived, the comparison of which are discussed in the next section, together with the experimental evaluations.

Table 5.2 Simulation cases implemented for the normal impact with fixed interface heat transfer coefficient 10^6 W/m²K, droplet temperature 3500 K, substrate temperature 823 K.

Case	4	5	6	7	10	13	14
V(m/s)	50	80	100	120	200	300	400

Another group of simulation is carried out, featuring different substrate temperature, droplet temperature and interface heat transfer coefficient, with high impact velocity 400 m/s to see the droplet splatting behavior under such extreme condition. Impact parameters of simulated cases are shown in **Table 5.3**.

The cross section of the bottom surface of the splat is shown in **Fig. 5.38**. All the cases give almost the same splat size, but different splat morphology. The cases (**Fig. 5.38(c)** and **Fig. 5.38(d)**) with higher droplet temperature 3800 K present the morphology characteristic of jetting-out fluid (fingers). The substrate temperature increase does not promote the jetting behavior. At higher droplet substrate temperature, a higher interface heat transfer coefficient makes the jetting

characteristic more evident. The jet diameter is larger for the case 17 (10^7 W/m²K, **Fig. 5.38(c)**) than that in case 16 (10^6 W/m²K, **Fig. 5.38(d)**).

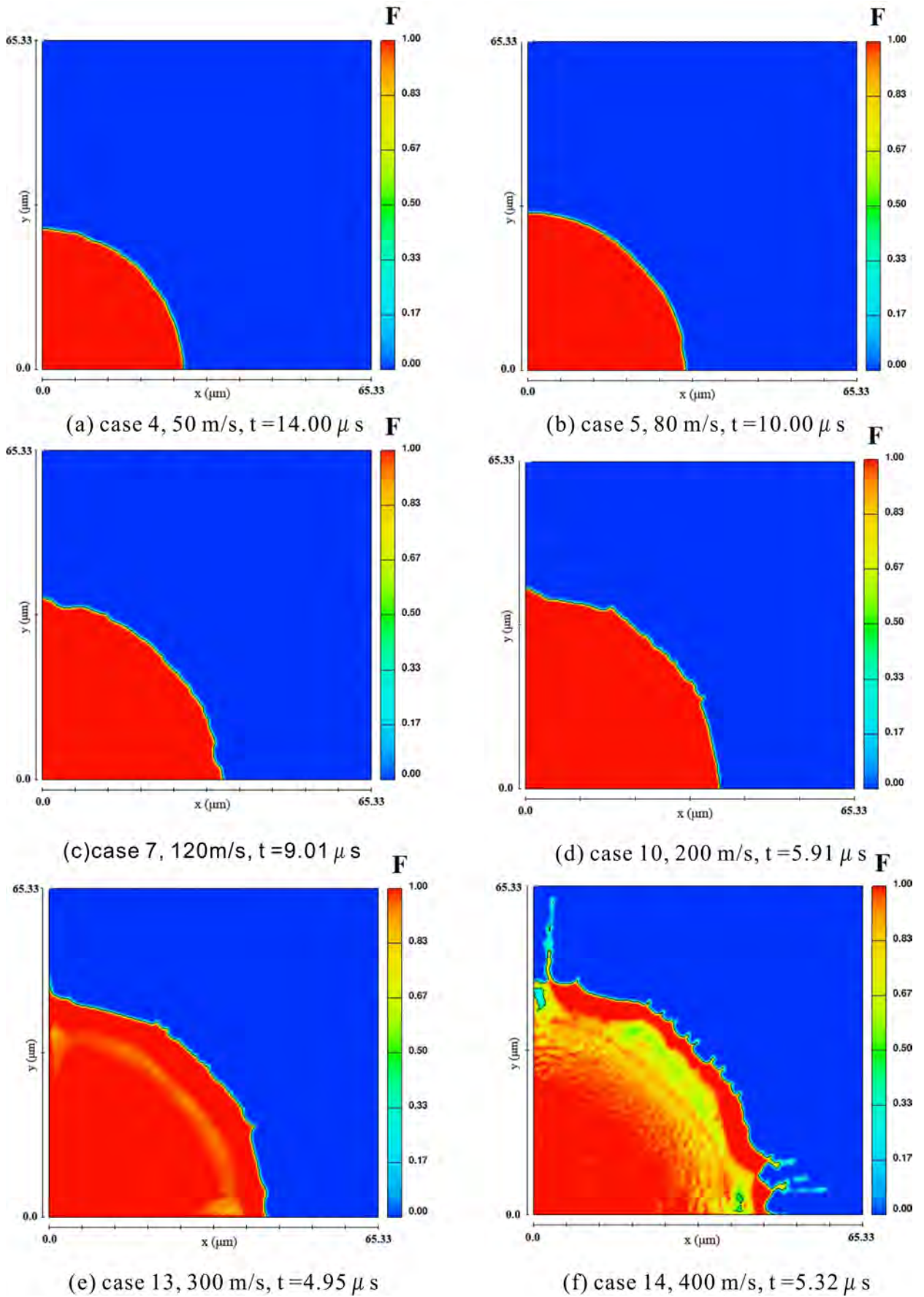


Fig. 5.37 Cross section of a splat at the bottom surface, showing different spread degree for different velocity. The contour is based on the value of Volume of Fluid.

Table 5.3 The impact parameters setting for the simulations on droplet jetting behavior.

Case	T (K)	T_s (K)	h (W/m ² K)
2	3200	823	10^6
3	3200	1573	10^6
16	3800	823	10^6
17	3800	823	10^7

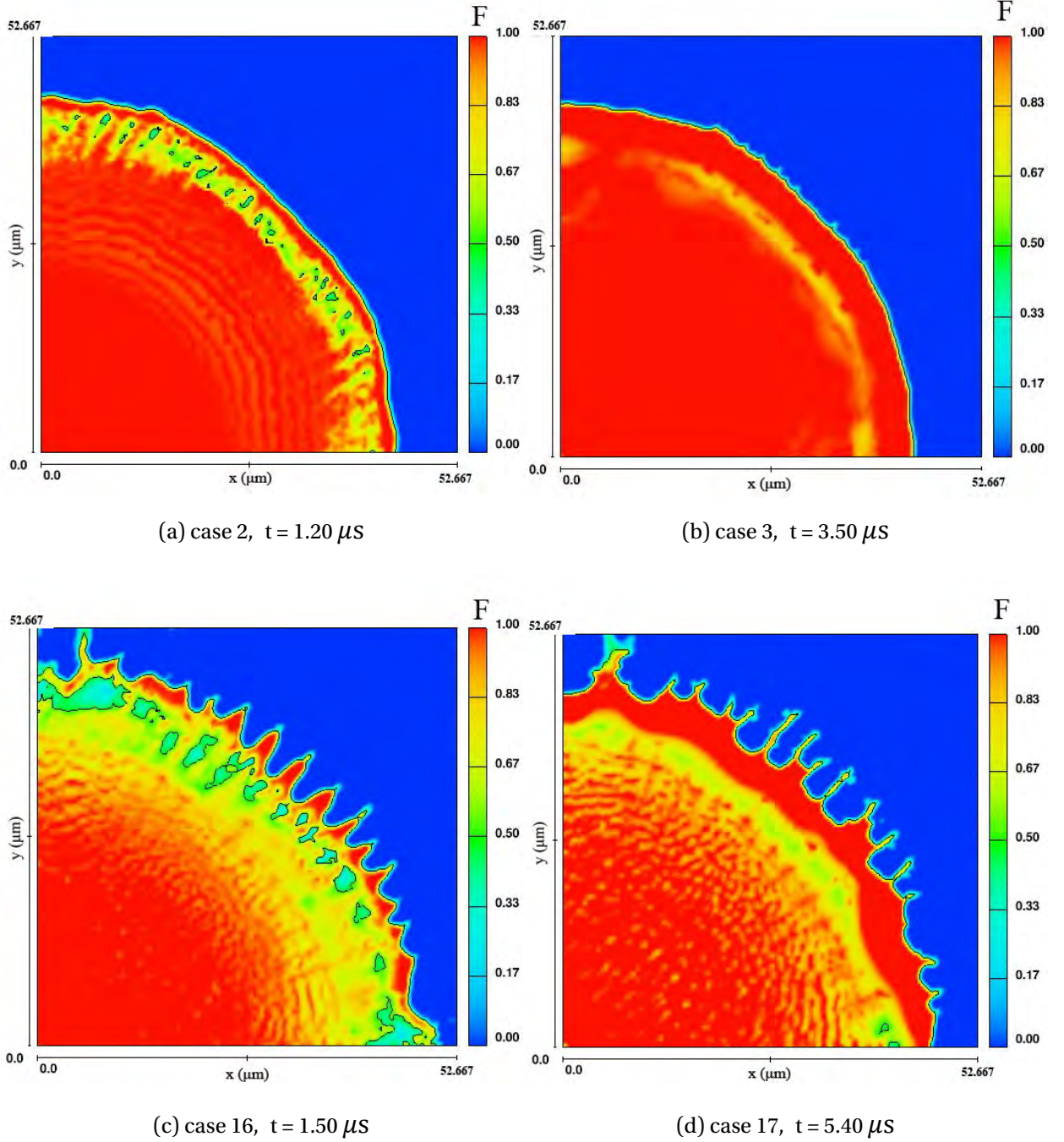


Fig. 5.38 Cross section of a splat at the bottom surface, showing different jetting behavior at different combinations of substrate temperature, droplet temperature and interface heat transfer coefficient. The contour is based on the value of Volume of Fluid.

5.3.2.5 Measurement of splat parameters

From simulation results, radius of the splats in **Fig. 5.37** are evaluated. Experimentally, the 3D profile data of the splats from confocal imaging profiler are processed to evaluate the splat area A_s and volume V_s . Then the droplet spread factor ξ can be derived and compared.

Good agreement is found between the experiments and the simulation. As shown in **Table 5.4**, the evaluated experimental spread factor ξ of the splats ranges from 3.36 to 4.61, while the simulation spread factor of splats under different velocities ranges from 3.24 at droplet velocity 80 m/s to 4.53 at 400 m/s. In order to quantify the effect of droplet velocity, the splat spread factor is related to the droplet velocity from simulation results as in **Fig. 5.39**.

Table 5.4 Calculated splat area, volume, diameter and the corresponding spread factor.

	splat area (μm^2)	volume (μm^3)	diameter (μm)	spread factor
1	1445.08	1295.04	21.45	3.36
2	4041.16	4915.20	35.86	3.40
3	3346.98	2759.32	33.12	3.80
4	3807.25	3166.97	34.81	3.82
5	3878.37	3402.19	36.72	3.94
6	3106.66	1882.7	31.45	4.10
7	7626.32	5147.11	49.27	4.61

It could be found that the final spread factor ξ and the droplet velocity V have a power function relationship. The fitted formula is as below:

$$\xi = 1.1532V^{0.24} \quad (5.12)$$

As the accepted method, this formula is converted into the format with respect to the Reynolds number. Because the initial droplet diameter is $20\mu\text{m}$, the density is 5890 kg/m^3 and the fluid viscosity $\mu = 0.0037\exp(6100/T) = 0.0037\exp(6100/3500) = 0.021\text{ Pa}\cdot\text{s}$, the spread factor could be rewritten as:

$$\xi = 0.7663Re^{0.24} \quad (5.13)$$

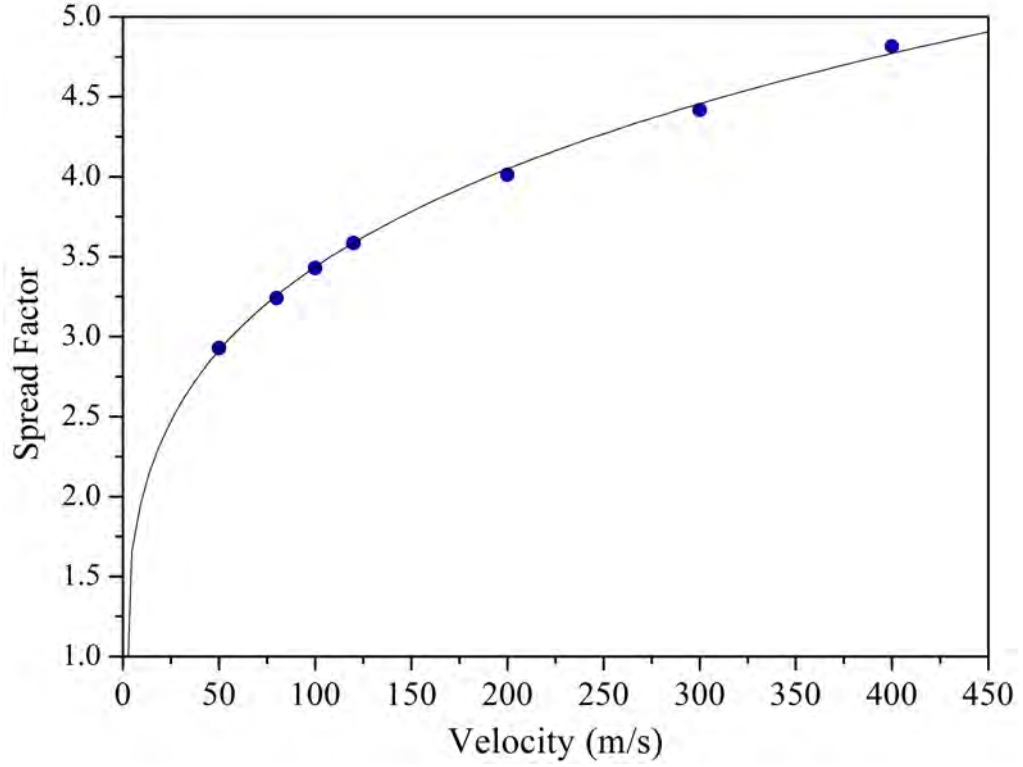


Fig. 5.39 Relationship of splat spread factor and the droplet velocities derived from the simulation.

The values of the scaling factor $a = 0.7663$ and the exponent $b = 0.24$ could be derived, which are comparable to the values by Watanable et al.[93] ($a = 0.8200, b = 0.21$) and Pasandideh-Fard et al.[88] ($a = 0.5000, b = 0.25$).

The good agreement of the spread factor between the experiments and simulation also means that the current input parameters setting (heat transfer coefficient $10^6 \text{ W/m}^2 \text{ K}$, droplet temperature 3500 K, substrate temperature 823 K) can predict well the morphology size.

5.3.2.6 Summary on droplet splatting behavior

Summary on the droplet splatting behavior is made from the discussion above. It is based on the analysis of the experimental and numerical results, together with some hypothesis supported by the literature.

Studies have shown that the droplet impact behavior is influenced by various parameters, mainly the Reynolds and Weber numbers, as well as the substrate surface roughness and thermal contact resistance (reciprocal of the heat transfer coefficient)[83, 98 and 99]. In the expression of Reynolds number $Re = \frac{\rho V D}{\mu}$,

the value of Re is proportional to the velocity V ; while the temperature T influences Re via changing the value of viscosity μ in an insignificant way of $\mu = 0.0037 \exp(6100/T)$. Thus the spread degree is significantly affected by the droplet velocity but changes little with the droplet temperature. The heat transfer coefficient affects the spread degree in a dynamic wetting way: higher heat transfer coefficient results in a higher fluid cooling rate and a higher solidification rate. Therefore, under a low heat transfer coefficient, the fluid solidifies slower, thus after the droplet reaches its maximum spread, it starts to recoil due to the surface tension effects. In a word, The small spread degree of low heat transfer coefficient is caused by the receding of the fluid after flattening. But at higher level of heat transfer coefficient ($1 \times 10^6 \text{ W/m}^2\text{K}$ and $1 \times 10^7 \text{ W/m}^2\text{K}$), the spread degree remains almost the same. In the spreading phase, the inertia takes a dominant place; while in the recoiling phase, the surface tension plays an important role. The solidification will modifies these two phases, which is influenced mainly by the heat transfer coefficient.

It is widely claimed that the substrate transition temperature is an important parameter that affects the droplet spread and splashing behavior, above which the splat presents a circular shape[103]. This phenomenon has been concluded to be attributed to the thermal contact resistance change due to chemical composition change of the substrate surface, removal of the contaminants and water molecules and the morphology change of the substrate in a micro-scale. From the simulation results, it seems that the magnitude of the substrate temperature (thermal contact resistance is considered separately) does not affect the impact behavior too much.

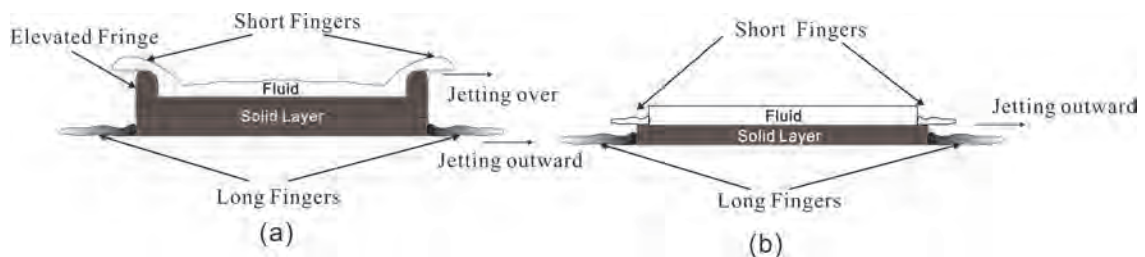


Fig. 5.40 Illustration of the formation of short and long fingers.

An illustration of the formation of short fingers and long fingers is shown in **Fig. 5.40**. At the early stage, the droplet experiences a drastic heat transfer with the substrate and forms a thin solid layer, which is defined as the solidified layer close to

the substrate at the moment when spreading ceases, just as the phenomenon mentioned by Dhiman et al.[121]. Higher velocity and higher droplet temperature result in low fluid viscosity decrease rate, thus the Rayleigh-Taylor instabilities caused by fluid deceleration promotes fluid jetting out from the periphery of the droplet to form fingers. It is shown by the droplet morphology of case 10 in **Table 5.3** and as shown in **Fig. 5.41**. The droplet remains as fluid before obvious jetting occurs. Because at this moment the droplet kinetic energy is very high, the fingers appear to be long in the radial direction, which is called long fingers in this work.

After jetting out, the fluid recedes a little bit due to the surface tension. As the higher heat transfer coefficient speeds up the solidification of the bottom layer, the jetting fluid freezes faster to make this phenomena more evident. This agrees with the conclusion by Zhang et al. that the droplet splashing is due to the high rate of solidification[131]. In the simulation, the fluid-substrate interface is considered as non-slip condition. It is believed that the surface roughness, the air gap between the droplet and the substrate, the physic of fluid undercooling will make the jetting behavior more pronounced and occur at lower droplet temperature and velocity.

As the fluid spread ceases, the remaining fluid in the interior of the splat continues to flow outward on top of the solidified layer. Higher droplet temperature, higher substrate temperature and lower heat transfer coefficient delays the solidification of the fluid. The fluid flows outward and accumulates at the periphery of the splat to elevate the fringe. The fringe elevation and the low fluid viscosity in the interior area of the splat may contribute to some other splatting behavior. The fluid disturbance caused by fluid turbulence, substrate roughness, or the air entrapment by the fluid, may cause the fluid on the solidified layer to jet over the elevated fringe to form fingers, as shown in **Fig. 5.40(a)**. In the case where the elevated fringe is not obvious, the fingers could also form due to Rayleigh-Taylor instabilities, as shown in **Fig. 5.40(b)**. Because at this moment the fluid velocity is much lower than the moment of impact, the fingers appear to be shorter. Therefore, the fingers formed at this moment is called short fingers. The two-layer characteristic, short and long fingers of the splat are shown in **Fig. 5.42**, which is produced by enlarging part of **Fig. 3.21(b)**.

5.3.3 Splat morphology on the curved substrates

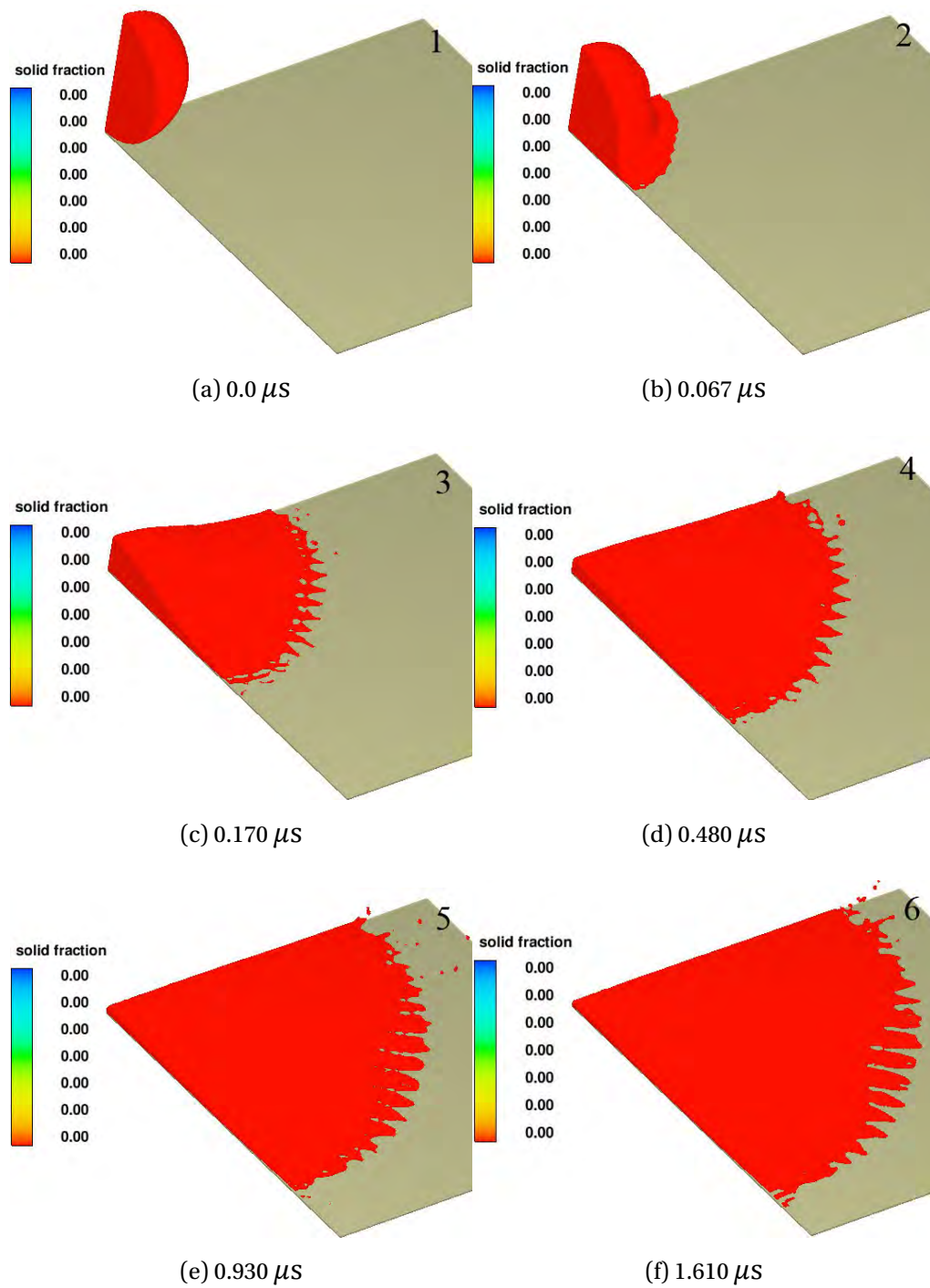


Fig. 5.41 Droplet morphology evolution during impact in the case of high velocity (400 m/s) and high temperature (3800 K). Legend displays 0 values for all contour range due to fully liquidus state at these time frames in the simulation.

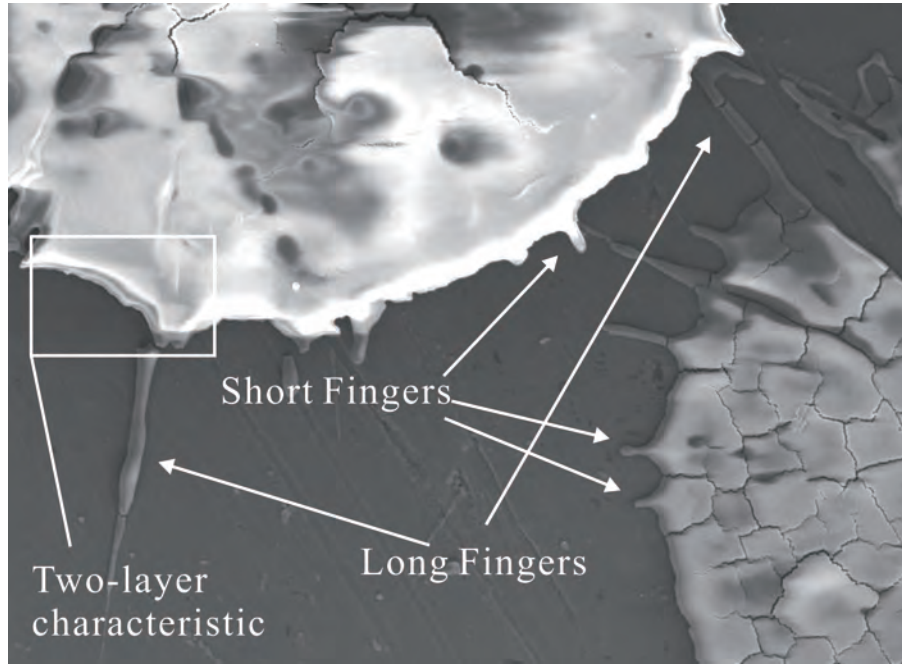


Fig. 5.42 SEM photo of the splat, showing two-layer characteristic, short and longer fingers.

5.3.3.1 Splats characterization and analysis

Splats on the curved substrate obtained by the optical microscope are evaluated geometrically. Major radius and minor radius are evaluated. The principle of deriving these parameters are shown below:

As in **Fig. 5.43**, the splat (a) can be simplified as an ellipse (b). The major radius a and minor radius b essentially define the shape of the ellipse. In Image-Pro Plus®, a closed line is drawn following the 'boundary' of the splat to form an ellipse. The area and circumference are extracted as A_e and S_e respectively.

In the simplified ellipse, the area of the ellipse is expressed as:

$$A_e = \pi ab \quad (5.14)$$

The circumference is expressed as an optimized quadratic approximation (derivation detail in **Appendix F**). :

$$S_e = 2\pi \sqrt{w \frac{a^2 + b^2}{2} + (1 - w)ab} \quad (5.15)$$

where $w = 0.7966106$ for minimum overall approximation error.

Eventually, the major radius and minor radius of the ellipse could be derived as:

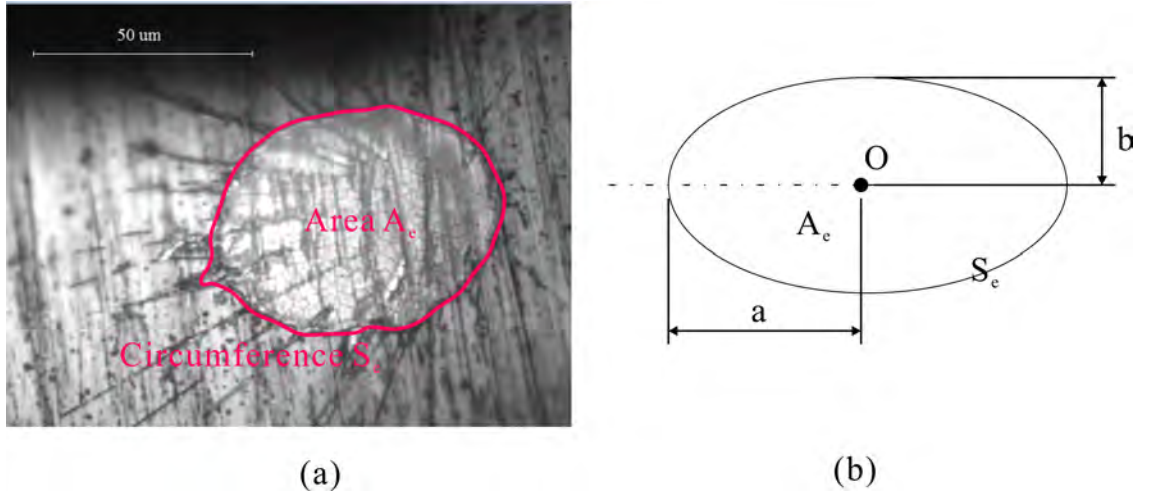


Fig. 5.43 An illustration of an ellipse, which is a simplified splat shape, used to represent a splat shape at oblique impact. (a) Example splat at the impact angle 46° , (b) Simplified elliptical shape.

$$a = \frac{\sqrt{0.06358S_e^2 + 0.4741A_e} + \sqrt{0.06358S_e^2 - 0.7991A_e}}{2}$$

$$b = \frac{\sqrt{0.06358S_e^2 + 0.4741A_e} - \sqrt{0.06358S_e^2 - 0.7991A_e}}{2}$$

In total 62 splats are captured and evaluated. A preliminary relationship between the aspect ratio and impact angle is derived from the plot in **Fig. 5.44**. UCL and LCL are the upper and lower control limit respectively. The derived formula is the polynomial fit of the aspect ratio (ζ).

$$\zeta = 0.93146 + 0.01684\theta - 2.70151E - 4\theta^2 + 4.30331E - 6\theta^3 \quad (5.16)$$

Images under confocal imaging profiler are evaluated using Surfer® to get the spread factor of droplets at different impact angles. The spread factors are plotted in **Fig. 5.45**. **Fig. 5.46** shows a selection of images (a-e) and 3D surface contours (f-j) of splats at different impact angles. It can be seen that the range of spread factor is from 3.21 to 4.49 without a trend in the scatter. A preliminary conclusion is that the impact angle θ do not significantly affect the spread factor ξ .

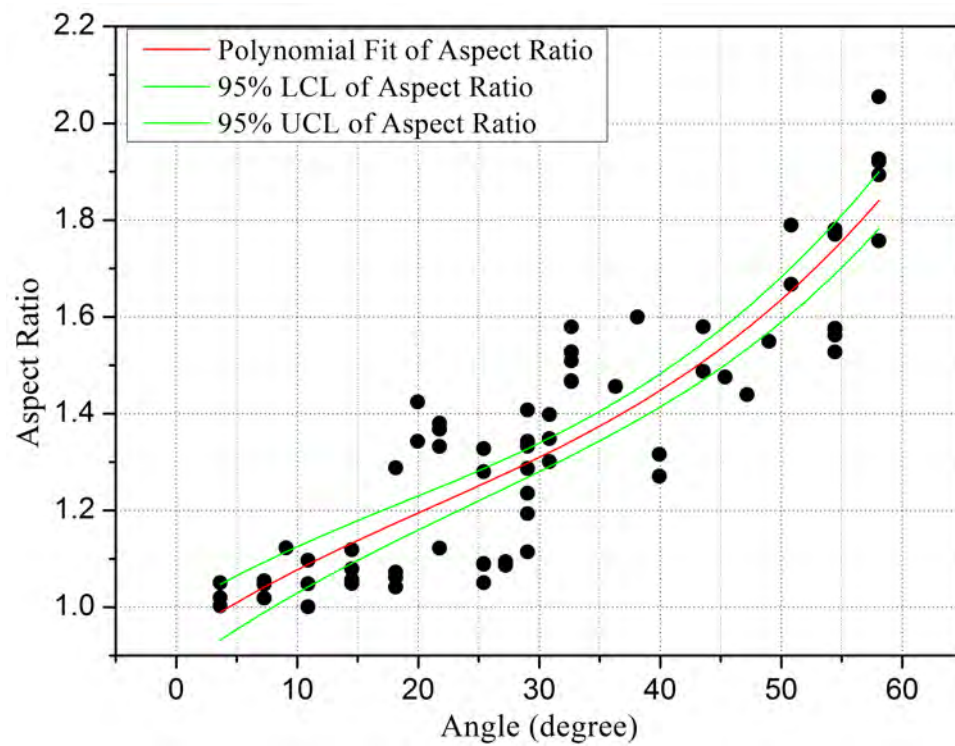


Fig. 5.44 Aspect ratio calculated from the splats with respect to the impact angle.

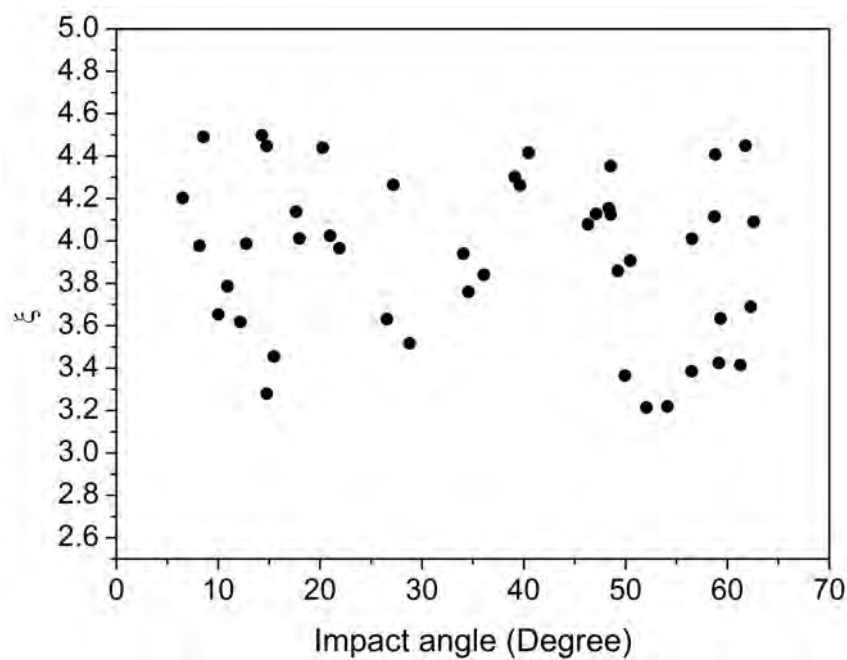


Fig. 5.45 Spread factors of splats at different impact angles of the substrate.

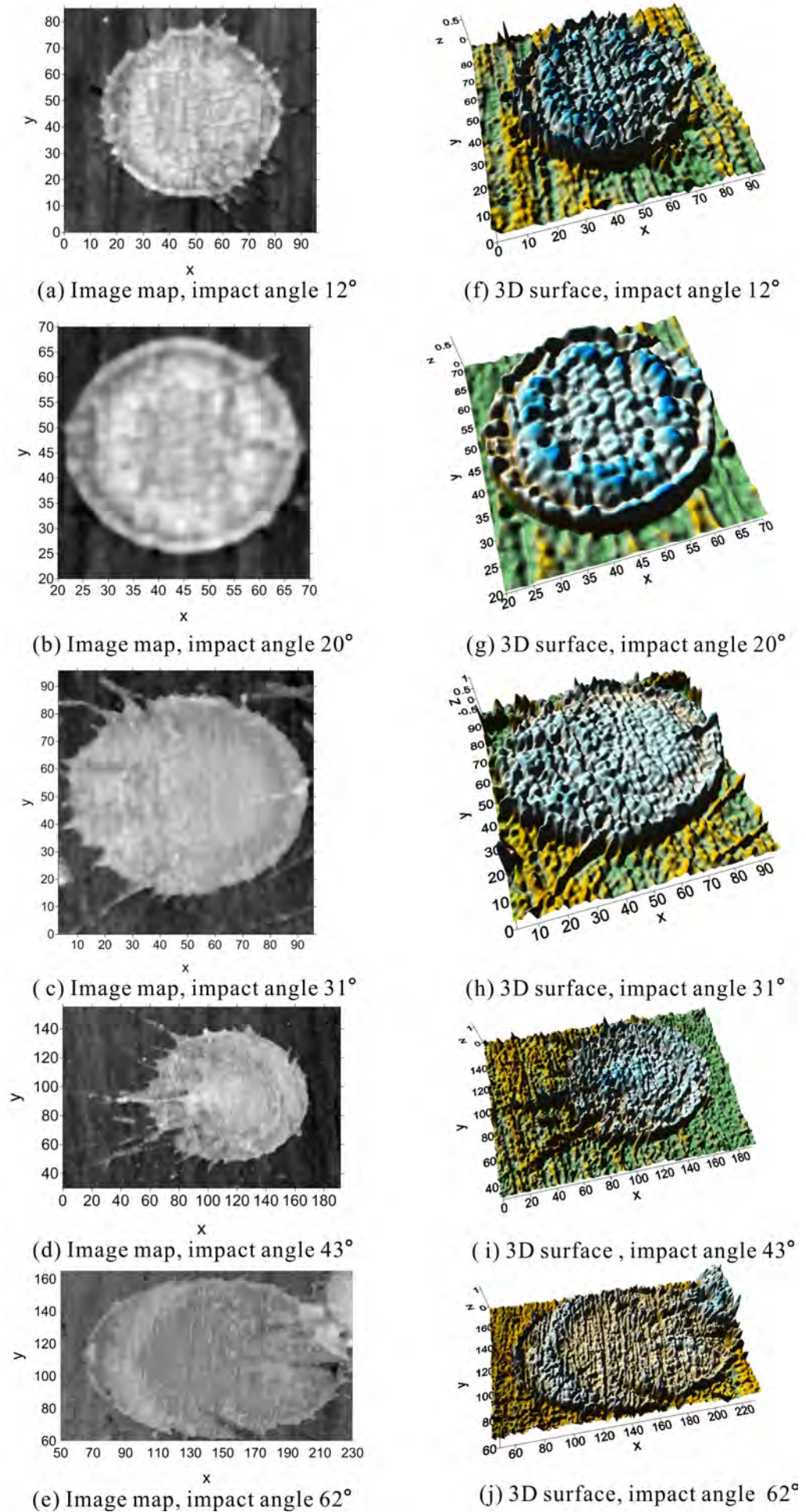


Fig. 5.46 Image and 3D surface contours of some of the splats at different impact angles, which are reconstructed from confocal data. The unit along all the three axes are μm , the curved surface radius is 13.8 mm.

5.3.3.2 Effects of surface curvature on the splat shape

The effect of substrate curvature on the splat shape is evaluated by simulation. **Fig. 5.47** shows the bottom surfaces of the splats on curved surface under the impact angle 0° (a–c) and under normal impact on flat surface (d–f). The velocities are varied at the values 120 m/s, 200 m/s and 300 m/s respectively.

It is found that the splats approximates a circular disk shape, even on the curved surface. From the initial droplet diameter $D = 20 \mu\text{m}$ and the derived diameter of the splat, the spread factors ξ are evaluated and listed in **Table 5.5**.

Table 5.5 Spread factor of splats when droplets impact at the impact angle of 0° on curved substrate surface and on flat surface under normal impact.

Velocity (m/s)	120	200	300
curved	3.38	3.78	4.30
flat	3.43	3.78	4.24

The spread factors remain unchanged for the same velocity between the case of curved substrate and the flat substrate. This could be explained by the large difference between the droplet and the substrate surface diameter. Therefore, the spreading area for individual splat can be considered as a flat facet on the curved substrate.

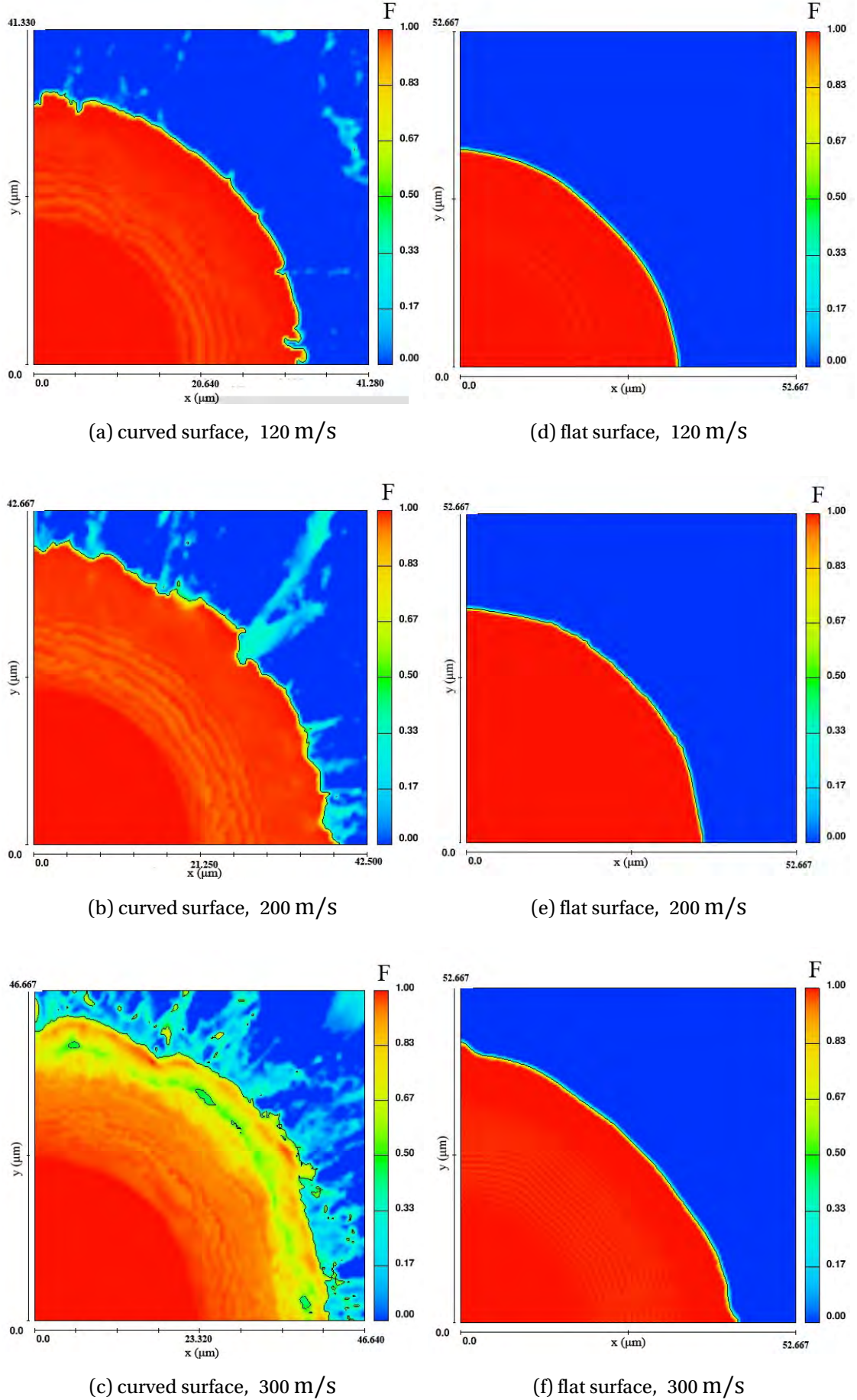


Fig. 5.47 Bottom surfaces of splats on curved surface at the impact angle of 0° (a-c) and under normal impact on flat surface (d-f). The radius of the curved surface is 13.5 mm, the curvature direction is along the x axis. The contour is based on the value of Volume of Fluid.

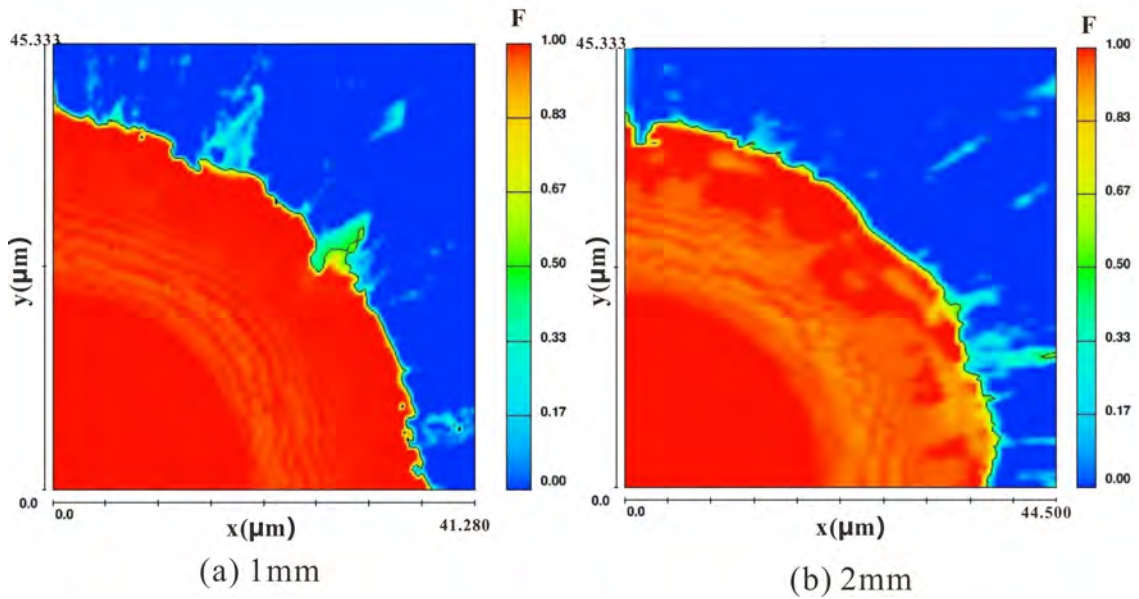


Fig. 5.48 Bottom surfaces of splats on curved substrate with diameter (a) 1mm and (b) 2mm.

The substrate curvature can be considered as the multiplicative inverse of the radius. Two other cases are carried out to investigate whether the surface curvature has effects to the splat spreading when the curvature is very large. The curved surface diameter is set as 2mm and 1 mm. The droplet impacts onto the substrate surface at the impact angle of 0° . The slices at the bottom surfaces of the two cases are shown in **Fig. 5.48**.

Combining with the flat surface case (curvature of zero) and the case of curved surface diameter 13.8 mm, comparison of spread factors is shown in **Table 5.6**, with respect to the surface curvature.

Table 5.6 Spread factor of splats when droplets impact at impact angle 0° with surface curvatures in the simulation.

Surface radius (mm)	flat	13.8	1	0.5
Curvature (m^{-1})	0	72.5	1000	2000
ξ	3.78	3.78	3.74	3.77

The splat shape still approximates a circular disk. The results reveals that even when the substrate curvature is as large as 2000, the splat spread factor remains almost constant, thus the surface to be impact can still be considered as a flat facet. This is the basis for the author's work on the deposit modeling, in which the surface

for individual droplet spreading is considered as flat surface with the same surface normal.

5.3.3.3 Effect of impact angle on droplet flattening behavior on curved substrate

The splat elongates to an ellipse under an oblique impact. The bottom surfaces of the splats are used to extract the splat geometry factors. **Fig. 5.49** shows the method to extract the values, taking the case at impact angle $\theta = 40^\circ$ under impact velocity $V = 200$ m/s. The distance from the focus to the ellipse center is denoted as c , which is also calculated. The ellipse center O is found firstly. Then the major radius a and minor radius b are measured, from which the ellipse focus distance c is computed. C denotes the elliptical splat focus, while the impact point I , due to the computing model setup, is at the point of $(0,0)$ in the figure. Thus the elongation distance l could be measured. The results are listed in **Table 5.8** for comparison.

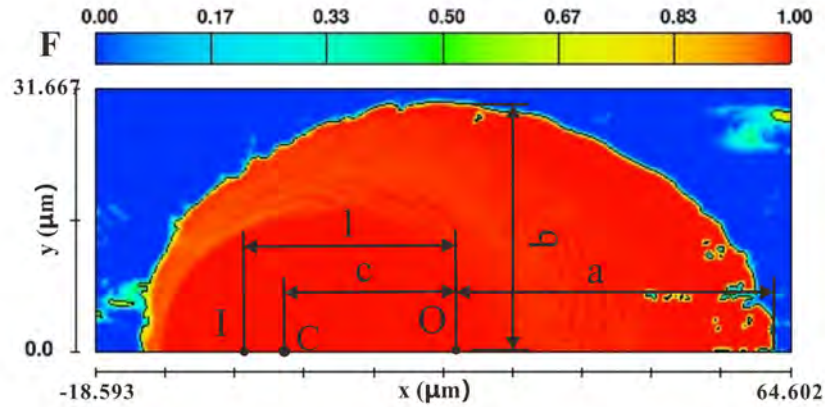


Fig. 5.49 Illustration of extraction of the elliptical distance c and elongation distance l , showing the case at impact angle $\theta = 40^\circ$ under velocity 200 m/s.

Bottom surfaces of splats on curved substrate at different impact angles are shown from **Fig. 5.50** to **Fig. 5.52**, for the cases under impact velocity 120 m/s, 200 m/s and 300 m/s respectively. In each figure, the subfigures are adjusted to be in the same scale, in order to see the splat shape and size changes. A quarter of the droplet and the substrate underneath it is modeled for the cases with droplet impacting under impact angle 0° .

Geometric evaluation of splats has been done to extract the major radius a and minor radius b . The corresponding spread factor ξ and aspect ratio ζ are also calculated. The data are listed in **Table 5.5**:

Table 5.7 Major radius a , minor radius b , spread factor ξ and aspect ratio ζ of splats when droplets impact at different impact angles with different impact velocities.

Velocity (m/s)		0°	20°	40°	60°
120	a (μm)	33.80	33.74	38.02	46.95
	b (μm)	33.80	33.48	29.51	25.08
	spread factor ξ	3.38	3.36	3.35	3.43
	aspect ratio ζ	1.00	1.01	1.29	1.87
200	a (μm)	37.80	38.10	41.90	53.25
	b (μm)	37.80	36.18	33.95	28.08
	spread factor ξ	3.78	3.71	3.77	3.88
	aspect ratio ζ	1.00	1.05	1.23	1.89
300	a (μm)	42.30	42.40	45.65	51.50
	b (μm)	42.30	40.3	38.78	32.50
	spread factor ξ	4.23	4.13	4.20	4.09
	aspect ratio ζ	1.00	1.05	1.17	1.58

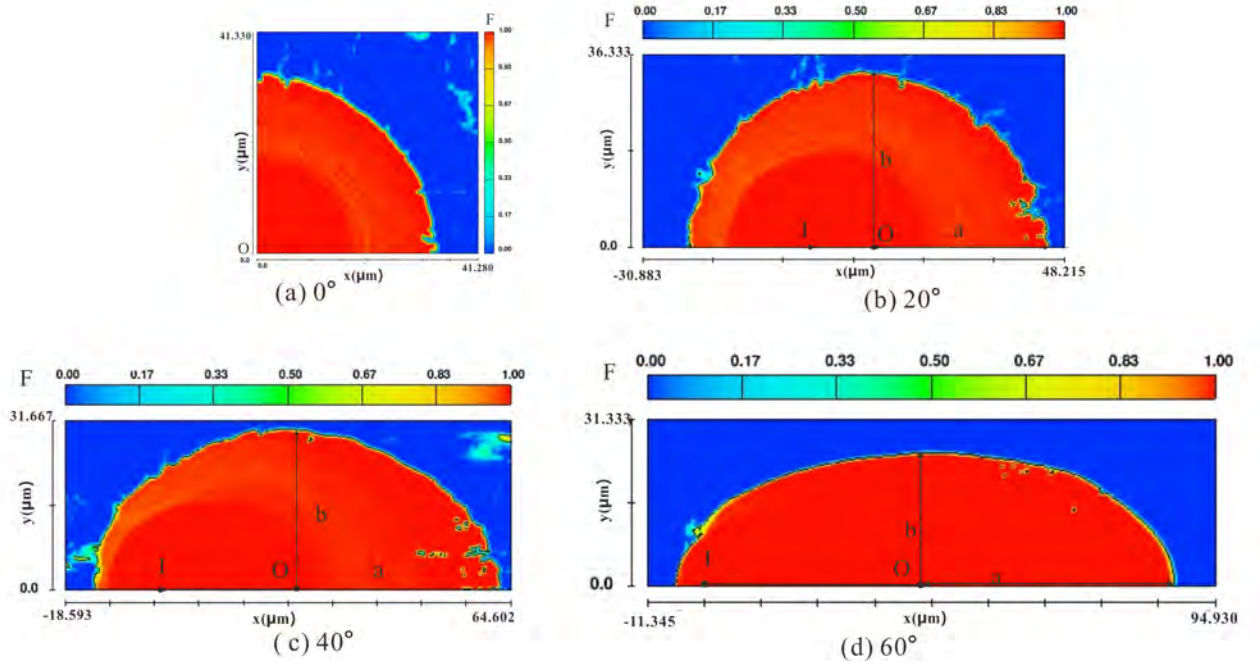


Fig. 5.50 “Bottom surfaces” of splats on curved surface (radius 13.8 mm) at different impact angles, impact velocity of 120 m/s.

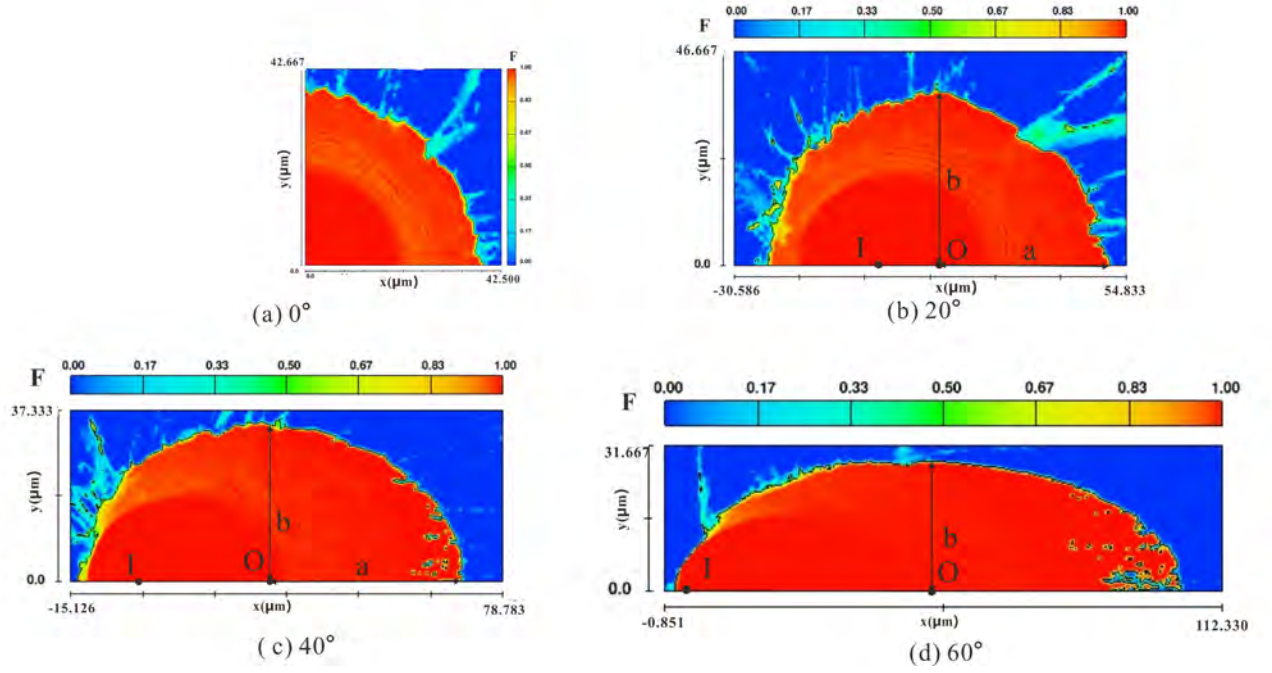


Fig. 5.51 “Bottom surface” of splats on curved surface (radius 13.8 mm) at different impact angles, impact velocity of 200 m/s.

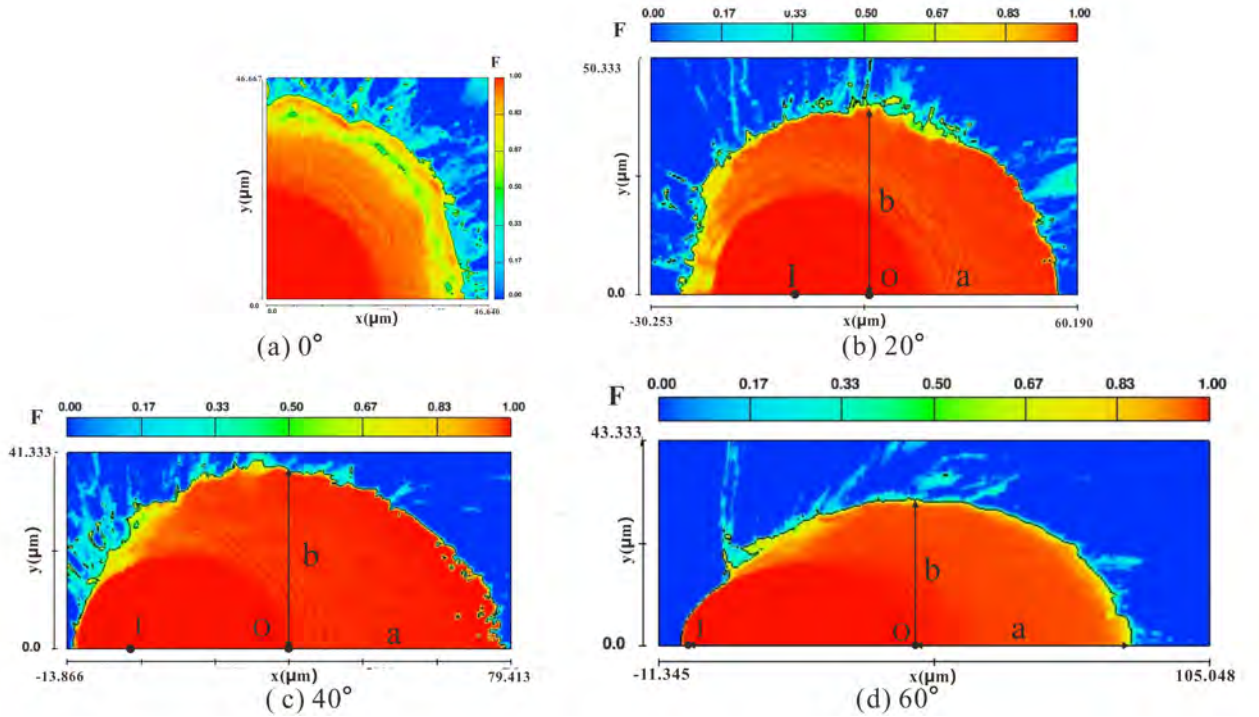


Fig. 5.52 “Bottom surface” of splats on curved surface (radius 13.8 mm) at different impact angles, impact velocity of 300 m/s.

The spread factor and aspect ratio fall within the range of the experimental results, which justifies the simulations. The results reveal that the spread factor increases with the impact velocity. Under the same velocity, the spread factor varies little with the impact angle. Considering the estimation error during the geometry extraction,

it can be concluded that the spread factor remains unchanged when the impact angle increases.

The aspect ratio ζ increases obviously with the impact angle, which is plotted in Fig. 5.53. The fitted curve under different velocities in the plot is shown in Equation 5.17. It seems that the case with impact angle 60° and velocity 300 m/s produces an unexpected result, which is significantly lower than the other two cases. This may attributed to the mass loss under higher velocity at such a high impact angle. Due to this reason, the aspect ratio formula of splats at different impact angles from experiment is used in the author's work.

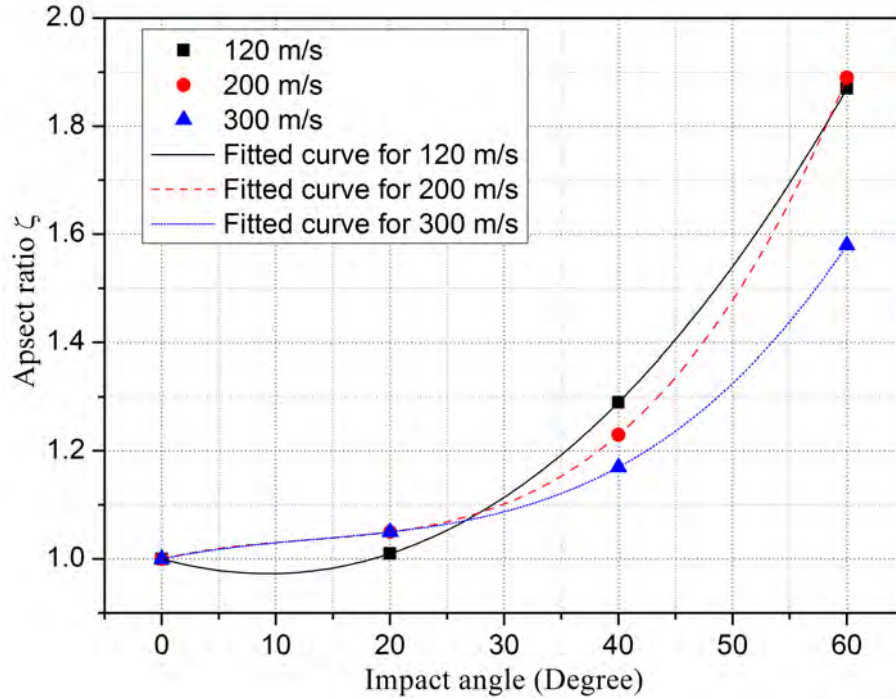


Fig. 5.53 Relationship of aspect ratio (ζ) and the impact angle θ derived from the simulation.

$$\begin{cases} \zeta(120) = 1 - 5.75e - 3\theta + 3e - 4\theta^2 + 6.25e - 7\theta^3 \\ \zeta(200) = 1 + 5.08e - 3\theta - 2.75e - 4\theta^2 + 7.29e - 6\theta^3 \\ \zeta(300) = 1 + 4.42e - 3\theta - 1.88e - 4\theta^2 + 4.58e - 6\theta^3 \end{cases} \quad (5.17)$$

Kang et al. [113] assumed that the impact point of individual droplet is one of the foci of the resulting elliptical splat. To verify this hypothesis, geometric evaluation has been done to extract the distance between the impact point I and the ellipse center O , which is denoted as elongation distance l .

Table 5.8 Elliptical splat focus distance c and elongation distance l at different impact angles under different impact velocities derived from the simulation.

Velocity (m/s)	Quantity (μm)	0°	20°	40°	60°
120	c	0	4.18	23.97	39.69
	l	0	11.9	29.51	42.18
200	c	0	11.94	24.56	45.24
	l	0	13.18	28.48	50.20
300	c	0	13.18	24.08	39.94
	l	0	15.64	33.30	47.82

Both c and l increase with the impact angle. However, the value of l is larger than that of c , which means the impact point is not one of the foci of the ellipse. To determine the elliptical splat center from the impact point, the elongation factor χ is defined as the ratio between l and the initial droplet diameter D .

$$\chi = \frac{l}{D} \quad (5.18)$$

The elongation factor χ with respect to the impact angle θ under different impact velocities are shown in Fig. 5.54.

A linear relationship between the elongation factor χ and the impact angle θ is found. Similarly, the cases under high velocity 300m/s deviates more with the other two velocities. In order to simplify the simulation, the case under the velocity (200 m/s) close to the mean velocity is considered. The fitted formula of that is as Equation 5.19.

$$\chi = 0.04147\theta - 0.096 \quad (5.19)$$

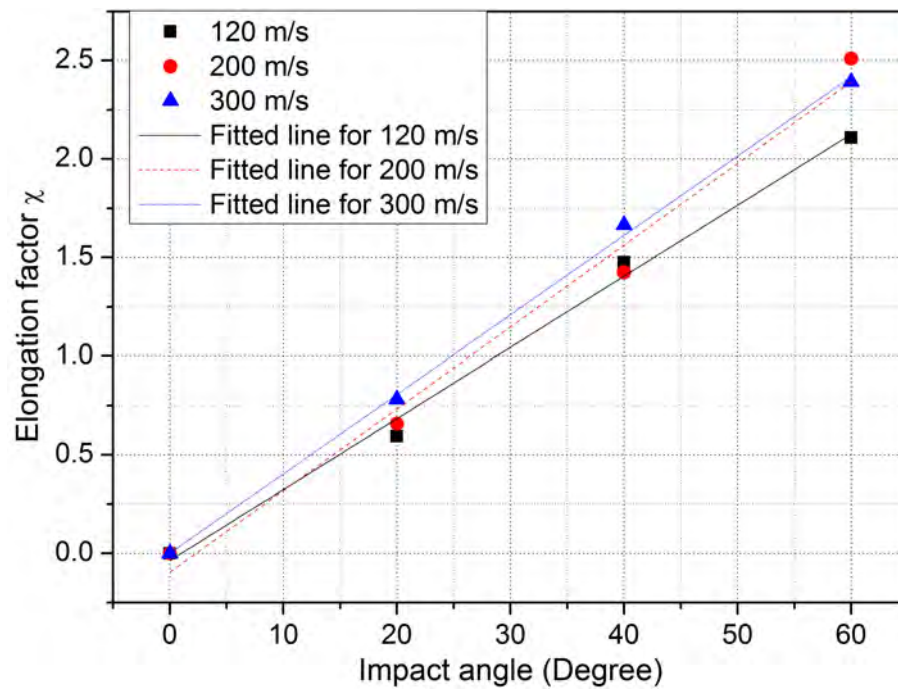


Fig. 5.54 Relationship of the elongation factor χ with respect to the impact angle under different velocities.

5.4 Deposit Formation

The observations by SprayWatch® of the deposit formation are analyzed to reveal the deposition procedure and involving phenomena. The correlation of focus distance and the width of field of view of SprayWatch® is used to evaluate the deposit profiles in the captured images. Simulation results are visualized to compare with the experimental observations and measurements, including the deposit profile growth.

The deposits formed on the upper, middle and lower part of the convex surface of the curved substrate are called case 1, 2 and 3 respectively. In addition, a numerical case is carried out to simulate the deposit formation on the flat substrate, which is compared with the experimental work done by Kang.

5.4.1 Experimental observations and analysis

Fig. 5.55 shows the deposit profile growth with time on the substrate curved surface for case 1 taken by SprayWatch®. The bright particle traces are mostly aligned in the horizontal direction, which justifies the assumption in the deposition code that the particles impact onto the virtual plane perpendicularly. The deposit profile can be observed clearly because of the illumination caused by higher temperature radiation.

It is obvious that the deposit profile curvature increase with the time. The initial substrate curvature is 11.7 m^{-1} . The final deposit curvature is not uniform at different positions of the surface. The maximum curvature is at the deposit summit, which is evaluated as in **Figure 5.56**. Two points A and A' at both sides of the deposit summit S are selected. The tangential lines of the deposit at these two points are drawn AB and $A'B'$.

The rotation angle between AB and $A'B'$ is

$$\alpha = \frac{45^\circ}{360} \times 2\pi = 0.785$$

The mean deposit curvature K between A and A' is

$$K = \frac{\alpha}{AA'} = \frac{0.785}{0.00165} = 475 \text{ m}^{-1} \quad (5.20)$$

This maximum curvature is much smaller than the threshold value 2000 m^{-1} evaluated in the droplet impact behavior simulation, less than which the substrate surface can be considered as flat surface. This observation justifies that single particle is assumed to impact onto a flat facet in the deposition code.

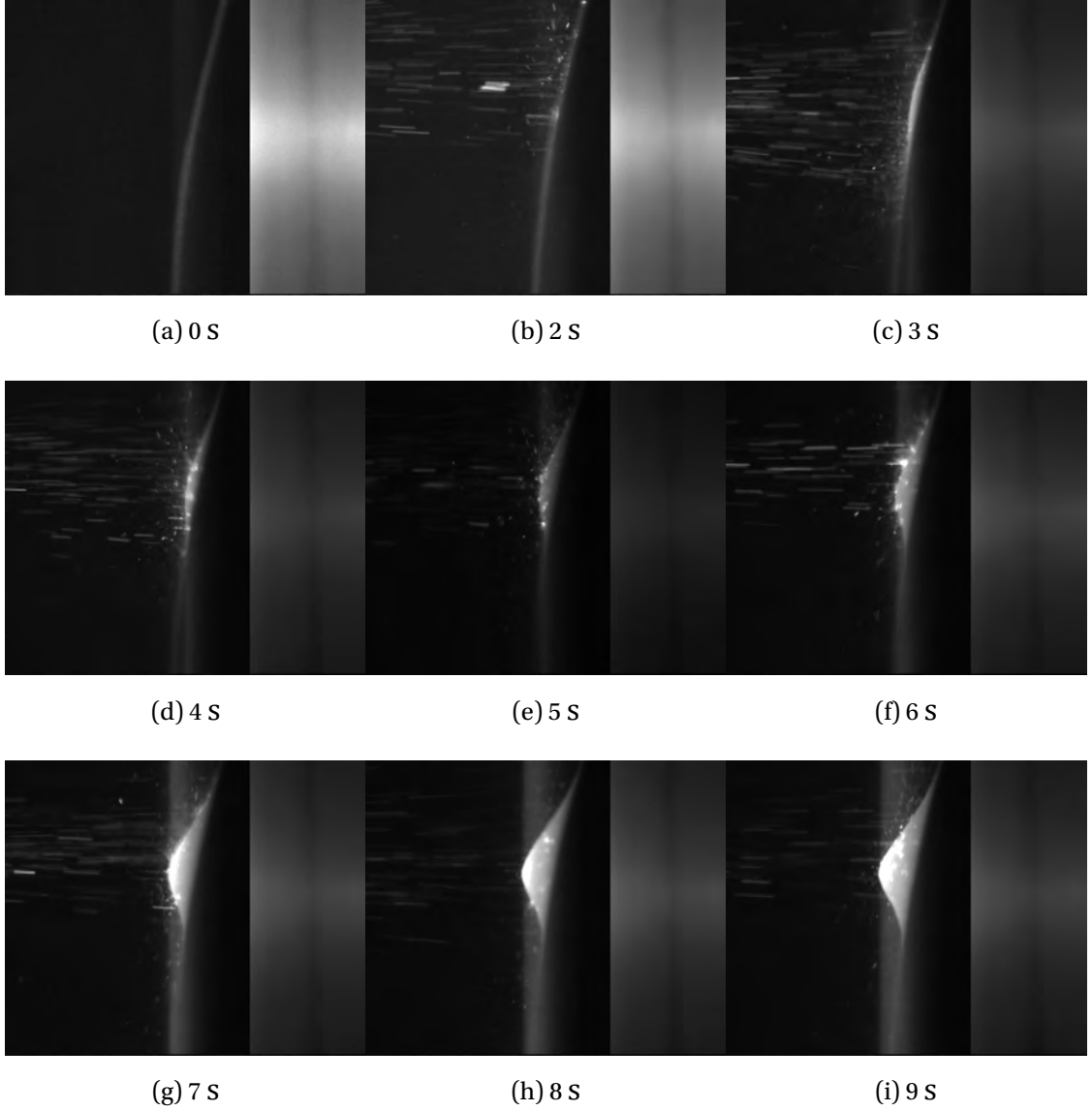


Fig. 5.55 Side view of deposit growing for case 1 by SprayWatch© diagnostics.

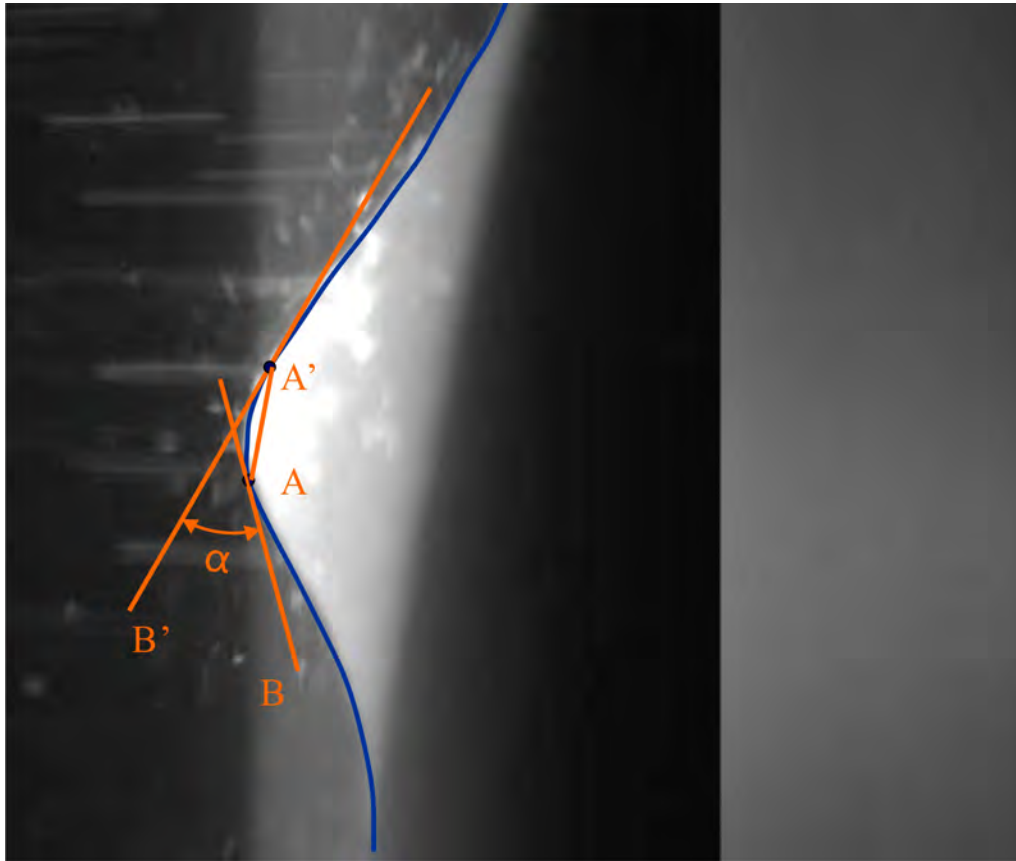
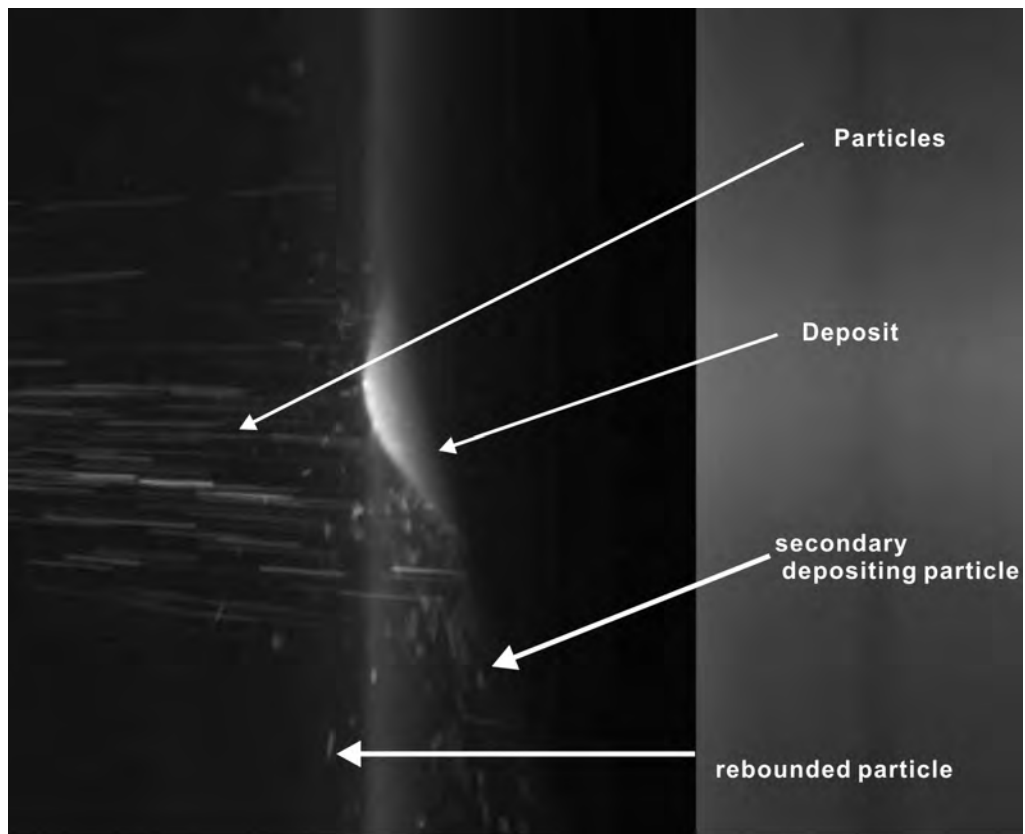
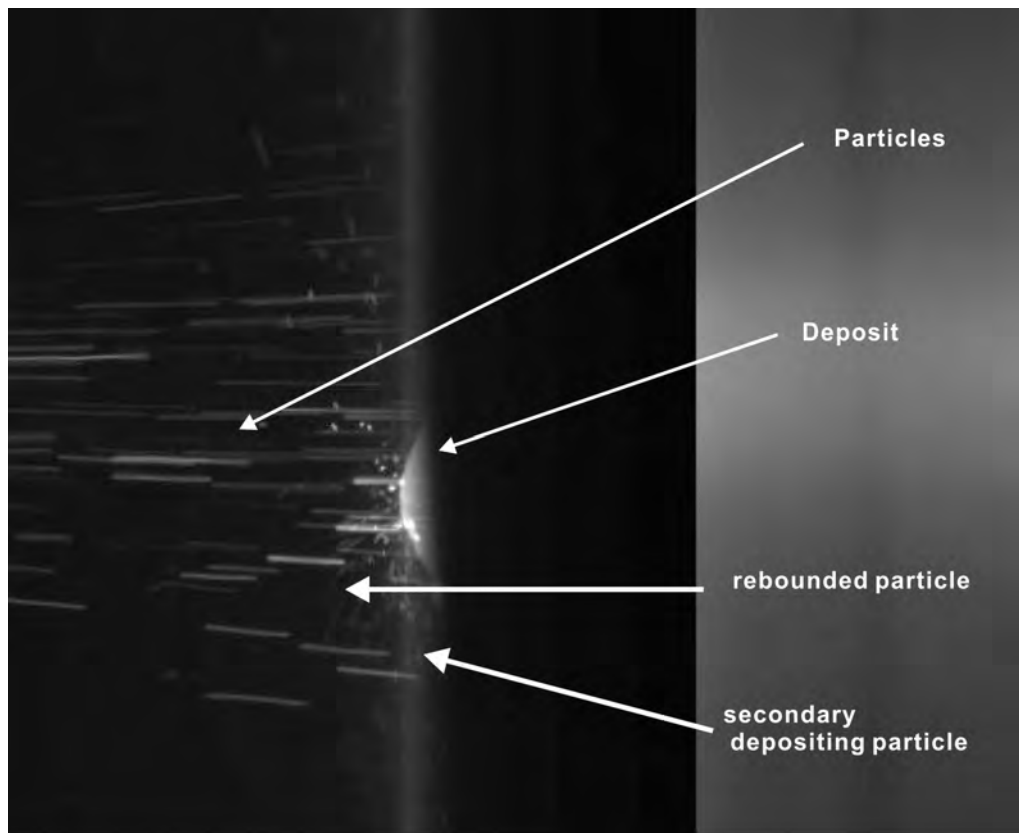


Fig. 5.56 Maximum curvature evaluation of the deposit at the last time frame for case 1.

Not all the particles adhere to the deposit (or substrate) surface. Some of the particles rebound into the environment and others impact onto the deposit and are deposited again at a different location, such particles are called secondary depositing particles. The rebound and secondary depositing phenomena are more clearly shown in **Fig. 5.57**, including case 2 and 3. The rebounded particles cause a dim glow around the deposit.



(a) case 2



(b) case 3

Fig. 5.57 Rebound phenomenon occurs during the depositing.

Fig. 5.58 shows the out-of-plane view of the as-sprayed substrate. It is noticed that the deposit presents a halo characteristic: the deposit fades out gradually outwards, presenting a relatively more obvious inner circle and a hazy donut between the inner circle and the outer circle. However, it is very difficult to define an exact boundary of the deposit. Although not clear, the outer boundary is observed roughly in a circular shape, which is about twice the size of the inner circle.

This structure could be explained by the contour of number of particles in unit time in the virtual plane shown in **Fig. 5.59(a)**. The size of the two circles is evaluated. The reason to choose case 2 is that the deposit is approximately at the summit of the substrate convex surface. The inner circle diameter is 13.2 mm, which corresponds to the contour value of 500; the outer circle diameter is 22.6 mm, which corresponds to the contour value of 100. The particle distribution ranges from FLUENT® output are $-17.2 \text{ mm} \leq x \leq 17.5 \text{ mm}$ and $-24.0 \text{ mm} \leq y \leq 5.98 \text{ mm}$. However, it is difficult to observe deposit material outside the outer circular boundary drawn in the figures. It may be attributed to the small particle numbers in that area.

The hazy area center does not coincide with the deposit summit, which may be attributed to two phenomena:

- The mass flow rate contour presenting a lower position contour center along y direction than the number of particles contour, as in **Fig. 5.59(b)**.
- As in **Fig. 5.57**, the rebound and secondary depositing changes the depositing area. This phenomenon is more pronounced when the particle impact angle (substrate inclination angle) is larger (**Fig. 5.57(b)**).

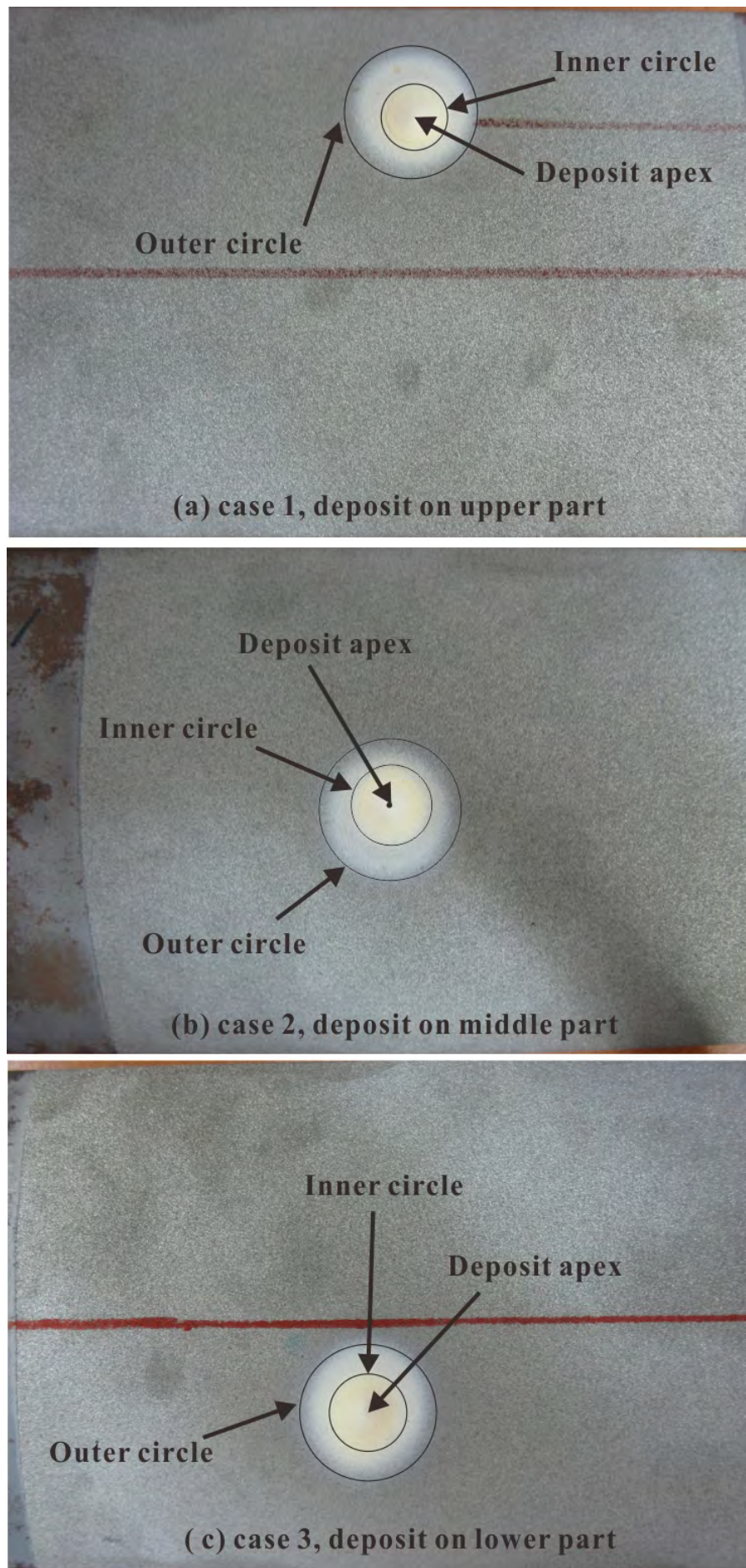


Fig. 5.58 Out-of-plane view of the as-sprayed substrates.

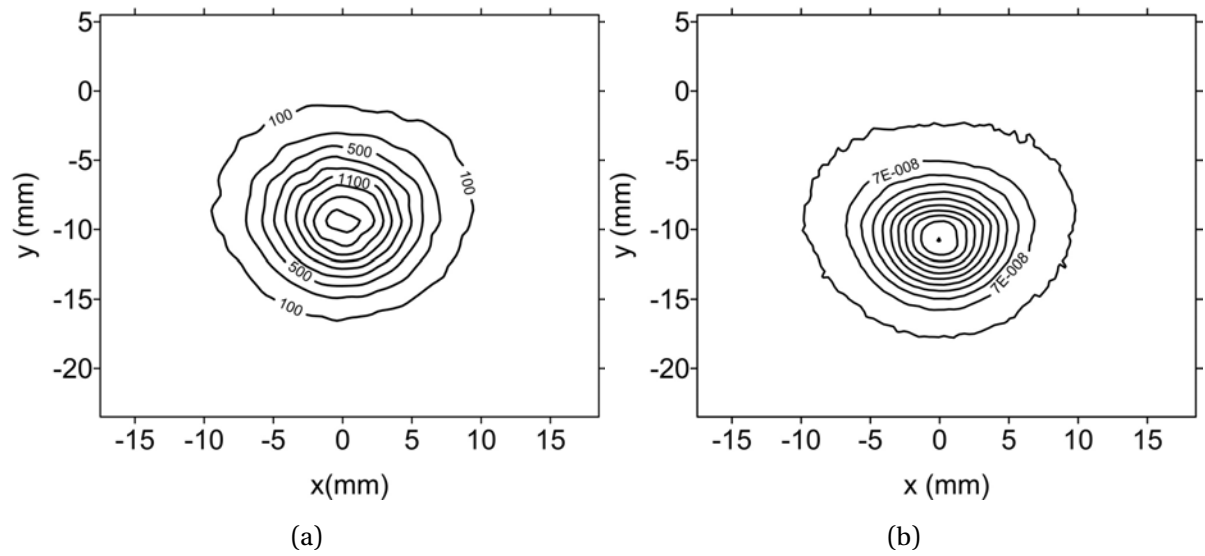


Fig. 5.59 Contours of (a) number of particles (b) mass flow rate in the virtual plane from simulation results for the freestream case.

5.4.2 Comparison between simulation results and experimental results of deposits

The deposit building-up is a time-dependent procedure. Fig. 5.60 shows the simulated deposit growth on the flat surface.

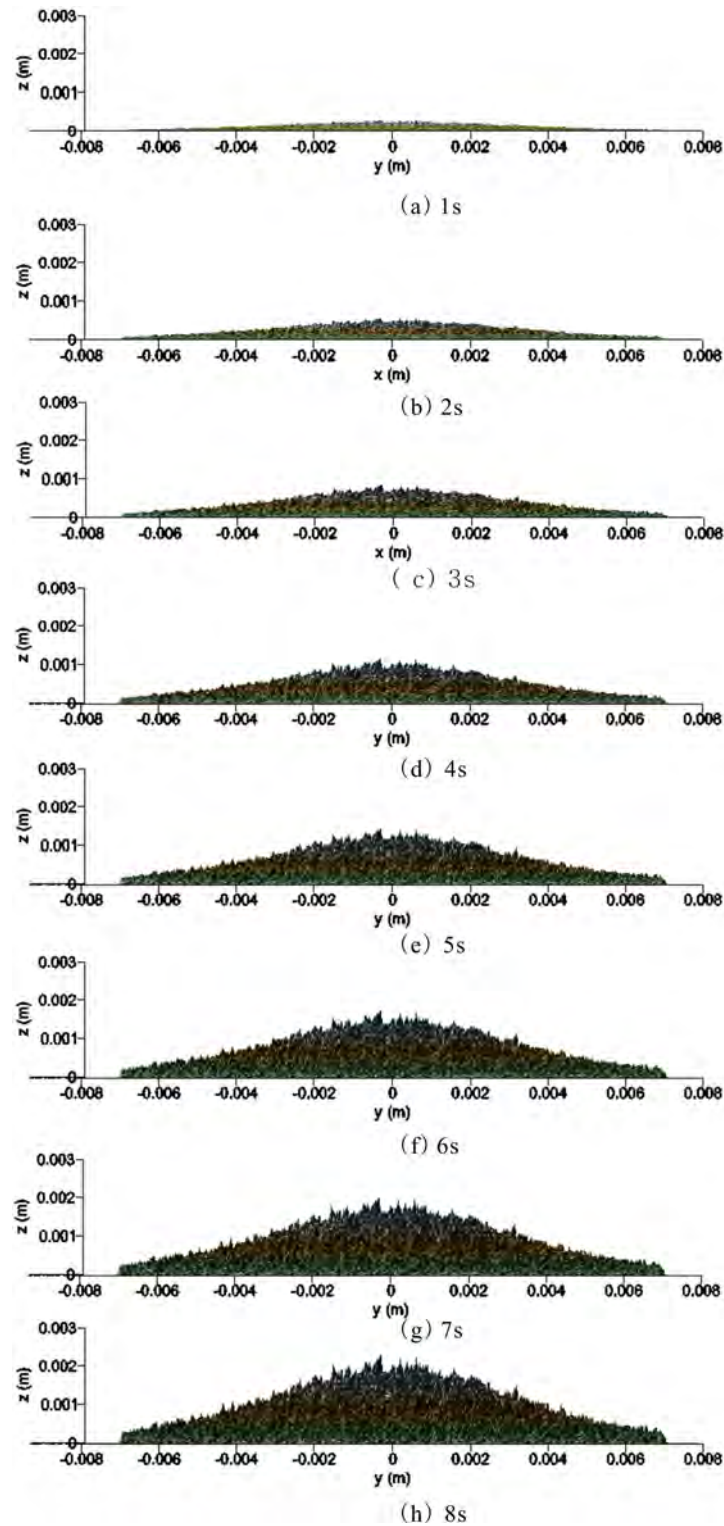


Fig. 5.60 Simulated deposit growth on the flat surface.

The peak deposit thickness at 5 s is compared with the experiment from Kang[113]. The plasma spray conditions are almost the same and the deposition efficiency is set the same as that in Kang's experiment as 0.4. **Fig. 5.61** shows the experimental profile obtained. The peak deposit thickness is 1.84 mm, while the value from simulation is 1.72 mm.

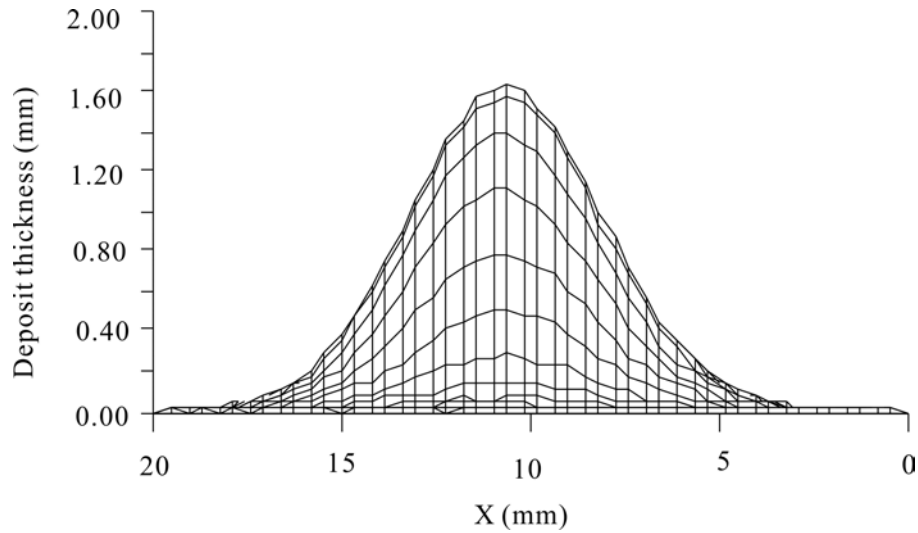


Fig. 5.61 Side view of experimentally obtained deposit on the flat substrate[113].

Fig. 5.62 to **Fig. 5.64** show side view of the deposit profile growing for the three cases on the curved substrate, in SprayWatch© diagnostics (a–c) and simulation (d–f) at different time frames. The length scale are adjusted to be the same. The deposit maximum peak thickness t_{pm} is evaluated at the selected time steps for each case in both simulation and experiments. The results are listed in **Table 5.9**. It can be seen that the author's code predicts the deposit profile growing trend well. The profiles present similar shapes between the experiment and the simulation.

Table 5.9 Comparison of maximum peak deposit thickness t_{pm} (mm) for three cases.

Case	Method	Time frame 1	Time frame 2	Time frame 3
1	Experiment	0.95	1.83	2.99
	Simulation	0.84	1.69	2.87
2	Experiment	0.57	1.05	1.67
	Simulation	0.49	0.88	1.58
3	Experiment	1.48	1.82	2.32
	Simulation	1.41	1.74	2.24

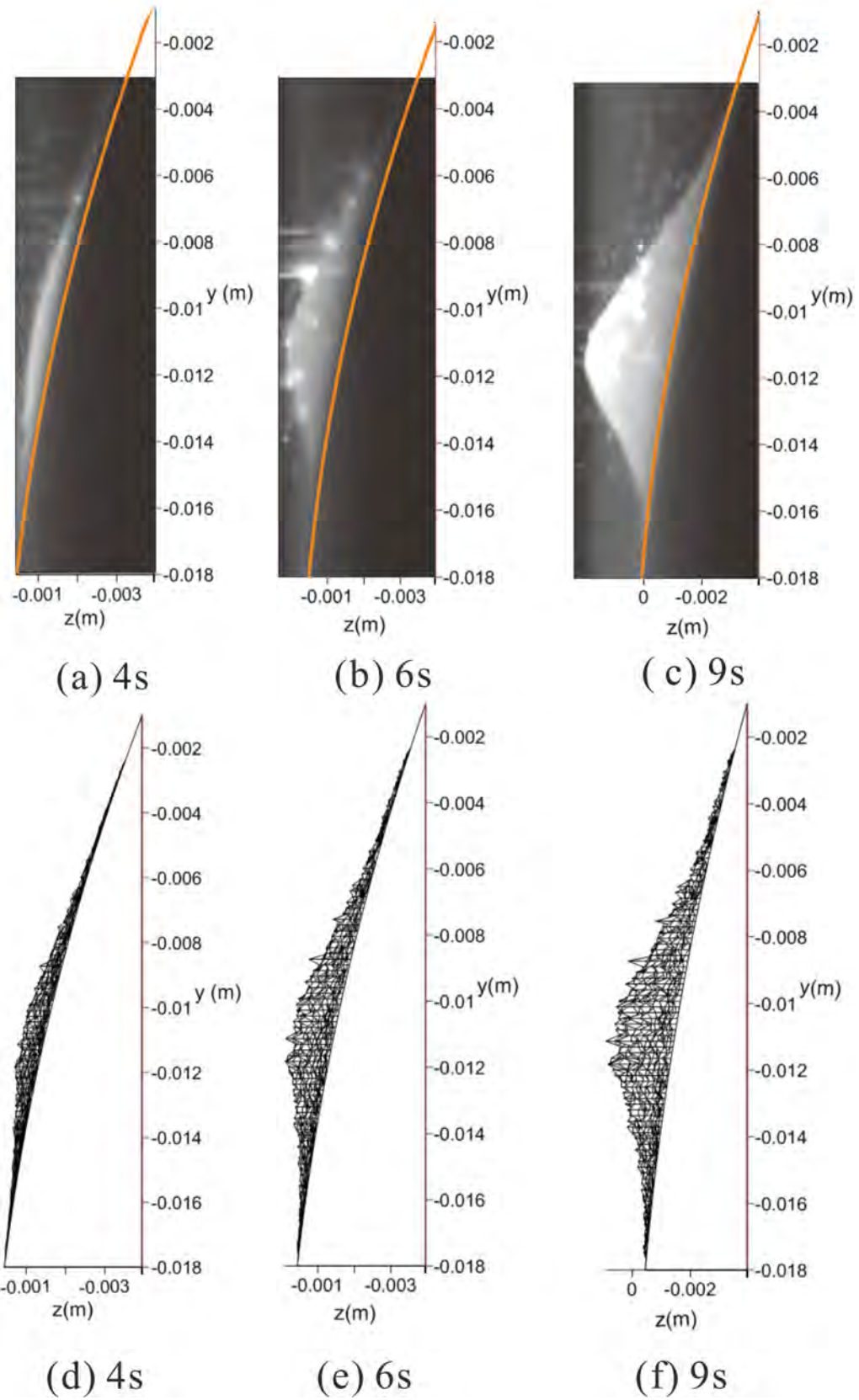


Fig. 5.62 Deposit profile growth for case 1 from (a-c) SprayWatch® diagnostics and (d-f) simulation . Time frame 1: 4s, time frame 2: 6s, time frame 3: 9s.

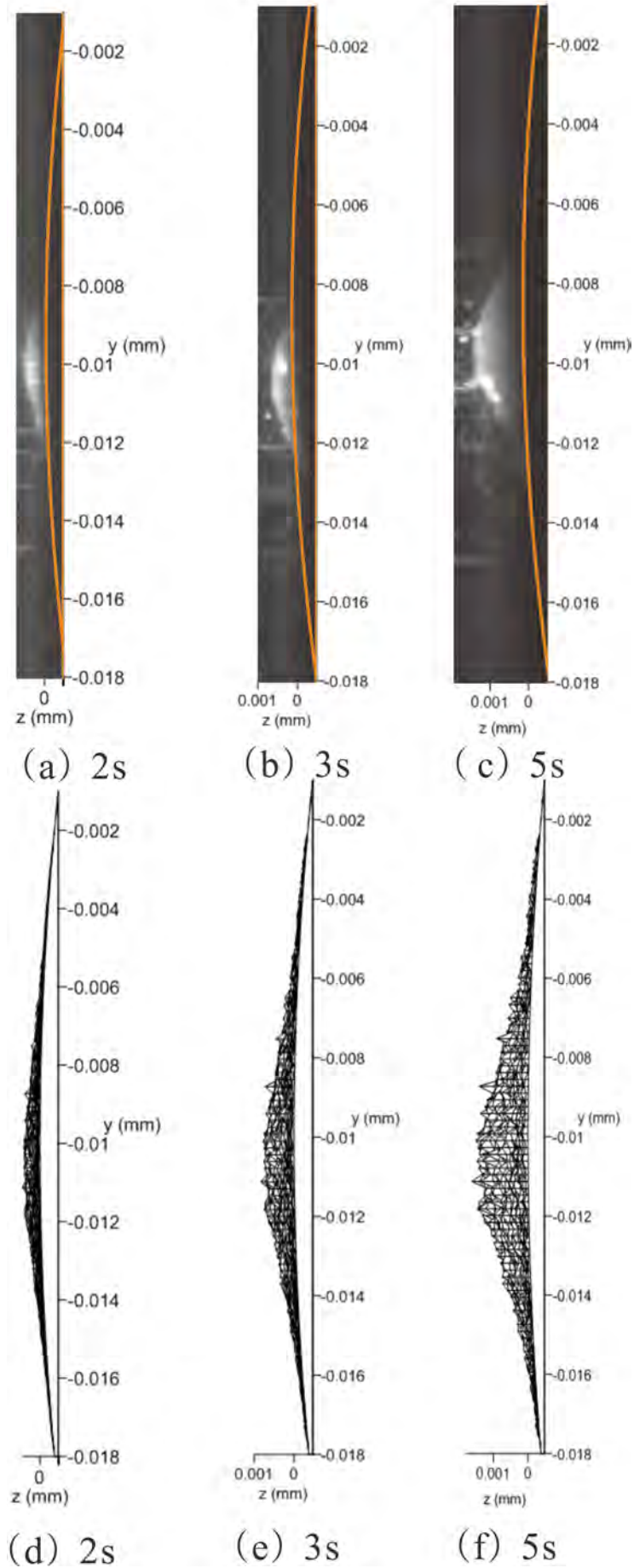


Fig. 5.63 Deposit profile growth for case 2 from SprayWatch© diagnostics (a-c) and simulation (d-f). Time frame 1: 2s, time frame 2: 3s, time frame 3: 5s.

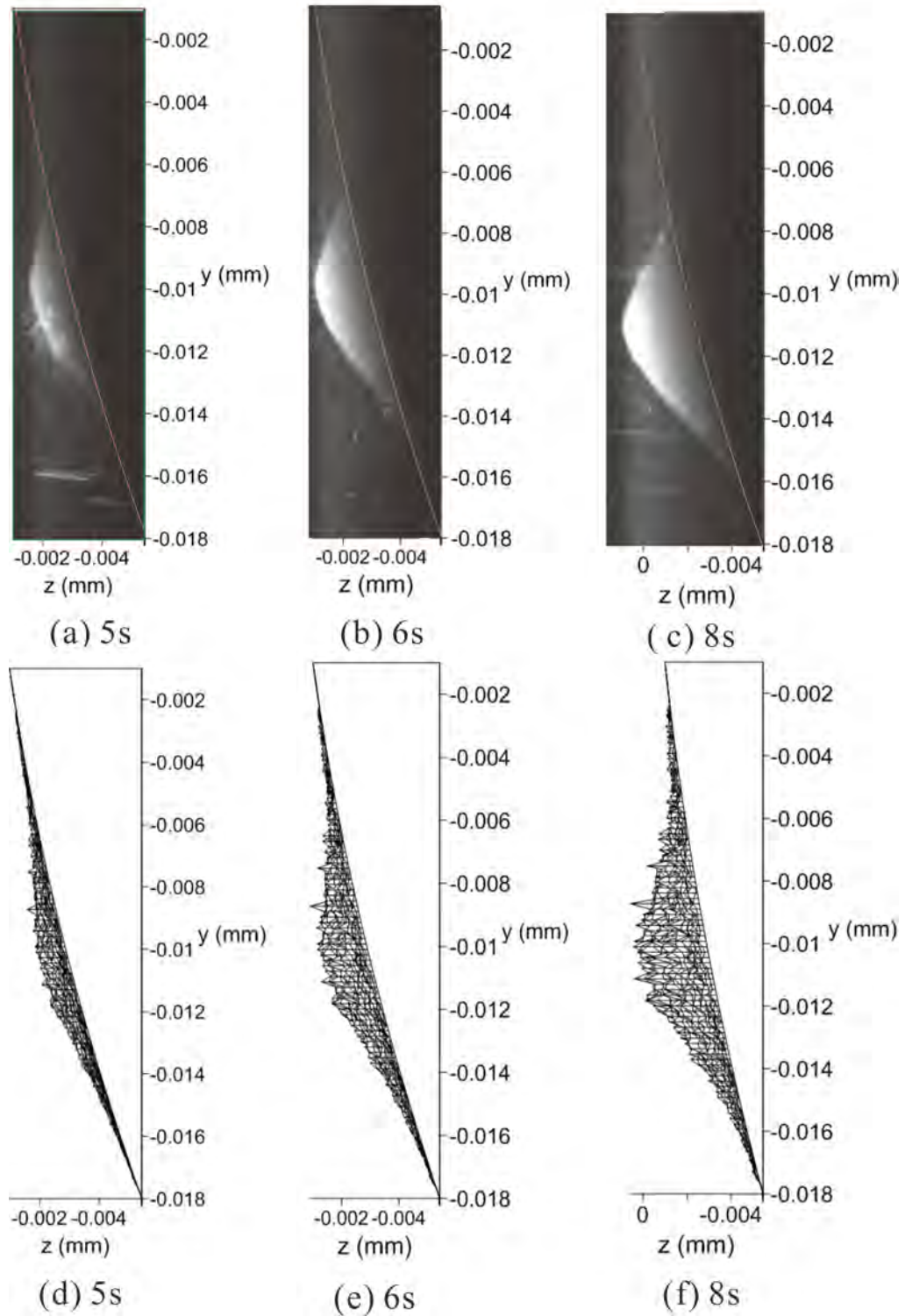


Fig. 5.64 Deposit profile growing for case 3 from SprayWatch© diagnostics (a-c) and simulation (d-f). Time frame 1: 5s, time frame 2: 6s, time frame 3: 8s.

Fig. 5.65 shows the deposit profiles from TalyScan measurements (a-c) and simulations (d-f) for the three cases. Because the TalyScan sets the starting point as origin, the position of which on the substrate surface is difficult to locate, these

profiles are used to show the shapes of these deposits, but not to quantify the deposit. The deposit profiles in the simulation has a square-like boundary, due to the particles selection mentioned in the methodology section.

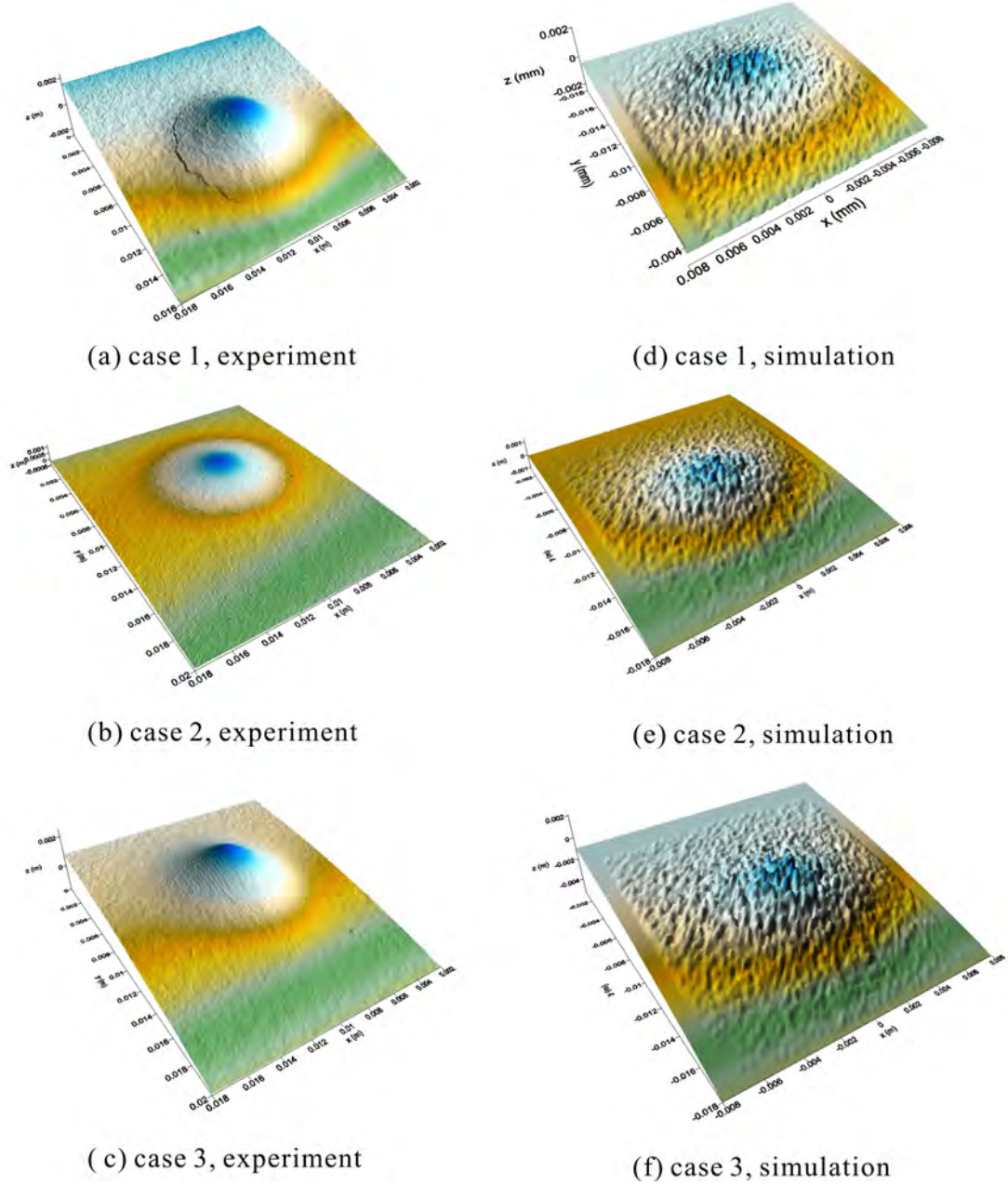


Fig. 5.65 3D profiles of deposit on case 1, 2 and 3 from TalyScan (a-c) and simulation (d-f).

The simulation results are in good agreement with the experimental measurements, except that the simulated profiles are not as smooth as their experimental counterparts. It could be attributed to the assumption that the splats overlap over others compactly. In reality, the splats are rigid body, i.e., pores form between these splats, making the deposit profile more smooth but with larger size.

Chapter 6

Conclusions and Future Work

6.1 Conclusions

6.1.1 Introduction

This thesis has presented work on three aspects of the plasma spraying coating process, namely 1) plasma and particle interaction, 2) droplet impact behavior on the substrate and 3) deposit formation. Combining these topics provide a significant investigation into the modeling of plasma spraying system. The important findings and contributions of the work will be summarized in three parts according to these aspects.

The first part concludes the plasma plume and in-flight particle behavior in freestream and with substrate obstruction. The influences of substrate inclusion and the particle size on the particle trajectory and temperature are also discussed.

The second part firstly discusses the complementary relationship between the simulation and experiments for the droplet impact behavior. It is then divided into two subparts: the droplet splatting behavior on the flat and the curved substrates. The former discussion mainly focuses on the type of formed splats and possible impacting phenomena causing these splats. In addition, the effect of velocity on splat spread factors is one of the concerns in this subpart. The part on curved substrates mainly focuses on the effect of impact angle and surface curvature on the splat shapes.

The third part describes the observation and analysis of deposit formation procedure and the final deposit shape resulting from the experiments. Simulation results are then compared with the experimental measurements, including the achievements and limitations.

The final part draws some overall conclusions and messages to the thermal spray research and technology, using concise sentences to conclude the the author's contributions.

6.1.2 Plasma plume and in-flight particle behavior

A numerical model of plasma spraying process has been modeled by Computational Fluid Dynamics (CFD) method using FLUENT® commercial package. The plasma plume and in-flight particle parameters for freestream case are validated by experimental measurements. The plasma plume temperature and velocity field along the plasma torch axial axis compare well with the investigations from the literature. As for the in-flight particle behavior such as velocity, temperature and flight angle, the simulation results also agree well with the SprayWatch® on-line monitoring system measurement carried out by the author. Based upon this accepted validation, sufficient confidence is achieved on the basic model. Further exploration on the impact of curved substrate are conducted on the strength of the basic model.

In the simulation, curved substrates with different sizes and orientations are introduced into the plasma plume to examine the effect of the substrate curvature and shape on the plasma flow field and in-flight particle behavior. It is found that the plasma flow temperature and velocity remains unaffected by the substrate inclusion until a short distance in front of the substrate. The substrates with larger curvature result in all upward-reversing flow (in Y direction) along the substrate front surface for concave case or a wave at rear of the substrate for convex case. Plasma velocity is more affected by the substrate obstruction than the plasma temperature.

Smaller particles are found to be more susceptible to the diverging flow caused by the substrate. There exists a threshold particle size of $10\text{ }\mu\text{m}$, above which there is no significant effect of flow change on the particle trajectory. Such small particles have low mass inertia, hence are very susceptible to influences of flow. For the commercial powders used in the current work, the particle size range are above the threshold. Thus the substrate inclusion has almost no effect on the particles spatial distribution and parameters. Smaller particles also tend to achieve

higher temperature comparing with larger particles due to their low thermal inertia. Simulations on droplet impact and deposit formation use the particles data in the freestream from SprayWatch© diagnostics and FLUENT© simulations respectively.

6.1.3 Droplet splatting behavior on flat and curved substrate

Numerical and experimental work is carried out to investigate the droplet splatting morphology on flat and curved substrates. The numerical model is developed using commercial computational fluid dynamics package Flow-3D®. The simulated spread factor and aspect ratio fall in the range of the experimental measurements. The experiments show that the aspect ratio increases with the impact angle while the spread factor remains unaffected. This finding is further investigated in the simulation.

6.1.3.1 Droplet splatting behavior on flat substrate

Different types of splats (near-perfect, minor splashing and flower-like) are observed under scanning electronic microscope (SEM) and confocal imaging profiler. From simulation, it is also found that the spread factor mainly increases with the Reynolds number. The solidification is affected by the droplet temperature, substrate temperature and interface heat transfer coefficient, thus modifies the morphology of the final splat. Higher droplet temperature, substrate temperature and lower interface heat transfer promotes the splat fringe elevation by lowering the fluid viscosity decrease rate. This in turn maintains the low viscosity at the highly fluid state. Accompanying phenomenon is the splat receding caused by the surface tension effects. The hypotheses of a two-layer characteristic during droplet impact is proposed from the simulation results. Higher velocity increases the possibility of long fingers formation, which occurs at the early stage of the impact; while the fluid layer on top of the solidified base layer results in short fingers characteristic.

From simulation the droplet velocity input is explicit, an equation of spread factor ξ can be developed with respect to the droplet velocity:

$$\xi = 1.1532V^{0.24} \quad (6.1)$$

where V is the droplet impact velocity.

The equation can be modified with respect to the dimensionless number Re

$$\xi = 0.7663Re^{0.24} \quad (6.2)$$

Which gives comparable values of the scaling factor and exponent to the literature.

6.1.3.2 Droplet splatting behavior on curved substrate

The simulation shows that the splat spread factor remains almost the same on the curved surfaces with different curvatures, if the curvature is less than a threshold of 2000 m^{-1} . The spread factor is also not significantly affected by impact angle. However, the splat elongates to an elliptical shape under an oblique impact. The elongation degree (given by the elongation factor) increases with the impact angle. It is found the impact point sometimes deviates far away from the elliptical splat focus point. The elongation factor χ is introduced to determine the splat center from the impact point location and has the correlation with the impact angle as the equation below:

$$\chi = 0.04147\theta - 0.096 \quad (6.3)$$

where θ is the droplet impact angle.

Simulated aspect ratio ζ also can be correlated with the impact angle. In order to include the droplet velocity effect in the deposit growth code, an equation is derived from the experimental results:

$$\zeta = 0.93146 + 0.01684\theta - 2.70151E - 4\theta^2 + 4.30331E - 6\theta^3 \quad (6.4)$$

The deduced relations of spread factor, aspect ratio and elongation factor are used to compute the splat shape in the deposit code.

6.1.4 Simulation and Experiment on Deposit Formation

Rebounding and secondary depositing phenomena are observed from the images captured by SprayWatch®. The rebounding phenomena is one of the factors

affecting the deposition efficiency. The secondary depositing after initial rebound may cause the depositing area shift and expand.

It is noticed that the deposits have a halo characteristic. Due to the particles spatial distribution, the deposit fades out continuously outwards. Thus it is difficult to define a real boundary of the deposit. But an inner circular boundary of the deposit is clearly observed. This structure characteristic helps the author to decrease the computation area of the deposition code, which significantly improves the code efficiency.

The predicted deposit increases with time, presenting similar shapes and growth tendency with the experimental measurements. The peak deposit thicknesses are close to the experiments, but show lower values consistently than the measurements, which are caused by the splat overlapping strategy in the code.

6.1.5 Contributions

- The Ansys Fluent simulation model could help to adjust the spray parameters in the practical thermal spray process, such as the input power, current and spray distance, to the user-desired range. The process parameters and its effect on the particle trajectory will lead to improvement of deposition efficiency.
- The work on the single splat formation improves our insight into the elementary aspects of the thermal spray process. Discussion on the physics underlying the splat formation may provide the other researchers some ideas worthy of further work. Besides, it provides helpful information on other high-speed droplet impact applications, such as soldering of multi-grid flip chip assembly in the semiconductor industry, paint spraying, ink jet printing and micro fluidics to name a few.
- The simulation model on the deposit formation may be helpful in the study of the deposit topological and mechanical properties of thermal spray coatings. Moreover, it may be useful for the optimization of processing conditions in thermal spray practices. Incidentally, the effort to consider the previous

deposit profile as the substrate for the latter incoming particles may provide an alternative idea for coating formation modeling.

6.2 Suggested Future Work

The work presented in this thesis brings insights into new exciting areas that should be investigated. These would provide suggestions of possible investigation directions. Moreover, it is necessary to do some improvements on the current work, if possible. All these will be listed below:

- The author's code for the deposit formation is practicable to model and predict deposit profile geometric characteristics and its growth with time. Currently the particles flight angle is assumed to be 0° (i.e., perpendicular to the virtual plane). In the future, the code can be improved by considering the particle in-flight directions. The individual impact point can be computed from the intersection of the particle trajectory and the virtual plane, taking the particle velocity at impact and the updated deposit profile. This procedure will make the simulation more realistic.
- The author's code can be further improved to include porosity. From the published literature, there are several different sources of porosity, such as peripheral curl up of individual splats, entrapment of gas between splats and unmelted particles presence. Experiments can be carried out to investigate the intersplat characteristics. Simulations by Flow-3D® also can be implemented as a complement to the experiments.
- The particle rebound and secondary depositing can be further investigated. If possible, a model can be developed to evaluate these phenomena, in order to determine the amount of particles involved in deposition in the simulation.

Appendix A

List of Publications

- T.Ba, C.W.Kang and H.W.Ng. Numerical study of the plasma flow field and Particle In-flight Behavior with the Obstruction of a Curved Substrate. *Journal of Thermal Spray Technology*,18:858–874,2009.
- T.Ba, H.W.Ng and C.W.Kang. Numerical simulation of the plasma flow and particle behavior with inclusion of curved substrates in the plasma spray process. *Proceedings of the 4th Asian Thermal Spray Conference*, Xi'an, China:219–224, October 2009.
- T.Ba, H.W.Ng and C.W.Kang. Single splat splatting behavior under plasma spray. *International Union of Materials Research Societies' International Conference in Asia 2011*, Taipei:Accepted, September 2011.

Appendix B

Governing Differential Equation for Plasma Flow

The rate of change of x -momentum of the fluid element equals the total force in the x -direction on the element due to surface stresses and the rate of increase of x -momentum due to sources; the x -component of the momentum equation is as below:

$$\frac{\partial(\rho u)}{\partial t} + \nabla(\rho \vec{u}u) = \frac{\partial(-p + \tau_{xx})}{\partial x} + \frac{\partial\tau_{yx}}{\partial x} + \frac{\partial\tau_{zx}}{\partial z} + S_{Mx} \quad (\text{B.1})$$

In a Newtonian fluid, the viscous stresses are proportional to the rates of deformation. In the case of incompressible flow, the nine viscous stress components, six of which are independent, are:

$$\begin{cases} \tau_{xx} = 2\mu \frac{\partial u}{\partial x} \\ \tau_{yy} = 2\mu \frac{\partial v}{\partial y} \\ \tau_{zz} = 2\mu \frac{\partial w}{\partial z} \\ \tau_{xy} = \tau_{yx} = \mu \left(\frac{\partial u}{\partial y} + \frac{\partial v}{\partial x} \right) \\ \tau_{xz} = \tau_{zx} = \mu \left(\frac{\partial u}{\partial z} + \frac{\partial w}{\partial x} \right) \\ \tau_{yz} = \tau_{zy} = \mu \left(\frac{\partial v}{\partial z} + \frac{\partial w}{\partial y} \right) \end{cases} \quad (\text{B.2})$$

Substituting Equation B.2 into Equation B.1:

$$\begin{aligned} \frac{\partial(\rho u)}{\partial t} + \nabla(\rho \vec{u}u) &= -\frac{\partial p}{\partial x} + \frac{\partial}{\partial x} \left(2\mu \frac{\partial u}{\partial x} \right) + \frac{\partial}{\partial y} \left[\mu \left(\frac{\partial u}{\partial y} + \frac{\partial v}{\partial x} \right) \right] + \frac{\partial}{\partial z} \left[\mu \left(\frac{\partial u}{\partial z} + \frac{\partial w}{\partial x} \right) \right] + S_{Mx} \\ \frac{\partial(\rho u)}{\partial t} + \nabla(\rho \vec{u}u) &= -\frac{\partial p}{\partial x} + \frac{\partial}{\partial x} \left(\mu \frac{\partial u}{\partial x} \right) + \frac{\partial}{\partial y} \left(\mu \frac{\partial u}{\partial y} \right) + \frac{\partial}{\partial z} \left(\mu \frac{\partial u}{\partial z} \right) \\ &\quad + \left[\frac{\partial}{\partial x} \left(\mu \frac{\partial u}{\partial x} \right) + \frac{\partial}{\partial y} \left(\mu \frac{\partial v}{\partial x} \right) + \frac{\partial}{\partial z} \left(\mu \frac{\partial w}{\partial x} \right) \right] + S_{Mx} \\ \frac{\partial(\rho u)}{\partial t} + \nabla(\rho \vec{u}u) &= -\frac{\partial p}{\partial x} + \nabla(\mu \nabla u) + S_{Mx} \end{aligned} \quad (\text{B.3})$$

For a steady, turbulent flow and without additional source to increase the momentum in x -direction, Equation B.3 can be rewritten as

$$\nabla(\rho \vec{u}u) = \nabla[(\mu_l + \mu_t)\nabla u] - \frac{\partial p}{\partial x} \quad (\text{B.4})$$

Comparing **Equation B.4** with the general form of governing equations given in **Equation 4.1**, the diffusion coefficient Γ_ϕ equals $\mu_l + \mu_t$ and the source term contains $-\frac{\partial p}{\partial x}$.

Appendix C

Thermodynamic and Transport Properties of Gases

C.1 Argon Gas

Argon gas was used as arc gas and carrier gas in the simulation. Its temperature-dependent properties of density, specific capacity, thermal conductivity and viscosity are presented in Fig. C.I.

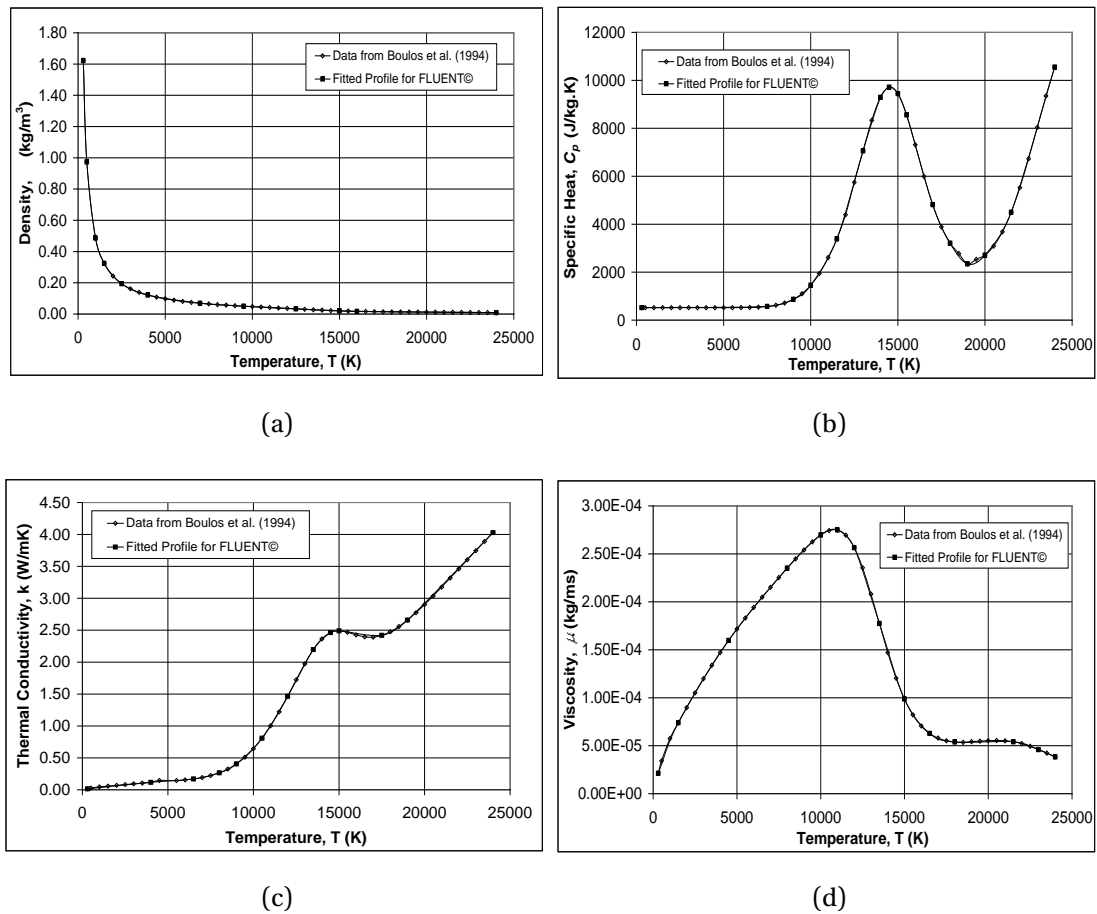


Fig. C.I Variation of argon gas (a) density (b) specific heat (c) thermal conductivity and (d) viscosity with respect to temperature.

C.2 Air

Similar to argon gas, thermodynamic and transport properties of air are presented in Fig. C.II.

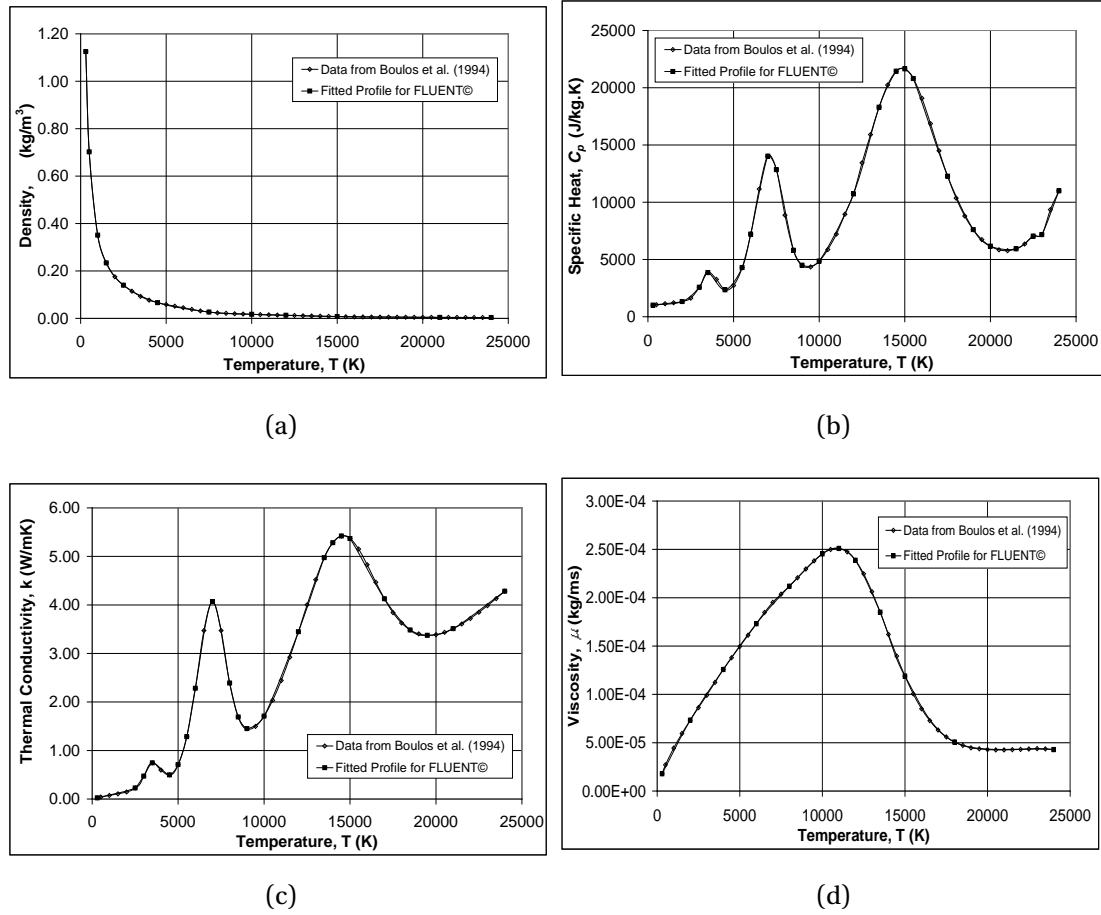


Fig. C.II Variation of air gas (a) density (b) specific heat (c) thermal conductivity and (d) viscosity with respect to temperature.

C.3 Mixture of Gases

Mixing law of different gases are listed below.

- Mixture Density

$$\rho = \frac{\sum_n V_n \rho_n}{\sum_n V_n} = \frac{\sum_n \frac{Y_n}{\rho_n} \rho_n}{\sum_n \frac{Y_n}{\rho_n}} = \frac{1}{\sum_n \frac{Y_n}{\rho_n}}$$

- Mixture Specific Heat

$$C_p = \frac{\sum_n Y_n C_{pn}}{\sum_n Y_n} = \sum_n Y_n C_{pn}$$

- Mixture Thermal Conductivity

$$k = \frac{\sum_n Y_n C_{pn}}{\sum_n Y_n} = \sum_n Y_n C_{pn}$$

- Mixture Viscosity

$$\mu = \frac{\sum_n Y_n \mu_n}{\sum_n Y_n} = \sum_n Y_n \mu_n$$

where V_n is the volume fraction and Y_n the mass fraction for species n .

Appendix D

Input Data Calculation for FLUENT© Simulation

Except for the gas properties, some other input data for Fluent simulation is calculated as below.

- Turbulence intensity at arc gas inlet. Argon gas volume flow rate $Q = 72 \text{ slm} = 1.20 \times 10^{-3} \text{ m}^3/\text{s}$.

$$U = \frac{Q}{A} = \frac{1.2 \times 10^{-3}}{\frac{\pi}{4}(0.008)^2} = 23.8732 \text{ m/s}$$

$$Re_{HD} = \frac{\rho_{Ar} U D_{noz}}{\mu_{Ar}} = \frac{1.6228 \times 23.8732 \times 8 \times 10^{-3}}{2.1250 \times 10^{-5}} = 14585.0086$$

$$\text{Turbulence Intensity} = 0.16(Re_{HD})^{-0.125} = 0.16 \times 14585.0086^{-0.125} = 4.83\%.$$

- Turbulence intensity at carrier gas inlet. Argon gas volume flow rate $Q = 4.20 \text{ slm} = 7 \times 10^{-5} \text{ m}^3/\text{s}$.

$$U = \frac{Q}{A} = \frac{7 \times 10^{-5}}{\frac{\pi}{4}(0.003)^2} = 9.9030 \text{ m/s}$$

$$Re_{HD} = \frac{\rho_{Ar} U D_{noz}}{\mu_{Ar}} = \frac{1.6228 \times 9.9030 \times 3 \times 10^{-3}}{2.1250 \times 10^{-5}} = 2268.7890$$

$$\text{Turbulence Intensity} = 0.16(Re_{HD})^{-0.125} = 0.16 \times 2268.7890^{-0.125} = 6.09\%.$$

- Power output Based on the operating conditions stated in Table ??, Current input 900A, Voltage 35V,

$$\text{Power Input} = UI = 900 \times 35 = 31.5 \text{ kW}$$

While the torch efficiency is 67%,

$$\text{Power Output} = 31.5 \times 0.67 = 21.11 \text{ kW}.$$

- Geometry dimension. Torch diameter is 8 mm, length is 10 mm.

$$\text{Torch volume} = \frac{\pi \times 0.008^2}{4} \times 0.01 = 5.0265 \times 10^{-7} \text{ m}^3.$$

- Energy source. Energy source for Fluent input is quantified in energy per unit volume

$$\frac{\text{Energy}}{\text{Volume}} = \frac{21.11 \times 10^3}{5.0265 \times 10^{-7}} = 4.1997 \times 10^{10} \text{ W} \cdot \text{m}^{-3}$$

Appendix E

Liquidus and Solidus Temperature of YSZ

The generally accepted melting point for pure zirconia is 2715°C[16], which always appears in the materials suppliers' data-sheets. The addition of yttria may cause this temperature to change. As the molecular weight of zirconia is 123.22, and that of Yttria is 225.81, the mole fraction of yttria in 8wt% YSZ is

$$\frac{\frac{8}{\frac{225.81}{92}}}{\frac{8}{\frac{225.81}{92}} + \frac{92}{123.22}} \times 100\% = \frac{0.03543}{0.03543 + 0.74661} \times 100\% = 4.53\% \quad (\text{E.1})$$

From the phase diagram of Yttria-Zirconia system (**Fig. E.I**), at 4.53mole% yttria composition, the liquidus temperature is about 3031K(2758°C), and the solidus temperature is about 2978K(2705°C).

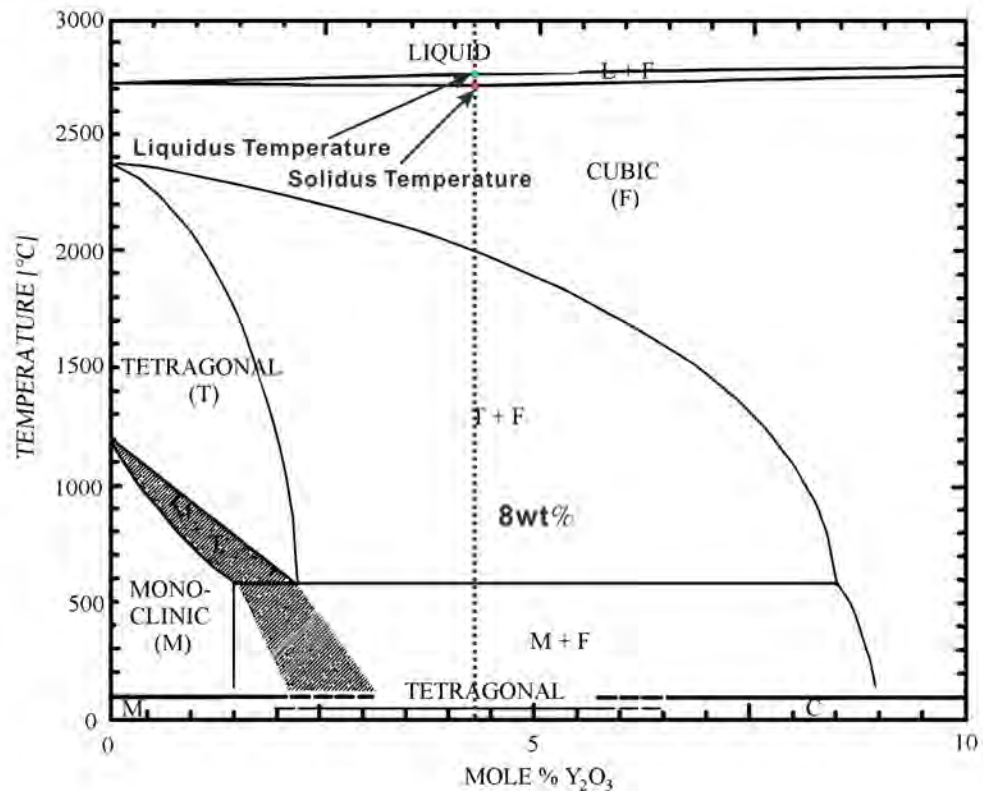


Fig. E.I Equilibrium phase diagram of Yttria-Zirconia system

Appendix F

The Ellipse Circumference Approximation

The ellipse circumference S is used to evaluate the elliptical splat major and minor radius. It is necessary to find an effective and relatively accurate method to approximate the value. The following methods are short review of Approximations of Ellipse Perimeters by Stanisav Sykora^{II}.

By elementary integration methods, the circumference of an ellipse

$$\frac{x^2}{a^2} + \frac{y^2}{b^2} = 1 \quad (\text{F.1})$$

is expressed as

$$S(a,b) = 4a \int_0^{\frac{\pi}{2}} \left(1 - \frac{a^2 - b^2}{a^2} \sin^2 \theta\right)^{0.5} d\theta \quad (\text{F.2})$$

where a and b are the major and minor radius of the ellipse respectively[132].

However, the evaluation of **Equation F.2** through infinite series or fractions is computationally inefficient. In addition, it is not easy for the reverse calculation of a and b in the current work. For this reason, an approximation to $S(a,b)$ using simple algebraic expressions is necessary.

Johannes Kepler used the arithmetic mean \sqrt{ab} as an equivalent radius to approximate the circumference:

$$S(a,b) = 2\pi\sqrt{ab} \quad (\text{F.3})$$

Leonhard Euler replaced the arithmetic mean with a quadratic mean $\sqrt{(a^2 + b^2)/2}$:

$$S(a,b) = 2\pi \sqrt{\frac{a^2 + b^2}{2}} \quad (\text{F.4})$$

Quadratic approximation is a hybrid between Kepler's geometric-mean approximation (**Equation F.3**) and Euler's square-mean approximation

^{II} <http://www.ebyte.it/library/docs/math05a/EllipsePerimeterApprox05.html>

(**Equation F.4**). A generalized quadratic mean $Q(a,b,w)$ dependent on a parameter w is defined:

$$\sqrt{w \frac{a^2 + b^2}{2} + (1 - w)ab} \quad (\text{F.5})$$

For $w = 0$, the value is the geometric mean; for $w = 1$ the value is the square mean.

The best approximation for the ellipse perimeter is obtained when $w = 0.7966106$.

Appendix G

2D Cartesian Coordinates Transformation

In the Real-time Substrate Node Model (RT-SNM) code, one of the major constituents is the 2D Cartesian coordinates transformation. This part will depict the point coordinate transformation between two 2D Cartesian coordinates.

In the RT-SNM code, the points on the deposit profile are projected onto the $x - y$ two dimensional coordinates, which is called “general coordinate system”. Take one of such points P as example, its coordinates in the general coordinate system (O, i, j) is (x, y) , as shown in **Fig. G.I**. A new coordinate system (O', i', j') , like the “splat coordinate system” is introduced. Point P becomes point P' in the new coordinate system, whose coordinate is (x', y') . The coordinates of the origin of the new coordinate system O' in the general coordinate system is (a, b) and the angle between i and i' is α .

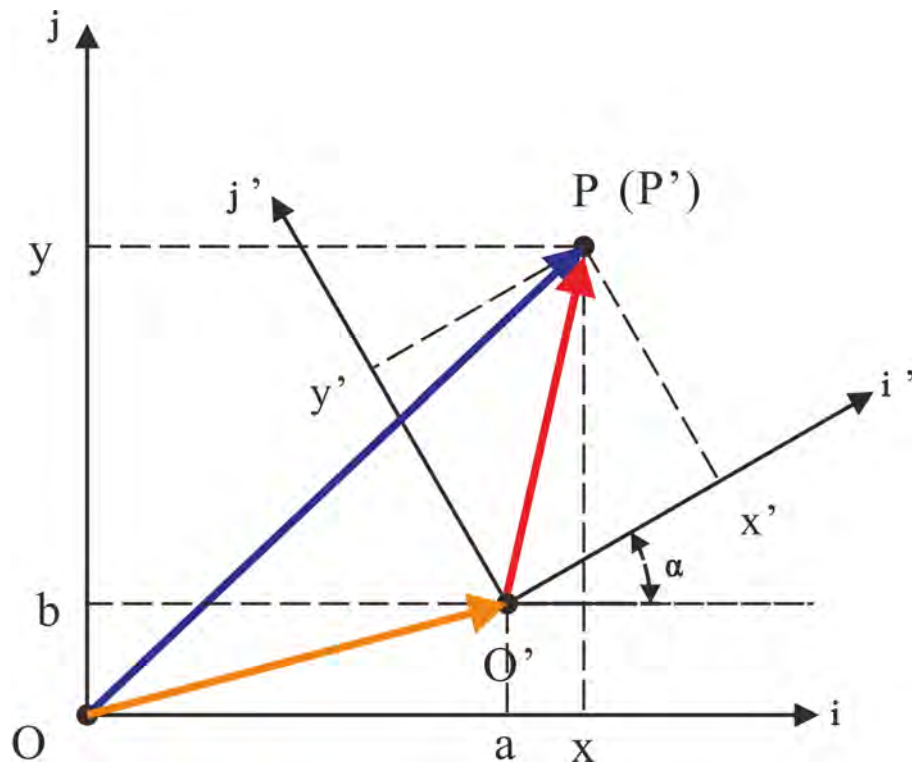


Fig. G.I Illustration of 2D Cartesian coordinate transformation.

The coordinates (x, y) in the general coordinate system can be expressed as formulae of the coordinates (x', y') in the new coordinate system, as **Equation G.1**.

$$\begin{cases} x &= x' \cos \alpha - y' \sin \alpha + a \\ y &= y' \sin \alpha + x' \cos \alpha + b \end{cases} \quad (\text{G.1})$$

Reversely, the coordinates (x', y') in the new coordinate system can be expressed as formulae of the coordinates (x, y) in the general coordinate system, as **Equation G.2**.

$$\begin{cases} x' &= (x - a) \cos \alpha + (y - b) \sin \alpha \\ y' &= -(x - a) \sin \alpha + (y - b) \cos \alpha \end{cases} \quad (\text{G.2})$$

Appendix H

The Deposition Code

```
1  #include<fstream>
2  #include<iostream>
3  #include<string>
4  #include<math.h>
5  #include <sstream>
6  using namespace std;
7  const int num = 298760;
8  const double gr = 0.000005;
9  const int xmin = -1600;
10 const int xmax = 1600;
11 const int ymin = -3600;
12 const int ymax = -200;
13 const int f = 0.00001/gr;
14 const int nx = xmax - xmin +1;
15 const int ny = ymax - ymin +1;
16 double particle[num][22];
17 double profile[3201][3401]={0};
18 double r1[2],r2[2],r3[2],r4[2],t[2],s[4];
19 int vert[num][2];
20 int dt = 0.5,sp = 30;
21 /** time interval in the unit second and the calculation round ***/
22 int i,j,l,m,n,k;
23 double theta,proj;
24 double ynul= -4.31e-3;
25 double w1[4],w2[4];
26 int facet;
27 double xg, yg, xpri, ypri, x_coor,y_coor;
```

```
28  int imp(double x, double y)
29  {
30      if (x+y-int(x)-int(y)>1)
31          return -1;
32      else
33          return 1;
34  }
35  double outMax(double *w)
36  {
37      double temp;
38      temp=w[0];
39      for (l=1;l<4;l++){
40          if(w[l]>temp)
41              temp = w[l];
42      }
43      return temp;
44  }
45  double outMin(double *w)
46  {
47      double temp;
48      temp=w[0];
49      for (l=1;l<4;l++){
50          if(w[l]<temp)
51              temp = w[l];
52      }
53      return temp;
54  }
55  int nor(double x)
56  {
57      if (x==0)
58          return 0;
```



```

59     else
60         return x/fabs(x);
61 }
62 void R(double px, double py, double qx, double qy, double alpha, double
63 *r)    //transform splat coordinate to substrate coordinate.
64 {     r[0] = px*cos(alpha)- py*sin(alpha) + qx;
65     r[1] = px*sin(alpha)+ py*cos(alpha) + qy;
66     }
67 void T(double px, double py, double qx, double qy, double alpha,
68 double *t)
69 {
70     t[0] = (px-qx)*cos(alpha)+(py-qy)*sin(alpha);
71     t[1] = (py-qy)*cos(alpha)-(px-qx)*sin(alpha);
72 }
73 int main()
74 {
75     /*##### Read data file and create output files #####*/
76     ifstream fin("particle.txt");
77     for (i=0; i<3201; i++)    //initialize the profile
78     {for (j=0; j<3401; j++)
79         profile[i][j]=-8.568e-2+sqrt(pow(8.568e-2,2)
80             -pow(((j+ymin)*gr-ynul),2));}
81     for (i=0; i<num;i++)    //initialize the particle data
82     {for(j=0;j<5;j++)
83         {fin>> particle[i][j];
84         }
85     }
86     /**** calculate the absolute impact position on the grid.****/
87     for (i=0; i<num; i++)
88         {particle[i][5] = particle[i][0]/gr;
89         particle[i][6] = particle[i][1]/gr;    // impact location y.

```

```

90         }
91     for (i=0; i<num; i++)
92     {
93         facet = imp(particle[i][5],particle[i][6]);
94         //determine the facet
95         vert[i][0] = int(particle[i][5] + 0.5*(1-facet))-xmin+1;
96         //determine the facet vertex x coordinate on grid
97         vert[i][1] = int(particle[i][6] + 0.5*(1-facet))-ymin+1;
98         //determine the facet vertex y coordinate on grid
99     }
100     //***** until here, the common procedure is done.
101     The following is time repetition dependent *****
102     for (k=1; k<=sp; k++)
103     {
104         std::stringstream ss;
105         ss<<"Deposit"<<k<<".txt";
106         // sh<<"Heposit"<<k<<".txt";
107         ofstream fout(ss.str().c_str());
108         // ofstream fouth(sh.str().c_str());
109         for (i=0; i<num; i++)
110         {
111             for (j=-f;j<f;j++)
112             {
113                 particle[i][7] = particle[i][7] + profile[vert[i][0]-f][vert[i][1]+j]
114                 - profile[vert[i][0]+f][vert[i][1]+j];
115                 particle[i][8] = particle[i][8] + profile[vert[i][0]+j][vert[i][1]-f]
116                 - profile[vert[i][0]+j][vert[i][1]+f];
117             }
118             particle[i][7] = particle[i][7]/(2*f);
119             particle[i][8] = particle[i][8]/(2*f);
120             particle[i][9] = atan(sqrt(pow(particle[i][7],2)

```

```

121 + pow(particle[i][8],2));
122 //the facet inclined angle
123     }
124     for (i=0; i<num; i++)
125     {
126         theta = particle[i][9]*180/3.1415926;
127         proj = cos(particle[i][9]);
128         particle[i][10] = 0.93146 + 0.01684*theta -2.70151e-4*pow(theta,2)
129 +4.30331e-6*pow(theta,3);    //aspect ratio
130         if (particle[i][10]<1)
131         {
132             particle[i][10]=1;
133         }
134         particle[i][11] = 0.5* particle[i][2]*sqrt(particle[i][10]);
135 //major axis
136         particle[i][12] = 0.5* particle[i][2]/sqrt(particle[i][10]);
137 //minor axis
138         particle[i][13] = sqrt(pow(particle[i][11],2)
139 - pow(particle[i][12],2));    //ellipse c
140         if (particle[i][8] == 0)    // transformation angle
141         {
142             particle[i][16] = 0;
143         }
144         else if ((particle[i][8]!=0) && (particle[i][7]==0))
145         {
146             particle[i][16] = 1.5707963;
147         }
148         else
149             particle[i][16] = atan(particle[i][8]/particle[i][7]);
150         particle[i][14] = particle[i][0] + particle[i][13]* proj
151 *nor(particle[i][7])*cos(particle[i][16]);    //ellipse center x

```

```

152     particle[i][15] = particle[i][1] + particle[i][13]
153     *proj*sin(particle[i][16]); //ellipse center y
154     particle[i][17] = 2*pow(particle[i][3],3)/(3*proj*
155     pow(particle[i][2],2));
156     // thickness of single splat
157     particle[i][11] = particle[i][11]*proj; // aprime
158     }
159     for (i=0; i<num; i++)
160     { R(particle[i][11],particle[i][12],particle[i][14],
161         particle[i][15],particle[i][16],r1);
162         R((-particle[i][11]),particle[i][12],particle[i][14],
163         particle[i][15],particle[i][16],r2);
164         R(particle[i][11],(-particle[i][12]),particle[i][14],
165         particle[i][15],particle[i][16],r3);
166         R((-particle[i][11]),(-particle[i][12]),particle[i][14],
167         particle[i][15],particle[i][16],r4);
168         w1[0]= r1[0];
169         w1[1]= r2[0];
170         w1[2]= r3[0];
171         w1[3]= r4[0];
172         w2[0]= r1[1];
173         w2[1]= r2[1];
174         w2[2]= r3[1];
175         w2[3]= r4[1];
176         particle[i][18] = outMin(w1)/gr -1;
177         //boundary points gridization
178         particle[i][19] = outMax(w1)/gr +2;
179         particle[i][20] = outMin(w2)/gr -1;
180         particle[i][21] = outMax(w2)/gr +2;
181     }
182     for (i=0; i<num; i++)

```

```

183     {
184         for (m=int(particle[i][18]); m<int(particle[i][19]); m++)
185             {
186                 for (n=int(particle[i][20]); n<int(particle[i][21]); n++)
187                     { xg = m*gr;          //real position x
188                       yg = n*gr;          //real position y
189                       T(xg,yg,particle[i][14],particle[i][15],particle[i][16],t);
190                       if (pow((t[0]/particle[i][11]),2)
191                           + pow((t[1]/particle[i][12]),2)<=1)
192                           {
193                             profile[m-xmin+1][n-ymin+1] = profile[m-xmin+1][n-ymin+1]
194 + particle[i][17]*2.589e-4*particle[i][4]*dt/pow(particle[i][3],3);
195                           }
196                       }
197             }
198     }
199 for (n=0; n<ny; n++)
200     {   y_coor = (n + ymin)*gr;
201         for (m=0; m<nx; m++)
202             {x_coor = (m + xmin)*gr;
203               fout<<x_coor<<"\t"<<y_coor<<"\t"<<profile[m][n]<<endl;
204             }
205     }
206 fout.close();
207 //fouth.close();
208 }
209 return 0;
210 }

```

References

- [1] P. Fauchais, A. Vardelle and B. Dussoubs. Quo vadis thermal spraying?. *Journal of Thermal Spray Technology* , 10(1): 44–66, 2001.
- [2] L. Pawlowski. *The Science and Engineering of Thermal Spray Coatings*. Wiley, 2008.
- [3] K. A. Khor and Y. W. Gu. Thermal properties of plasma-sprayed functionally graded thermal barrier coatings. *Thin Solid Films* , 372(1-2): 104–113, 2000.
- [4] R. Dal Maschio, V. Sglavo, L. Mattivi, L. Bertamini and S. Sturlese. Indentation method for fracture resistance determination of metal/ceramic interfaces in thick tbc. *Journal of Thermal Spray Technology* , 3(1): 51–56, 1994.
- [5] M. Vardelle, A. Vardelle and P. Fauchais. Spray parameters and particles behavior relationships during plasma spraying. *Journal of Thermal Spray Technology* , 2: 79–91, 1993.
- [6] W. Zhang, L. Zheng, H. Zhang and S. Sampath. Study of injection angle and carrier gas flow rate effects on particles in-flight characteristics in plasma spray process: Modeling and experiments. *Plasma Chemistry and Plasma Processing* , 27(6): 701–716, 2007.
- [7] E. Pfender. Thermal plasma technology: Where do we stand and where are we going?. *Plasma Chemistry and Plasma Processing* , 19(1): 1–31, 1999.
- [8] J.V. Heberlein. Electrode phenomena in dc arcs and their influence on plasma torch design. *High Temperature Material Processes* , 6: 321–328, 2002.
- [9] J.R. Davis. *Handbook of Thermal Spray Technology*. ASM International, Materials Park, OH, 2004.
- [10] Praxair Surface Technologies Inc.. *Model 1264 Powder Feeder, Thermal Spray Products Catalogue.*, 1997.
- [11] C.C. Berndt. *Handbook of Thermal Spray Technology*. ASM International, 2004.
- [12] P. A. Vityaz', I. N. Ermolenko, I. L. Fedorova and T. M. Ul'yanova. Zirconia ceramics (review). *Powder Metallurgy and Metal Ceramics* , 28(12): 947–951, 1989.
- [13] R. C. GARVIE, R. H. HANNINK and R. T. PASCOE. Ceramic steel?. *Nature* , 258(5537): 703–704, 1975.
- [14] E. C. Subbarao, H. S. Maiti and K. K. Srivastava. Martensitic transformation in zirconia. *Physica Status Solidi (a)* , 21(1): 9–40, 1974.
- [15] H. G. Scott. Phase relationships in the zirconia-yttria system. *Journal of Materials Science* , 10(9): 1527–1535, 1975.
- [16] J.F. Shackelford and W. Alexander. *The CRC Material Science and Engineering Handbook*. CRC Press, Boca Raton, 1994.
- [17] J.F. Shackelford and W. Alexander. *The CRC Material Science and Engineering Handbook: Third Edition*. CRC Press, Boca Raton, 2001.
- [18] D. Simon and U. Pal. Mathematical modeling of a melt pool driven by an electron beam. *Metallurgical and Materials Transactions B* , 30(3): 515–525, 1999.
- [19] I. Ahmed and T. L. Bergman. Simulation of thermal plasma spraying of partially molten ceramics: Effect of carrier gas on particle deposition and phase change phenomena. *Journal of Heat Transfer* , 123(1): 188–196, 2001.
- [20] J. M. Lihmann and J. S. Haggerty. Surface tensions of alumina-containing liquids. *Journal of the American Ceramic Society* , 68(2): 81–85, 1985.

References

- [21] K. Shinoda, Y. Kojima and T. Yoshida. In situ measurement system for deformation and solidification phenomena of yttria-stabilized zirconia droplets impinging on quartz glass substrate under plasma-spraying conditions. *Journal of Thermal Spray Technology* , 14(4): 511-517, 2005.
- [22] J. D. Ramshaw and C. H. Chang. Computational fluid dynamics modeling of multi component thermal plasmas. *Plasma Chemistry and Plasma Processing* , 12(3): 299-325, 1992.
- [23] J. Mostaghimi and M.I. Boulos. Effect of frequency on local thermodynamic equilibrium conditions in an inductively coupled argon plasma at atmospheric pressure. *Journal of Applied Physics* , 68(6): 2643-2648, 1990.
- [24] V. Rat and J. F. Coudert. A simplified analytical model for dc plasma spray torch: influence of gas properties and experimental conditions. *Journal of Physics D: Applied Physics* , 39(22): 4799-, 2006.
- [25] E. Moreau, C. Chazelas, G. Mariaux and A. Vardelle. Modeling the restrike mode operation of a dc plasma spray torch. *Journal of Thermal Spray Technology* , 15(4): 524-530, 2006.
- [26] J. Trelles and J. Heberlein. Simulation results of arc behavior in different plasma spray torches. *Journal of Thermal Spray Technology* , 15(4): 563-569, 2006.
- [27] J. Trelles, E. Pfender and J. Heberlein. Multiscale finite element modeling of arc dynamics in a dc plasma torch. *Plasma Chemistry and Plasma Processing* , 26(6): 557-575, 2006.
- [28] S. E. Selezneva and M. I. Boulos. Supersonic induction plasma jet modeling. *Nuclear Instruments and Methods in Physics Research Section B: Beam Interactions with Materials and Atoms* , 180(1-4): 306 - 311, 2001.
- [29] C. Kang, H. Ng and S. Yu. Comparative study of plasma spray flow fields and particle behavior near to flat inclined substrates. *Plasma Chemistry and Plasma Processing* , 26(2): 149-175, 2006.
- [30] Fluent Inc.. *Fluent User's Guide*. Lebanon, 2001.
- [31] P. Eichert, M. Imbert and C. Coddet. Numerical study of an arh2 gas mixture flowing inside and outside a dc plasma torch. *Journal of Thermal Spray Technology* , 7(4): 505-512, 1998.
- [32] A. Fridman. *Plasma Chemistry*. Cambridge University Press, 2008.
- [33] C.K. Birdsall and A.B. Langdon. *Plasma Physics via Computer Simulation*. Adam Hilger, 1991.
- [34] R. Westhoff and J. Szekely. A model of fluid, heat flow, and electromagnetic phenomena in a nontransferred arc plasma torch. *J. Appl. Phys.* , 70(7): 3455-3466, 1991.
- [35] J. Szekely and R. Westhof. Recent advances in the mathematical modeling of transport phenomena in plasma systems. *Thermal Plasma Applications in Materials and Metallurgical Processing* , 55-72, 1992.
- [36] C. H. Chang and J. D. Ramshaw. Numerical simulations of argon plasma jets flowing into cold air. *Plasma Chemistry and Plasma Processing* , 13(2): 189-209, 1993.
- [37] K. Remesh, H.W. Ng and S. Yu. Influence of process parameters on the deposition footprint in plasma-spray coating. *Journal of Thermal Spray Technology* , 12(3): 377-392, 2003.
- [38] K. Remesh, S. Yu, H.W. Ng and C.C. Berndt. Computational study and experimental comparison of the in-flight particle behavior for an external injection plasma spray process. *Journal of Thermal Spray Technology* , 12(4): 508-522, 2003.
- [39] J. H. Park, J. Heberlein, E. Pfender, Y. C. Lau and J. Ruud et al.. Particle behavior in a fluctuating plasma jet. *Annals of the New York Academy of Sciences* , 891: 417-424, 1999.
- [40] B. Liu, T. Zhang and D. T. Gawne. Computational analysis of the influence of process parameters on the flow field of a plasma jet. *Surface and Coatings Technology* , 132(2-3): 202-216, 2000.

References

- [41] K.Y. Chen and M.I. Boulos. Turbulence in induction plasma modelling. *Journal of Physics D: Applied Physics* , 27(5): 946–, 1994.
- [42] F. A. Muggli, R. J. Molz, R. McCullough and D. Hawley. Improvement of plasma gun performance using comprehensive fluid element modeling: Part i. *Journal of Thermal Spray Technology* , 16(5): 677–683, 2007.
- [43] L.C. Li and W.D. Xia. Time-dependent 2D modeling of magnetron plasma torch in turbulent flow. *Plasma Science and Technology* , 10(3): 328–, 2008.
- [44] Y. C. Lee, Y. P. Chyou and E. Pfender. Particle dynamics and particle heat and mass transfer in thermal plasmas. part ii. particle heat and mass transfer in thermal plasmas. *Plasma Chemistry and Plasma Processing* , 5(4): 391–414, 1985.
- [45] R. Bolot, D. Sokolov, D. Klein and C. Coddet. Nozzle developments for thermal spray at very low pressure. *Journal of Thermal Spray Technology* , 15(4): 827–833, 2006.
- [46] K. Ramachandran, N. Kikukawa and H. Nishiyama. 3D modeling of plasma-particle interactions in a plasma jet under dense loading conditions. *Thin Solid Films* , 435(1-2): 298–306, 2003.
- [47] J. Mostaghimi, S. Chandra, R. Ghafouri-Azar and A. Dolatabadi. Modeling thermal spray coating processes: a powerful tool in design and optimization. *Surface and Coatings Technology* , 163-164: 1–11, 2003.
- [48] G. Gouesbet and A. Berlemont. Eulerian and lagrangian approaches for predicting the behaviour of discrete particles in turbulent flows. *Progress in Energy and Combustion Science* , 25(2): 133–159, 1998.
- [49] S. Joshi. Plasma spraying of wc-co part i: Theoretical investigation of particle heating and acceleration during spraying. *Journal of Thermal Spray Technology* , 2(2): 127–130, 1993.
- [50] K. Ramadan and P. Butler. Analysis of particle dynamics and heat transfer in detonation thermal spraying systems. *Journal of Thermal Spray Technology* , 13(2): 248–264, 2004.
- [51] M. Haim and H. Kalman. The effect of internal particle heat conduction on heat transfer analysis of turbulent gas-particle flow in a dilute state. *Granular Matter* , 10(4): 341–349, 2008.
- [52] C. T. Crowe. Numerical models for dilute gas-particle flows. *Journal of Fluids Engineering* , 104: 297–303, 1982.
- [53] V. V. Sobolev, J. M. Guilemany and A. J. Martín. In-flight behaviour of steel particles during plasma spraying. *Journal of Materials Processing Technology* , 87(1-3): 37–45, 1999.
- [54] E. Pfender and Y. C. Lee. Particle dynamics and particle heat and mass transfer in thermal plasmas. part i. the motion of a single particle without thermal effects. *Plasma Chemistry and Plasma Processing* , 5(3): 211–237, 1985.
- [55] R. Clift, J.R. Grace and M.E. Weber. *Bubbles, Drops, and Particles*. Dover Publications, 2005.
- [56] B. Waldie. Review of recent work on the processing of powders in high temperature plasmas. *The Chemical Engineer* , 3: 92–06, 1972.
- [57] Y. P. Wan, V. Prasad, G.-X. Wang, S. Sampath and J. R. Fincke. Model and powder particle heating, melting, resolidification, and evaporation in plasma spraying processes. *J. Heat Transfer* , 121(3): 691–699, 1999.
- [58] E. Bourdin, P. Fauchais and M. I. Boulos. Transient heat conduction to a single sphere under plasma conditions. *International Journal of Heat and Mass Transfer* , 26: 567–582, 1983.
- [59] H.B. Xiong, L.L.Zheng and L. Liand A. Vaidya. Melting and oxidation behavior of in-flight particles in plasma spray process. *International Journal of Heat and Mass Transfer* , 48(25-26): 5121–5133, 2005.
- [60] N. Singh, M. Razafinimanana and J.Hlina. Determination of plasma velocity from light fluctuations in a dc plasma torch. *Journal of Physics D: Applied Physics* , 33(3): 275–, 2000.

References

- [61] M. Vardelle, A. Vardelle, P. Fauchais and M. I. Boulos. Particle dynamics and heat transfer under plasma conditions. *AIChE Journal* , 34(4): 567–573, 1988.
- [62] J. Ma, S. Yu, H.W. Ng and Y.C. Lam. Some observations on particle size and velocity measurements using phase doppler anemometry in plasma spray. *Plasma Chemistry and Plasma Processing* , 24: 85-115, 2004.
- [63] J. Ma, S. Yu and H. W. Ng. The particle in-flight characteristics in plasma spraying process measured by phase doppler anemometry (pda). *Plasma Chemistry and Plasma Processing* , 25: 55-86, 2005.
- [64] P. Wang, S. Yu and H. W. Ng. Particle velocities, sizes and flux distribution in plasma spray with two powder injection ports. *Materials Science and Engineering A* , 383(1): 122–136, 2004.
- [65] K.T. Scott, R. Kingswell and D. Rickerby. *Advanced Surface Coatings: Handbook of Surface Engineering*. Blackie Academic and Professional, New York, 1991.
- [66] O.G. Engelman. Waterdrop collisions with solid surfaces. *Journal of Research of the National Bureau of Standards* , 54(5): 281-298, 1955.
- [67] Z. Levin and P. V. Hobbs. Splashing of water drops on solid and wetted surface: hydrodynamics and charge. *Phil. Trans. R. Soc. London A* , pages 555–585, 1971.
- [68] P.R. Gunjal, V.V. Ranade and R.V. Chaudhari. Experimental and computational study of liquid drop over flat and spherical surfaces. *Catalysis Today* , 79-80: 267–273, 2003.
- [69] J. E. Field, J. P. Dear and J. E. Ogren. The effects of target compliance on liquid drop impact.. *Journal of Applied Physics* , 65(2): 533, 1989.
- [70] L. Li, X. Y. Wang, G. Wei, A. Vaidya and H. Zhang et al.. Substrate melting during thermal spray splat quenching. *Thin Solid Films* , 468(1-2): 113–119, 2004.
- [71] M.Y. Zhang, H. Zhang and L. L. Zheng. Numerical investigation of substrate melting and deformation during thermal spray coating by sph method. *Plasma Chemistry and Plasma Processing* , 29(1): 55–68, 2009-02-01.
- [72] T. Wu, M. Bussmann and J. Mostaghimi. The impact of a partially molten ysz particle. *Journal of Thermal Spray Technology* , 18(5): 957–964, 2009-12-01.
- [73] O. G. Engel. Crater depth in fluid impacts. *J. Appl. Phys.* , 37(4): 1798–1808, 1966.
- [74] M. Rein. Phenomena of liquid drop impact on solid and liquid surfaces. *Fluid Dynamics Research* , 12(2): 61–93, 1993.
- [75] A.L. Yarin. Drop impact dynamics: Splashing, spreading, receding, bouncing.... *Annual Review of Fluid Mechanics* , 38(1): 159–192, 2006.
- [76] A.M. Worthington. *The Splash of a Drop*. Project Gutenberg, 1894.
- [77] M. Bussmann, J. Mostaghimi and S. Chandra. On a three-dimensional volume tracking model of droplet impact. *Phys. Fluids* , 11(6): 1406–1417, 1999.
- [78] S. Sikalo and E.N. Ganic. Phenomena of droplet-surface interactions. *Experimental Thermal and Fluid Science* , 31(2): 97 - 110, Second International Thermal Science Seminar (ITSS II).2006.
- [79] R. Dhiman and S. Chandra. Rupture of thin films formed during droplet impact. *Proceedings of the Royal Society A: Mathematical, Physical and Engineering Science* , 466(2116): 1229–1245, 2010.
- [80] S. L. Manzello and J. C. Yang. On the collision dynamics of a water droplet containing an additive on a heated solid surface. *Proceedings of the Royal Society of London. Series A: Mathematical, Physical and Engineering Sciences* , 458(2026): 2417–2444, 2002.

References

- [81] M. Vardelle, A. Vardelle, P. Fauchais and C. Moreau. Pyrometer system for monitoring the particle impact on a substrate during a plasma spray process. *Measurement Science and Technology*, 5(3): 205–, 1994.
- [82] N. Mehdizadeh, M. Lamontagne, C. Moreau, S. Chandra and J. Mostaghimi. Photographing impact of molten molybdenum particles in a plasma spray. *Journal of Thermal Spray Technology*, 14(3): 354–361, 2005.
- [83] A. McDonald, S. Chandra, M. Lamontagne and C. Moreau. Photographing impact of plasma-sprayed particles on metal substrates. *Journal of Thermal Spray Technology*, 15(4): 708–716, 2006.
- [84] A. McDonald, S. Chandra and C. Moreau. Photographing impact of plasma-sprayed particles on rough substrates. *Journal of Materials Science*, 43(13): 4631–4643, 2008.
- [85] H. Liu, E. Lavernia and R. Rangel. Numerical simulation of impingement of molten ti, ni, and w droplets on a flat substrate. *Journal of Thermal Spray Technology*, 2(4): 369–378, 1993.
- [86] A.-S. Yang, M.-T. Yang and M.-C. Hong. Numerical study for the impact of liquid droplets on solid surfaces.. *Proceedings of the Institution of Mechanical Engineers – Part C – Journal of Mechanical Engineering Science*, 221(3): 293–301, 2007.
- [87] P. R. Gunjal, V. V. Ranade and R. V. Chaudhari. Dynamics of drop impact on solid surface: Experiments and vof simulations. *AIChE Journal*, 51(1): 59–78, 2005.
- [88] M. Pasandideh-Fard, Y. M. Qiao, S. Chandra and J. Mostaghimi. Capillary effects during droplet impact on a solid surface. *Phys. Fluids*, 8(3): 650–659, 1996.
- [89] M. Pasandideh-Fard, R. Bhola, S. Chandra and J. Mostaghimi. Deposition of tin droplets on a steel plate: simulations and experiments. *International Journal of Heat and Mass Transfer*, 41(19): 2929–2945, 1998.
- [90] J. Madejski. Solidification of droplets on a cold surface. *International Journal of Heat and Mass Transfer*, 19(9): 1009–1013, 1976.
- [91] G. Trapaga and J. Szekely. Mathematical modeling of the isothermal impingement of liquid droplets in spraying processes. *Metallurgical and Materials Transactions B*, 22(6): 901–914, 1991.
- [92] T. Yoshida, T. Okada, H. Hamatani and H. Kumaoka. Integrated fabrication process for solid oxide fuel cells using novel plasma spraying. *Plasma Sources Science and Technology*, 1(3): 195–, 1992.
- [93] T. Watanabe, I. Kuribayashi, T. Honda and A. Kanzawa. Deformation and solidification of a droplet on a cold substrate. *Chemical Engineering Science*, 47(12): 3059–3065, 1992.
- [94] H. Fukanuma. A porosity formation and flattening model of an impinging molten particle in thermal spray coatings. *Journal of Thermal Spray Technology*, 3(1): 33–44, 1994.
- [95] J.-P Delplanque and R. Rangel. An improved model for droplet solidification on a flat surface. *Journal of Materials Science*, 32(6): 1519–1530, 1997-03-01.
- [96] A.C. Leger, M. Vardelle, A. Vardelle, B. Dussoubs and P. Fauchais. Splat formation: Ceramic particles on ceramic substrate. *Thermal Spray Science and Technology*, 169–174, 1995.
- [97] A. Kucuk, R. S. Lima and C. C. Berndt. Influence of plasma spray parameters on formation and morphology of zrO_2 - wt% Y_2O_3 deposits. *Journal of the American Ceramic Society*, 84(4): 693–700, 2001.
- [98] M. Pasandideh-Fard and J. Mostaghimi. On the spreading and solidification of molten particles in a plasma spray process effect of thermal contact resistance. *Plasma Chemistry and Plasma Processing*, 16(0): S83–S98, 1995.

References

- [99] K. Shinoda, M. Raessi, J. Mostaghimi, T. Yoshida and H. Murakami. Effect of substrate concave pattern on splat formation of yttria-stabilized zirconia in atmospheric plasma spraying. *J. Therm. Spray. Technol.*, 18(4): 609–618, 2009.
- [100] J. Shimizu, E. Ohmura, Y. Kobayashi, S. Kiyoshima and H. Eda. Molecular dynamics simulation of flattening process of a high-temperature, high-speed droplet influence of impact parameters. *Journal of Thermal Spray Technology*, 16(5): 722–728, 2007.
- [101] M. Fukumoto, H. Hayashi and T. Yokoyama. Relationship between particle's splat pattern and coating adhesive strength of hvof sprayed cu-alloy. *Journal of Japan Thermal Spraying Society*, 32(3): 149–156, 1995.
- [102] M. Fukumoto and Y. Huang. Flattening mechanism in thermal sprayed nickel particle impinging on flat substrate surface. *Journal of Thermal Spray Technology*, 8(3): 427–432, 1999.
- [103] M. Fukumoto, T. Yamaguchi, M. Yamada and T. Yasui. Splash splat to disk splat transition behavior in plasma-sprayed metallic materials. *Journal of Thermal Spray Technology*, 16(5): 905–912, 2007.
- [104] S. Chandra and P. Fauchais. Formation of solid splats during thermal spray deposition. *Journal of Thermal Spray Technology*, 18(2): 148–180, 2009.
- [105] S. R. L. Werner, J. R. Jones, A. H. J. Paterson, R. H. Archer and D. L. Pearce. Droplet impact and spreading: Droplet formulation effects. *Chemical Engineering Science*, 62(9): 2336–2345, 2007.
- [106] K. P. Gatne, M. A. Jog and R. M. Manglik. Surfactant-induced modification of low weber number droplet impact dynamics. *Langmuir*, 25(14): 8122–8130, 2009.
- [107] Y. P. Wan, H. Zhang, X. Y. Jiang, S. Sampath and V. Prasad. Role of solidification, substrate temperature and reynolds number on droplet spreading in thermal spray deposition: Measurements and modeling. *J. Heat Transfer*, 123(2): 382–389, 2001.
- [108] G. Montavon, S. Sampath, C.C. Berndt, H. Herman and C. Coddet. Effects of the spray angle on splat morphology during thermal spraying. *Surface and Coatings Technology*, 91(1-2): 107 - 115, 1997.
- [109] M. Bussmann, S. Chandra and J. Mostaghimi. Numerical results of off-angle thermal spray particle impact. *Proceedings of UTSC 99*, 783–786, 1999.
- [110] S.H. Leigh and C.C. Berndt. Evaluation of off-angle thermal spray. *Surface and Coatings Technology*, 89(3): 213 - 224, 1997.
- [111] M. Kanouff, R. Neiser and T. Roemer. Surface roughness of thermal spray coatings made with off-normal spray angles. *Journal of Thermal Spray Technology*, 7(2): 219–228, 1998.
- [112] S. Beauvais, V. Guipont, M. Jeandin, D. Jeulin and A. Robisson et al.. Study of the porosity in plasma-sprayed alumina through an innovative three-dimensional simulation of the coating buildup. *Metallurgical and Materials Transactions A*, 39(11): 2711–2724, 2008.
- [113] C. Kang, H. Ng and S. Yu. Plasma spray deposition on inclined substrates: Simulations and experiments. *Journal of Thermal Spray Technology*, 16(2): 261–274, 2007.
- [114] R. Ghafouri-Azar, J. Mostaghimi, S. Chandra and M. Charmchi. A stochastic model to simulate the formation of a thermal spray coating. *Journal of Thermal Spray Technology*, 12: 53–69, 10.1361/105996303770348500.2003.
- [115] MXXue, C. Sanjeev, J. Mostaghimi and C. Moreau. A stochastic coating model to predict the microstructure of plasma sprayed zirconia coatings. *Modelling and Simulation in Materials Science and Engineering*, 16(6): 065006, 2008.
- [116] Kentaro Shinoda, Hideyuki Murakami, Seiji Kuroda, Kohsei Takehara and Sachio Oki. In-situ visualization of impacting phenomena of plasma-sprayed zirconia: From single splat to coating formation. *Journal of Thermal Spray Technology*, 17(5): 623–630, 2008.

References

- [117] C. Kang, H. Ng and S. Yu. Imaging diagnostics study on obliquely impacting plasma-sprayed particles near to the substrate. *Journal of Thermal Spray Technology* , 15(1): 118–130, 2006-03-01.
- [118] J. R. Fincke and W. D. Swank. Air-plasma spraying of zirconia: Spray characteristics and standoff distance effect on deposition efficiency and porosity. *Thermal Spray: International Advances in Coating Technology* ,513-518, 1992.
- [119] L. Leblanc, P. Gougeon and C. Moreau. Investigation of the long-term stability of plasma spraying by monitoring characteristics of the sprayed particles. *Thermal Spray: A United Forum for Scientific and Technological Advances* ,567-576, 1997.
- [120] T.J. Jewett, W.C. Smith, H. Herman, J. Margolies and S. Sampath. Plasma processing of functionally graded materials part ii: Deposit formation. *Thermal Spray: A United Forum for Scientific and Technological Advances* ,607-612, 1997.
- [121] R. Dhiman, A. G. McDonald and S. Chandra. Predicting splat morphology in a thermal spray process. *Surf. Coat. Technol.* , 201(18): 7789 - 7801, 2007.
- [122] M.I. Boulous, P. Fauchais and E. Pfender. *Thermal Plasmas: Fundamentals and Applications*. Plenum Press, New York, London, 1994.
- [123] C. B. Ang, A. Devasenapathi, H. W. Ng, S. C. M. Yu and Y. C. Lam. A proposed process control chart for dc plasma spraying process. part ii. experimental verification for spraying alumina. *Plasma Chemistry and Plasma Processing* , 21(3): 401–420, 2001.
- [124] B. E. Launder and D. B. Spalding. The numerical computation of turbulent flows. *Computer Methods in Applied Mechanics and Engineering* , 3(2): 269–289, 1974.
- [125] C. L. V. Jayatilleke. The influence of prandtl number and surface roughness on the resistance of laminar sub-layer to momentum and heat transfer, volume 1 of progress in heat transfer. *Pergamon Press, Oxford* ,pages193, 1969.
- [126] S. A. Morsi and A. J. Alexander. An investigation of particle trajectories in two-phase flow systems. *Journal of Fluid Mechanics* , 55(02): 193–208 M3 - 10.1017/S0022112072001806, 1972.
- [127] W.E. Ranz and W.R. Marshall. Evaporation from drops. *Chemical Engineering Progress* , 3: 141-146, 1952.
- [128] M. Pasandideh-Fard and J. Mostaghimi. Deformation and solidification of molten particles on a substrate in thermal plasma spraying. *Proceedings of the 7th National Thermal Spray Conference* ,405-414, 1994.
- [129] J.W. McKelliget, G. Trapaga, E. Gutierrez-Miravete, Rensselaer and M. Cybulski. An integrated mathematical model of the plasma spraying process. *Thermal Spray 1998: Meeting the Challenges of the 21st Century* ,335-340, 1998.
- [130] R. Bolot, J. Li and C. Coddet. Some key advices for the modeling of plasma jets using fluent. *Thermal Spray 2005: Thermal Spray Connects: Explore Its Surfacing Potential* ,1367-1371, 2005.
- [131] H. Zhang, X.Y. Wang, L.L. Zheng and X.Y. Jiang. Studies of splat morphology and rapid solidification during thermal spraying. *International Journal of Heat and Mass Transfer* , 44(24): 4579 - 4592, 2001.
- [132] G.B. Arfken and H. Weber. *Mathematical Methods for Physicists*. Academic Press, 2000.